Improving Our Understanding of Arctic Tropospheric Pollution Through Measurements and Models

by

Tyler T. Wizenberg

A thesis submitted in conformity with the requirements
for the degree of Doctor of Philosophy

Department of Physics
University of Toronto

Improving Our Understanding of Arctic Tropospheric Pollution Through Measurements and Models

Tyler T. Wizenberg
Doctor of Philosophy

Department of Physics
University of Toronto
2024

Abstract

In this thesis, ground-based Fourier transform infrared (FTIR) measurements from the Polar Environment Atmospheric Research Laboratory (PEARL) in Eureka, Nunavut are used to retrieve total columns of CO, C_2H_2, C_2H_4, C_2H_6, CH_3OH, HCOOH, H_2CO, and PAN over the period of 2006–2020. The retrievals of C_2H_4 and PAN were developed as part of this thesis, and are the first long-term ground-based FTIR measurements of these gases in the high Arctic.

A global inter-comparison of the TROPOMI and ACE-FTS CO satellite datasets shows strong correlations but a latitudinal dependence of the biases, with positive biases in high-latitude regions and negative biases near the equator. At Eureka, the TROPOMI CO total columns were highly correlated with the ground-based FTIR measurements but with a mean bias of $14.7 \pm 0.16\%$. ACE-FTS and the FTIR CO partial columns show good correlations and a mean bias of $7.89 \pm 0.21\%$. All mean TROPOMI biases fall within the TROPOMI mission accuracy requirement.

FTIR measurements of CO, C_2H_4, CH_3OH, HCOOH, and PAN at Eureka were strongly enhanced in August 2017 due to wildfires in British Columbia and the Northwest Territories. For CO, C_2H_4, HCOOH, and PAN, these were the largest observed enhancements at Eureka. The emissions of these fires were estimated using FTIR and IASI measurements at Eureka, and for C_2H_4 and HCOOH they were found to be higher than previously reported. The fires were also simulated using the GEOS-Chem model, and the impact of the modeled biomass burning injection height and secondary VOC production was investigated.

The inter- and intra-annual variability of the eight trace gases were derived from FTIR measurements at Eureka, Nunavut (2006–2020) and Thule, Greenland (1999–2022). Consistent seasonal cycles were observed at both sites. Decreasing trends were observed for CO, C_2H_2, and CH_3OH at both sites, and for HCOOH at Eureka. Increasing trends were detected for C_2H_6 and H_2CO at both sites, and for PAN at Eureka. A GEOS-Chem simulation for 2003–2021 was performed. The model reproduced the seasonality of all gases, but showed large negative biases for some species. The modeled trends broadly agreed with observations for all species except C_2H_6, H_2CO, and PAN.

Acknowledgements

I would like to first acknowledge my doctoral supervisor, Kim Strong, for her years of guidance and support, and for facilitating the research presented in this dissertation. I would also like to acknowledge my doctoral committee members Dylan Jones and Kaley Walker. I am thankful for Kaley's support and insight throughout my TROPOMI validation project, and for her role in organizing the Canadian Arctic ACE/OSIRIS Validation Campaigns to Eureka. I am thankful for Dylan's help, support, and patience while I was learning to use GEOS-Chem, and for his insight when interpreting the model results.

I would also like to acknowledge Erik Lutsch, Sébastien Roche, and all of the students who have come before them who have contributed to the FTIR measurements at Eureka; if it were not for them we would not have the extensive time-series of trace gas measurements upon which this thesis work relies. I would also like to acknowledge all of the PEARL support staff including the Site Manager Pierre Fogal, and the on-site operators Peter McGovern, John Gallagher, and Andrew Hall. I would also like to thank the ECCC Eureka Weather Station staff for making our stays in the Arctic an enjoyable and memorable experience.

Lastly, I would like to acknowledge my family. I want to specifically acknowledge my parents Julie Tabata Wizenberg and Anatol Wizenberg, who have supported me throughout my long education, and who always ensured that I was on the right path. I would also like to acknowledge my wife, Sydney Barrett Wizenberg who has always been there for me through my undergraduate and graduate studies, and has provided her love and support throughout. Last but not least, I would like to acknowledge my two Pomeranians, Rosie and Vinny, who were my work-from-home co-workers throughout the lengthy COVID-19 pandemic.

Contents

List of Tables

List of Figures

List of Abbreviations

ACE-FTS Atmospheric Chemistry Experiment - Fourier Transform Spectrometer

ATom Atmospheric Tomography missions

BB Biomass burning

BC British Columbia

CAMS Copernicus Atmospheric Monitoring Service

CANDAC Canadian Network for the Detection of Atmospheric Change

CEDS Community Emissions Data System

CST Community Solar Tracker

CrIS Cross-track Infrared Sounder

DOFS Degrees of freedom for signal

ECCC Environment and Climate Change Canada

FORLI Fast Optimal Retrievals on Layers for IASI

FOV Field of view

FRP Fire radiative power

FTS Fourier transform spectrometer

FWHM Full width at half maximum

GCHP GEOS-Chem High Performance

GEOS-Chem Goddard Earth Observing System - Chemical transport model

GFAS Global Fire Assimilation System

GFED Global Fire Emissions Database

GMAO Global Modeling and Assimilation Office

HEMCO Harmonized Emissions Component

HITRAN High-resolution transmission molecular absorption database

HWHM Half-width at half-maximum

IASI Infrared Atmospheric Sounding Interferometer

ILS Instrument line shape

IRWG Infrared Working Group

LBLRTM Line-by-line radiative transfer model

MAP Maximum a posteriori

MCT Mercury Cadmium Telluride

MEGAN Model of Emissions of Gases and Aerosols from Nature

MERRA Modern-Era Retrospective analysis for Research and Applications

ME Modulation efficiency

MOPD Maximum optical path difference

MOPITT Measurements of Pollution in The Troposphere

MIR Mid-infrared

MODIS Moderate Resolution Imaging Spectroradiometer

NASA National Aeronautics and Space Administration

NCAR National Center for Atmospheric Research

NCEP National Centers for Environmental Prediction

NDACC Network for the Detection of Atmospheric Composition Change

NH Northern hemisphere

NMHC Non-methane hydrocarbon

NMVOC Non-methane volatile organic compound

NWT Northwest Territories

OEM Optimal estimation method

OPD Optical path difference

PBL Planetary boundary layer

PDF Probability density function

PEARL Polar Environment Atmospheric Research Laboratory

PSB Pituffik Space Base

PNE Pacific northwest event

RD Rapid delivery

RMS Root mean square

SH Southern hemisphere

SNR Signal-to-noise ratio

TCCON Total Carbon Column Observing Network

TES Tropospheric Emission Spectrometer

TM5 Tracer Model, version 5

TOA Top of atmosphere

TROPOMI Tropspheric Monitoring Instrument

UTLS Upper troposphere and lower stratosphere

VOC Volatile organic compound

VMR Volume mixing ratio

VNC Virtual network computing

ZPD Zero path difference

Chapter 1

Introduction and Motivation

1.1 Introduction

Earth's Polar regions act as receptors of global pollution, making them highly sensitive to atmospheric composition changes. The Arctic frequently experiences poor air quality due to the long-range transport of mid-latitude emissions, as well as scattered local sources (Law et al., 2014; Law and Stohl, 2007; Schmale et al., 2018; Shindell et al., 2008). The transport pathways of these emissions and the sensitivity of the Arctic environment, particularly to local sources of pollution, are currently not well understood (Arnold et al., 2016). In recent years, reductions in the extent of Arctic summer sea ice have accelerated the rate of industrialization in the Arctic and local emissions from mining, shipping, fossil fuel extraction and infrastructure development have already begun to affect the Arctic atmosphere (Marelle et al., 2016; Roiger et al., 2015). Additionally, wildfires have been found to be a significant periodic source of air pollution to the Arctic, and contribute significant concentrations of both aerosols and reactive trace gases to the region (Lutsch et al., 2016, 2019; Roiger et al., 2011; Viatte et al., 2013, 2014, 2015). Trace gases and aerosols emitted from fossil fuels and biomass burning can directly impact both air quality and the climate, and contribute to the acidification of soil and precipitation (Erisman et al., 2007, 2011; Sutton et al., 2011; Wentworth et al., 2018).

One of the greatest difficulties faced when attempting to monitor and assess the inter- and intra-annual variability of atmospheric pollutants in the Arctic region is the scarcity of reliable long-term measurements. In the past, efforts to measure tropospheric pollution in the Arctic were largely carried out on a short-term campaign basis, and it is difficult to extrapolate information on

annual or inter-annual trends from these temporally limited measurements (e.g., Alvarado et al., 2010; Liang et al., 2011; Singh et al., 1992; Wofsy et al., 1992). As a result, the budgets, seasonal cycles, and trends of many reactive tropospheric trace gases, including the contributions of biomass burning, are currently not well quantified. For studies of reactive tropospheric species at high latitudes, the use of a ground-based Fourier transform infrared (FTIR) spectrometer is advantageous because these instruments provide a consistent dataset at a specific site, and generally possess greater vertical sensitivity and lower detection limits than nadir-viewing satellite instruments, particularly in the Arctic where low thermal contrast presents challenges for space-based infrared measurements. Additionally, the use of a ground-based FTIR enables the simultaneous measurements of many atmospheric constituents, and can provide a long-term time series of each measured trace gas. The primary drawbacks of such an instrument for this type of application are that it requires direct sunlight, meaning that measurements are not possible during cloudy conditions or during polar night (approximately late October to late February each year at 80°N), and that they provide limited information on the spatial distributions and variability of these trace-gas species since measurements are made only at a single site.

Ground-based FTIR measurements can be complemented by satellite observations where available, and concentrations of many tropospheric pollutant species have been retrieved from several satellite instruments including the Measurements of Pollution in The Troposphere (MOPITT; e.g., Deeter et al., 2003), the Atmospheric Chemistry Experiment Fourier Transform Spectrometer (ACE-FTS; e.g., Coheur et al., 2007; Dufour et al., 2006; González Abad et al., 2009; Tereszchuk et al., 2013), the Tropospheric Emission Spectrometer (TES; e.g., Cady-Pereira et al., 2012, 2014; Dolan et al., 2016; Payne et al., 2014), the Infrared Atmospheric Sounding Interferometer (IASI; e.g., Coheur et al., 2009; Pommier et al., 2016; Razavi et al., 2011), and the Cross-track Infrared Sounder (CrIS; e.g., Payne et al., 2022; Shogrin et al., 2023). However, due to low ambient concentrations, high cloud cover, and the aforementioned issue of poor thermal contrast, difficulties are often encountered when attempting to retrieve these reactive species from satellite measurements in the polar regions. Recently, artificial neural network retrievals for IASI (ANNI) have been developed (Franco et al., 2018, 2022). These ANNI retrievals provide improved sensitivity over classical optimal estimation method (OEM) retrievals, potentially enhancing our ability to observe more species over high-latitude regions (Franco et al., 2018). ANNI products have already been used in biomass burning studies of ammonia (NH_3) (Whitburn et al., 2015, 2016, 2017), formic acid (HCOOH) and acetic acid (CH_3COOH) (Franco et al., 2020), and most recently hydrogen cyanide (HCN) (Rosanka et al., 2021). Due to the difficult retrieval conditions over high-latitude regions, it is imperative to

validate and inter-compare satellite measurements against ground-based datasets whenever possible, to improve our confidence in these observations.

In addition to ground- and space-based observations, global chemical transport models (CTMs) such as GEOS-Chem (http://geos-chem.org) can provide another valuable perspective on the transport, chemistry, and trends of these tropospheric pollutants, filling in gaps where there are sparse or no measurements available. However, the high Arctic is a notoriously difficult region to simulate with CTMs due to the extreme atmospheric and solar conditions, and complex transport pathways often leading to discrepancies across models (Eckhardt et al., 2015; Monks et al., 2015; Shindell et al., 2008; Stohl et al., 2013; Whaley et al., 2022, 2023; Yang et al., 2020). CTMs also rely heavily on external emissions inventories that can often have large uncertainties due a reliance on experimentally determined emission factors. In the case of biomass burning inventories, these uncertainties can be particularly large as a result of the heterogeneity in fuel types and the variability in emissions as a function of combustion phase (Akagi et al., 2011; Andreae and Merlet, 2001; Andreae, 2019). Furthermore, CTMs can also suffer from model and transport errors resulting from the use of finite chemical and transport operator time-steps and the assimilated meteorological fields, and from the presence of a singularity at the poles where the lines of longitude converge when using a rectilinear latitude-longitude grid (Philip et al., 2016; Stanevich et al., 2020; Yu et al., 2018). Previous studies have shown that CTMs, including GEOS-Chem, consistently underestimate the mixing ratios of many tropospheric constituents including CO, HCOOH and methanol (CH_3OH) relative to observations, with the largest biases occurring at high latitudes, possibly indicating unknown local sources, missing chemistry, or inaccurate emissions (Bates et al., 2021; Chen et al., 2019; Franco et al., 2021; Millet et al., 2015; Paulot et al., 2011; Schobesberger et al., 2016; Stavrakou et al., 2012; Whaley et al., 2022). As a result, it is important to routinely evaluate model performance against observations, particularly for lesser-studied atmospheric constituents, to identify areas for improvement and to increase our confidence in these model simulations.

1.2 Overview of Arctic Pollution and Transport Pathways

Due to the remoteness of the high-Arctic region, it is often perceived to be extremely clean and free of many of the atmospheric pollutants which beset our densely populated urban centres. However, even the earliest European Arctic explorers documented dirty snow deposits, and a thin layer of haze in the air (Nordenskiöld, 1883), while the Inuit were also familiar with this phenomenon and called it “poo-jok” (Schnell, 1984). During the 1950s, pilots flying over the Arctic again made observations

of reduced visibility and a strange haze blanketing the area, but its origins remained unknown (Mitchell, 1957). It was not until the mid-1970s that the link was drawn between the northerly transport of mid-latitude anthropogenic emissions and the seasonal 'Arctic haze' phenomenon that would manifest in the region each spring and winter (Barrie, 1986; Shaw, 1981). The Arctic haze is primarily composed of sulfate, organic particulate matter, and black carbon and also contains high concentrations of tropospheric ozone precursors such as nitrogen oxides ($NO_x = NO + NO_2$), peroxyacetyl nitrate (PAN) and volatile organic compounds (VOCs) (Law et al., 2014; Law and Stohl, 2007; Stohl et al., 2013). This haze can also have a variety of climatic and environmental effects on the pan-Arctic region. Measurements at Utqiaġvik (formerly Barrow), Alaska have demonstrated that the albedo of the aerosols within the layer of haze can reach a minimum of 0.9 during the winter, suggesting the presence of high concentrations of light-absorbing material, with the majority of the absorption being attributed to black carbon aerosols (Quinn et al., 2002). Black carbon is emitted from both anthropogenic sources and wildfires, and when it settles out of the atmosphere and lands on the snow and ice, it can have significant implications for surface albedo (Kim et al., 2005; Quinn et al., 2008). In comparison to lower latitudes, the efficiency of sunlight absorption by a layer of pollution near the surface in the Arctic is much greater due to the high albedo of ice and snow, which can result in multiple reflections between the surface and scattered light from the layer of haze (Law and Stohl, 2007). Measurements made by Ritter et al. (2005) on Svalbard showed that the Arctic haze had a measurable radiative forcing effect, altering the flux of downwelling long-wave infrared radiation by +3 to +4.7 W/m^2 and outgoing radiation by −0.23 to +1.17 W/m^2. Furthermore, recent increases in emissions of black carbon and ozone (O_3) precursors from the Asian continent are estimated to have contributed to two-thirds of the observed warming in the Arctic (Quinn et al., 2008; Shindell and Faluvegi, 2009). The accelerated warming of the Arctic region has already begun to negatively impact northern indigenous populations through uncertain weather patterns, reduced sea-ice coverage, and harm to their food security (IPCC, 2022; Sansoulet et al., 2020; Weatherhead et al., 2010).

Arctic tropospheric air pollution has a pronounced seasonal cycle, with peaks in the late winter and early spring, and this seasonality is driven by various factors. Firstly, during the polar winter, strong temperature inversions are able to form above the surface, which causes the atmosphere to become extremely stable (Curry, 1983; Kahl et al., 1992). These stable atmospheric conditions restrict the turbulent vertical mixing between atmospheric layers, and inhibit the removal of aerosols and gases (Law and Stohl, 2007; Shaw, 1995). This significantly increases the lifetime of tropospheric pollutants, as the removal or loss processes via dry and wet deposition are almost non-existent. Sec-

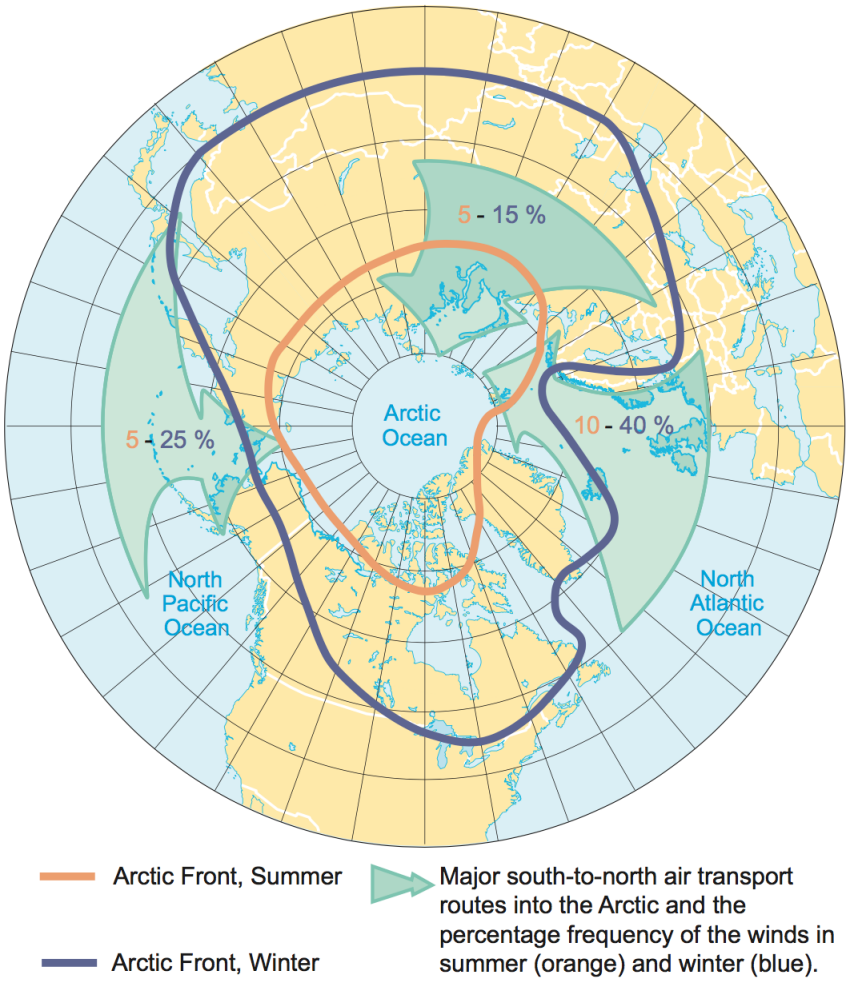

Figure 1.1: Mean position of the Arctic air mass in winter (blue) and summer (orange), overlaid with the percentage frequency of south-to-north pollution transport routes in summer and winter. Image reproduced from AMAP (2006).

ondly, due to the absence of sunlight (and thus the absence of the hydroxyl radical OH) during polar night, the removal of tropospheric pollutants via photolysis and photochemistry is also inhibited, further increasing the lifetimes of these pollutant species.

The high Arctic lower troposphere is generally quite well isolated from lower latitudes due to the very cold air masses in this region. This region is characterized by strong temperature contrasts near the surface and sloping isentropes (i.e., surfaces of constant potential temperature), and is referred to as the 'Arctic front' or 'polar dome' (Bozem et al., 2019; Klonecki, 2003; Stohl, 2006). Air parcels tend to maintain near-constant potential temperatures during transport, since atmospheric circulation can be closely described by adiabatic motions in the absence of diabatic processes relating to turbulence, clouds, and radiation. As a result, since the potential temperature within the polar

dome area is low, only air parcels which have undergone some degree of diabatic cooling are able to enter the polar dome from outside (Bozem et al., 2019; Stohl, 2006).

During the summer months, the Arctic front is generally constrained to the high Arctic region, preventing any transported low-level air masses from mid-latitudes from entering the high Arctic lower troposphere (see Fig. 1.1) (Klonecki, 2003). One notable transport pathway for pollution during the summertime is via the direct injection of biomass burning smoke into the upper troposphere and lower stratosphere (UTLS) by pyrocumulonimbus (pyroCb) storms caused by intense wildfires (illustrated in Fig. 1.2) (Fromm et al., 2008, 2010; Peterson et al., 2018). These pyroCbs have been likened to volcanic eruptions in terms of their scale, and a recent example of this is the August 2017 Canadian wildfires, which injected smoke plumes directly into the lower stratosphere (at a height of approximately 12–13 km), resulting in subsequent rapid transport to the high-Arctic region (Fromm et al., 2021; Lutsch et al., 2019; Peterson et al., 2018). This particular event is discussed in detail in Chapter 5. Another transport pathway during the summer months is the vertical lifting of polluted mid-latitude airmasses along the boundary of the polar dome, and subsequent mixing into the polar dome, however this process is very slow, meaning that most short-lived pollutants and aerosols are removed before reaching the Arctic atmosphere (Law and Stohl, 2007; Quinn and Stohl, 2015). It should be noted that any direct emissions within the boundaries of the polar dome (e.g., from Arctic shipping, industry, or high-latitude fires) can be freely transported to the high Arctic troposphere during the summer months. Sources of air pollution from within the Arctic Circle and the nearby sub-Arctic have already been found to be important in some areas, and local sources are anticipated to increase rapidly in the near future (Arnold et al., 2016; Peters et al., 2011; Stohl et al., 2013)

During the winter months, the Arctic front descends southward towards the mid-latitudes, often extending as low as 40°N over North America and Eurasia as shown in Fig. 1.1 (AMAP, 2006). This facilitates the trapping of emissions from both continents, and allows them to be transported rapidly northward above the Arctic Circle as shown in Fig. 1.2 (AMAP, 2006; Arnold et al., 2016). These factors allow for the accumulation of significant quantities of pollutants and aerosols in the Arctic troposphere during the wintertime, resulting in the springtime Arctic haze phenomenon. As a result, the Arctic region is extremely sensitive to mid-latitude emissions, particularly those from Eurasia. As wildfire frequency and severity grow, and anthropogenic emissions from Eurasia and North America continue to rise, the subsequent impacts on the Arctic climate, ecosystem, and environment are expected to worsen, but the extent and nature of these impacts are highly uncertain (Boulanger et al., 2014; Law et al., 2014; Law and Stohl, 2007).

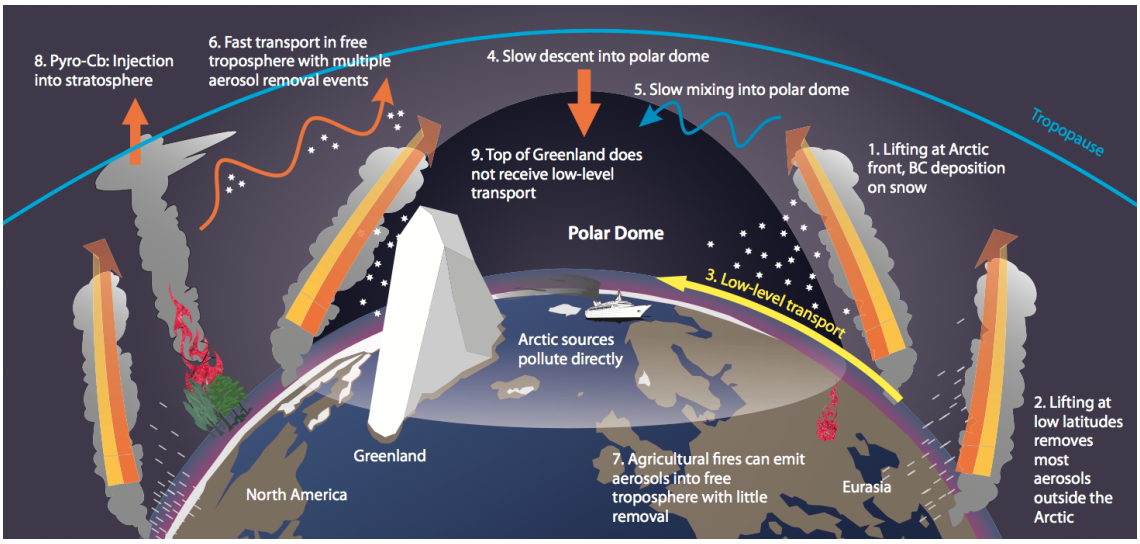

Figure 1.2: Various transport pathways of pollution from mid-latitude regions to the Arctic Circle. Image reproduced from Quinn and Stohl (2015).

1.3 Sources and Impacts of Tropospheric Pollutants in the Arctic

As briefly discussed in Sect. 1.2, Arctic air pollution is comprised of a broad range of aerosols and reactive trace gases. Of the trace gases, carbon monoxide (CO), PAN, and VOCs comprise a significant majority of non-particulate pollution in the Arctic, particularly during the springtime (Law et al., 2014; Quinn et al., 2008). These gases have very few local sources, and are primarily emitted from mid-latitude sources, but they can adversely impact the Arctic climate, environment, and atmosphere in a variety of ways. In the following subsections, the sources and impacts of CO, PAN, VOCs and other reactive tropospheric gases will be discussed.

1.3.1 Carbon Monoxide

CO is an ubiquitous air pollutant that has wide-reaching impacts on atmospheric chemistry and the oxidative capacity of the atmosphere through its influence on the global OH budget. It is estimated that the reaction of CO with OH accounts for 40% of OH removal in the global troposphere (Lelieveld et al., 2016). As a result, CO is a precursor of O_3 and it affects the atmospheric lifetime of methane (CH_4), making it an indirect greenhouse gas. The primary sources of CO in the troposphere are fossil fuel burning, biomass burning, and the oxidation of CH_4 (Deeter et al., 2017; Jaffe, 1968; Zheng et al., 2019). The mean global lifetime of CO is approximately two months, which is long

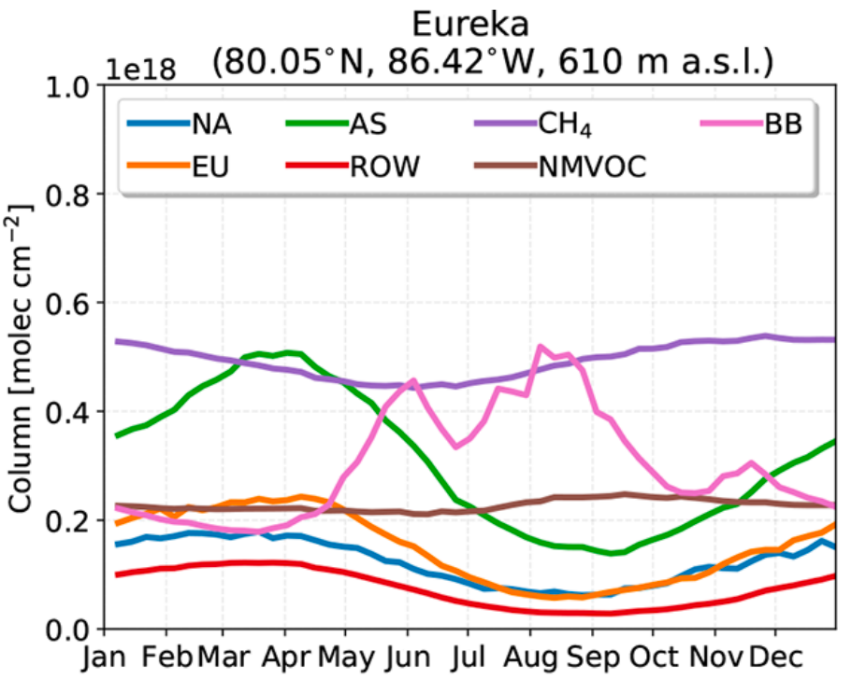

Figure 1.3: GEOS-Chem tagged-CO simulation for the period 2003–2018 showing the various source contributions to total CO column concentrations at Eureka, Nunavut. NA, EU, AS, and ROW are North American, European, Asian, and rest of world anthropogenic emissions, respectively. CH_4 and NMVOC represent CO produced by CH_4 and non-methane VOC oxidation, while BB represents CO emissions from biomass burning. Figure reproduced from Lutsch et al. (2020).

enough to allow it to be transported from the mid-latitudes to the high Arctic, however under the conditions of polar night the lifetime of CO can be as long as one year (Holloway et al., 2000; Khalil and Rasmussen, 1990; Yurganov, 1997). GEOS-Chem tagged-CO simulations covering the period of 2003–2018 by Lutsch et al. (2020) are shown in Fig. 1.3 and illustrate that anthropogenic emissions from Asia are one of the largest sources of CO to Eureka, Nunavut during the late winter and early springtime and that biomass burning is the most significant source during the summer months, while atmospheric CH_4 and non-methane VOC (NMVOC) oxidation provide relatively consistent sources throughout the whole year.

1.3.2 PAN

PAN is a significant component of springtime Arctic air pollution, and airplane measurements made during the 2008 NASA Arctic Research of the Composition of the Troposphere from Aircraft and Satellites (ARCTAS) campaign discovered that PAN was the dominant form of tropospheric odd nitrogen ($NO_y = NO_x + PAN + HNO_3 +$ organic nitrates) in the Arctic, accounting for approxi-

mately 50% of NO_y in the spring and 70% in the summer (Liang et al., 2011). The average lifetime of PAN is 1 hour at 298 K, and this lifetime has been shown to increase by a factor of 2 with each decrease in air temperature of 4 K (Tuazon et al., 1991; Fischer et al., 2014). This property of PAN allows it to form in polluted regions and within biomass burning plumes, be lifted into the colder regions of the UTLS where its lifetime can be as long as several weeks, and then be transported more than 10,000 km to remote areas of the globe (Glatthor et al., 2007; Tereszchuk et al., 2013). When the air masses eventually descend from the UTLS, PAN thermally decomposes to re-release NO_x. The resultant NO_x is then photolyzed, producing tropospheric O_3 which is a primary component of photochemical smog and acts as a powerful greenhouse gas, having a direct warming effect on the Arctic region. Model studies have estimated that increases in tropospheric O_3 due to rising mid-latitude fossil fuel emissions have contributed between +0.4° and +0.5°C to surface temperatures in the Arctic over the 20th century (approximately 30% of the observed warming) (Shindell et al., 2006).

1.3.3 VOCs and Other Reactive Gases

VOCs, often referred to as solvents, are a large group of reactive organic compounds that have high vapor pressures at room temperature (i.e., they easily evaporate), and typically have low water solubility (Anand et al., 2014). Many VOCs can have adverse health impacts when inhaled in high concentrations or ingested in drinking water, and they can be serious environmental contaminants (Anand et al., 2014). VOCs are used in a broad range of household and industrial applications, and also occur naturally, such as being emitted biogenically from plants, or from biomass burning (Akagi et al., 2011; Alwe et al., 2019; Anand et al., 2014; Fall and Benson, 1996; Holzinger et al., 1999). In the work presented in this thesis, we focus on a few VOCs in particular that can readily be measured and retrieved in the mid-infrared region of the electromagnetic spectrum, namely acetylene (C_2H_2), formaldehyde (H_2CO), and CH_3OH.

C_2H_2 is a NMVOC primarily emitted from biofuel and fossil fuel combustion, as well as biomass burning. It is strongly correlated with CO in the atmosphere as they share very similar sources and sinks (Duflot et al., 2015; Xiao et al., 2007). H_2CO is one of the most abundant VOCs in the atmosphere, and it plays an important role in atmospheric photochemistry and air quality (Luecken et al., 2012). H_2CO is directly emitted from a variety of anthropogenic and natural sources including fossil fuel combustion, biomass burning, and biogenic emissions, but it is also produced in large quantities via secondary formation in the atmosphere through the oxidation of CH4 and NMVOCs

(Holzinger et al., 1999; Luecken et al., 2012, 2018; Wittrock et al., 2006). It is primarily removed via its reaction with OH yielding hydroperoxy radicals (HO_2), which can subsequently be converted back into OH, meaning that OH plays an important role in both the formation and removal of H_2CO from the atmosphere (Mahajan et al., 2010; Nussbaumer et al., 2021; Wittrock et al., 2006). CH_3OH is the second-most abundant organic gas (after CH_4) found in the global remote atmosphere (Bates et al., 2021). It is primarily emitted biogenically from plants during their growth stage (and to a lesser extent when they decay), however, it is also emitted from biomass burning (Fall and Benson, 1996; Holzinger et al., 1999; MacDonald and Fall, 1993; Stavrakou et al., 2011; Wells et al., 2014). Through its oxidation, CH_3OH influences global OH concentrations, produces HO_2 radicals and H_2CO, and it can influence the budget of tropospheric O_3 (Folberth et al., 2006; Tie et al., 2003).

In addition to the VOCs, three other reactive species of importance are ethylene (C_2H_4), ethane (C_2H_6), and HCOOH. C_2H_4 is one of the most abundant atmospheric unsaturated hydrocarbons, with global emissions on the order of 20 Tg/year, half of which is estimated to be the product of biomass burning (Folberth et al., 2006; Herbin et al., 2009; Horowitz et al., 2003). The atmospheric lifetime of C_2H_4 is short, at approximately one to three days due to its high reactivity with OH and O_3. C_2H_4 is directly emitted from anthropogenic sources such as motor vehicle exhaust and petrochemical production, and natural sources including direct emissions from plants and soils, and forest fires (Folberth et al., 2006; Morgott, 2015; Sawada and Totsuka, 1986). There are currently no known secondary production pathways of C_2H_4 in the atmosphere. C_2H_6 is the most abundant non-methane hydrocarbon (NMHC) in the atmosphere, and is an important precursor to tropospheric O_3 and PAN through its oxidation in the presence of NO_x in polluted airmasses (Fischer et al., 2014; Franco et al., 2016a). C_2H_6 also acts as an indirect greenhouse gas through its influence on the global lifetime of CH_4 as a result of its removal from the atmosphere by OH. C_2H_6 differs from many other hydrocarbons in that it is primarily emitted from the various stages of natural gas production and distribution as opposed to the direct combustion of fossil fuels (Franco et al., 2016a; Friedrich et al., 2020; Xiao et al., 2008). HCOOH is the most abundant carboxylic acid in the global troposphere, with a relatively short lifetime on the order of four days (Stavrakou et al., 2012). Sources of HCOOH include anthropogenic emissions, direct emissions from plant leaves, and biomass burning, while the main sinks of HCOOH are oxidation by OH, as well as dry and wet deposition (Chameides and Davis, 1983; Chen et al., 2021). As a result of its removal from the atmosphere by dry and wet deposition, HCOOH directly contributes to soil and rainwater acidity in remote regions (Paulot et al., 2011; Stavrakou et al., 2012).

Figure 1.4: The PEARL Ridge Lab in late February 2019.

1.4 The Polar Environment Atmospheric Research Laboratory

In order to improve our understanding of tropospheric pollution in the high Arctic, we require a long time-series of reliable measurements in a sparsely sampled region of the globe. To this end, the Canadian Network for the Detection of Atmospheric Change (CANDAC) has established the Polar Environment Atmospheric Research Laboratory (PEARL) at Eureka, Nunavut (80.05°N, 86.42°W) on Ellesmere Island to perform long-term atmospheric measurements in the high Arctic (Fogal et al., 2013). PEARL consists of three individual facilities: the Ridge Lab (formerly the Arctic Stratospheric ozone Observatory, or AStrO; shown in Fig. 1.4) which is located at 610 m.a.s.l. approximately 15 km from the Environment and Climate Change Canada (ECCC) Eureka Weather Station, the Zero-altitude PEARL Auxiliary Laboratory (ØPAL), and the Surface and Atmospheric Flux, Irradiance and Radiation Extension (SAFIRE).

Key to the work presented in this thesis is the Bruker IFS 125HR high-spectral-resolution FTIR

spectrometer, which is located in the IR lab at the PEARL Ridge Lab. The mid-infrared measurements from this instrument are regularly contributed to the Network for the Detection of Atmospheric Composition Change (NDACC) (De Mazière et al., 2018). The instrument was installed in July 2006 and made regular measurements during the sunlit portion (approximately late February to early October) of the year up until March 2020, when the COVID-19 pandemic halted nominal operations. Full details on the PEARL FTIR are provided in Sect. 2.3. The PEARL FTIR data have been used to validate measurements from many satellite instruments including ACE-FTS (Batchelor et al., 2010; Bognar et al., 2019; Fu et al., 2011; Griffin et al., 2017), TANSO-FTS onboard the Japanese GOSAT satellite (Holl et al., 2016; Olsen et al., 2017), MOPITT on NASA Terra (Buchholz et al., 2017; Jalali et al., 2022), and the TROPospheric Monitoring Instrument (TROPOMI) onboard Sentinel-5P (Sha et al., 2021; Vigouroux et al., 2020). The PEARL FTIR has also played a vital role in several past studies of Arctic pollution including many which were focused on wildfires (e.g., Lutsch et al., 2016, 2019, 2020; Viatte et al., 2013, 2014, 2015).

1.5 Thesis Overview

1.5.1 Scientific Objectives

The primary scientific objectives of this thesis are summarized as follows:

1. To inter-compare and validate satellite observations of tropospheric pollutants over the high Arctic with ground-based measurements and model simulations.

2. To investigate the enhancements of reactive tropospheric species in the Arctic due to the August 2017 Canadian wildfires, and to place this event in the context of previously observed fires.

3. To investigate the inter- and intra-annual variability of tropospheric pollutants in the high Arctic region over long time-scales.

To achieve the first objective, we utilized the CO total column time-series (2006–2020) retrieved from the ground-based Bruker 125HR FTIR at Eureka, Nunavut to inter-compare and validate the CO products from TROPOMI and ACE-FTS over the high Arctic region. The results of this study are described in Chapter 4.

To address objective two, we have evaluated the PEARL FTIR total column time-series of CO, C_2H_4, CH_3OH, HCOOH, and PAN and used them to quantify the emissions from the August 2017

Canadian fires in terms of the enhancement ratios, emission ratios, and emission factors. Additionally, we performed GEOS-Chem model simulations of these fires and investigated the influence of the plume injection scheme of the model on the resulting enhancements at Eureka. We have also performed comparisons of the IASI CO, C_2H_4, CH_3OH, PAN, and HCOOH products with PEARL FTIR measurements and GEOS-Chem model simulations during the August 2017 wildfire event, further addressing thesis objective one. The results of this study are presented in Chapter 5.

Lastly, to address objective three, we utilize the total column time-series from the PEARL FTIR, as well as another Bruker 125HR located at the Pituffik Space Base (PSB; formerly the Thule Air Force Base) in Thule, Greenland (76.53°N, 68.74°W) to investigate long-term trends and intra-annual variability of CO, C_2H_2, C_2H_4, C_2H_6, CH_3OH, H_2CO, HCOOH, and PAN in the high Arctic. FTIR data from the latter site are currently associated with Thule, so we use that designation throughout this thesis. We complement these measurements with long simulations covering the period of 2003–2021 from the GEOS-Chem High Performance (GCHP) model to provide an additional point of comparison and to examine the capabilities of the model in the high Arctic. This study is summarized in Chapter 6.

1.5.2 Outline

The remaining chapters of this thesis are outlined as follows:

Chapter 2 provides an overview of Fourier transform spectroscopy, the Eureka PEARL Bruker IFS 125HR spectrometer, and a summary of retrieval theory in the context of trace gas retrievals.

Chapter 3 summarizes the Eureka SFIT4 retrievals, including the newly implemented retrievals of PAN and C_2H_4.

Chapter 4 presents the results of the inter-comparison and validation of global TROPOMI and ACE-FTS CO measurements, and the localized comparisons of both satellite instruments with PEARL Bruker 125HR CO measurements at Eureka. This study provides insights into the data quality and latitudinal biases present in the TROPOMI CO dataset, particularly over high-latitude regions.

Chapter 5 investigates the enhancements of CO, C_2H_4, CH_3OH, HCOOH, and PAN over the high Arctic resulting from the August 2017 Canadian wildfires in British Columbia and the Northwest Territories as observed by the PEARL FTIR and the IASI satellite instruments.

The observational results are complemented by GEOS-Chem model simulations of the wildfire smoke plumes and their transport, and sensitivity tests relating to the injection height of the plume in the model were also performed.

Chapter 6 investigates the seasonal variability and long-term trends of CO, C_2H_2, C_2H_4, C_2H_6, CH_3OH, HCOOH, H_2CO, and PAN in the high Arctic as measured by the PEARL (2006–2020) and Thule (1999–2022) FTIR spectrometers. The intra- and inter-annual variabilities of these eight trace gas species were also investigated using a long simulation performed with the new GEOS-Chem High Performance model covering the period of 2003–2021, providing an additional point of comparison with observations, and allowing for an evaluation of the model's performance at these two high-Arctic sites.

Chapter 7 presents the conclusions of this thesis, and provides suggestions for avenues of future work.

1.5.3 Contributions

The work in Chapter 3 was carried out by the author, Erik Lutsch, Stephanie Conway, and Kim Strong. During the period of this thesis work, operation of the PEARL FTIR was performed by the author, Beatriz Herrera, Erik Lutsch, and Sébastien Roche. Stephanie Conway implemented the SFIT4 retrieval algorithm at the University of Toronto. The author implemented the retrievals of PAN and C_2H_4 with support and input from Emmanuel Mahieu and Mathias Palm.

The work in Chapter 4 was carried out by the author, Kim Strong, Kaley Walker, Erik Lutsch, Tobias Borsdorff, and Jochen Landgraf. The study was designed by the author, Kim Strong, and Kaley Walker. The author performed the formal analysis, software development and presentation of the results, and the PEARL FTIR CO retrievals for 2018–2020. Erik Lutsch performed the CO retrievals for 2006–2018. Tobias Borsdorff and Jochen Landgraf oversaw the TROPOMI data analysis and provided support. All authors discussed the results and provided feedback on the study.

The work in Chapter 5 was carried out by the author, Kim Strong, Dylan Jones, Erik Lutsch, Emmanuel Mahieu, Bruno Franco, and Lieven Clarisse. The study was designed by the author, Kim Strong, and Dylan Jones. The author performed the GEOS-Chem model simulations, formal analysis, software development and presentation of the results, and the

PEARL FTIR PAN and C_2H_4 retrievals with support from Emmanuel Mahieu, and the retrievals of the other species for 2018–2020. Erik Lutsch performed the retrievals of the other species for 2006–2018, and provided support for the GEOS-Chem simulations. Bruno Franco and Lieven Clarisse provided the IASI data during the fire period, and assisted in the preparation of the figures. All co-authors discussed the results and provided feedback on the study.

The work in Chapter 6 was carried out by the author, Kim Strong, Dylan Jones, Jim Hannigan, Ivan Ortega, and Emmanuel Mahieu. The study was designed by the author, Kim Strong, and Dylan Jones. The author performed the GEOS-Chem High Performance model simulations, formal analysis, software development and presentation of the results. Jim Hannigan and Ivan Ortega implemented the PAN and C_2H_4 retrievals at Thule, and provided the time-series of all species at that site. All co-authors discussed the results and provided feedback on the study.

Chapter 2

Fourier Transform Spectroscopy

2.1 Atmospheric Spectroscopy

Spectroscopy is a widely used technique for the analysis of mixtures of substances in the solid, liquid, and gas phases. By analyzing the absorption, emission or scattering of electromagnetic radiation by molecules or atoms, we are able to infer information about the chemical composition, structure, and the distribution of electrons (Hollas, 2004). Spectroscopy relies on the core principles of quantum mechanics, and the two fields have evolved in tandem. The discoveries by Planck, Einstein and Bohr in the early 20th century, which demonstrated that atoms and molecules possess quantized energy states, laid the groundwork for the field of modern spectroscopy. Molecules have energy that is distributed between different modes: vibrational energy, resulting from a displacement of their atoms from the centre of equilibrium; rotational energy, which originates from a rotation of the molecule about its centre of gravity; electronic energy, which is potential energy associated with the distribution of the electrons within the atoms themselves; and translational energy, which is the kinetic energy of the molecule resulting from its motion in space, although this is not quantized (Hollas, 2004). A molecule that is in one of its energy levels (defined by the combination of its vibrational, rotational, and electronic energy states), can move to a different energy level only through the absorption or emission of a finite quantum of electromagnetic energy. Knowledge of these quantized energy levels provides the basis for the determination of atmospheric trace-gas composition from solar absorption spectra.

2.1.1 Vibrational-Rotational Spectroscopy

In the case of infrared spectroscopy, we are primarily concerned with the transitions between vibrational and rotational energy levels. The energies of rotational transitions are relatively small, and these lines these tend to occur in the longer wavelength regions of the electromagnetic spectrum (i.e., in the far-infrared or microwave). In contrast, vibrational transitions tend to emit or absorb larger quantities of energy, with transitions typically manifesting in the mid- or near-infrared (Griffiths and De Haseth, 2007). Vibrational transitions tend to be coupled with a rotational excitation, and the spectroscopic study of transitions of this type is known as *vibrational-rotational spectroscopy*. Since this work is centered on the infrared spectroscopy of the atmosphere, we will only discuss vibrational-rotational spectroscopy for the remainder of this section.

Here we provide a basic overview of vibrational-rotation spectroscopy following the derivations in Hollas (2004) and Griffiths and De Haseth (2007). For the sake of simplicity, we consider the most basic example of the vibrational-rotational spectra, which is that of a diatomic molecule. If we make the assumption that it is a rigid rotor (i.e., bond length remains constant regardless of rotational velocity), and that the molecule undergoes electronic, vibrational, and rotational transitions separately (the Born-Oppenheimer Approximation), then the total energy, E_{tot}, is given by the sum of the individual energy contributions (Hollas, 2004):

$$E_{tot} = E_{electronic} + E_{rot} + E_{vib}. \tag{2.1}$$

However, in the context of infrared spectroscopy we can disregard the electronic energy contribution in Eq. 2.1 because these higher-energy transitions tend to occur in the visible and ultraviolet regions of the electromagnetic spectrum. The rotational energy component is given by:

$$E_{rot} = E_J = BJ(J+1), \tag{2.2}$$

where $B = \frac{h}{8\pi^2 cI}$ is the rotational constant, J is the rotational quantum number (an integer), h is Planck's constant, I is the moment of inertia, and c is the speed of light.

The vibrational energy component for a harmonic oscillator is given by:

$$E_{vib} = E_v = h\omega(v + \frac{1}{2}), \tag{2.3}$$

where ω is the frequency of the vibration, and v is the vibrational quantum number. Since the

vibrational energy transition is considerably larger than the rotational transition, the resulting vibrational-rotational spectrum consists of several rotational lines located around the central vibrational wavenumber. Combining Eqs. 2.2 and 2.3, the total vibrational-rotational energy can be written as:

$$E_{tot} = BJ(J+1) + h\omega(v + \frac{1}{2}). \tag{2.4}$$

For the rotational energy states of diatomic molecules, the selection rule is $\triangle J = \pm 1$, so that (Griffiths and De Haseth, 2007):

$$E_J - E_{J-1} = BJ(J+1) - BJ(J-1) = 2BJ. \tag{2.5}$$

From Eq. 2.5, we see that for a rigid rotor, the pure rotation spectrum is comprised of a series of lines which are equally spaced by 2B cm^{-1} (see Fig. 2.1a). For most molecules, B will be small and the pure rotational spectrum will occur in the microwave region of the electromagnetic spectrum. However, in the case of lighter molecules such as CO, H_2O and HCl, their rotational transitions absorb in the mid and far-infrared (Griffiths and De Haseth, 2007).

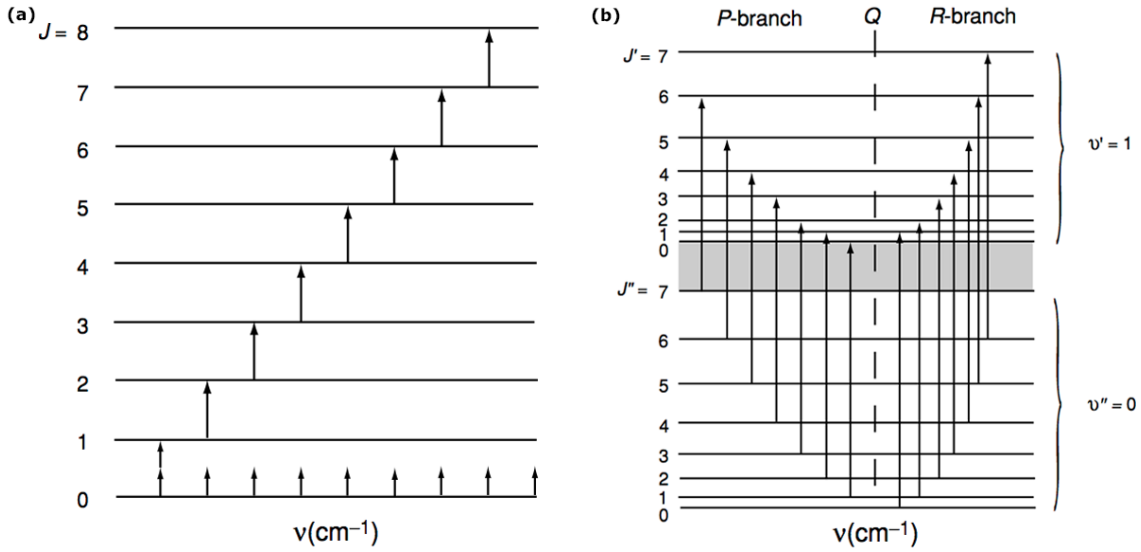

Figure 2.1: (a) Pure rotational transitions, following the selection rule of $\triangle J = +1$ and equally spaced by 2B cm^{-1}. (b) Simultaneous vibrational and rotational transitions for a non-rigid rotor where $\triangle J = -1$ corresponds to the P-branch, and $\triangle J = +1$ corresponds to the R-branch. The Q-branch ($\triangle J = 0$) is also shown, but is forbidden for diatomic molecules. Figure reproduced from Liou (2002).

A diatomic molecule, X-Y, will have a single fundamental vibration mode at wavenumber $\tilde{\nu}_0$, however this will be infrared active only if X≠Y because of the presence of a dipole moment (Griffiths

and De Haseth, 2007). For any vibrational transition of a gaseous diatomic molecule, a simultaneous rotational transition must also occur, i.e., $\triangle v_i = \pm 1$ and $\triangle J = \pm 1$. As a result, the vibrational-rotational spectrum of a rigid diatomic molecule consists of a series of equally spaced lines above and below $\tilde{\nu}_0$ which correspond to the $\triangle J = +1$ and $\triangle J = -1$ transitions, respectively. The series of lines which correspond to the $\triangle J = -1$, and which are located below $\tilde{\nu}_0$ is referred to as the P-branch, while the lines above $\tilde{\nu}_0$ corresponding to $\triangle J = +1$ are known as the R-branch (see Fig. 2.1b) (Griffiths and De Haseth, 2007). Additionally, there is a Q-branch which corresponds to $\triangle J = 0$, however this is forbidden for diatomic molecules. For complex molecules, the selection rules depend largely on the type of vibration (i.e., perpendicular or parallel to the axis of rotation) and rotation that the molecule is undergoing.

In practice, the assumption of a rigid rotor does not hold and centrifugal forces cause the bond length of X-Y to increase as the angular velocity of the molecule increases. This is known as centrifugal distortion, and it has the effect of increasing the moment of inertia of the molecule, and thus decreasing B at high values of J (Griffiths and De Haseth, 2007). To a first approximation, the effects of centrifugal distortion can be accounted through the inclusion of a second term in Eq. 2.2:

$$E_J = BJ(J+1) - DJ^2(J+1)^2, \tag{2.6}$$

where D is the centrifugal distortion constant. Typically, $0.1 < B < 10$ cm^{-1} and $D \sim 10^{-4}$ cm^{-1} (Griffiths and De Haseth, 2007). Centrifugal distortion results in a decrease in the spacing between rotational transitions at high values of J, which is illustrated in Fig. 2.1b.

For this basic overview of vibrational-rotational spectroscopy, we have only considered the case of a simple diatomic molecule. However, as molecules become larger and less symmetrical, their spectra become more complex and the spacing of their vibrational-rotational lines decreases (Griffiths and De Haseth, 2007). For a detailed description of the vibrational-rotational spectra of triatomic and polyatomic molecules, refer to Liou (2002) and Hollas (2004).

2.1.2 Line Broadening and Lineshapes

When making spectroscopic measurements of the atmosphere, one must additionally consider the effects of spectral line broadening. Line broadening can be caused by three factors: the loss or gain of energy during emission or absorption, which affects the oscillator's vibration as a consequence of the Heisenberg Uncertainty Principle (natural line broadening), perturbations due to collisions between molecules, and the Doppler effect resulting from variations in the velocities of molecules

along the line of sight. In comparison to the broadening that results from collisions and from the Doppler effect, natural broadening is practically negligible. In the middle atmosphere, line broadening tends to result from a combination of collisional and Doppler broadenings, meanwhile in the lower atmosphere (<20 km) collisional broadening dominates due to the higher pressures present there (Liou, 2002).

The shape of spectral lines due to collisions, referred to as pressure broadening, is given by the Lorentz profile (Lorentz, 1906). The Lorentz approximation can be expressed by:

$$k_\nu = \frac{S}{\pi}\frac{\alpha_L}{(\tilde{\nu}-\tilde{\nu}_0)^2+\alpha_L^2} = Sf(\tilde{\nu}-\tilde{\nu}_0), \tag{2.7}$$

where k_ν is the absorption coefficient, $\tilde{\nu}_0$ is the wavenumber of an ideal monochromatic line, α_L is the half-width at half-maximum (HWHM) of the line, $f(\tilde{\nu}-\tilde{\nu}_0)$ represents the shape factor of a given spectral line, and S is the line strength given by:

$$S = \int_{-\infty}^{\infty} k_\nu d\tilde{\nu}. \tag{2.8}$$

The HWHM, α_L, depends on both pressure and temperature, and this can be derived using the kinetic theory of ideal gases as:

$$\alpha_L = \alpha_0 \left(\frac{p}{p_0}\right)\left(\frac{T_0}{T}\right)^n, \tag{2.9}$$

where α_0 is the width at standard atmospheric pressure ($p_0 = 1013$ mb) and temperature ($T_0 = 273$ K), and n is an index ranging from 1/2 to 1 depending on the type of molecule in question (Liou, 2002).

In a very low-pressure gas for which collisional broadening is negligible the Doppler effect is the primary source of line broadening. If a molecule has a velocity component in the line of sight (i.e., the molecule is moving towards or away from the observer), and is moving at a velocity $u \ll c$, then its original wavenumber $\tilde{\nu}_0$ will be Doppler shifted and the observed wavenumber will be $\tilde{\nu} = \tilde{\nu}_0\left(1 \pm \frac{u}{c}\right)$. If we assume that the molecules follow a Maxwell-Boltzmann distribution in the velocity interval of u to $u + du$, we find that the absorption coefficient for Doppler broadening is given by (Liou, 2002):

$$k_\nu = \frac{S}{\alpha_D\sqrt{\pi}} exp\left[-\left(\frac{\tilde{\nu}-\tilde{\nu}_0}{\alpha_D}\right)^2\right], \tag{2.10}$$

where $\alpha_D = \tilde{\nu}_0(2KT/mc^2)^{1/2}$ is the Doppler width of the line, k is the Boltzmann constant, and m is the mass of the molecule. Here, the Doppler HWHM is given by $\alpha_D\sqrt{\ln 2}$.

At the altitudes of the middle atmosphere (20–50 km), both Doppler and collisional broadening must be accounted for when determining the effective line shapes. The Doppler shift component must be added to pressure-broadened lines at wavenumbers $\tilde{\nu}' - \tilde{\nu}_0$ in order for the two effects to be combined. The Doppler effect shifts the Lorentz line at wavenumber $\tilde{\nu}'$ to $\tilde{\nu}$, and the Lorentz and Doppler lineshapes are then expressed by $f_L(\tilde{\nu}' - \tilde{\nu}_0)$ and $f_D(\tilde{\nu} - \tilde{\nu}')$, respectively. To account for the range of all possible velocities of molecules, the Doppler and Lorentz lineshapes can be convolved to obtain (Liou, 2002):

$$\begin{aligned} f_v(\tilde{\nu} - \tilde{\nu}_0) &= \int_{-\infty}^{\infty} f_L(\tilde{\nu}' - \tilde{\nu}_0)\, f_D(\tilde{\nu} - \tilde{\nu}') d\nu' \\ &= \frac{1}{\pi^{3/2}} \frac{\alpha}{\alpha_D} \int_{-\infty}^{\infty} \frac{1}{(\tilde{\nu}' - \tilde{\nu}_0)^2 + \alpha^2} \exp\left[\frac{-(\tilde{\nu} - \tilde{\nu}')^2}{\alpha_D^2}\right] d\tilde{\nu}'. \end{aligned} \tag{2.11}$$

This lineshape is known as the Voigt profile. For all of the retrievals in this work, the Voigt profile is used and the required spectral line parameters and broadening coefficients are obtained from the High-Resolution Transmission Molecular Absorption (HITRAN) spectral linelist databases (Rothman et al., 2009, 2013), or the Atmospheric (ATM) linelist databases (Toon, 2015, 2022).

2.1.3 Equation of Radiative Transfer

To relate the fundamental concepts of vibrational-rotational spectroscopy to the solar absorption measurements made by the FTIR at PEARL, we must consider the Radiative Transfer Equation and its applications to the Earth's atmosphere. In this section, we will describe a simple model for the transmission of solar radiation through the atmosphere, following the derivation in Liou (2002).

For a thin beam of monochromatic radiation passing through a medium, the intensity of the incident beam will be reduced through the interaction with matter (i.e., an absorptive trace gas). If the intensity of the beam $I_{\tilde{\nu}}$ becomes $I_{\tilde{\nu}} + dI_{\tilde{\nu}}$ upon traveling a distance ds in the direction of its propagation, then the change in intensity is given by (Liou, 2002):

$$dI_{\tilde{\nu}} = -\sigma_{\tilde{\nu}} \rho I_{\tilde{\nu}} ds, \tag{2.12}$$

where $\sigma_{\tilde{\nu}}$ is the mass extinction cross-section for radiation of wavenumber $\tilde{\nu}$ (in units of area per molecule), and ρ is the number density of the medium. Here, $\sigma_{\tilde{\nu}}$ is the sum of the mass absorption and scattering cross-sections, and thus the extinction of the beam is due to both absorption and scattering by the medium.

Conversely, the intensity of the beam of radiation may be increased by emission from the medium,

as well as through multiple scattering from all other directions into the beam at the same wavelength. In a similar fashion to Eq. 2.12, here we define the source function coefficient $j_{\tilde{\nu}}$ such that the strengthening of the intensity of the beam due to emission and multiple scattering is given by (Liou, 2002):

$$dI_{\tilde{\nu}} = j_{\tilde{\nu}} \rho I_{\tilde{\nu}} ds, \tag{2.13}$$

where $j_{\tilde{\nu}}$ has the same units as the mass extinction cross-section. Combining Eqs. 2.12 and 2.13 , we then obtain:

$$dI_{\tilde{\nu}} = -\sigma_{\tilde{\nu}} \rho I_{\tilde{\nu}} ds + j_{\tilde{\nu}} \rho I_{\tilde{\nu}} ds. \tag{2.14}$$

It is often convenient to define the source function $J_{\tilde{\nu}}$ as $J_{\tilde{\nu}} \equiv j_{\tilde{\nu}}/\sigma_{\tilde{\nu}}$, then using this Eq. 2.14 can be rearranged to yield:

$$\frac{dI_{\tilde{\nu}}}{\sigma_{\tilde{\nu}} \rho ds} = -I_{\tilde{\nu}} + J_{\tilde{\nu}}. \tag{2.15}$$

This is the general Radiative Transfer Equation, and it is fundamental to the discussion of any radiative transfer process (Liou, 2002).

Now, we can examine the Radiative Transfer Equation directly in the context of solar radiation passing through the Earth's atmosphere. We start by considering a direct beam of solar radiation which approximately covers the wavelength range of 0.2 to 5 μm. In most cases, the emission contributions from the Earth-atmosphere system in this spectral region can be neglected, and furthermore, for infrared wavelengths the effect of multiple scattering can be ignored. Thus, Eq. 2.15 can then be reduced to (Liou, 2002):

$$\frac{dI_{\tilde{\nu}}}{\sigma_{\tilde{\nu}} \rho ds} = -I_{\tilde{\nu}}. \tag{2.16}$$

If we let the incident intensity at the top of the atmosphere ($s = 0$) be $I_{\tilde{\nu}}(0)$, then the intensity of the beam after traveling a distance s_1 through the atmosphere can be found by integrating Eq. 2.16:

$$I_{\tilde{\nu}}(s) = I_{\tilde{\nu}}(0)\, exp\left(-\int_0^{s_1} \sigma_{\tilde{\nu}} \rho ds\right). \tag{2.17}$$

If we make the assumption that the atmosphere is homogeneous (i.e., $\sigma_{\tilde{\nu}}$ is independent of distance s), and define the column density u along the path length as:

$$u = \int_0^{s_1} \rho ds, \tag{2.18}$$

then Eq. 2.17 can be re-written as:

$$I_{\tilde{\nu}}(s_1) = I_{\tilde{\nu}}(0)\, e^{-\sigma_{\tilde{\nu}} u}. \tag{2.19}$$

This is known as the Beer-Bouguer-Lambert Law (or more commonly as Beer's Law). From Beer's Law, we can define the monochromatic transmissivity $T_{\tilde{\nu}}$ as:

$$T_{\tilde{\nu}} = I_{\tilde{\nu}}(s)/I_{\tilde{\nu}}(0) = e^{-\sigma_{\tilde{\nu}} u}. \tag{2.20}$$

Similarly, we can define the monochromatic absorptivity (the fraction of the incident radiation which has been absorbed by the atmosphere) as:

$$A_{\tilde{\nu}} = 1 - T_{\tilde{\nu}} = 1 - e^{-\sigma_{\tilde{\nu}} u}. \tag{2.21}$$

To a first-order approximation, Beer's Law can be used to model the extinction of a beam of solar radiation passing through the Earth's atmosphere. The example presented in this section has been simplified for the sake of conciseness, but for further details on atmospheric radiative transfer one can refer to Liou (2002).

For the SFIT4 retrievals described in this work, a line-by-line radiative transfer model (LBLRTM) is used. The SFIT4 LBLRTM generates a simulated atmosphere which is divided into many altitude layers (47 in the case of the Eureka retrievals), ranging from the top of the atmosphere to the surface. It then computes the absorption of solar radiation (assuming a Voigt lineshape profile) for a given wavelength by summing the individual absorption contributions of each trace gas included in the retrieval, starting at the upper-most layer and progressing downwards towards the surface (Notholt et al., 2006). The end result of the LBLRTM is a calculated spectrum which is then iteratively fitted to the observed spectrum during the retrieval process. Further discussions on retrieval theory and the SFIT4 algorithm are provided in Sect. 2.4.

2.2 FTIR Spectroscopy

The FTIR instrument located at the PEARL Ridge Lab is a Bruker IFS 125HR produced by Bruker Optics GmbH. It is a high-spectral-resolution spectrometer, and is currently one of the most widely used high-resolution FTIR spectrometers around the world. The Bruker 125HR operates on the principles of the Michelson interferometer, which is briefly described in the following section. Further

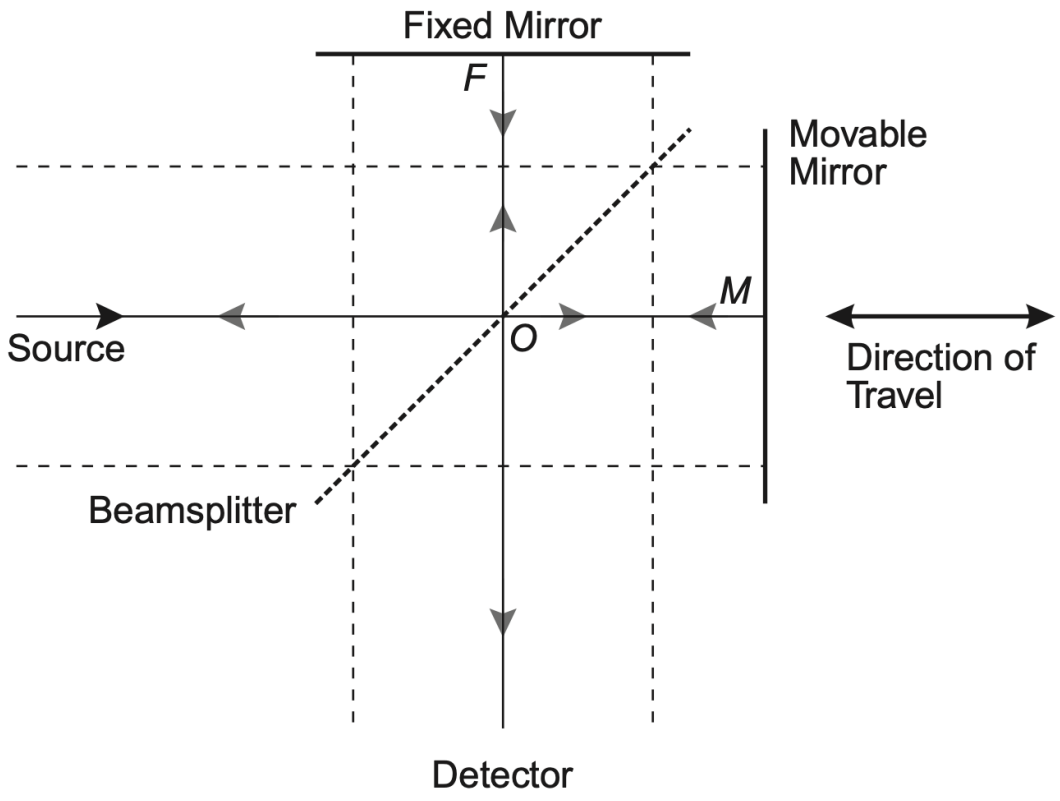

Figure 2.2: Diagram of the basic Michelson interferometer. Figure reproduced from Griffiths and De Haseth (2007).

details on the PEARL Bruker IFS 125HR instrument itself are provided in Sect. 2.3.

2.2.1 The Michelson Interferometer

Fourier transform infrared spectrometers can be used to measure the absorption spectrum of solar radiation passing through the Earth's atmosphere. Many modern FTIRs rely on the original principles of the Michelson interferometer to measure the absorption spectra. The Michelson interferometer is a conceptually straightforward optical device designed by Albert Abraham Michelson in 1880, and was first detailed in Michelson (1881). A diagram of the basic Michelson interferometer is shown in Fig. 2.2.

Put simply, the Michelson interferometer is a device which is capable of splitting a single beam of radiation into two separate paths using a beamsplitter, with one beam reflecting off a fixed mirror and the other beam reflecting off a movable mirror, eventually recombining the beams after a certain optical path difference (OPD) has been introduced. The OPD between the two separated beams is given by $2(\mathrm{OM} - \mathrm{OF})$, where OM and OF are the physical distances from the beamsplitter to

the moving and fixed mirrors respectively. The OPD is also referred to as the retardation, and is denoted by δ. Under these conditions, interference between the two beams occurs, and a detector measures the variation in intensity in this interference pattern as a function of the path difference.

A detailed description of the mathematical formalism of the Michelson interferometer is provided in Griffiths and De Haseth (2007), and a brief overview is presented here. We first consider the idealized situation where the source is an infinitely narrow beam of monochromatic, perfectly collimated light. If we let the wavelength of the beam be λ (in cm), then the wavenumber $\tilde{\nu}$ (in cm^{-1}) is given by:

$$\tilde{\nu} = \frac{1}{\lambda}, \tag{2.22}$$

and additionally, we denote intensity of this beam at a given OPD by $I(\delta)$. For simplicity, we take the beamsplitter to be ideal, such that its reflectance and transmittance are both precisely 50%, and no intensity is lost from the beam when being reflected or transmitted through the beamsplitter. We now examine the intensity of the recombined beam measured by the detector when the moving mirror is held fixed at different positions along the optical path.

If we place the fixed and moving mirrors at equal distances from the beamsplitter, then this is known as zero path difference (ZPD) or zero retardation, and the two beams will be perfectly in phase when they are recombined at the beamsplitter. In this situation, upon recombination the two beams will interfere constructively, and the intensity measured by the detector will be the sum of the intensities of the individual beams (see Fig. 2.3a). If we now introduce a path difference between the beams by displacing the movable mirror a distance of $\lambda/4$, the OPD will now be $\lambda/2$ and the beams will interfere destructively, and the detector will measure a minimum in the intensity (Fig. 2.3b). If the moving mirror is displaced by an additional $\lambda/4$ (such that it is now at a distance of $\lambda/2$ from the beamsplitter), the beams will again interfere constructively and the detector will measure an intensity of $I(\delta)$ (Fig. 2.3c).

If we now allow the movable mirror to move with a constant velocity along the optical path, the detector will measure a sinusoidally varying intensity, and a peak will be observed each time the OPD is an integer multiple of λ (i.e., $\delta = n\lambda$). The intensity measured by the detector is measured as a function of the OPD, and is given by:

$$I'(\delta) = 0.5\, I(\tilde{\nu}) \left(1 + \cos 2\pi \frac{\delta}{\lambda}\right), \tag{2.23}$$

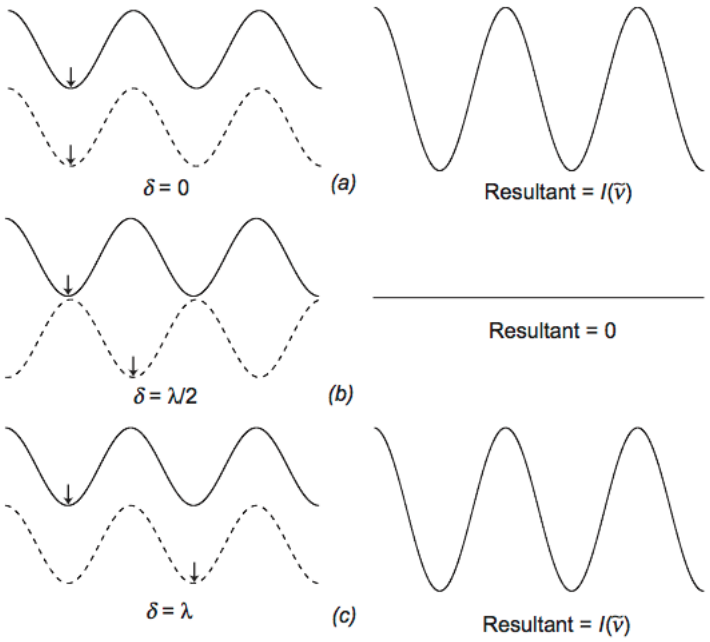

Figure 2.3: Phase of the beams from the fixed (solid line) and moving (dashed line) mirrors at varying optical path differences: (a) ZPD; OPD of $\lambda_0/2$, and (c) OPD of λ_0. Note that constructive interference occurs at integer multiples of λ_0. Image reproduced from Griffiths and De Haseth (2007)

or, written in terms of the wavenumber:

$$I'(\delta) = 0.5\, I(\tilde{\nu})\, (1 + \cos 2\pi\delta\tilde{\nu})\,. \tag{2.24}$$

From the above equations, we can see that there are actually two separate contributions to $I'(\delta)$, a constant $0.5\, I(\tilde{\nu}_0)$ component, and a modulated alternating component. For spectroscopic measurements, one is typically only concerned with the alternating component, which is often referred to as the *interferogram* and is denoted by $I(\delta)$. For an ideal interferometer and a monochromatic source, the interferogram is given by:

$$I(\delta) = 0.5\, I(\tilde{\nu})\cos 2\pi\delta\tilde{\nu}. \tag{2.25}$$

So far, we have only been considering an ideal instrument using a monochromatic source, however in reality several other factors can affect the intensity of the signal measured by the detector. First of all, beamsplitters almost never possess the ideal characteristics of 50% transmission and 50% reflection. This can be accounted for in Eq. 2.25 by multiplying the $I(\tilde{\nu})$ term by a wavenumber-dependent factor which is less than 1, representing the relative beamsplitter efficiency. Secondly, many detectors used for infrared measurements do not have a uniform response across all wavenumbers, and

furthermore the response of many amplifiers within the detectors are dependent on the modulation frequency. Taking all of this into account, the simplest representation of the interferogram is:

$$S(\delta) = B(\tilde{\nu}) \cos 2\pi\delta\tilde{\nu}, \tag{2.26}$$

where $S(\delta)$ is the AC signal measured by the detector (in units of volts), and $B(\tilde{\nu})$ is a parameter that describes the spectral intensity of the source at wavenumber $\tilde{\nu}$ modified by the characteristics of the beamsplitter and detector. In mathematical terms, $S(\delta)$ is the cosine Fourier transform of $B(\tilde{\nu}_0)$, and the spectrum is computed using the interferogram by taking the cosine Fourier transform of $S(\delta)$.

If we consider a non-monochromatic source (such as the Sun), then the interferogram measured by the detector is given by the integral:

$$S(\delta) = \frac{1}{2} \int_0^\infty B(\tilde{\nu}) \cos 2\pi\delta\tilde{\nu}\, d\tilde{\nu}. \tag{2.27}$$

If we take the Fourier transform of Eq. 2.27 and make use of the fact that $S(\delta)$ is an even function, we arrive at:

$$B(\tilde{\nu}) = 2 \int_0^\infty S(\delta) \cos 2\pi\delta\tilde{\nu}\, d\delta. \tag{2.28}$$

It can be noted from the above equations that one could theoretically measure the entire spectrum (0 to ∞, in cm^{-1}) at infinitely high resolution. However, this would require that the movable mirror of the interferometer be displaced an infinite distance (or in other words, this requires an infinite OPD). In all modern FTIR spectrometers that are based upon the Michelson interferometer, the spectral resolution is limited by the maximum OPD (MOPD) of the instrument. To account for the finite OPD of the the FTIR instrument, an apodization is applied to Eq. 2.27. Typically, a boxcar apodization is applied, which is of the form (Griffiths and De Haseth, 2007):

$$D(\delta) = \begin{cases} 0 & \text{if } \delta > \delta_{max} \\ 1 & \text{if } \delta \leq \delta_{max} \end{cases}, \tag{2.29}$$

where δ_{max} is the MOPD. Convolving the interferogram (Eq. 2.27) with the boxcar function yields a sinc function following the Fourier transform. As a result, the apodization influences the resolution of the measured spectrum. In the case of a boxcar apodization, the spectral resolution is typically

defined by the full width at half maximum (FWHM) criterion which gives a resolution of $0.605/\delta_{max}$ (Griffiths and De Haseth, 2007). In the case of the PEARL-FTS, Bruker Optics GmbH defines the spectral resolution as $0.9/\delta_{max}$.

Once an interferogram has been generated while using the Sun as the source, Eq. 2.28 can be applied to obtain a solar absorption spectrum. From the resulting spectrum, we are able to use an OEM retrieval method such as that described later in Sect. 2.4 to derive information on the concentrations and vertical distribution of trace gases in the Earth's atmosphere.

2.2.2 Advantages of FTIR Spectroscopy

FTIR instruments provide three fundamental advantages over dispersive grating spectrometers which make them ideal for atmospheric trace-gas measurements, and these are summarized briefly below.

The Fellgett Advantage

FTIR instruments sample the entire wavelength range of interest in a single scan of the moving mirror, and multiple scans can be co-added to reduce random noise in the measurement. A shorter MOPD can be selected to decrease the time per scan, while a longer MOPD can be used to increase the spectral resolution of the measurement. Meanwhile, with dispersive spectrometers each wavelength must be sampled individually as the grating scans. This allows for several scans by an FTIR to be completed in the time it would take for a single measurement by a dispersive spectrometer. This is known as the Fellgett (or multiplex) advantage (Griffiths and De Haseth, 2007).

The Jacquinot Advantage

FTIR instruments have significantly higher throughput than a grating spectrometer since the absence of slits allows for much greater intensity in the beam reaching the detectors, providing a higher signal-to-noise ratio (SNR) (Griffiths and De Haseth, 2007). In the case of many modern FTIRs including the Bruker IFS 125HR, apertures are used to finely control the amount of light entering the instrument, yielding greater SNR and decreased signal loss in comparison to dispersive instruments where the power through the instrument is limited by the area of the entrance slit. This is commonly referred to as the Jacquinot (or throughput) advantage.

The Connes Advantage

The Connes (or wavenumber precision) advantage refers to the fact that modern FTIRs use an internal laser (of a precisely known wavelength) to control both the velocity and position of the moving mirror, as well as to time the collection of data, leading to a precisely calibrated wavenumber axis (Griffiths and De Haseth, 2007). In contrast, grating spectrometers often rely on external calibration standards, and the wavenumber axis is defined by the position of the grating which may change over time.

An additional minor advantage of FTIR instruments is that they are less sensitive to stray light (i.e., light from one wavelength appearing at another region in the spectrum). In grating spectrometers, this can occur as a result of accidental reflections inside the instrument or imperfections in the dispersion grating itself. The combination of these advantages make FTIR instruments ideal for applications in long-term, high-precision measurements of trace-gas concentrations.

2.3 The PEARL Bruker IFS 125HR FTIR

2.3.1 Instrument Description

As briefly discussed in Sect. 2.2, the Bruker 125HR is based upon the principles of the Michelson interferometer, and we first describe the general function of the instrument below. An optical schematic diagram of the Eureka Bruker IFS 125HR is provided in Fig. 2.4. The general operation of the instrument can be described as follows: an input beam of light from either the Sun or the internal sources (a globar source for the mid-infrared and a tungsten filament for the near-infrared) passes through the entrance aperture in the source compartment into the interferometer compartment. The beam of light is then collimated using a parabolic collimating mirror before being directed onto the beamsplitter. The beamsplitter then divides the full beam into two beams of equal intensity, with one beam being directed onto the fixed mirror, and the other onto the moving mirror, which is a corner-cube mirror that sits on a carriage and is pulled along a straight, flat track consisting of two polished steel tubes by a DC motor and a thin steel cable. The beams are then both directed back towards the beamsplitter, where they are re-combined, however, due to the OPD between the fixed and moving mirrors there is a phase difference introduced into the final resulting beam. The recombined beam is then directed towards the exit aperture using a series of flat and parabolic mirrors. It should be noted that in the case of the Bruker IFS 125HR, the entrance and exit apertures are variable in diameter, and are controlled by a rotating aperture wheel. After the recombined beam passes

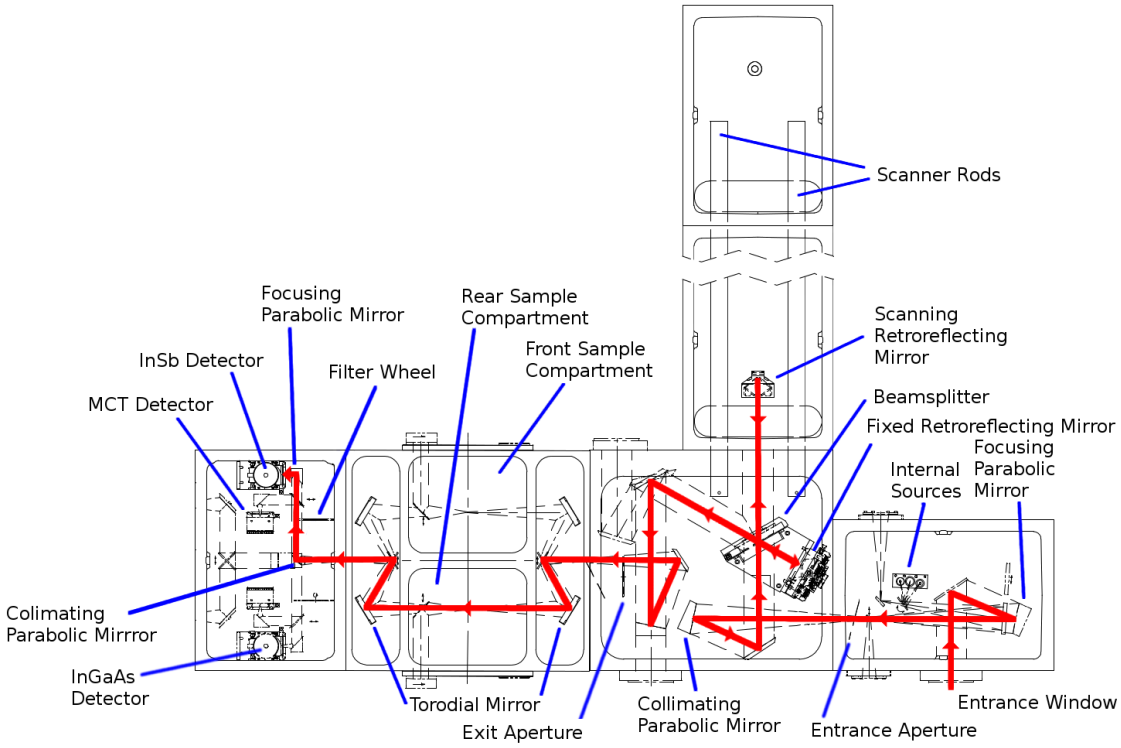

Figure 2.4: Schematic diagram of the Eureka Bruker IFS 125HR showing the optical path of the solar beam (red arrows), and the internal components which are labelled and indicated by the blue lines. Figure reproduced from Lutsch (2019).

through the exit aperture, it can be directed through either the front or rear sample compartments. The front sample compartment permanently contains the hydrogen chloride (HCl) cell used for the near-infrared cell tests, so for all mid-infrared measurements, the beam is directed through the rear sample compartment. After passing through the sample compartments, the beam enters the detector compartment where the mid-infrared indium antimonide (InSb) and mercury-cadmium-telluride (HgCdTe or MCT) detectors are located. Before reaching the mid-infrared detectors, the beam is collimated using a parabolic collimating mirror and directed through the filter wheel. The rotating filter wheel holds several spectral bandpass filters that limit the sampled spectral range of the incoming beam. The NDACC Infrared Working Group (IRWG) prescribed spectral filters used in the filter wheel are provided in Table 2.1. Finally, the filtered beam is directed to one of the two mid-infrared detectors using a moving flat mirror and a focusing parabolic mirror, and the incoming signal is recorded by the detector.

The PEARL Bruker IFS 125HR was installed in July 2006 as a replacement for the Environment and Climate Change Canada (ECCC) ABB Bomem DA8 FTIR, which was in operation from 1993

Table 2.1: NDACC narrow-band filters used with the Eureka Bruker IFS 125HR, their wavenumber ranges, and the retrieved trace gas species.

NDACC Filter #	Wavenumber Range (cm^{-1})	Input Aperture (mm)	Species Retrieved
1	3950–4300	1.0	HF
2	2700–3500	1.15	C_2H_2, HCN, H_2CO
3	2420–3080	1.0	CH_4, C_2H_6, HCl, H_2CO N_2O, O_3
4	1950–2700	1.15	CO
5	1800–2200	1.3	CO, NO
6	700–1350	1.5	CH_3OH, $ClONO_2$, C_2H_4, HCOOH, NH_3, O_3, PAN
7	700–1000	1.5	$ClONO_2$, C_2H_4, NH_3

to 2009 (Fast et al., 2011). An image of the instrument and the solar tracker dome are shown in Fig. 2.5. The instrument measures high-spectral-resolution solar-absorption spectra during sunlit clear-sky conditions, typically between late-February and mid-October of each year (Batchelor et al., 2009). The PEARL 125HR has an MOPD of 372 cm, providing a maximal wavenumber resolution (defined by Bruker Optics as 0.9/MOPD) of 0.0024 cm^{-1} (Batchelor et al., 2009). Two beamsplitters are used in the instrument; a potassium bromide (KBr) beamsplitter for the mid-infrared with a spectral range of 50–4800 cm^{-1}, and a calcium fluoride (CaF_2) beamsplitter for the near-infrared with a wavenumber range of 1200–15000 cm^{-1}. During normal operation, the instrument is kept under vacuum except when changing the beamsplitter. When taking mid-infrared solar measurements, the instrument cycles through the seven NDACC narrowband spectral filters (listed in Table 2.1), making a measurement with each before repeating the cycle. It should be noted that the input aperture size is filter-dependent, and these are listed in Table 2.1 as well. All mid-infrared solar measurements are made with an MOPD of 257 cm, which corresponds to a spectral resolution of 0.0035 cm^{-1}. The instrument contains three detectors: a photovoltaic InSb detector which covers the wavenumber range from 1850–10000 cm^{-1}, a photoconductive MCT detector that is sensitive in the range of 600–6000 cm^{-1}, and an InGaAs detector which is sensitive in the range of 4000–15000 cm^{-1}. Both the InSb and MCT detectors require liquid nitrogen cooling, while the InGaAs detector does not. Further details on the PEARL-FTS can be found in Batchelor et al. (2009).

A heliostat is a necessary component of any solar-measuring FTIR system. The PEARL Bruker 125HR employs a custom-built Community Solar Tracker (CST) which was jointly designed at Dalhousie University and the University of Toronto (Franklin, 2015). A diagram of the CST is provided in Fig. 2.6. The CST was installed in July 2013, and replaced the older ECCC photodiode solar tracker. A description of the ECCC solar tracker can be found in Lindenmaier (2012). The

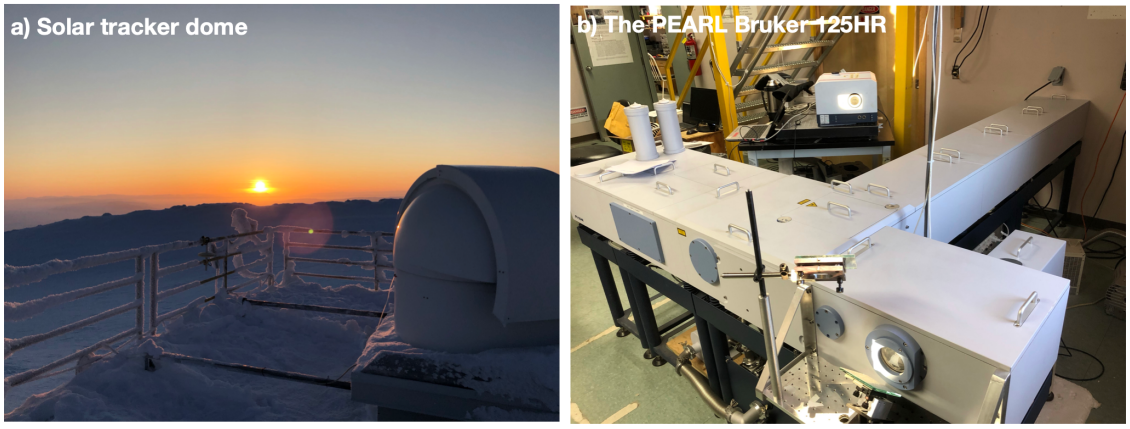

Figure 2.5: (a) The roof-mounted solar tracker dome which houses the Community Solar Tracker, and (b) the Bruker IFS 125HR in the infrared lab at PEARL. Note that a Bruker EM27/SUN can be seen in the background of panel (b) as it was making side-by-side measurements with the PEARL Bruker 125HR during the 2019 and 2020 Canadian Arctic ACE/OSIRIS Validation Campaigns.

CST is housed in a commercially available Robodome which is located on the roof of the PEARL Ridge Lab (see Fig. 2.5a). The Robodome and the CST are controlled by the Trax software which is written in Python, and allows both of these components to be remotely controlled through the use of a graphical user interface. The CST is capable of tracking the position of the Sun in two modes, active or passive. When in active tracking mode, continuous real-time corrections are provided to the tracker by using a webcam (located below the input window of the PEARL Bruker), and fitting an ellipse to the image of the Sun to precisely locate its center. The tracker then continues to make minor azimuthal and altitudinal corrections to keep the image of the Sun centered relative to the camera input. In passive tracking mode, no input from the webcam is needed, and the position of the Sun is located purely based on ephemeris calculations. However, the primary downside of passive tracking is that it is prone to systematic errors due to the physical drift of the solar tracker components. When performing normal solar measurements, the Trax software uses a combination of active and passive tracking to maintain the position of the Sun even if it becomes obscured by clouds. The CST and Robodome are controlled using their own laptop which houses the Trax software, and this laptop can be remotely accessed via a virtual network computing (VNC) connection, allowing the tracker and dome to be operated from off-site (even from Toronto). During the July 2023 summer campaign, an additional upward-facing webcam was installed in the solar tracker dome to enhance remote operation capabilities, allowing off-site operators to confirm the status of the dome (i.e., whether it is opened or closed).

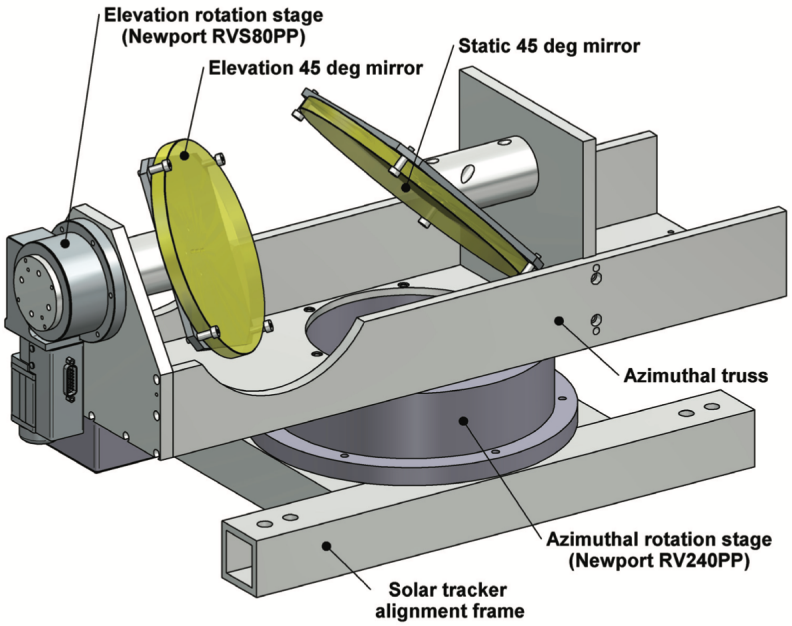

Figure 2.6: A schematic of the Community Solar Tracker (CST). Diagram reproduced from Franklin (2015).

2.3.2 Data Acquisition

Due to the remote nature of the PEARL Ridge Lab and the limited on-site support, the operation of the PEARL Bruker and the CST have largely been automated to maximize the number of observations. As it currently stands, operator support is typically only required at the start of measurements each day. The InSb and MCT detectors must be cooled manually before the start of measurements using liquid nitrogen. During the summertime, when there is ample sunlight throughout the entire day, the detectors (particularly the MCT detector) will sometimes need to be re-filled if measurements continue long enough. The tracker must then be initialized, and the measurements must be started using the Bruker OPUS software, however these tasks can both be done either manually by an on-site operator, or remotely via a VNC connection. Solar measurements are performed using a set of macros via the Bruker OPUS software. These automated macros cycle through each filter, check for sufficient signal, and then collect a measurement, with the measurement sequence being terminated when there is no longer sufficient input signal in any of the filters. Cloud cover can cause the macros to prematurely terminate, and as such it is still necessary to monitor the weather conditions (using webcams installed at the Ridge Lab) and the instrument throughout the day. On-site operator support is also required for performing beamsplitter swaps, which is typically done mid-way

through each day to change from mid-infrared to near-infrared measurements (or vice-versa). In the future, the addition of a large automatic liquid nitrogen dewar and the use of an extended range KBr beamsplitter (covering both the mid- and near-infrared ranges), which are currently undergoing testing within the Total Carbon Column Observing Network (TCCON) and NDACC-IRWG networks, would allow for further automation of the PEARL-Bruker and its measurements.

2.3.3 Instrument Alignment and Performance

When maintaining a long time-series of trace-gas measurements from an FTIR spectrometer, it is important to periodically assess the optical alignment and performance of the instrument. Each Bruker IFS 125HR is aligned during the initial delivery and installation of the instrument, however, the optical alignment may drift over long time-scales as a result of routine operation, and from rapid pressure or temperature changes (e.g., from venting and evacuating the instrument). The PEARL-FTS is used for both mid- and near-infrared measurements, and thus the beamsplitter is changed regularly (typically half-way through each measurement day), which requires the instrument to be vented and re-evacuated. Frequently changing the beamsplitter, as well as venting and evacuating the instrument may subject the Bruker 125HR to additional stresses which could impact the optical alignment.

The alignment of the PEARL-FTS is assessed through 'cell tests', whereby the absorption spectrum of a gas-filled cell with a known quantity of a particular gas is measured using an internal lamp source. At PEARL, three gas cells are used: HCl, hydrogen bromide (HBr), and nitrous oxide (N_2O). The HCl cell is larger than the HBr and N_2O cells, and is permanently installed in the front sample compartment of the instrument (highlighted in Fig. 2.4). The HCl cell is used in conjunction with the CaF_2 beamsplitter and tungsten lamp source to assess the near-infrared alignment and performance of the instrument, while the HBr and N_2O cells are used with the KBr beamsplitter and globar source to evaluate the mid-infrared alignment. Full details of the HCl cell tests for the near-infrared alignment can be found in Mendonca (2017).

The HBr cell at the PEARL Ridge Lab (HBr cell #30) was obtained from the National Institute for Environmental Studies (NIES) in Japan from a batch of cells produced specifically for the NDACC-IRWG. The cell is made of glass with fused sapphire windows, measures approximately 2.5 cm long and 2 cm in diameter, and is filled with a known quantity of HBr gas (see Fig. 2.7) (Coffey et al., 1998). For each HBr cell test, a background spectrum is first collected (i.e., with no cell in the instrument), followed by a cell measurement with the gas cell placed in the rear sample

Figure 2.7: HBr cell #30 in its holder inside the PEARL Bruker IFS 125HR rear sample compartment.

compartment. For both the background measurement and the cell measurement, 50 scans are performed using the internal globar source at a spectral resolution of 0.0035 cm^{-1} (corresponding to a MOPD of 257 cm) which are then co-added. The HBr cell test is performed using the NDACC-IRWG filter 4 (listed in Table 2.1) with a 1.15 mm input aperture to replicate the conditions of a filter 4 solar measurement. The Bruker OPUS software is then used to divide the cell spectrum by the background spectrum to obtain a transmission spectrum containing the absorption lines to be fitted.

The transmission spectrum is currently analyzed using version 14.5 of the LINEFIT retrieval software, which is described in Hase et al. (1999) and Hase (2012). The LINEFIT software generates a theoretical instrument lineshape (ILS), modulation efficiency (ME), and phase error (PE) based on the field-of-view (FOV) of the instrument and the OPD. A synthetic HBr spectrum is generated, and the ILS, ME, and PE are iteratively adjusted until the simulated spectra matches the measured HBr spectra. LINEFIT also retrieves the column concentration of HBr within the cell during the iterative fitting procedure. However, as highlighted by Lutsch (2019), the column concentration of the PEARL HBr cell has been steadily decreasing over time likely as a result of outside air entering the cell. LINEFIT is able to account for this during the fitting procedure, but an initial cell pressure and concentration of 1.55 mbar and 7.6×10^{20} molec. cm^{-2} respectively, is assumed by the software. LINEFIT is run iteratively, until a pressure convergence threshold of 0.001 mbar is reached, typically only requiring a maximum of three iterations to converge. Fourteen microwindows are used for fitting the HBr absorption features, and these are listed in Table 2.2, with an example

Table 2.2: Fitting microwindows used for the LINEFIT v14.5 analysis of the HBr cell transmission spectra at PEARL.

Microwindow	Wavenumber Range (cm^{-1})
1	2590.32–2590.72
2	2590.71–2591.11
3	2605.60–2606.00
4	2606.00–2606.40
5	2620.39–2620.79
6	2620.80–2621.20
7	2634.70–2635.10
8	2635.10–2635.50
9	2648.50–2648.90
10	2648.90–2649.30
11	2661.76–2662.16
12	2662.18–2662.58
13	2674.52–2674.92
14	2674.94–2675.34

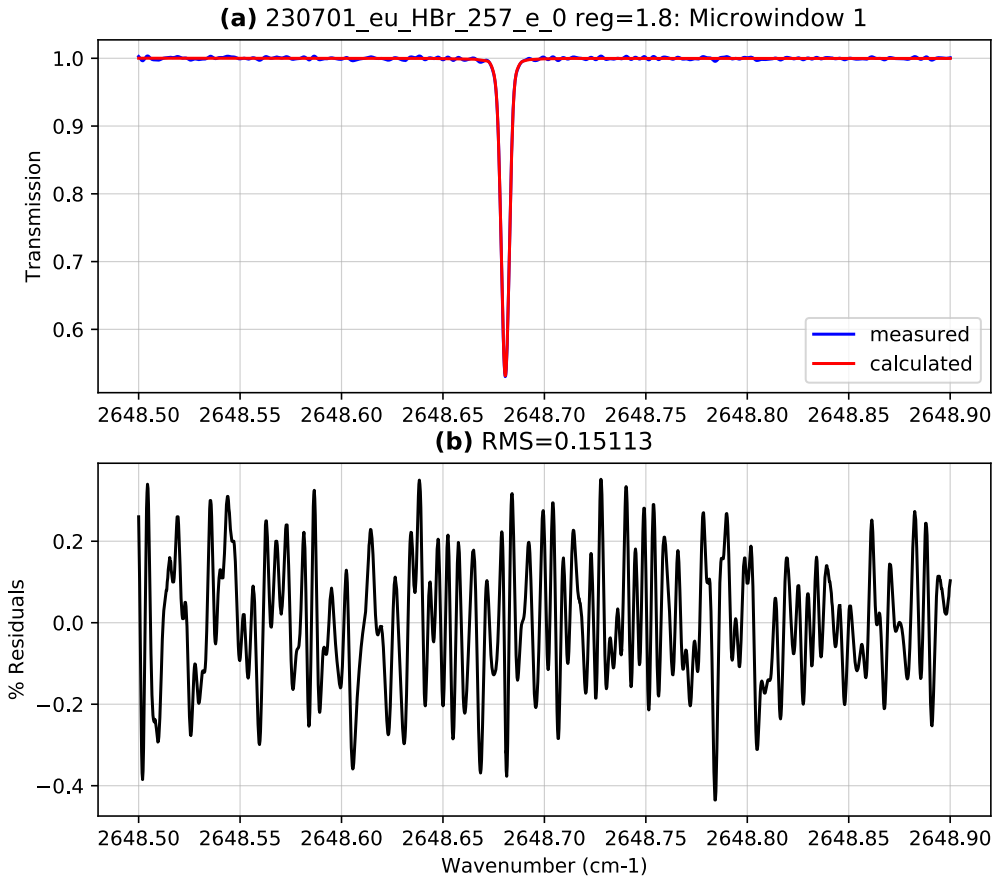

Figure 2.8: (a) A example fit for microwindow 1, and (b) the corresponding residuals from LINEFIT v14.5 for an HBr cell spectrum collected with the PEARL-FTS on 1 July 2023.

of a fitted HBr transmission spectra shown in Fig. 2.8.

The MEs, PEs, and mean column scale factors for HBr cell tests performed since March 2007 are shown in Fig. 2.9. The retrieved ME for the HBr cell tests varies from approximately 0.90 to 1.025 at MOPD, indicating generally favorable alignment. It should be noted that the ME is normalized to 1.0 at ZPD by LINEFIT, however this may not always be the case in reality as shear misalignment can result in an ME lower than unity at ZPD. As noted by Wunch et al. (2011), shear misalignment is a common issue with the Bruker IFS 125HR caused by gradual wear on the Teflon pads that support the scanning mirror, and will often manifest in the LINEFIT results in the form of a ME greater than unity at MOPD due to the normalization of the ME at ZPD. Angular misalignment is another type of instrument misalignment which can negatively impact the retrieved ME, and is the

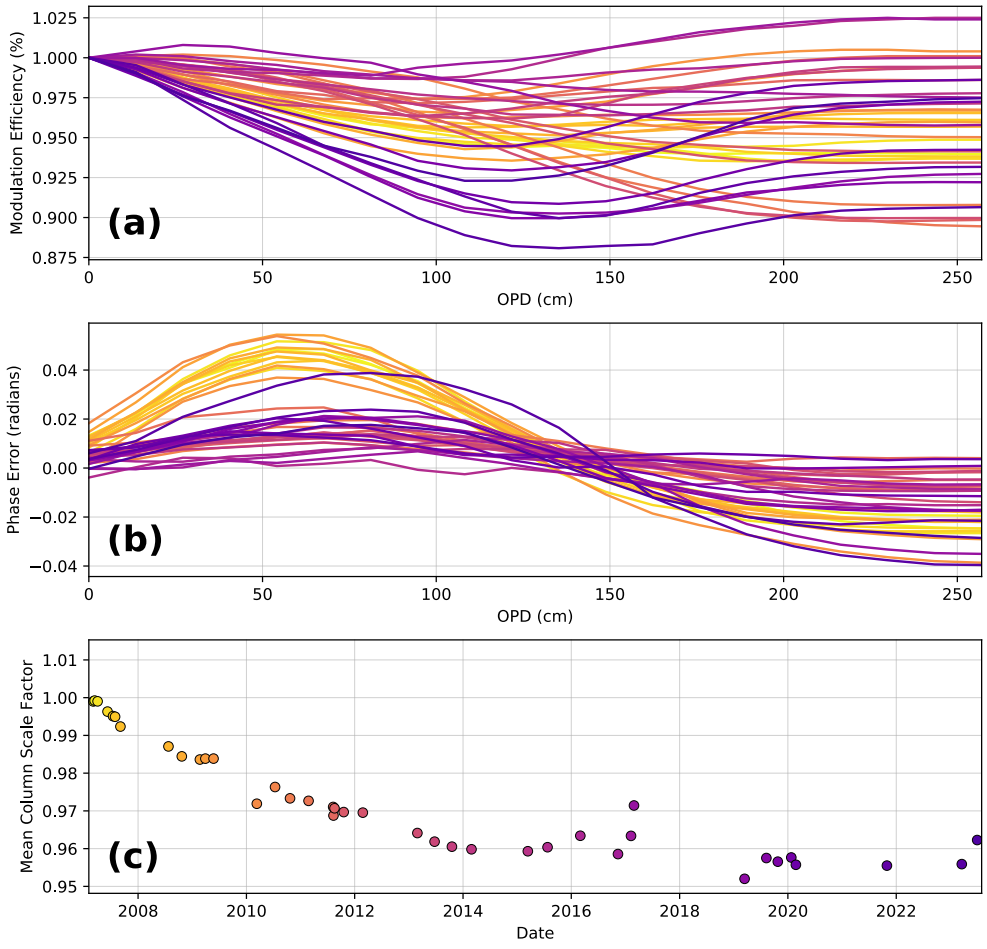

Figure 2.9: (a) Modulation efficiency as a function of OPD, (b) phase error as a function of OPD, and (c) the mean column scale factor (calculated over all microwindows) for PEARL-FTS HBr cell tests collected between March 2007 and July 2023 analyzed with LINEFIT v14.5.

result of the path of the beam being misaligned with respect to the axis of motion of the moving mirror (Wunch et al., 2011). Angular misalignment generally presents as a decrease in ME as a function of OPD. The retrieved PE is generally in the range of -0.04 to 0.05 radians. One HBr cell test collected on 19 March 2023 displays a higher phase error between -0.04 to 0.04 radians when compared to similar recent tests. This cell test from 19 March 2023 also shows a lower ME than all other tests, and it has been attributed to the temperature of the infrared lab being much lower than usual. Subsequent cell tests collected shortly after produced results which were considerably more consistent with other recent cell tests. Uncertainty in the instrument temperature, which is obtained from the recorded scanner temperature in OPUS, introduces some degree of variability in the HBr cell test results even for cell tests that are performed in close succession where true changes to the optical alignment are unlikely. The position of the beamsplitter can also lead to some variation in the retrieved ME and PE, as its position changes slightly each time it is removed and replaced. The mean retrieved HBr column scale factor shows a measurable decline between 2007 and 2019, and has decreased from 1.00 to approximately 0.96 in this time period, indicating that the HBr gas has steadily been leaking from the cell as highlighted previously by (Lutsch, 2019). The mean column scale factor is largely unchanged between 2019–2023, and appears to suggest that the rate of leakage from the cell within this period has slowed.

In addition to the HBr cell tests, an N_2O cell is also used to diagnose the mid-infrared alignment of the instrument. The N_2O cell (cell #11) was acquired in March 2016 and was produced by the NDACC-IRWG to the same physical specifications as the HBr cells. N_2O gas is inert, making it less prone to leakage from the cell than HBr. The NDACC-IRWG has begun to prioritize N_2O cell tests over the older HBr tests as they are likely to provide more consistent results over longer periods, however many sites still continue to perform HBr cell tests to maintain a consistent record of instrument alignment. Each N_2O cell test consists of 60 co-added scans that are performed at a lower resolution than the HBr cell tests, with the background and cell spectra being recorded at spectral resolutions of 0.05 cm^{-1} (18 cm MOPD) and 0.005 cm^{-1} (180 cm MOPD), respectively (Hase, 2012). These lower spectral resolutions provide the advantage of faster measurement times in comparison to the HBr cell tests. Three microwindows are used for fitting the N_2O absorption features in LINEFIT (see Table 2.3), and an example fitted N_2O microwindow is shown in Fig. 2.10. The N_2O cell test results are provided in Fig. 2.11.

The ME of the N_2O cell tests at MOPD are generally in the range of 0.8 to 1.0, with some tests from 2016 and early 2017 displaying some degree of over-modulation up to a maximum of approximately 1.05 ME at MOPD. A similar over-modulation is observed in the HBr cell tests

Table 2.3: Fitting microwindows used for the LINEFIT v14.5 analysis of the N_2O cell transmission spectra at PEARL.

Microwindow	Wavenumber Range (cm^{-1})
1	2167.03–2185.25
2	2222.825–2223.019
3	2224.475–2224.715

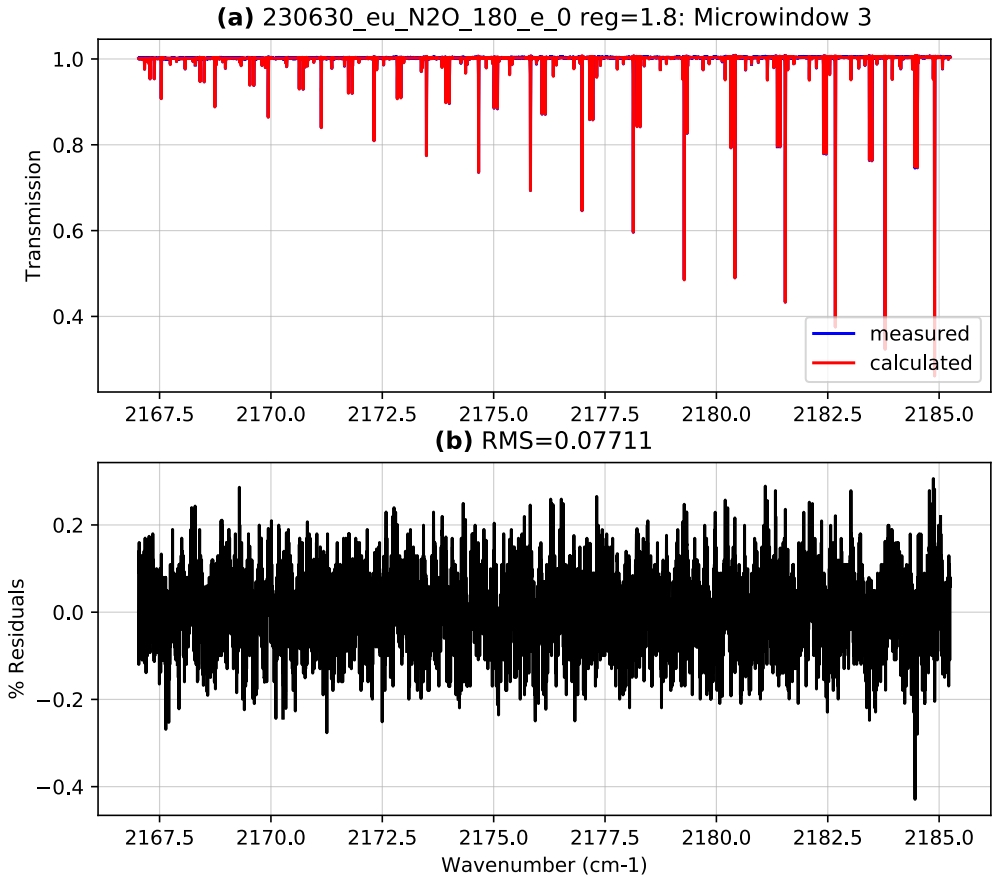

Figure 2.10: (a) A example fit for microwindow 3, and (b) the corresponding residuals from LINEFIT v14.5 for an N_2O cell spectrum collected with the PEARL-FTS on 30 June 2023.

collected around the same time. The N_2O cell results generally show smaller test-to-test variability in comparison to the HBr results in Fig. 2.9, which may be a consequence of the leaking HBr cell. In 2017, it was found that the near-infrared alignment had fallen outside of the required TCCON specifications (0.95–1.05 ME at 45 cm MOPD), and this misalignment was attributed to wear on the Teflon pads supporting the scanning mirror. A re-alignment of the instrument was performed during the Spring 2017 Canadian Arctic ACE/OSIRIS Validation Campaign, and a drop in the N_2O cell test ME at MOPD to below 0.9 can be seen in Fig. 2.11a. To ensure proper near-infrared alignment to meet TCCON specifications, the alignment process was performed using a 1 mm aperture, and the

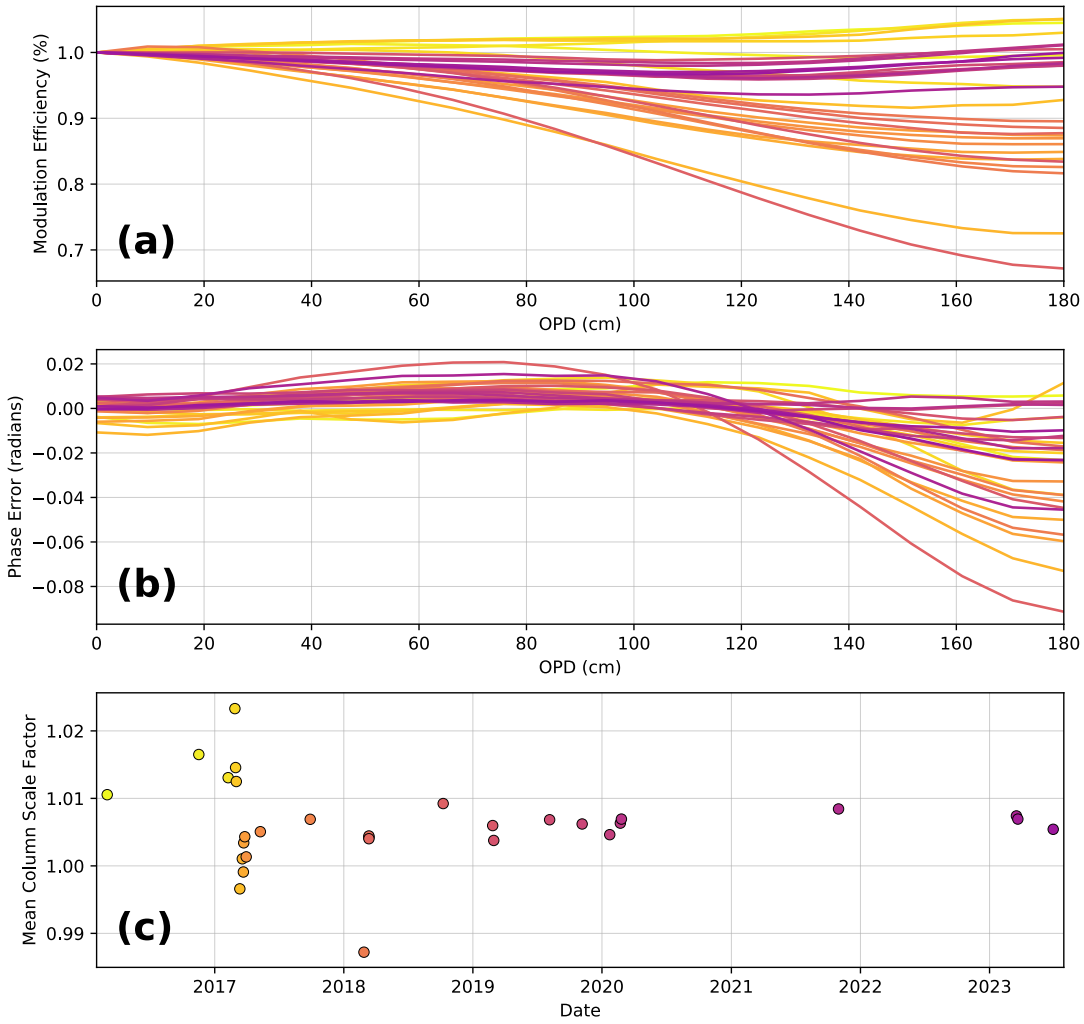

Figure 2.11: (a) Modulation efficiency as a function of OPD, (b) phase error as a function of OPD, and (c) the mean column scale factor (calculated over all microwindows) for PEARL-FTS N_2O cell tests analyzed with LINEFIT v14.5. Note: for consistency, cell tests with aperture sizes other than 1.15 mm were excluded from the figure.

CaF_2 beamsplitter. After the re-alignment process was completed, the near-infrared alignment was significantly improved, and met TCCON requirements, however it was found that the mid-infrared alignment was negatively impacted, and lower ME at MOPD was observed for both the HBr and N_2O results in subsequent cell tests. During the 2018 Canadian Arctic ACE/OSIRIS Validation Campaign, it was discovered that the Bruker aperture wheel was incorrectly milled (an issue that had been noted with other older Bruker 125HR instruments), resulting in changes of the aperture center position when rotating through different aperture sizes, and causing poorer alignment in the mid-infrared when using the larger 1.15 mm apertures. N_2O cell tests were performed using the 1 mm aperture instead of the typical 1.15 mm aperture, and significantly improved alignment across all OPDs was found, which was consistent with the near-infrared HCl cell test results.

During the 2019 Canadian Arctic ACE/OSIRIS Validation Campaign, corrected entrance and exit Bruker aperture wheels were installed on 27 February 2019, followed by a full re-alignment of the instrument. Cell tests performed following the installation of the new aperture wheels show significantly improved mid-infrared alignment, and greater consistency between the near-infrared and mid-infrared alignment and cell test results. Following the re-alignment procedure during the 2019 Canadian Arctic ACE/OSIRIS Validation Campaign, good alignment in the mid-infrared has been maintained, with ME at MOPD near unity and only a minor degree of over-modulation observed in some cell tests.

2.4 Trace Gas Retrievals

A fundamental component of this work is the determination of atmospheric concentrations of trace gases from solar absorption spectra measured by ground-based FTIR instruments. From the solar absorption spectra measured by an FTIR spectrometer, we are able to indirectly determine the concentration of a given gas in the atmosphere using both a forward and an inverse model through a process known as a "retrieval". The solution to the inverse problem is a volume mixing ratio (VMR) profile that is the best estimate of the true state of the atmosphere observed in the measurements. However, the inverse problem is under-determined, meaning that the number of unknown parameters to be solved for is greater than the number of known parameters. In order to achieve a solution to the inverse problem, an initial guess of the atmospheric state known as the *a priori* profile, is required. The procedure by which we solve this inverse problem is known as the OEM, which is detailed in Rodgers (2000), and is summarized in the following subsection.

2.4.1 Retrieval Theory

We start by defining a measurement vector $\mathbf{y}$ comprised of m elements given by:

$$\mathbf{y} = \mathbf{F}(\mathbf{x}, \mathbf{b}) + \boldsymbol{\varepsilon}, \tag{2.30}$$

where $\mathbf{F}(\mathbf{x}, \mathbf{b})$ is the forward model which encapsulates the physics of the measurement, $\mathbf{x}$ is a state vector of n unknown elements that we are aiming to retrieve, $\mathbf{b}$ is a vector representing all other variables upon which the measurement is dependent (such as profiles of temperature and pressure), and $\boldsymbol{\varepsilon}$ is the measurement error.

Due to the under-determined nature of the inverse problem, it is helpful to perform a linearization of the forward model about a reference state $\mathbf{x}_a$. In the case of trace-gas retrievals, this reference state $\mathbf{x}_a$ is the *a priori* profile, which is the best estimate of the true state of the atmosphere. Likewise, we also choose a best estimate for $\mathbf{b}$ denoted by $\hat{\mathbf{b}}$, and include an additional vector $\mathbf{c}$ which encompasses any supplementary parameters used in the retrieval process but which do not appear in the forward model. Taking into account all of the aforementioned assumptions, we define the inverse model $\mathbf{I}$ as the process through which we obtain the retrieved profile $\hat{\mathbf{x}}$ from the measurement vector $\mathbf{y}$, which is given by:

$$\hat{\mathbf{x}} = \mathbf{I}(\mathbf{y}, \hat{\mathbf{b}}, \mathbf{c}) = \mathbf{I}(\mathbf{F}(\mathbf{x}, \mathbf{b}) + \boldsymbol{\varepsilon}, \hat{\mathbf{b}}, \mathbf{c})\,. \tag{2.31}$$

Then, linearizing Eq. 2.31 about $\mathbf{x}_a$ we obtain:

$$\hat{\mathbf{x}} = \mathbf{I}[\mathbf{F}(\mathbf{x_a}, \hat{\mathbf{b}}), \hat{\mathbf{b}}, \mathbf{c}] + \frac{\partial \mathbf{I}}{\partial \mathbf{y}} \frac{\partial \mathbf{F}}{\partial \mathbf{x}} (\mathbf{x} - \mathbf{x_a}) + \frac{\partial \mathbf{I}}{\partial \mathbf{y}} \frac{\partial \mathbf{F}}{\partial \mathbf{b}} (\mathbf{b} - \hat{\mathbf{b}}) + \frac{\partial \mathbf{I}}{\partial \mathbf{y}} \boldsymbol{\varepsilon}\,. \tag{2.32}$$

Here, for convenience we can define the gain matrix $\mathbf{G}$ as:

$$\mathbf{G} = \frac{\partial \mathbf{I}}{\partial \mathbf{y}}, \tag{2.33}$$

which specifies the sensitivity of the retrieval to the measurement. Similarly, it is helpful to define the partial derivative of the forward model $\mathbf{F}$ with respect to the state vector $\mathbf{x}$ as the weighting function matrix $\mathbf{K}$:

$$\mathbf{K} = \frac{\partial \mathbf{F}}{\partial \mathbf{x}}\,. \tag{2.34}$$

This weighting function is an $m \times n$ matrix which defines the sensitivity of the forward model to the state vector. The columns of $\mathbf{K}$ describe the variability in the measured spectrum resulting from

a change in the state profile at each altitude level of the retrieval, while its rows describe the part of the profile that is represented by each measurement (Rodgers, 1990). Additionally, we define another weighting function matrix $\mathbf{K_b}$ for the partial derivative of the forward model with respect to the forward model parameters:

$$\mathbf{K_b} = \frac{\partial \mathbf{F}}{\partial \mathbf{b}} \,. \tag{2.35}$$

Similar to $\mathbf{K}$, this weighting function describes the sensitivity of the forward model to its parameters.

We then define the averaging kernel matrix $\mathbf{A}$ as the partial derivative of the inverse model with respect to the state vector:

$$\mathbf{A} = \frac{\partial \mathbf{I}[\mathbf{F}(\mathbf{x}, \mathbf{b}), \mathbf{b}, \mathbf{c}]}{\partial \mathbf{x}} = \mathbf{GK}. \tag{2.36}$$

The rows of $\mathbf{A}$ are smoothing functions (or 'averaging kernels'), which describe the sensitivity of the layers of the retrieved state to the true state, and the shape of the averaging kernels provides information about the vertical resolution of the measurement. Here, the sensitivity of the retrieval is defined by the sum of the rows of $\mathbf{A}$, and represents the fraction of the retrieved information that comes from the measurement versus the *a priori* (Vigouroux et al., 2009). Additionally, the degrees of freedom for signal (DOFS) is defined as the trace of $\mathbf{A}$, and serves as a measure of the number of independent pieces of information contained within the retrieval. In an ideal scenario, $\mathbf{A}$ would be a unit matrix, meaning that the retrieval at a given altitude originates only from the retrieval layer at that altitude, however in reality this is generally not the case.

Using the definitions above, the retrieved profile $\hat{\mathbf{x}}$ can be rewritten as:

$$\hat{\mathbf{x}} = \mathbf{I}[\mathbf{F}(\mathbf{x_a}, \hat{\mathbf{b}}), \hat{\mathbf{b}}, \mathbf{x_a}, \mathbf{c}] + \mathbf{A}(\mathbf{x} - \mathbf{x_a}) + \mathbf{GK_b}(\mathbf{b} - \hat{\mathbf{b}}) + \mathbf{G}\boldsymbol{\varepsilon}. \tag{2.37}$$

If no measurements are made and if the retrieval method is unbiased, then the *a priori* profile would be the only source of information, and thus Eq. 2.37 would only return the *a priori* profile:

$$\mathbf{I}[\mathbf{F}(\mathbf{x_a}, \hat{\mathbf{b}}), \hat{\mathbf{b}}, \mathbf{x_a}, \mathbf{c}] = \mathbf{x_a} \,. \tag{2.38}$$

Finally, combining Eq. 2.37 and Eq. 2.38, we can write the retrieved profile as:

$$\hat{\mathbf{x}} = \mathbf{x_a} + \mathbf{A}(\mathbf{x} - \mathbf{x_a}) + \mathbf{GK_b}(\mathbf{b} - \hat{\mathbf{b}}) + \mathbf{G}\boldsymbol{\varepsilon} \,. \tag{2.39}$$

In order to arrive at a solution for $\hat{\mathbf{x}}$ in the form of Eq. 2.39, Bayesian statistics are used to determine the most probable retrieved VMR profile $\hat{\mathbf{x}}$ given measurement $\mathbf{y}$ (Bayes, 1763). This process is

known as finding the maximum a posteriori (MAP) solution. Here, we apply Bayes' theorem:

$$P(\mathbf{x} \mid \mathbf{y}) = \frac{P(\mathbf{y} \mid \mathbf{x})P(\mathbf{x})}{P(\mathbf{y})}, \tag{2.40}$$

where $P(\mathbf{x} \mid \mathbf{y})$ is the posterior probability density function (PDF) of the state given the measurement (i.e., the conditional probability of obtaining a state vector $\mathbf{x}$ given measurement $\mathbf{y}$), $P(\mathbf{y} \mid \mathbf{x})$ describes the knowledge of $\mathbf{y}$ that would be obtained given the state $\mathbf{x}$, $P(\mathbf{x})$ represents the prior knowledge of the state, and $P(\mathbf{y})$ is the probability of obtaining $\mathbf{y}$. The process for achieving the MAP solution is described in considerable detail in Rodgers (2000), and here we will only focus on final results. This is an optimization problem at its core, and the goal is to find a solution for $\mathbf{x}$ which maximizes the PDF while appropriately weighting information from both the measurement and the *a priori* profile. To find the most probable solution of $\mathbf{x}$ given $\mathbf{y}$, we can define a cost function $\mathbf{J}(\mathbf{x})$:

$$\mathbf{J}(\mathbf{x}) = (\mathbf{y} - \mathbf{K}\mathbf{x})^T {\mathbf{S}_\varepsilon}^{-1} (\mathbf{y} - \mathbf{K}\mathbf{x}) + (\mathbf{x} - \mathbf{x_a})^T {\mathbf{S_a}}^{-1} (\mathbf{x} - \mathbf{x_a}). \tag{2.41}$$

Assuming Gaussian error probabilities and by taking the derivative of Eq. 2.41 and setting it to zero, we will arrive at a solution of the form:

$$\hat{\mathbf{x}} = \mathbf{x_a} + \mathbf{S_a}\mathbf{K^T}(\mathbf{K}\mathbf{S_a}\mathbf{K^T} + \mathbf{S}_\varepsilon)^{-1}\mathbf{K}(\mathbf{x} - \mathbf{x_a}), \tag{2.42}$$

where $\mathbf{S_a}$ and $\mathbf{S}_\varepsilon$ denote the *a priori* and measurement error covariance matrices, respectively. In this process, we have assumed that there is a linear relationship between $\mathbf{x}$ and $\mathbf{y}$ (i.e., $\mathbf{y} = \mathbf{K}\mathbf{x}$).

However, the relationship between $\mathbf{x}$ and $\mathbf{y}$ is typically non-linear, and we will have a more general cost function of the form:

$$\mathbf{J}(\mathbf{x}) = (\mathbf{y} - \mathbf{F}(\mathbf{x}))^T {\mathbf{S}_\varepsilon}^{-1} (\mathbf{y} - \mathbf{F}(\mathbf{x})) + (\mathbf{x} - \mathbf{x_a})^T {\mathbf{S_a}}^{-1} (\mathbf{x} - \mathbf{x_a}), \tag{2.43}$$

and similarly, we define the gradient of this cost function as:

$$\nabla_x \mathbf{J}(\mathbf{x}) = -[\nabla_x \mathbf{F}(\mathbf{x})]^T {\mathbf{S}_\varepsilon}^{-1} (\mathbf{y} - \mathbf{F}(\mathbf{x})) + {\mathbf{S_a}}^{-1} (\mathbf{x} - \mathbf{x_a}). \tag{2.44}$$

We then aim to find the solution to $\nabla_x \mathbf{J}(\mathbf{x}) = 0$, which is done iteratively using the Gauss-Newton method:

$$\mathbf{x}_{i+1} = \mathbf{x}_i - [\nabla_x \nabla_x \mathbf{J}]^{-1} \nabla_x \mathbf{J}(\mathbf{x}_i)\,. \tag{2.45}$$

We can then substitute the expression for the cost function into Eq. 2.44. In addition, it is also helpful to express the iteration $\mathbf{x}_{i+1}$ as a departure from $\mathbf{x_a}$ instead of $\mathbf{x}_i$, to obtain:

$$\mathbf{x}_{i+1} = \mathbf{x_a} + \mathbf{S_a}\left\{\mathbf{K}_i^T\left[\mathbf{K}_i\mathbf{S_a}\mathbf{K}_i^T + \mathbf{S}_\varepsilon{}^{-1}\right][(\mathbf{y} - \mathbf{y}_i) + \mathbf{K}_i(\mathbf{x}_i - \mathbf{x_a})]\right\} \tag{2.46}$$

where we have used the substitution of $\mathbf{K}_i = \nabla_x\mathbf{F}(\mathbf{x}_i)$, and where $\mathbf{y}_i = \mathbf{F}(\mathbf{x}_i)$ results from the forward model using the i^{th} estimate of $\mathbf{x}$. Eq. 2.46 provides us with means of finding a solution to the inverse problem. Typically, a convergence criterion is applied to terminate the iterative process once a suitable solution has been achieved, and usually this is done through the comparison of $\mathbf{y}_i = \mathbf{F}(\mathbf{x}_i)$ to the measured spectrum, terminating the iterations when the difference between the original $\mathbf{y}$ and $\mathbf{y}_i$ is smaller than the estimated error multiplied by a tolerance factor. When the iteration is terminated and the convergence criterion has been met, we have arrived at the optimal solution for $\mathbf{x}$.

2.4.2 SFIT4 Retrieval Software

To retrieve trace gas concentrations from the solar absorption spectra measured by the PEARL-FTS, we use the SFIT4 retrieval software, the most recent iteration of the SFIT retrieval algorithm. SFIT4 is based upon an earlier version of the SFIT algorithm, SFIT2, which was jointly developed by researchers at NASA Langley and NIWA Lauder (Pougatchev et al., 1995). The primary purpose of SFIT4 is the analysis of ground-based IR solar spectra, however SFIT4 can also be used to analyze emission spectra such as from the Extended-range Atmospheric Emitted Range Interferometer (E-AERI) instrument located at ØPAL. SFIT4 is used by most NDACC-IRWG member sites, however a few sites use the PROFFIT retrieval software (Hase et al., 2004).

SFIT4 is largely built upon the OEM of Rodgers (2000) previously summarized in Sect. 4.2.1, and it works by fitting a theoretical calculated spectrum to the observed spectrum. To do this, the *a priori* VMR profile of the gas of interest is iteratively adjusted using the OEM to more closely match the observed spectrum. In SFIT4, the iterative process of adjusting the VMR profile of the target gas continues until the difference between subsequent iterations is lower than a specified tolerance. Generally, the tolerance value is defined by some factor (typically 0.1) multiplied by the measurement error covariance ($\mathbf{S}_e$), which is calculated in SFIT4 as:

$$\mathbf{S}_e = \frac{\mathbf{I}}{\text{SNR}^2}, \tag{2.47}$$

where $\mathbf{I}$ is the identity matrix, and the SNR is estimated directly from the observed spectra in user-specified microwindows for each filter. The iteration proceeds until the difference falls below the tolerance value, or until a specified maximum number of iterations is exceeded. If the maximum number of iterations is exceeded, the retrieval is said to diverge and no result is produced.

The forward model of SFIT4 is an LBLRTM, which encompasses multiple atmospheric layers (47 for Eureka) and multiple trace-gas species (Notholt et al., 2006). A few assumptions are made in the SFIT4 forward model, primarily that the atmospheric layers are homogeneous, and that each layer is in a state of local thermodynamic equilibrium. It also assumes a Voigt line shape function, which was described in Sect. 2.1.2.

As outlined in Sect. 2.4.1, the OEM requires several pieces of prior information in order for the inverse problem to be solved. In the case of the Eureka trace-gas retrievals, this includes: 1) a pressure-temperature profile for the atmosphere; 2) absorption parameters for the target gas and any interfering species in the selected microwindows, 3) an *a priori* profile of the target gas, and 4) the *a priori* error covariance matrix $\mathbf{S}_a$. For the atmospheric pressure-temperature profile, daily averaged profiles from the US National Centers for Environmental Prediction (NCEP) are used. Spectroscopic absorption parameters for most trace gases of interest are taken from the HITRAN 2008 linelist database (Rothman et al., 2009) following NDACC-IRWG recommendations, however, for some target or interfering trace-gas species spectroscopic lines from newer versions of HITRAN or the ATM linelist are used (Toon, 2022). This is discussed in further detail in Chapter 3. For the *a priori* profiles of all target gases in this work, we use a 40-year average (1980–2020) for the site from the Whole Atmosphere Community Climate Model v4.0 (WACCMv4) (Marsh et al., 2013).

Additionally, choosing an appropriate *a priori* error covariance matrix is an important part of the retrieval process. In general, the diagonals of the *a priori* error covariance matrix $\mathbf{S}_a$ are given by:

$$\mathbf{S}_a = \mathbf{I} \cdot \sigma^2, \tag{2.48}$$

where σ is the standard deviation of the target species (in %) which is often derived from the WACCM *a priori* profile. Although the diagonals of the $\mathbf{S}_a$ should generally represent the variability of the target gas in the atmosphere, these values can be manually adjusted and used as tuning parameter for the retrieval to optimize the DOFS and to reduce unphysical profile variations. When the diagonals of the $\mathbf{S}_a$ are adjusted in this manner, it is referred to as an "empirical implementation of optimal estimation" or an OEM $\mathbf{S}_a$ (Pougatchev et al., 1995; Sussmann et al., 2011). To dampen unphysical oscillations in the retrieved VMR profiles, an optional inter-layer correlation (ILC) may be applied

to the retrieval. By using an ILC, an assumption is made that the VMR is correlated between adjacent retrieval layers, and thus the ILC is used to define the off-diagonal values of the $\mathbf{S}_a$ matrix. An exponential ILC is commonly used in SFIT4 retrievals where the $\mathbf{S}_a$ elements are defined by:

$$\mathbf{S}_{a,ij} = \mathbf{S}_{a,ii} e^{-\frac{|z_i - z_j|}{W}}, \tag{2.49}$$

where z_i is the altitude at the respective level and W is the correlation width. The correlation width can be species dependent, however 4 km is the standard value used by the NDACC-IRWG.

For target gases which exhibit a high degree of natural profile variability or where the true profiles are highly uncertain, it may be difficult to derive a reliable $\mathbf{S}_a$ through the OEM approach. In these cases, the $\mathbf{S}_a$ can alternatively be derived through a first-order Tikhonov regularization scheme (Tikhonov, 1963).

Tikhonov Regularization

In early retrievals from solar absorption spectra, total column concentrations were derived through the iterative scaling of an *a priori* VMR profile via a single (unconstrained) altitude-constant factor. This approach is widely used in older non-linear least squares fitting algorithms such as SFIT1 and GFIT (Rinsland et al., 1984; Toon et al., 1992). Full profile retrievals are now performed with SFIT4, but to prevent over-fitting, a regularization is applied via a diagonal *a priori* covariance matrix that must be empirically tuned to avoid oscillations in the retrieved profiles. If done incorrectly, an empirically tuned OEM $\mathbf{S}_a$ can smooth out true variability in the retrieved profile (Pougatchev et al., 1995; Sussmann et al., 2011). This issue becomes more critical in cases where the retrieval contains only low information content, which is true for the retrieval of PAN and C_2H_4 (Sussmann et al., 2011). Both the profile scaling and full profile retrieval approaches have their own benefits and drawbacks, and we ideally want a robust approach that provides the advantages of both, while minimizing their drawbacks. For the retrievals of PAN and C_2H_4, we have used the Tikhonov regularization scheme to construct an *a priori* covariance matrix that allows for some flexibility in the retrieved profiles while also ensuring that profile-scaling variations are allowed to occur (Tikhonov, 1963).

A brief description of Tikhonov regularization is provided here. As was outlined in Sect. 2.4.1, the inverse-model of the OEM is ill-posed and is formulated as a least squares problem. Since the forward model $\mathbf{F}$ is non-linear, a Gauss-Newton iteration is applied and a regularization term $\mathbf{R} \in \mathcal{R}^{n \times n}$ (for an inverse model with n layers), defined by $\mathbf{R} = \mathbf{S}_a^{-1}$, is included to reduce oscillations in the retrieved profile by constraining the solution. Rewriting Eq. 2.46 from Sect. 2.4.1 in an alternative

form, following the formulation of Sussmann et al. (2011) we have:

$$\mathbf{x}_{i+1} = \mathbf{x}_i + \left(\mathbf{K}_i^T \mathbf{S}_\varepsilon{}^{-1} \mathbf{K}_i \mathbf{R}\right)^{-1} \times \left[\mathbf{K}_i^T \mathbf{S}_\varepsilon{}^{-1} (\mathbf{y} - \mathbf{F}(\mathbf{x}_i)) - \mathbf{R}(\mathbf{x}_i - \mathbf{x_a})\right] \tag{2.50}$$

where $\mathbf{K} = \partial\mathbf{F}/\partial\mathbf{x}$ is the Jacobian, and $\mathbf{S}_\varepsilon$ is the measurement error covariance matrix. Using a first-order Tikhonov regularization scheme (Tikhonov, 1963), we can generate $\mathbf{R}$ by the relation:

$$\mathbf{R} = \alpha \mathbf{L}_1^T \mathbf{L}_1 \in \mathcal{R}^{n \times n}, \tag{2.51}$$

where α is the regularization strength, and $\mathbf{L}_1$ is the discrete first derivative operator given by:

$$\mathbf{L}_1 = \begin{pmatrix} -1 & 1 & 0 & \cdots & 0 \\ 0 & -1 & 1 & \ddots & \vdots \\ \vdots & \ddots & -1 & \ddots & 0 \\ 0 & \cdots & 0 & -1 & 1 \end{pmatrix} \in \mathcal{R}^{(n-1) \times n}. \tag{2.52}$$

What remains is to select a value of the regularization strength parameter α that allows for appropriate variability in the retrieved profile without over-constraining the retrieval. If the value of α is chosen to be too large such that the retrieval is over-constrained, then the DOFS will be limited to 1, and the retrieval will in essence be a scaling of the *a priori* profile. Conversely, if the value of α is chosen to be too small then the retrieved profile may exhibit unrealistic oscillations, and the total column concentrations may be highly variable and can even become negative.

Chapter 3

PEARL-FTS Retrievals

In this chapter, we describe the methods used to retrieve VMR profiles and the column concentrations of CO, C_2H_2, C_2H_4, C_2H_6, CH_3OH, H_2CO, HCOOH, and PAN from the measured PEARL-FTS mid-infrared solar absorption spectra. In this work, all retrievals were performed using version 0.9.4.4 of the SFIT4 retrieval algorithm (accessible at: https://wiki.ucar.edu/display/sfit4/).

CO, C_2H_6, and H_2CO are standard NDACC-IRWG species, and thus, the retrieval strategy implemented at Eureka for these gases follows NDACC-IRWG guidelines. The remaining gases are non-standard, meaning that NDACC member sites are not required to retrieve them, and that there may not be harmonized retrieval strategies for a given species. SFIT2 retrievals of CO and C_2H_6 were first implemented for the PEARL-FTS by Batchelor et al. (2009) and Lindenmaier (2012), while the retrievals of C_2H_2, CH_3OH, HCOOH, and H_2CO were implemented by Viatte et al. (2014). When SFIT4 was released in 2014, work was done by Stephanie Conway to adapt the retrievals from SFIT2, and these retrieval strategies have been largely unchanged since then, with the exception of CO and H_2CO. The CO and H_2CO retrievals were most recently revised by Erik Lutsch as part of the EU-funded Copernicus Atmospheric Monitoring Service (CAMS) Rapid Delivery (RD) project that began in March 2018, and the Sentinel-5 Precursor TROPOMI validation efforts described in Vigouroux et al. (2018), respectively. The retrievals of C_2H_4 and PAN are new, and were developed and implemented for the PEARL-FTS as part of this thesis. A description of the retrieval parameters and methods for each trace-gas are summarized in Table 3.1 and are described in the following subsections. For the *a priori* profiles of all target gases described in this chapter, we use a 40-year average (1980–2020) for Eureka from the Whole Atmosphere Community Climate Model v4.0 (WACCMv4) (Marsh et al., 2013).

Table 3.1: Retrieval microwindows, interfering species, retrieval parameters, and mean DOFS for the PEARL-FTS SFIT4 retrievals and corresponding references. The standard deviation of the DOFS is provided in parentheses.

Target species	Microwindows (cm^{-1})	Interfering species[a]	ILC[b](km)	$\mathbf{S}_a$ (%)	Linelist	Mean DOFS	References
CO	2057.700–2058.000, 2069.560–2069.760, 2157.500–2159.150	CO_2, H_2O, N_2O, O_3, OCS	2	2[c]	ATM12 (CO), HIT08 (others)	2.17 (0.34)	Notholt et al. (2000), Zhao et al. (2002), Viatte et al. (2014)
C_2H_2	3250.430–3250.770, 3255.180–3255.725, 3304.825–3305.350	H_2O, HDO	4	50[c]	HIT08	1.40 (0.30)	Petersen et al. (2008), Paton-Walsh et al. (2010), Viatte et al. (2014)
C_2H_4	948.800–952.400	CO_2, COF_2, H_2O, N_2O, NH_3, O_3, SF_6	Tikhonov	50[d]	ATM20	1.00 (0.01)	Paton-Walsh et al. (2005), Rinsland et al. (2005), Vander Auwera et al. (2014), Toon et al. (2018)
C_2H_6	2976.660–2976.950, 2983.200–2983.550, 2986.500–2986.950	H_2O, O_3, CH_4	4	50	HIT08	1.87 (0.34)	Notholt et al. (1997), Meier et al. (2004), Paton-Walsh et al. (2010), Viatte et al. (2014)
CH_3OH	992.000–998.700, 1029.000–1037.000	CO_2, H_2O, O_3, O_3^{686}, O_3^{676}, O_3^{668}, O_3^{667}	4	100[c]	HIT08	1.04 (0.04)	Vigouroux et al. (2012), Viatte et al. (2014), Bader et al. (2014)
HCOOH	1102.000–1109.000, 1178.400–1178.800	CCl_2F_2, CH_4, CHF_2Cl, H_2O, HDO, N_2O, NH_3, O_3	Tikhonov	5[d]	HIT08	1.12 (0.05)	Zander et al. (2010), Vigouroux et al. (2012), Yamanouchi et al. (2020)
H_2CO	2763.420–2764.170, 2765.650–2766.010, 2778.150–2779.100, 2780.650–2782.000	HDO, CH_4, O_3, N_2O	Tikhonov	25[d]	ATM16	1.25 (0.15	Notholt et al. (1997), Paton-Walsh et al. (2005), Viatte et al. (2014), Vigouroux et al. (2018)
PAN	779.900–811.370	CO_2, CCl_4, CHF_2Cl, $ClONO_2$, CFC-113, H_2O, O_3	Tikhonov	35[d]	Pseudolines (PAN), HIT2016 (H_2O), HIT08 (others)	1.02 (0.02)	Mahieu et al. (2021)

[a] Superscripts denote isotopologues.
[b] Exponential ILC was used unless Tikhonov regularization was applied.
[c] $\mathbf{S}_a$ diagonals were scaled by the square-root of the inter-layer thickness.
[d] Tikhononov regularization strength α value.

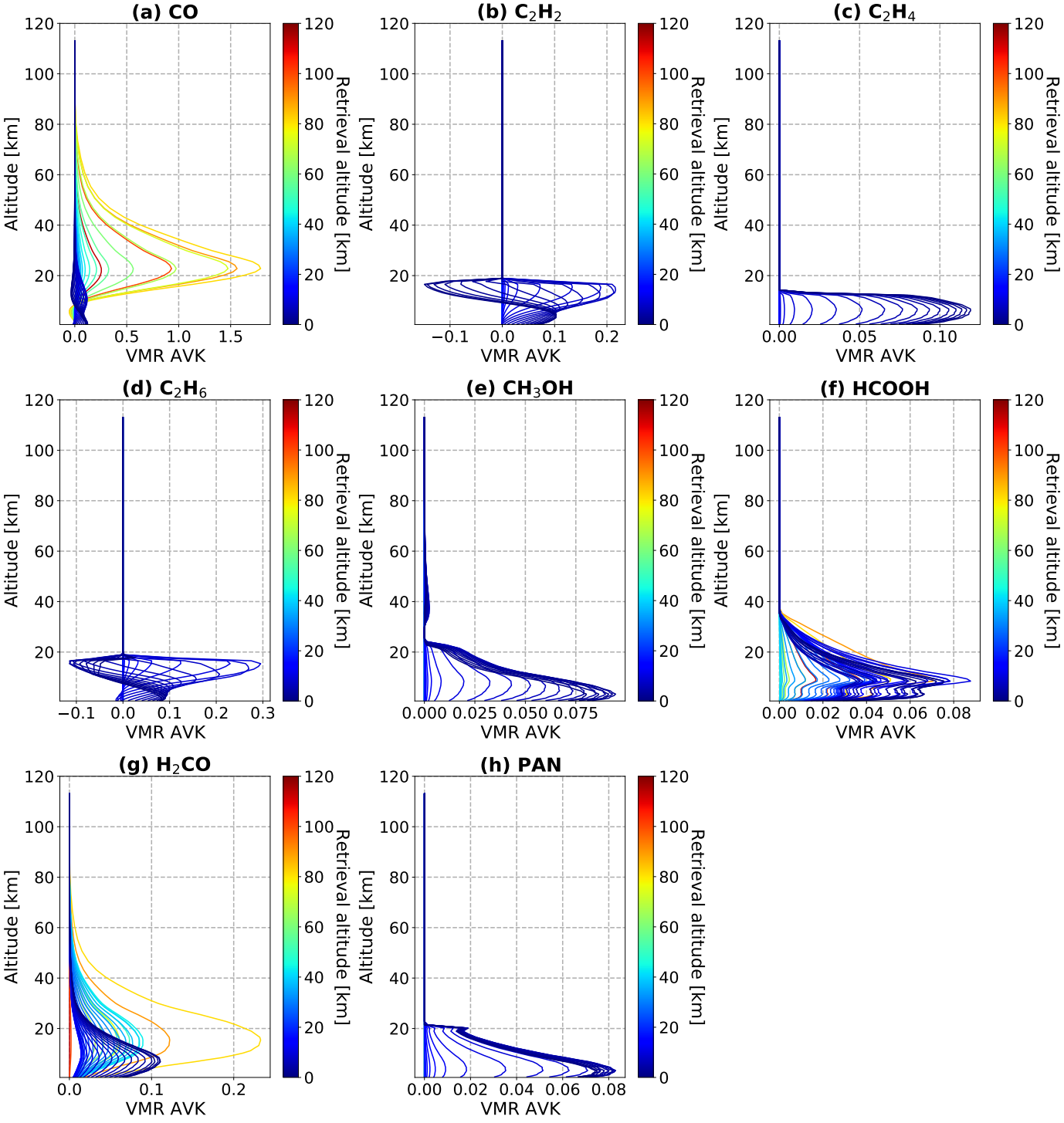

Figure 3.1: Mean 2006–2020 PEARL-FTS VMR averaging kernels for **(a)** CO, **(b)** C_2H_2, **(c)** C_2H_4, **(d)** C_2H_6, **(e)** CH_3OH, **(f)** HCOOH, **(g)** H_2CO, and **(h)** PAN.

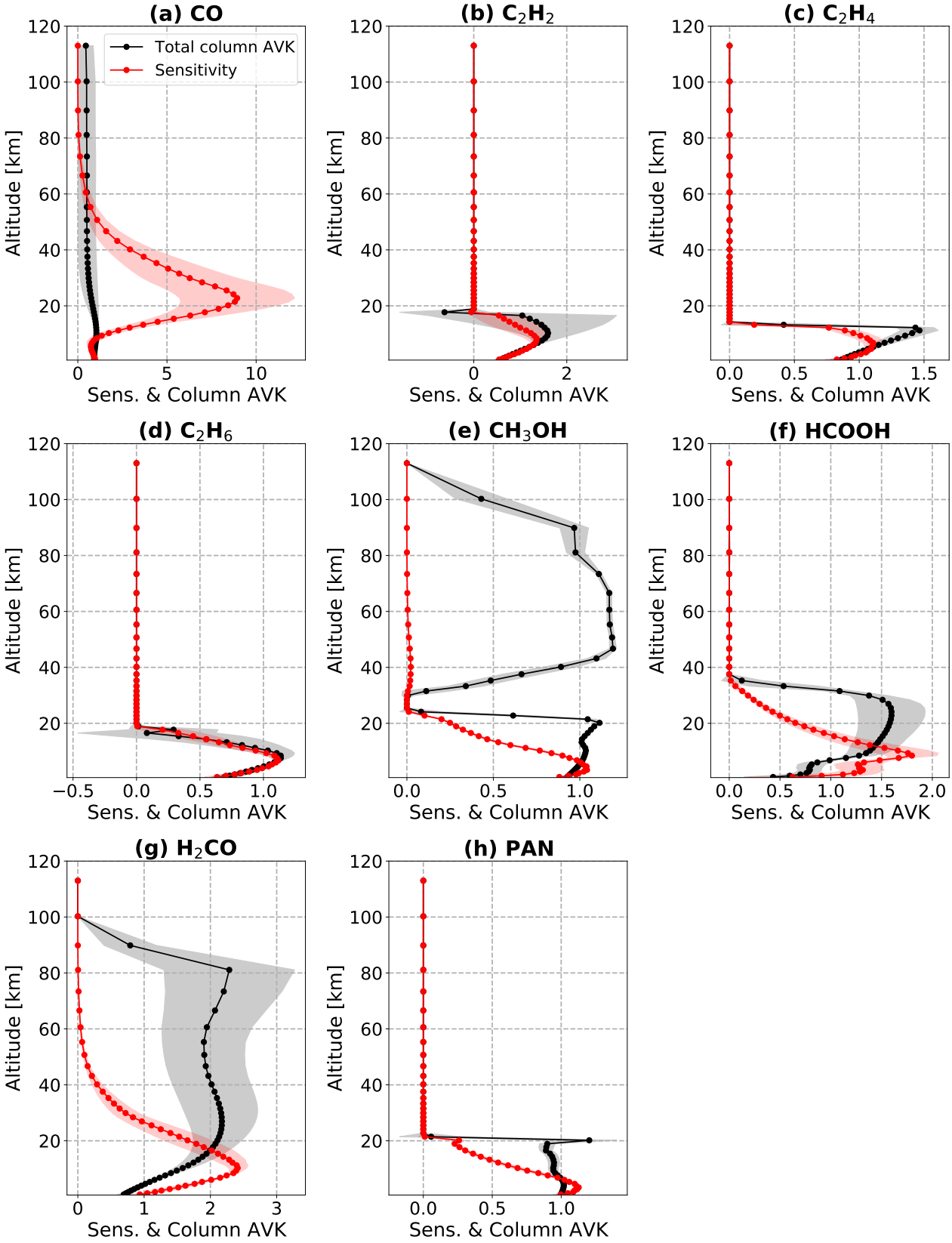

Figure 3.2: Mean 2006–2020 PEARL-FTS total column averaging kernels and retrieval sensitivity for **(a)** CO, **(b)** C_2H_2, **(c)** C_2H_4, **(d)** C_2H_6, **(e)** CH_3OH, **(f)** HCOOH, **(g)** H_2CO, and **(h)** PAN. The black and red shaded areas denote one standard deviation from the means.

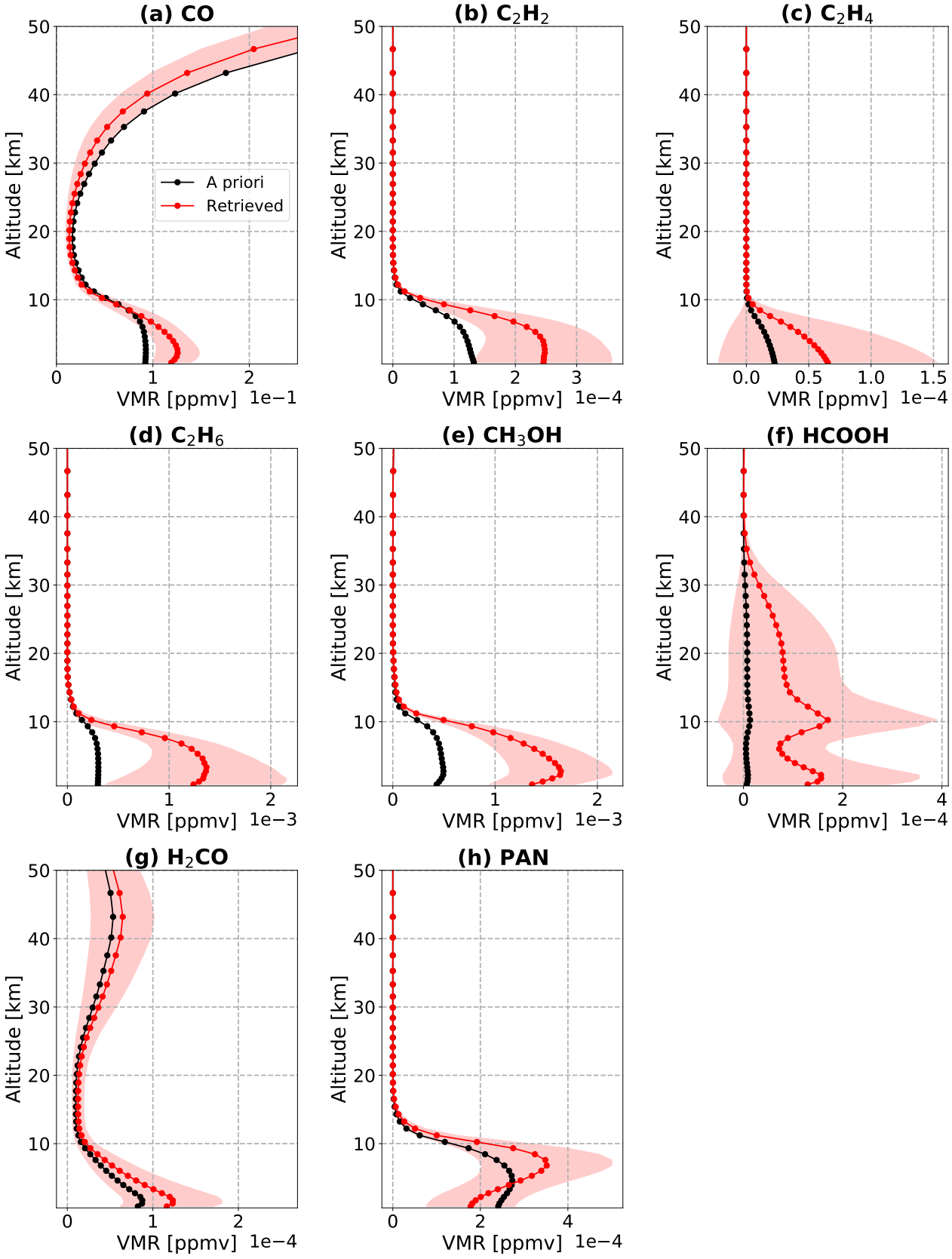

Figure 3.3: PEARL-FTS *a priori* profiles and mean 2006–2020 retrieved VMR profiles for **(a)** CO, **(b)** C_2H_2, **(c)** C_2H_4, **(d)** C_2H_6, **(e)** CH_3OH, **(f)** HCOOH, **(g)** H_2CO, and **(h)** PAN. The red shaded area denotes one standard deviation from the mean.

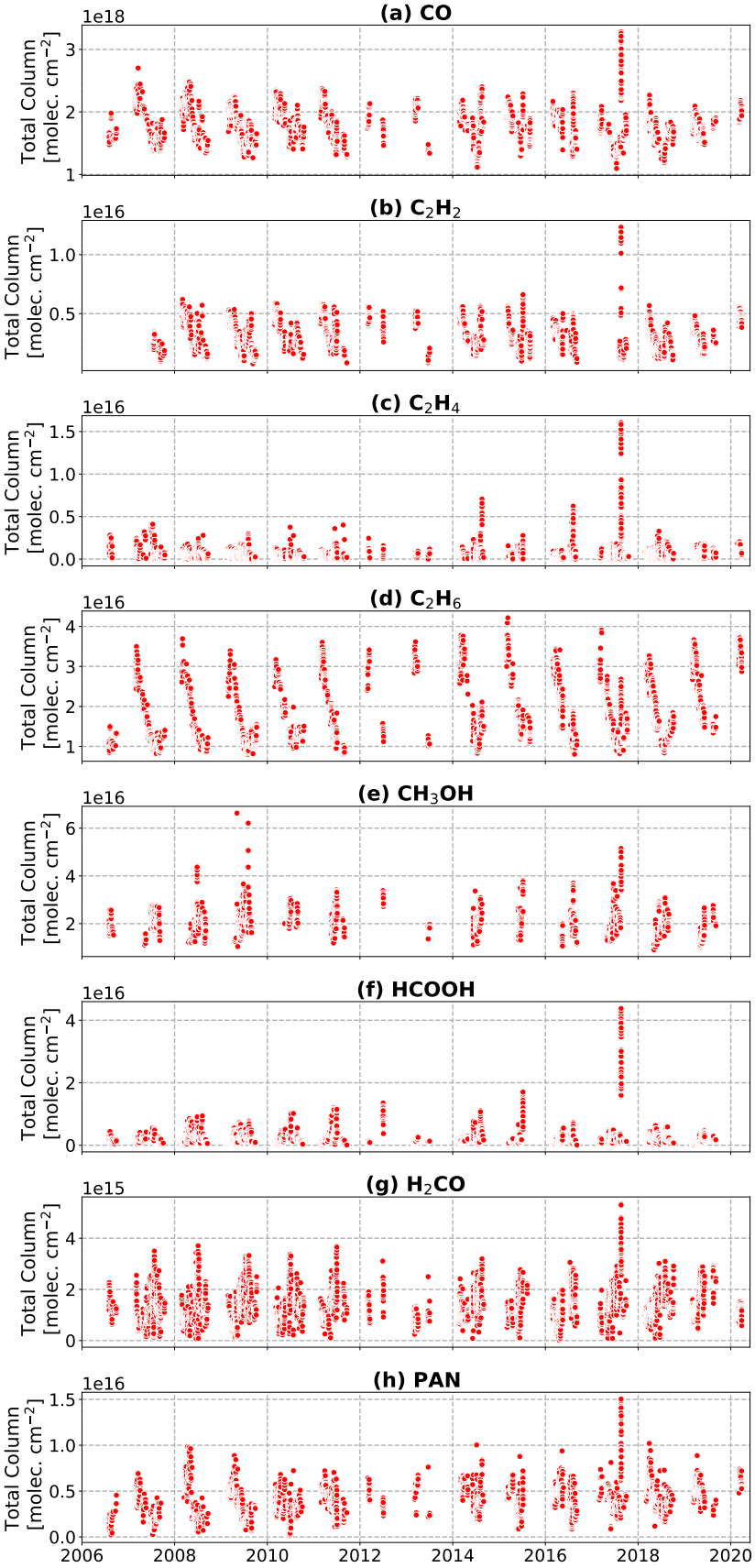

Figure 3.4: PEARL-FTS retrieved total column time-series at Eureka of **(a)** CO, **(b)** C_2H_2, **(c)** C_2H_4, **(d)** C_2H_6, **(e)** CH_3OH, **(f)** HCOOH, **(g)** H_2CO, and **(h)** PAN.

3.1 CO

The PEARL-FTS CO retrievals are performed following NDACC-IRWG guidelines using a harmonized retrieval strategy. The retrieval microwindows, interfering gases, ILC width, $\mathbf{S}_a$ constraints, and the corresponding references are provided in Table 3.1. There are three standard microwindows for CO: a strong line at 2157.50–2159.15 cm^{-1}, and two weak lines at 2057.70–2058.00 cm^{-1}, and 2069.56–2069.76 cm^{-1} (Notholt et al., 2000; Viatte et al., 2014; Zhao et al., 2002). The use of both strong and weak lines provides enhanced vertical sensitivity when compared to retrievals with only a single line (Barret et al., 2003; Lutsch, 2019). The $\mathbf{S}_a$ was adjusted by Erik Lutsch based on the requirements of the earlier ESA-funded Quality Assurance for Essential Climate Variable (QA4ECV) project in 2016, and more recently the CAMS27 RD initiative in 2018. These main requirements were (Lutsch, 2019):

1. A retrieved DOFS between 1.5 and 3.5 in the altitude range from the surface to 35 km.
2. Total column averaging kernel values between 0 and 1.4 from the surface to 35 km.
3. A harmonized error analysis approach that is consistent across all sites.

To meet these requirements, the diagonal values of the $\mathbf{S}_a$ matrix were reduced from 20% used by (Viatte et al., 2014) to 2% (Lutsch, 2019). The SNR in SFIT4 is significantly higher ($\sim$1100 for the PEARL-FTS CO retrievals) than in the earlier SFIT2 retrievals which used an ad hoc SNR value of 85 derived from a trade-off curve of the root mean square (RMS) error residuals versus SNR. This provides an increase in the information content from the measurement versus the *a priori*, and thus motivates a reduction in the $\mathbf{S}_a$ diagonal values in the SFIT4 retrieval. The off-diagonal elements were generated using an exponential ILC with a 2 km correlation width following Eq. 2.49 (Lutsch, 2019). CO_2, H_2O, N_2O, O_3, and OCS are interfering species in the CO retrieval, with N_2O and O_3 being retrieved as profiles, while all other interferers are retrieved as total columns through a scaling of the *a priori* values. As highlighted by Lutsch (2019), the strong constraints placed on the $\mathbf{S}_a$ result in a reduction of CO variability in the stratosphere and mesosphere as a result of the profiles being constrained to the *a priori* profile shape. There is a significant strato-mesospheric CO component in the high Arctic during the early spring months (Jin et al., 2005; Kasai et al., 2005), and this is not properly captured in the WACCMv4 CO *a priori* profile since it is an average over a 40-year period (1980–2020). Consequentially, the averaging kernel values near the top of the retrieval grid are lower, while the values in the stratosphere below 50 km are greater than unity, giving very high sensitivity in this altitude region (shown in Fig. 3.1a and Fig. 3.2a).

For the spectroscopic parameters, the ATM12 linelist (Toon, 2015) is used for CO, while for the interfering species the HITRAN 2008 linelist parameters are used (Rothman et al., 2009). Pseudo-linelists generated by G. C. Toon (Jet Propulsion Laboratory, California Institute of Technology, Pasadena, CA; available from https://mark4sun.jpl.nasa.gov/pseudo.html) are used to supplement the spectroscopic databases where absorption parameters were not available, namely those of carbon tetrachloride (CCl_4), chlorine nitrate ($ClONO_2$), CFC-12 (CCl_2F_2), HCFC-22 ($CHClF_2$), HFC-23 (CHF_3), and CFC-113 (CCl_2FCClF_2).

The mean retrieved DOFS for CO over the period of 2006–2020 are 2.17 with a standard deviation of 0.34 (listed in Table 3.1). The mean retrieved CO VMR profile is plotted along with the *a priori* profile in Fig. 3.3a. The mean retrieved VMR profile is larger than the *a priori* between the surface to approximately 9 km, with surface values of approximately 120 ppb and 90 ppb, respectively. Between 9 and 20 km above the surface, the *a priori* and retrieved profiles are relatively close, however, above 20 km the retrieved and *a priori* profiles begin to diverge more. The CO VMR can be seen increasing with height in the stratosphere due to production of CO from the oxidation of CH_4 and the photolysis of CO_2, and this is reflected in both the retrieved and *a priori* profiles. The time-series of retrieved CO total columns is shown in Fig. 3.4a. CO displays a strong seasonal cycle at Eureka, with the largest columns during the springtime, and a steady decrease in the columns going towards the summer months. Additionally, significant enhancements in the CO total columns due to transported biomass burning plumes can often be observed during the late summer months. The seasonal cycle of CO and biomass burning enhancements are discussed in greater detail in Chapters 5 and 6.

3.2 C_2H_2

The retrieval of C_2H_2 for the PEARL-FTS is performed following the approach of Viatte et al. (2014). Three spectral fitting microwindows are used: one window spanning 3250.43–3250.77 cm^{-1} based on the work by Petersen et al. (2008), and two windows from Paton-Walsh et al. (2010) covering 3255.180–3255.725 cm^{-1} and 3304.825–3305.350 cm^{-1}. H_2O and deuterated water (HDO) are the only interfering species in the C_2H_2 retrieval, and they are retrieved by scaling the *a priori* profiles. Spectroscopic absorption parameters are sourced from the HITRAN 2008 linelist database for all species in the retrieval. The diagonals of the C_2H_2 $\mathbf{S}_a$ matrix correspond to a standard deviation of 50%, but are scaled by the square root of the layer thickness to optimize the DOFS and to increase the variability of the retrieved profiles in the troposphere. An exponential ILC with a

correlation width of 4 km is used to set the off-diagonal elements of the $\mathbf{S}_a$, and dampens unphysical oscillations in the retrieved C_2H_2 profiles.

A mean retrieved DOFS of 1.4 with a standard deviation of 0.3 is found over the period of 2007–2020 (see Table 3.1). The mean C_2H_2 VMR averaging kernel is plotted in Fig. 3.1b and the mean total column averaging kernel and sensitivity are shown in Fig. 3.2b. The C_2H_2 retrieval has a sensitivity greater than 0.5 in the altitude range from the surface to approximately 16 km. The *a priori* and mean retrieved C_2H_2 VMR profiles are plotted in Fig. 3.3b. The mean retrieved profile is approximately double the *a priori* near the surface with values of 0.24 ppbv and 0.12 ppbv, respectively. The mean retrieved profile is relatively constant from the surface to approximately 6 km, and then rapidly decreases to near zero around 15 km. The total column time-series of C_2H_2 is shown in Fig. 3.4. C_2H_2 displays a similar seasonal cycle to CO at Eureka due to their common anthropogenic emission sources (mainly fossil fuel combustion) and atmospheric sinks (primarily removal by OH). The largest total columns are observed during the spring months and the smallest total columns are seen during the summertime. Biomass burning also presents a periodic source of C_2H_2 during the late summer months at Eureka.

3.3 C_2H_4

Ground-based retrievals of C_2H_4 were previously implemented in SFIT2 by Paton-Walsh et al. (2005), Rinsland et al. (2005), and Vander Auwera et al. (2014). However, to the best of our knowledge these retrievals have not yet been performed using SFIT4. Here, we describe the implementation of the C_2H_4 retrieval for the PEARL-FTS in SFIT4 based most closely on the spectral fitting windows used by Vander Auwera et al. (2014) at Jungfraujoch, Switzerland. Only a single wide microwindow spanning 948.80–952.40 cm^{-1} is used in the retrieval of C_2H_4, CO_2, COF_2, H_2O, N_2O, NH_3, O_3, and SF_6 are interfering species in this spectral fitting microwindow. All of these interferers are fitted simultaneously and retrieved as total columns via a scaling of their *a priori* profiles. An example spectral fit of C_2H_4 and the interfering species is shown in Fig. 3.5. Additionally, the C_2H_4 retrieval microwindow falls within the wavenumber bandpass range of both NDACC filters 6 and 7 (listed in Table 2.1), significantly increasing the number of available measurements. For the spectroscopic parameters, the ATM20 linelist was used for C_2H_4 and all of the interfering gases (Toon, 2022). The retrieval was also tested with the HITRAN 2008 and HITRAN 2016 linelist databases, but the ATM20 linelist was found to yield the lowest RMS errors in the residuals of the fits for C_2H_4 and the interfering species. Similar to PAN, Tikhonov regularization was used

to construct the $\mathbf{S}_a$ matrix for C_2H_4. A range of regularization strength values were tested, and a final value of $\alpha = 50$ was found to minimize unphysical oscillations in the retrieved profiles without constraining the retrieved profiles too strongly to the *a priori* profile shape.

A mean DOFS of 1.00 with a small standard deviation of 0.01 was retrieved for C_2H_4 over the full 2006–2020 PEARL-FTS time-series (Table 3.1), meaning that the retrieval is in essence a profile scaling of the *a priori*. The mean C_2H_4 VMR averaging kernel is shown in Fig. 3.1c, and the mean total column averaging kernel and sensitivity are shown in Fig. 3.2c. The C_2H_4 retrieval has a sensitivity greater than 0.5 from the surface to approximately 12 km, and has little to no sensitivity above 12 km. The *a priori* and mean retrieved C_2H_4 profiles are provided in Fig. 3.3c. The mean retrieved C_2H_4 profile is larger than the *a priori* profile below 10 km, with surface values of 0.02 ppbv and 0.06 ppbv, respectively. Above 10 km, both the *a priori* and the mean retrieved profile are zero. The time-series of retrieved C_2H_4 total columns is shown in Fig. 3.4c. In general, due to absence of local sources of C_2H_4 in the Arctic, the column concentrations are extremely low at Eureka for much of the year and there is no detectable seasonal cycle. The primary source of C_2H_4 at Eureka is transported biomass burning plumes, and large enhancements in the C_2H_4 total columns can regularly be observed during the late summer months as a result of wildfires. Because of the

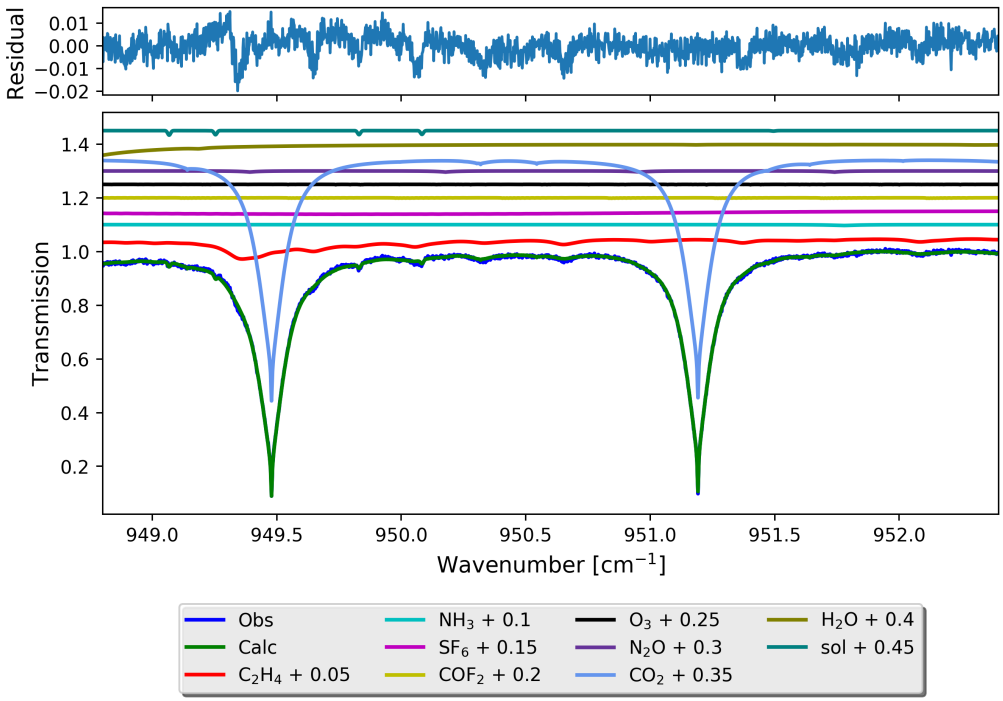

Figure 3.5: An example spectral fit of C_2H_4 and interfering species for a PEARL-FTS measurement taken on 19 August 2017.

extremely low ambient concentrations at Eureka, the C_2H_4 product may hold value in identifying wildfire enhancements in the PEARL-FTS data record. Biomass burning enhancements of C_2H_4 at Eureka are discussed in further detail in Chapter 5.

3.4 C_2H_6

Since C_2H_6 is a standard NDACC species, the PEARL-FTS retrieval of C_2H_6 is performed following NDACC-IRWG reccomendations. The original SFIT2 retrieval of C_2H_6 at Eureka is described in Viatte et al. (2014), and the retrieval was later implemented in SFIT4 by Stephanie Conway. Three retrieval microwindows are used: 2976.66–2976.95 cm^{-1} (Paton-Walsh et al., 2010), 2983.20–2983.55 cm^{-1} (Meier et al., 2004), and 2986.50–2986.95 cm^{-1} (Notholt et al., 1997). The diagonals of the $\mathbf{S}_a$ matrix are set to a standard deviation of 50% and the off-diagonal values are set using an exponential ILC with a correlation width of 4 km. H_2O, O_3, and CH_4 are interfering species, and are retrieved as scaled *a priori* profiles. Spectroscopic parameters are taken from the HITRAN 2008 linelist database for C_2H_6 and all interfering species.

The mean DOFS for 2006–2020 is 1.87 with a standard deviation of 0.34 (provided in Table 3.1). The mean C_2H_6 VMR averaging kernel is plotted in Fig. 3.1d and the mean total column averaging kernel and sensitivity are shown in Fig. 3.2d. The C_2H_6 VMR and total column averaging kernels have a similar shape to C_2H_2, and the retrieval has sensitivity (> 0.5) from the surface to approximately 14 km. The *a priori* and mean retrieved profiles are plotted in Fig. 3.3d. The mean retrieved profile is greater than the *a priori* below approximately 11 km, with surface values of 1.2 ppbv and 0.03 ppbv, respectively. The mean retrieved profile is largely constant throughout the lower- to mid-troposphere, with a small increase in the VMR from the surface to 4 km, and then a rapid decrease from approximately 5 km to near zero around 11 km. The retrieved total column time-series of C_2H_6 is plotted in Fig. 3.4d. C_2H_6 displays a similar seasonal cycle to CO and C_2H_2 at Eureka again due to their common sources from fossil fuel combustion and their removal from the atmosphere via oxidation by OH. Enhancements in the C_2H_6 total columns due to transported wildfire plumes can be seen during the late summer months, however these tend to be smaller than other biomass burning species due to the lower C_2H_6 emissions from boreal wildfires (Akagi et al., 2011; Andreae, 2019; Andreae and Merlet, 2001; Lutsch et al., 2019).

3.5 CH_3OH

The retrieval of CH_3OH at Eureka is based upon the approach of Vigouroux et al. (2012), Bader et al. (2014), and Viatte et al. (2014). Two wide microwindows are used: 992.00–998.70 cm^{-1} and 1029.00–1037.00 cm^{-1}. H_2O, CO_2, and O_3 and its isotopologues (listed in Table 3.1) are the main interfering species in these microwindows. O_3 is retrieved as a profile, while all of the other interferers are retrieved only as columns. The spectroscopic parameters for CH_3OH and the interfering species are taken from HITRAN 2008. Since CH_3OH concentrations are highly variable throughout the year, the diagonals of the $\mathbf{S}_a$ matrix are set to a standard deviation of 100%, but are scaled based on the retrieval layer thickness, which allows for greater variability in the retrieved profiles in the troposphere. The off-diagonal elements of the $\mathbf{S}_a$ matrix are generated using an exponential ILC with a correlation width of 4 km.

A mean retrieved DOFS of 1.04 with a standard deviation of 0.04 is found for the period of 2006–2020 (Table 3.1). The mean CH_3OH VMR averaging kernel is shown in Fig. 3.1e and the mean total column averaging kernel and sensitivity are plotted in Fig. 3.2e. The CH_3OH retrieval has a sensitivity greater than 0.5 in the altitude range from the surface to approximately 13 km. The CH_3OH *a priori* and mean retrieved profiles are plotted in Fig. 3.3e. The retrieved profile is notably larger than the *a priori* throughout the troposphere, with surface values of 1.4 ppbv and 0.5 ppbv, respectively. The mean retrieved profile increases from the surface to approximately 3 km, before decreasing rapidly in the upper troposphere and lower stratosphere. The CH_3OH total column time-series is plotted in Fig. 3.4e. As highlighted by Lutsch (2019), the retrievals of CH_3OH during the spring and fall months generally do not converge as a result of the strong interference from O_3 and the low CH_3OH abundance during these periods. Consequentially, CH_3OH columns are typically only reliably retrieved between May and August each year, which can be seen in Fig. 3.4e. Some enhancements from biomass burning can be seen in the CH_3OH total column time series during the late summer months, however, these enhancements tend to be small relative to some of the other biomass burning tracer species.

3.6 HCOOH

The PEARL-FTS retrieval strategy for HCOOH is based upon the approach of Vigouroux et al. (2012) and Viatte et al. (2014). Two microwindows are used: a primary microwindow spanning 1102.00–1109.00 cm^{-1} that contains the main HCOOH absorption feature, and a secondary mi-

crowindow covering 1178.40–1178.80 cm^{-1} that does not contain any HCOOH absorption features but is used to improve the fitting of the interfering species HDO. HDO is not fitted in the primary microwindow, but rather a strong HDO absorption line is fitted in the secondary microwindow and this information is used to constrain the HDO retrieval through the SFIT4 forward model calculation. This approach using the primary and secondary microwindows was found to improve the spectral fits, and increase the stability of the retrieval (i.e., fewer profile oscillations and more converged measurements) in comparison to using only a single microwindow (Viatte et al., 2014; Vigouroux et al., 2012). For HCOOH, it was found that the WACCMv4 *a priori* profile was very low in comparison to the retrieved profiles (shown in Fig. 3.3f), and as a result the $\mathbf{S}_a$ matrix is constructed using Tikhonov regularization, with a relatively weak regularization strength of $\alpha = 5$. This regularization strength was chosen to maintain a DOFS greater than 1, and to allow for sufficient variability in the retrieved profiles relative to the very low *a priori* values. CCl_2F_2, CH_4, chlorodifluoromethane (CHF_2Cl), H_2O, HDO, N_2O, NH_3, and O_3 are all interfering gases in the specified microwindows. O_3 is retrieved as a profile, while all other interfering species are retrieved via *a priori* profile scaling.

The mean retrieved DOFS of HCOOH for 2006–2020 is 1.12 with a standard deviation of 0.05 (provided in Table 3.1), indicating that there is little to no vertical profile information in the retrieval. The mean VMR averaging kernel is plotted in Fig. 3.1f and the mean total column averaging kernel and sensitivity are shown in Fig. 3.2f. The HCOOH retrieval has a sensitivity greater than 0.5 in the altitude range from the surface to approximately 21 km. The HCOOH *a priori* and mean retrieved VMR profiles are shown in Fig. 3.3f. The VMR profile displays two peaks at approximately 2 km and 10 km, but generally high concentrations of HCOOH are found between the surface and 20 km. The HCOOH VMR decreases slowly above 20 km to near zero at around 40 km. Although HCOOH is primarily a tropospheric gas, a lower-stratospheric component is visible in the mean VMR profile in Fig. 3.3f. The HCOOH total column time-series is plotted in Fig. 3.4f. Similar to CH_3OH and H_2CO, transported biogenic emissions are a major driver of the seasonal cycle of HCOOH at Eureka, and the largest columns are observed during the summer months, while the smallest columns are seen during the early and late year. Significant biomass burning enhancements can also be observed during the late summer months, in particular during August 2017. This will be discussed in further detail in Chapter 5.

3.7 H_2CO

The PEARL-FTS retrievals of H_2CO were revised by Erik Lutsch in 2017–2018 as part of the ESA Nitrogen Dioxide and Formaldehyde for Validation (NIDFORVal) harmonization project with the purpose of validating the TROPOMI H_2CO product. The current retrieval strategy is described in Vigouroux et al. (2018) and references therein, and is summarized here for the PEARL-FTS retrievals. The H_2CO retrieval uses four microwindows: two windows containing weak absorption features from 2763.42–2764.17 cm^{-1} and 2765.65–2766.01 cm^{-1}, and two narrow microwindows containing strong absorption lines from 2778.15–2779.10 cm^{-1} and 2780.65–2782.00 cm^{-1}. Although the retrieval is possible using only the two microwindows with strong lines, the microwindows with the weak lines were added to improve the DOFS of the retrieval (Vigouroux et al., 2018). Tikhonov regularization with a regularized strength $\alpha = 25$ was used to construct the $\mathbf{S}_a$ matrix and constrain the retrieved profiles. HDO, CH_4, O_3, and N_2O are interfering species in the retrieval with HDO, CH_4, and O_3 being retrieved as full profiles, while N_2O is retrieved as a column through *a priori* profile scaling. The ATM16 linelist (Toon et al., 2016) is used for all species in the retrieval, which was found to provide better spectral fits in comparison to HITRAN 2008 (Vigouroux et al., 2018). In the ATM16 linelist, the H_2CO and N_2O lines correspond to the HITRAN 2012 spectroscopic database (Rothman et al., 2013).

The H_2CO retrieval has a mean retrieved DOFS of 1.25 with a standard deviation of 0.15 over the period of 2006–2020 (Table 3.1). The mean H_2CO VMR averaging kernel is plotted in Fig. 3.1g and the mean total column averaging kernel and sensitivity are provided in Fig. 3.2g. The H_2CO retrieval has a sensitivity greater than 0.5 from the surface to approximately 33 km, with the majority of the information content in the retrieval coming from the region below 20 km (shown in Fig. 3.1g). The mean H_2CO VMR profile and *a priori* profile are plotted in Fig. 3.3g. The mean retrieved profile does not differ significantly from the *a priori* with surface values of approximately 0.12 ppbv and 0.8 ppbv, respectively. The mean VMR profile decreases rapidly from the surface to around 15 km, above which it begins to increase again into the stratosphere, reaching a second peak around 42 km. The total column time-series of H_2CO at Eureka is plotted in Fig. 3.4g, and shows a seasonal cycle with larger total columns during the summer months, and lower total columns during the spring and fall, similar to CH_3OH (shown in Fig. 3.4e) due to their common biogenic sources. Biomass burning enhancements are also visible in the H_2CO time-series during the late summer months.

3.8 PAN

The ground-based FTIR retrieval of PAN is novel and was first described by Mahieu et al. (2021), which included the Eureka retrievals. The absorption features of PAN are extremely broad (shown in Fig. 3.6), with full-width at half-maximum values on the order of 20 cm^{-1}, necessitating wide microwindows. Two wide retrieval microwindows were tested for PAN: 779.90–811.37 cm^{-1} (hereafter referred to as MW1) and 1150.57–1178.83cm^{-1} (hereafter referred to as MW2). MW1 encompasses the absorption feature with a center at approximately 794 cm^{-1}, while MW2 encompasses the absorption feature centered around 1163 cm^{-1}. Unfortunately, the strongest absorption feature that can be seen in Fig. 3.6, which is located at 1740 cm^{-1}, falls just outside of the NDACC filter bandpass ranges, and thus we are unable to retrieve PAN from this stronger feature. As discussed in Mahieu et al. (2021), MW2 was found to yield inconsistent and often unphysical retrieved columns at the polar sites, and a lower signal-to-noise ratio on average than MW1. A retrieval was also tested using both MW1 and MW2 simultaneously, however, due to the broad width of the two retrieval microwindows, the retrieval was unfeasibly slow and did not provide a significant benefit over a single-window retrieval using MW1 only. As a result, the final PAN retrieval at Eureka only uses MW1. An example spectral fit is shown in Fig. 3.7. The spectral region selected for the computation of the SNR is located between 1139.205 cm^{-1} and 1139.260 cm^{-1}, and does not contain any absorption features, providing an optimal SNR calculation. The HITRAN and ATM linelist databases did not have absorption cross-sections for PAN available, so G.C. Toon's pseudo-linelist was used. A description of the PAN pseudo-lines and how they were generated can be found at: https://mark4sun.jpl.nasa.gov/data/spec/Pseudo/Readme.pan. The HITRAN 2016 linelist was used for H_2O, while for all other interfering species the standard HITRAN 2008 linelist database was used. To construct the $\mathbf{S}_a$ matrix for PAN, Tikhonov regularization was employed. A broad range of regularization strengths α were tested for PAN, and a value of $\alpha = 35$ was found to sufficiently limit unphysical oscillations, while still allowing for a sufficient degree of variability in the retrieved profile with respect to the *a priori*.

A DOFS of 1.02 with a standard deviation of 0.02 was retrieved over the full 2006–2020 time-series (provided in Table 3.1). The mean PAN VMR averaging kernel is shown in Fig. 3.1h, while the mean total column averaging kernel and the sensitivity are shown in Fig. 3.2h. The PAN retrieval has sensitivity (> 0.5) in the altitude range from the surface to approximately 12 km, and has no sensitivity above 20 km. The mean retrieved PAN profile and *a priori* profile are plotted in Fig. 3.3h. The retrieved profile is lower than the *a priori* from the surface to around 4 km, with surface

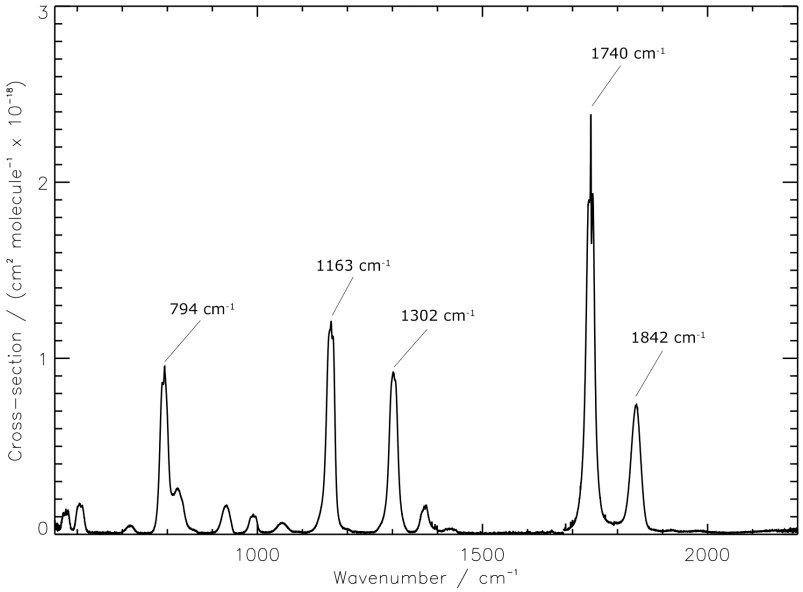

Figure 3.6: PAN absorption cross-sections with peak positions labeled, measured at 295 K. Figure adapted from Allen et al. (2005).

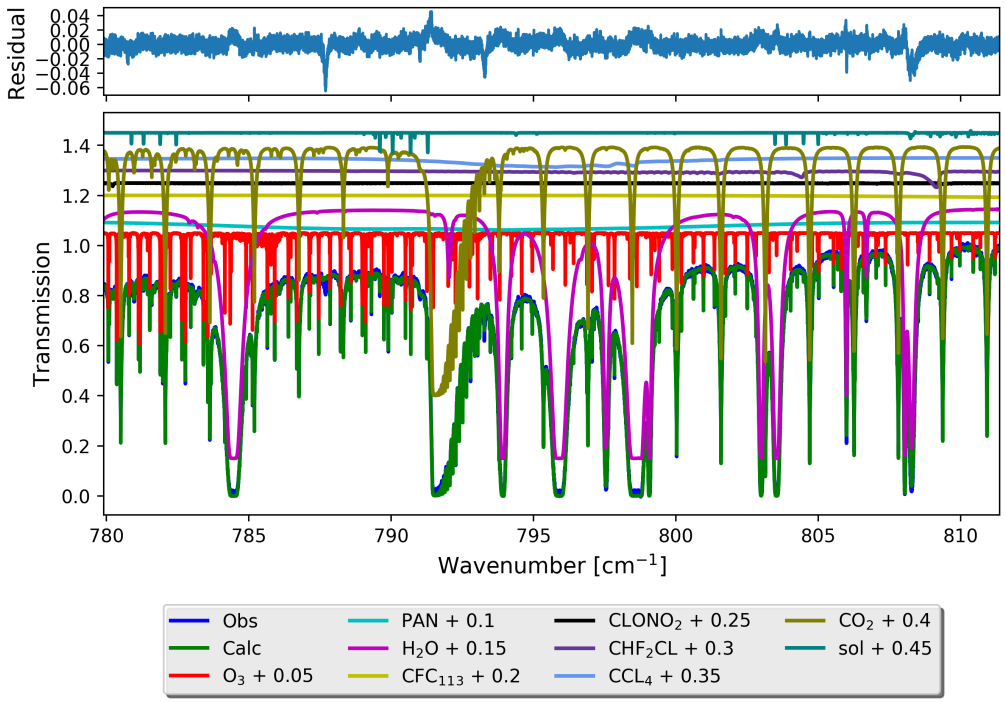

Figure 3.7: An example spectral fit of PAN and interfering species in MW1 for a PEARL-FTS measurement taken on 19 August 2017.

values of 0.19 ppbv and 0.23 ppbv, respectively. Between 4 km and 13 km, the retrieved profile is larger than the *a priori*, with a peak in the retrieved VMR at approximately 8 km. Both the *a priori* and mean retrieved profile decrease rapidly above 8 km, approaching near zero values around 16 km. The total column time-series of PAN is shown in Fig. 3.4h. The largest PAN columns are observed during the springtime, and the measured columns gradually decrease towards the summer months due the temperature dependence of the lifetime of PAN in the atmosphere. Biomass burning enhancements of PAN are often observed during the summertime, and this is discussed in more detail in Chapter 5.

3.9 Error Analysis

SFIT4 includes a full error calculation based on the methodology of Rodgers (1990) and Rodgers (2000). The error budget for the PEARL-FTS is described in detail in Batchelor et al. (2009), and we briefly summarize the uncertainty components here. In addition to the measurement noise error ($\mathbf{S}_{meas}$), the uncertainty calculation takes into account forward model errors including the solar zenith angle (SZA) error ($\mathbf{S}_{sza}$), spectroscopic line errors ($\mathbf{S}_{line}$) (typically calculated from the HITRAN 2008 errors), and uncertainties in the assumed temperature profiles ($\mathbf{S}_{temp}$). As described in Rodgers and Connor (2003), interference errors due to both the simultaneous retrieval of interfering species ($\mathbf{S}_{intspec}$), and errors due to retrieval parameters ($\mathbf{S}_{retparam}$) such as wavelength shift, ILS, background slope and curvature, and phase error, are also included in the error budget. Lastly, the finite nature of the SFIT4 retrieval grid introduces a smoothing error ($\mathbf{S}_{sm}$; also referred to as the null-space error) which is calculated, but is not included in the final error budget as recommended by the NDACC-IRWG. The various uncertainty components are divided into two groups: random errors ($\mathbf{S}_{ran}$) and systematic errors ($\mathbf{S}_{sys}$). The temperature profile uncertainty has both a random and systematic component. The line intensity and air broadening uncertainties are considered as systematic errors, while all other uncertainties are considered as random errors. The total error ($\mathbf{S}_{tot}$) is determined by adding all of the random and systematic error components in quadrature.

The systematic and random temperature profile uncertainties used for the PEARL-FTS retrievals were determined by comparisons of the daily NCEP profiles to Eureka radiosonde measurements, with the average difference taken to be the systematic error and the standard deviation taken to be the random uncertainty. The systematic and random temperature profile uncertainties used for the PEARL-FTS retrievals are summarized in Table 3.2. The spectroscopic line errors include

Table 3.2: Temperature uncertainties used for the PEARL-FTS retrievals. For retrieval layers at 50.70 km and above, the uncertainties are constant at the values indicated.

Retrieval layer centre (km)	Systematic uncertainty (K)	Random uncertainty (K)
113.00 - 50.70	1.00	9.00
46.68	1.00	7.00
43.19	1.00	7.00
40.17	1.00	7.00
37.56	1.00	6.00
35.29	1.00	6.00
33.30	1.00	5.00
31.53	1.00	5.00
29.92	1.04	1.30
28.40	1.08	1.37
26.94	1.04	1.36
25.52	0.84	1.11
24.13	0.74	0.90
22.77	0.65	0.81
21.45	0.61	0.76
20.17	0.60	0.68
18.93	0.60	0.71
17.72	0.58	0.69
16.54	0.50	0.62
15.40	0.52	0.64
14.30	0.50	0.63
13.24	0.49	0.65
12.21	0.61	0.79
11.21	0.75	1.21
10.25	0.81	1.44
9.33	1.07	1.45
8.45	1.10	1.10
7.61	0.80	1.08
6.80	0.79	0.96
6.03	0.78	0.96
5.30	0.74	0.95
4.61	0.76	0.98
3.95	0.85	1.10
3.33	0.88	1.16
2.75	0.92	1.22
2.21	1.04	1.38
1.70	1.04	1.33
1.24	1.25	1.54
0.81	1.60	1.95

uncertainties due to line intensity, pressure-broadening, and temperature-broadening, and these are provided for all species in Table 3.3. For the SZA uncertainty, a standard value of 0.06° is used for all retrievals at Eureka since this is the approximate variation in the SZA over the course of a single mid-IR measurement (approximately 12 minutes each). The mean random, systematic, and total uncertainties for the retrievals of CO, C_2H_2, C_2H_4, C_2H_6, CH_3OH, HCOOH, H_2CO, and PAN are listed in Table 3.4. The relative total uncertainty of $\sim 67\%$ associated with the C_2H_4 total columns appears very large, however this is primarily due to the extremely low ambient concentrations of C_2H_4 in the Arctic in the absence of biomass burning pollution. During the 17–23 August 2017 biomass burning event, the mean relative total uncertainty in the retrieved C_2H_4 columns was 7.9%.

Table 3.3: Line intensity, pressure-broadening half-width, and temperature-broadening half-width errors for all species used in the PEARL-FTS retrieval uncertainty budget. Uncertainties are sourced from HITRAN 2008 unless specified otherwise.

Species	Line intensity (%)	Pressure-broadening (%)	Temperature-broadening (%)
CO	2.0	5.0	5.0
C_2H_2	15.0	15.0	15.0
C_2H_4	5.0[a]	10.0[a]	N/A[b]
C_2H_6	4.0	4.0	4.0
CH_3OH	15.0	20.0[c]	20.0[c]
HCOOH	7.5	20.0[c]	20.0[c]
H_2CO	15.0	20.0[c]	20.0[c]
PAN	8.0[d]	2.0[e]	3.0[e]

[a] Uncertainties based on Vander Auwera et al. (2014).
[b] No estimate of the C_2H_4 temperature broadening was available in the literature.
[c] Assumed value/rough estimate.
[d] Value based on Tereszchuk et al. (2013).
[e] Empirically estimated values from Mahieu et al. (2021).

Table 3.4: Mean random, systematic, and total retrieval uncertainties of the PEARL-FTS retrievals calculated over 2006–2020.

Species	Random uncertainty (%)	Systematic uncertainty (%)	Total uncertainty (%)
CO	1.6	2.3	2.75
C_2H_2	5.4	0.29	5.4
C_2H_4	64.0	17.9	67.3[a]
C_2H_6	1.0	4.2	4.3
CH_3OH	4.7	10.5	11.8
HCOOH	5.3	11.3	13.2
H_2CO	11.7	12.4	18.5
PAN	22.4	8.0	25.6

[a] Mean total uncertainty was 7.9% during the August 2017 enhancement event.

3.10 Quality Assurance

The final step of the PEARL-FTS data processing routine is quality assurance and quality control (QA/QC). Since the retrieved PEARL-FTS datasets are publicly available on the NDACC archive (accessible at: https://ndacc.org), it is important to remove measurements with poor quality spectra and erroneous outliers from the time-series. Quality assurance is often a trade-off between optimizing data quality and maintaining a sufficient number of observations in the time-series. One possible approach is to filter the dataset based on the total column amounts and their deviation from the monthly means across all years, however, this may inadvertently remove measurements during transient events such as transported wildfire smoke plumes which can result in total columns significantly above the baseline concentrations. Alternatively, using diagnostics based on the quality of the spectra and the spectral fits such as the RMS error and the DOFS to filter the data may be preferable. The RMS error of the fit between the measured spectra and the simulated spectra from the SFIT4 LBLRTM is often used as a metric for the goodness-of-fit for the retrieval microwindows. Large RMS values typically correspond to poor quality spectra with small SNR values. The retrieved DOFS are another diagnostic quantity that can be used to assess the quality of the data. The DOFS are generally inversely correlated with the RMS error of the fits, and poor quality spectra typically have a smaller than average DOFS. The retrieved DOFS has a seasonal cycle, with larger values of the DOFS found early and late in the year due to the longer measured slant-path through the atmosphere (as a result of the higher SZA values). However, the RMS errors follow a similar seasonal cycle, with larger RMS errors occurring during the spring and fall months due to the smaller SNR and a greater contribution from interfering species during this time.

It is standard practice in the NDACC-IRWG to use the ratio of the RMS/DOFS as a filtering criterion based on the approach of Sussmann et al. (2011), and this method is applied to the PEARL-FTS retrievals. As discussed above, the ratio of the RMS to the DOFS should remain relatively constant throughout the year, and values that are significantly above a pre-defined RMS/DOFS threshold are likely to be poor quality measurements. The value of the RMS/DOFS filter is typically determined through the use of a trade-off curve of the number of observations excluded as outlined in Sussmann et al. (2011). The RMS/DOFS threshold values for the retrieved species in this work are listed in Table 3.5. On occasion, erroneous outliers will evade the RMS/DOFS filtering routine. In these cases, a visual inspection of the spectral fits and manual removal of the individual observations may be necessary. In addition to the RMS/DOFS filter, any observations with negative partial or total columns are filtered out of the final time-series, as well as any measurements with a recorded

SZA $> 90°$.

Table 3.5: RMS/DOFS filtering thresholds used for QA/QC of the PEARL-FTS retrievals.

Species	RMS/DOFS threshold
CO	2.5
C_2H_2	2.0
C_2H_4	2.0
C_2H_6	1.5
CH_3OH	5.0
H_2CO	3.0
HCOOH	2.5
PAN	3.5

Chapter 4

Validation of TROPOMI CO Measurements Over the High Arctic

4.1 Introduction

In this chapter, we perform a global intercomparison of CO measurements from the TROPOMI instrument on-board the Sentinel-5 Precursor satellite with partial column measurements from ACE-FTS on board the SCISAT satellite, as well as localized comparisons of the measurements from each satellite instrument against CO column measurements from the PEARL-FTS in Eureka, Nunavut to quantify the relative biases in each satellite dataset over the high-Arctic region. Prior to this study, no comparisons had been performed between TROPOMI and a limb-sounding satellite instrument. Due to their differing orbits, TROPOMI and ACE-FTS benefit from the highest degree of overlap in their measurements at the north and south polar regions, providing a unique opportunity for an intercomparison of these two data products at high latitudes. Through the inclusion of correlative high-spectral-resolution ground-based measurements from the PEARL-FTS, we gain additional context and a baseline standard to which the two satellite instruments can be compared. This study is published in: Wizenberg et al., Intercomparison of CO measurements from TROPOMI, ACE-FTS, and a high-Arctic ground-based Fourier transform spectrometer, *Atmos. Meas. Tech.*, 2021 (Wizenberg et al., 2021).

4.2 Datasets

4.2.1 TROPOspheric Monitoring Instrument (TROPOMI)

TROPOMI is the exclusive payload aboard the European Space Agency's Sentinel 5-Precursor (S5-P) satellite, which was launched on 13 October 2017 into a high-inclination (98.7°), sun-synchronous orbit at an altitude of 824 km, with a 13:30 local standard time Equator crossing time (Veefkind et al., 2012). The TROPOMI instrument is a nadir-viewing push-broom grating spectrometer array, comprised of four individual spectrometers (UV-Vis-NIR-SWIR), with a swath width of 2600 km, and a 7.2×7.2 km^2 footprint at nadir for CO (Veefkind et al., 2012). The footprint at nadir was further reduced to 7×5.6 km^2 from 6 August 2019 on-wards through improvements to the electronic read-out rate of the spectrometer analog-to-digital converter. For CO, total column densities are obtained from Earth radiance spectra in the shortwave infrared spectral window around 2.3 μm, where the first overtone absorption band of CO is located. Retrievals over land are performed for both clear-sky and cloudy conditions, however retrievals over oceans and other large bodies of water are only possible during cloudy conditions due to the low reflectivity of open water (Landgraf et al., 2016). The TROPOMI CO version 1 processor uses spectroscopic parameters from the HITRAN 2008 linelist database (Rothman et al., 2009) with updates to the water vapor spectroscopy (Scheepmaker et al., 2013).

Vertically integrated CO column densities are retrieved from TROPOMI's shortwave infrared measurements using the Shortwave Infrared Carbon Monoxide Retrieval (SICOR) algorithm, which was developed specifically for the S5-P and S5 missions (Vidot et al., 2012). The SICOR retrieval algorithm employs a profile-scaling approach whereby the retrieval state vector contains a single scaling factor that represents the ratio of the retrieved CO total column to the *a priori* CO total column abundance. The *a priori* reference profiles are generated from the Tracer Model, version 5 (TM5) 3D global chemical transport model (Krol et al., 2005), and they vary based on location, month, and year. The radiative transfer calculations in the retrievals are performed on a 50-layer fixed height vertical grid relative to the topographic surface, typically spanning 0–50 km above sea level (Landgraf et al., 2018). Thus, the final retrieved CO total column density corresponds to the vertically-integrated scaled reference profile (Landgraf et al., 2016). The shape of the column averaging kernels of the CO retrievals varies based on the cloud fraction of a given measurement, reflecting the sensitivity loss of the retrieval due to cloud contamination. In general, for clear-sky retrievals over land, the averaging kernel of the SICOR retrieval is near unity for the entire vertical extent of the profile, meaning that all altitudes contribute equally to the final retrieved

column value. However, for retrievals performed in the presence of cloud fractions greater than 0, the column averaging kernel values will decrease towards zero in the region below the clouds, while simultaneously increasing to values larger than one above the cloud, leading to an increased sensitivity to the CO partial column above the height of the clouds (Landgraf et al., 2016). This approach compensates for the effects of cloud shielding on the retrieved CO column, however for retrievals made in these conditions, the shape of the *a priori* profiles may introduce some additional error into the retrieved total columns (Borsdorff et al., 2014). The mission accuracy and precision requirements for TROPOMI's CO product are 15 % and 10 %, respectively (Landgraf et al., 2016). Further details on the TROPOMI CO retrieval algorithm can be found in Landgraf et al. (2016).

In this work, we analyze TROPOMI CO measurements for the period from 28 November 2017 to 31 May 2020. We use either the reprocessed (RPRO) or offline (OFFL) data files from processor versions 010202, 010300, 010301, and 010302 depending on availability for a given day of observations. Processor versions earlier than 010202 were not used due to wrongly flagged sunglint pixels (Landgraf et al., 2020). Individual pixels are filtered using the quality flag variable "qa_value"), which is a discrete value that provides a quality percentage (Landgraf et al., 2018). Pixels with a qa_value < 0.5 are removed prior to analysis as suggested in the algorithm theoretical baseline document (ATBD) (Landgraf et al., 2018). Furthermore, the quality values were also used to differentiate clear-sky scenes (qa_value $= 1.0$, representing an optical thickness < 0.5 and cloud height $<$ 500 m) from cloudy scenes ($0.5 \leq$ qa_value ≤ 0.7, representing an optical thickness ≥ 0.5 and cloud height $<$ 5000 m) for later analysis, as described in the CO product read-me file (Landgraf et al., 2020).

4.2.2 ACE-FTS

ACE-FTS was launched on board the Canadian Space Agency's SCISAT satellite into a low-Earth circular orbit at an altitude of 650 km and an inclination of 74° on 12 August 2003. This orbit provides ACE with latitudinal coverage between 85° N and 85° S (Bernath et al., 2005). The FTS is the primary instrument aboard SCISAT, but it is also accompanied by Measurement of Aerosol Extinction in the Stratosphere and Troposphere Retrieved by Occultation (MAESTRO), a dual spectrophotometer primarily aimed at improving our understanding of polar ozone chemistry (McElroy et al., 2007). In this work, we focus solely on measurements from ACE-FTS.

ACE-FTS is an infrared Michelson interferometer that was designed and constructed by ABB Inc. in Quebec City, Canada. It has a high spectral resolution of 0.02 cm^{-1}, and it covers the

wavenumber range 750-4440 cm^{-1}. ACE-FTS makes up to 30 measurements per day by solar occultation at sunrise and sunset, and provides vertical profile information (typically between 5–120 km) of temperature, pressure and volume mixing ratios (VMR) for 68 molecules and isotopologues in the version 4.1 data product (Boone et al., 2020). ACE-FTS has a variable vertical sampling of 1.5–6 km, and a mean vertical resolution of ∼3-4 km, which varies based on the orbit, beta angle, and instrument field-of-view (Boone et al., 2005).

CO VMR profiles from version 4.1 of the ACE-FTS data are used in this study (Boone et al., 2020). The VMR profiles are retrieved from the measured infrared spectra using a global-fit algorithm which employs a Levenburg-Marquardt non-linear least-squares fitting method as described in Boone et al. (2005). For the version 4 ACE-FTS dataset, a general retrieval uncertainty estimate of 5% is provided by Bernath et al. (2020). ACE-FTS L2 data are provided in two versions: one that is on the original retrieval altitude grid, and another that has been interpolated onto a fixed 1-km grid. Here, we use only the version with the 1-km grid. Individual ACE-FTS occultations are filtered using the quality flags, following the suggestions provided in Sheese et al. (2015). Furthermore, to maximize the vertical information coming from ACE-FTS, we discard retrieved profiles with an excessive number of fill values (i.e., missing data), and those for which the lowest measured altitude is above 10.5 km.

4.2.3 PEARL-FTS

A detailed description of the PEARL-FTS instrument in Eureka, Nunavut is provided in Chapter 2, while a description of the PEARL-FTS CO retrieval is provided in Chapter 3. The PEARL-FTS was installed in July 2006, and has been involved in the annual Canadian Arctic ACE-OSIRIS Validation Campaigns held during polar sunrise since Spring 2007 (Kerzenmacher et al., 2005). Measurements from the PEARL-FTS have been previously compared with ACE-FTS and other satellite-borne instruments, for example: Clerbaux et al. (2008), Batchelor et al. (2010), Holl et al. (2016), Buchholz et al. (2017), Griffin et al. (2017), Olsen et al. (2017), Bognar et al. (2019), Weaver et al. (2019), and Vigouroux et al. (2020).

The PEARL-FTS CO retrievals have a mean DOFS of 2.2, and a mean total retrieval uncertainty of 2.75% over the full 2006 to 2020 time series. This retrieval uncertainty estimate was calculated by adding the systematic and random uncertainty components in quadrature, and it consists of the measurement error (determined from the SNR of the observed spectra), the smoothing error, the spectroscopic line width and line intensity uncertainties from HITRAN, and temperature and SZA

uncertainties.

4.3 Methods

4.3.1 Collocations and Averaging

In this study, we consider a pair of instruments to be collocated when they are observing the same approximate airmass, at the same approximate time. For the comparisons presented here, broad collocation criteria of 24 hours in time, and 500 km in space were used to maximize the quantity of data available. A range of stricter collocation criteria were tested, but no significant trend between the inter-instrument differences and the spatial and temporal collocation criteria was found. Similarly broad collocation criterion were used in previous ACE-FTS CO validation studies by Clerbaux et al. (2008) and Griffin et al. (2017).

In the determination of collocated measurements, we consider each ACE-FTS profile as a point measurement, using the geographical location of the 30-km tangent-point for the calculation of the inter-instrument distances. For comparisons involving the PEARL-FTS, we use the location of the PEARL Ridge Laboratory. It should be noted that for both ACE-FTS and the PEARL-FTS, these measurements do not occur at a single point, but rather along a broad horizontal slant path through the atmosphere. Drawing upon the example provided in Holl et al. (2016), for a limb-sounding measurement with a 10-km tangent height, the horizontal extent of the slant path is approximately 715 km in the altitude range of 10–50 km.

For the comparison of ACE-FTS and TROPOMI, collocations between the two instruments occur globally, spanning the latitudinal range of 82° N to 81° S. For comparisons involving the PEARL-FTS, collocations are limited to the geographical area within a great-circle radius of 500 km surrounding the PEARL Ridge Laboratory. A summary of the collocation statistics for each instrument pair is provided in Table 4.1.

Due to the broad swath width of TROPOMI, a single ACE-FTS or PEARL-FTS measurement can collocate with thousands of TROPOMI pixels at once. As a result, for the comparisons of TROPOMI with ACE-FTS and the PEARL-FTS, we compute the arithmetic average of all collocated TROPOMI pixels for each ACE-FTS or PEARL-FTS observation. A similar approach was applied in the comparisons of CH_4 measurements from ACE-FTS and the nadir-sounder TANSO-FTS onboard GOSAT in Holl et al. (2016), as well as in De Mazière et al. (2008). To ensure the statistical robustness of the averaging, collocations with a small number of TROPOMI pixels (< 50)

Table 4.1: Summary of the collocation statistics for each pair of instruments. Collocations between TROPOMI and ACE-FTS occur globally, while collocations involving the PEARL-FTS are limited to the region within a 500 km radius from the Ridge Laboratory. The uncertainties provided for the mean distances and times are the standard deviations.

Primary instrument Secondary instrument	ACE-FTS TROPOMI	PEARL-FTS ACE-FTS	PEARL-FTS TROPOMI
First collocation	28 November 2017	25 February 2007	3 March 2018
Last collocation	31 May 2020	18 March 2020	27 March 2020
No. collocations	5955	3015	1875
Mean distance (km)	145.01 ± 135.79	327.44 ± 100.31	122.83 ± 126.10
Mean time (h)	7.73 ± 7.69	11.95 ± 8.73	7.23 ± 6.88

are removed prior to analysis. These cases displayed significantly larger variances than those with a larger number of pixels. In the comparisons of ACE-FTS to TROPOMI, the mean number of pixels included in the averages was 11,452, and a total of 1190 collocations were removed due to this pixel filtering criterion. In the comparisons of PEARL-FTS to TROPOMI, the mean number of pixels included in the collocations was 124,858 and only 8 collocations were removed. For comparisons of ACE-FTS to the PEARL-FTS, no averaging was applied, and a single ACE-FTS profile was allowed to collocate with multiple PEARL-FTS measurements and vice-versa.

4.3.2 TROPOMI versus ACE-FTS

To assess how TROPOMI's CO measurements compare with retrieved ACE-FTS profiles, we first compare these datasets on a global scale. During the period of interest from 28 November 2017 to 31 May 2020, there were 5955 unique collocations after filtering and averaging (i.e., TROPOMI averages collocated with 5955 unique ACE-FTS observations). These collocations spanned a latitude range encompassing the polar, mid-latitude and equatorial regions, providing a broad basis for an intercomparison of the two instruments. For the collocated observations, the mean number of TROPOMI pixels included in the averages was 11,452, indicating that the computed TROPOMI averages are statistically robust, and that pixel-to-pixel variability should be negligible. Given that each ACE-FTS solar occultation provides a CO VMR profile (typically in the altitude range of 5–120 km) instead of a total column value, some additional steps are needed to allow for a direct comparison between these two instruments.

As previously mentioned in Sect. 4.2.1, the TROPOMI CO retrieval employs a profile-scaling approach, and a single scaling factor, which represents the ratio of the retrieved to the prior column, is applied to the reference profile to obtain the "retrieved" profile. However, these scaling factors are not provided in the TROPOMI CO product files, so these must be calculated. First, however, the

CO reference profiles (provided in units of mol mol^{-1} with respect to dry air) must be converted to partial columns, and then summed to obtain the total column concentration c. For a VMR profile with respect to dry air, this can be done using the following equation:

$$c = \sum_{i=1}^{N} \rho_{da}\mathbf{x} = \sum_{i=1}^{N} \frac{(1-q_i)\Delta p_i x_i}{M_{\mathrm{da}} g(h_i)} \approx \sum_{i=1}^{N} \frac{\Delta p_i x_i}{M_{\mathrm{da}} g(h_i)}, \tag{4.1}$$

where $N = 25$ is the number of layers in the TM5 *a priori* grid, ρ_{da} is the dry air partial column profile, $\mathbf{x}$ is the TM5 VMR profile, q is the specific humidity, Δp is the thickness of a given partial column layer in Pa, x is the mean VMR in the layer above level i, $M_{da} = 0.02897$ is the molar mass of dry air in kg mol^{-1}, and $g(h_i)$ is the height-dependent gravitational acceleration calculated at each level from the WGS84 reference ellipsoid (National Imagery and Mapping Agency, 2000). In the above equation, due to the lack of H_2O profile information in the TM5 priors, we have made the approximation that $q = 0$ and thus $\rho_{da} \approx \frac{\Delta p_i}{M_{da} g(h_i)}$. An identical approximation was made by Sha et al. (2021), who found that this resulted in only a small difference of 0.2% in the bias in comparisons of TROPOMI CO against a ground-based FTS at the tropical site of Paramaribo. The scaling factors for each collocation are then calculated by taking the ratio of the retrieved to the *a priori* total column. The scaling factor is then applied to the TM5 reference profile to obtain the"retrieved" profile, allowing for a direct comparison against ACE-FTS profiles.

Following a similar approach to what was done for the TROPOMI reference profiles, since the ACE-FTS profiles are reported in VMR units (with respect to wet air), these must converted to partial columns as well. In addition to the VMR profiles, the ACE-FTS L2 product includes retrieved profiles of temperature and pressure that can be used in accurately determining the partial column profile ρ^{ace}. Following the method of Holl et al. (2016), this is done using the ideal gas law (Clapeyron, 1834):

$$\rho^{\mathrm{ace}} = \frac{\mathbf{xp}}{k\mathbf{T}}\Delta h, \tag{4.2}$$

where $\mathbf{x}$ is the VMR profile, $\mathbf{p}$ is the retrieved pressure in Pa, $\mathbf{T}$ is the retrieved ACE-FTS temperature profile in K, $k = 1.380653 \times 10^{-23}$ J K^{-1} is Boltzmann's constant, and Δh is the thickness of each layer in m. The resulting partial column profiles only extend to the lowest ACE-FTS VMR measurement altitude, so for altitudes below this point, the partial column profile is filled using the nearest value from the TM5 reference profile, yielding a complete partial column profile from the surface to the top of the atmosphere (TOA).

Since ACE-FTS has a significantly higher vertical resolution than TROPOMI, the partial column

profiles are linearly interpolated from the 1-km altitude grid of ACE-FTS, to the 50-layer retrieval grid used by the TROPOMI SICOR retrievals. As discussed in Sect. 4.2.1, for cloudy observations, TROPOMI retrievals are more sensitive to the above-cloud column than the below-cloud portion, which is reflected in the column averaging kernel values. As a result, to correctly inter-compare the measurements from ACE-FTS and TROPOMI, we must smooth the interpolated ACE-FTS partial column profiles with the TROPOMI column averaging kernels. Following the methods of Borsdorff et al. (2014), Landgraf et al. (2016), and Landgraf et al. (2018), the smoothed ACE-FTS partial column profile $\rho^{\text{ace}}_{\text{smooth}}$ is given by:

$$\rho^{\text{ace}}_{\text{smooth}} = \mathbf{A}_{\text{col}} \rho^{\text{ace}}, \tag{4.3}$$

where $\mathbf{A}_{\text{col}}$ is the TROPOMI column averaging kernel, and ρ^{ace} is the ACE-FTS partial column profile interpolated to the TROPOMI 50-layer retrieval grid. Generally, in comparisons such as this, the *a priori* profile of the higher-vertical-resolution instrument would typically be substituted with that of the lower-vertical-resolution instrument to reduce the smoothing error (Rodgers and Connor, 2003). However, since ACE-FTS performs solar occultation measurements, a sensitivity (i.e., the ratio of information coming from the measurement versus the *a priori* as defined by Rodgers (2000)) of 1 is assumed at each level with a negligible influence from the *a priori* profile except at the uppermost altitudes of the ACE-FTS grid, which is beyond the ACE-FTS retrieval and the range of the TROPOMI CO retrieval grid (which typically spans 0-50 km) (Boone et al., 2005). As a result, a full *a priori* substitution is not performed in the comparison of ACE-FTS with TROPOMI.

To minimize the influence of filling the missing lower altitudes of the ACE-FTS profile with the TROPOMI *a priori* profile, the column from the lowest ACE-FTS altitude to the top of the TROPOMI retrieval grid is computed by integrating the smoothed ACE-FTS partial column profile above the altitude of the lowest ACE-FTS measurement. Similarly, to estimate the TROPOMI partial column in the same altitude range, the partial column below the lowest ACE-FTS altitude is computed by summing the scaled TM5 reference profile from the surface to the lowest measured ACE-FTS altitude. This "below-ACE" column is then subtracted from the retrieved TROPOMI total column, providing an estimate of the measured partial column in the same altitude range as ACE-FTS, thus allowing a direct comparison of the two measurements. A similar method was applied in Martínez-Alonso et al. (2020) for comparisons of TROPOMI's CO measurements with above-cloud partial columns computed from ATom-4 in-situ airplane profiles.

Furthermore, to assess the retrieval error associated with using the shape of the TROPOMI TM5 reference profiles to approximate the shape of the atmospheric CO profile below the lowest ACE-FTS

measurement, we calculate the smoothing error $e_{\text{smoothing}}$ following the method of Borsdorff et al. (2014), Wassmann et al. (2015), and Landgraf et al. (2016):

$$e_{\text{smoothing}} = (\mathbf{I} - \mathbf{A}_{\text{col}})\rho^{\text{true}}, \tag{4.4}$$

where $\mathbf{I}$ is the corresponding altitude integral operator (a unit vector in the case of a profile in partial column units), and ρ^{true} represents the true CO profile (Wassmann et al., 2015). For retrievals performed over clear, cloudless scenes, the smoothing error will be small since the column averaging kernel values are close to one at all altitude levels. For retrievals over cloudy scenes however, the magnitude of the smoothing error is expected to be significantly larger. Here, we determine the relative smoothing error (in %) in reference to the coincident unsmoothed ACE-FTS columns. If the reference profile accurately represents the true vertical trace gas distribution ρ^{true}, then we expect that $e_{\text{smoothing}}$ should disappear and the column retrieved by TROPOMI should be an estimate of the true total column (Landgraf et al., 2016). Furthermore, the direction of the relative smoothing error (i.e., positive or negative) can indicate whether the TROPOMI reference profiles underestimate or overestimate the true vertical CO distribution.

Lastly, we compute the partial column bias values of TROPOMI with respect to ACE-FTS (TROPOMI − ACE), as well as the relative bias values (in %) between ACE-FTS and TROPOMI as (100 ×(TROPOMI−ACE)/ACE). Biases are computed both globally, and within the following latitude bands: south Polar (90° S to 60° S), south Mid-latitudes (60° S to 20° S), Equatorial (20° S to 20° N), north Mid-latitudes (20° N to 60° N), and north Polar (60° N to 90° N) to investigate latitudinal trends in the differences. For each comparison, we provide the standard deviation of the differences σ_{bias} as a measure of the spread in the observed differences as well as the standard error of the mean, defined as $\sigma_{\text{bias}}/\sqrt{N}$ with N the number of collocations, as a metric for the statistical significance of the reported bias.

4.3.3 TROPOMI versus PEARL-FTS

Ground-based instruments such as the PEARL-FTS provide context and a point of reference for instrument inter-comparisons such as that of ACE-FTS and TROPOMI. The following section describes the methods used to compare the TROPOMI and PEARL-FTS datasets. Since the PEARL-FTS only makes measurements during the period of polar sunlight, no collocations between these instruments occurred in 2017. The earliest collocation between TROPOMI and the PEARL-FTS dates to 3 March 2018, and the final collocation took place on 27 March 2020, after which mid-

infrared measurements by the PEARL-FTS were halted due to the lack of an on-site operator as a result of the COVID-19 pandemic.

Similar to the methodology applied to the ACE-FTS and TROPOMI comparison, for each PEARL-FTS observation the arithmetic mean of all collocated TROPOMI pixels within a 500 km radius of Eureka is computed to reduce the pixel-to-pixel variability and enhance the statistical robustness of the comparisons. However, unlike in the ACE-FTS and TROPOMI comparison, *a priori* information is provided for both the PEARL-FTS and TROPOMI, so we perform an additional step of prior substitution to place both retrievals on a common *a priori* (in this case, the TROPOMI *a priori*) (Rodgers and Connor, 2003). This additional step serves to minimize the smoothing error when comparing two remote sensing retrievals, and a similar method was applied for the recent comparisons of ground-based TCCON and NDACC measurements in Zhou et al. (2019), and of TROPOMI and MOPITT by Martínez-Alonso et al. (2020). Following Rodgers and Connor (2003), the prior substitution to obtain the optimized retrieved profile $\mathbf{x}_{\mathrm{op}}^{\mathrm{fts}}$ is done by the following:

$$\mathbf{x}_{\mathrm{op}}^{\mathrm{fts}} = (\mathbf{I} - \mathbf{A})(\mathbf{x}_{a}^{\mathrm{s5p}} - \mathbf{x}_{a}^{\mathrm{fts}}), \tag{4.5}$$

where $\mathbf{I}$ is the identity matrix, $\mathbf{A}$ is the unitless VMR/VMR averaging kernel of the PEARL-FTS, $\mathbf{x}_{a}^{\mathrm{s5p}}$ is the TROPOMI *a priori* which has been interpolated to the PEARL-FTS retrieval grid, and $\mathbf{x}_{a}^{\mathrm{fts}}$ is the PEARL-FTS *a priori* profile.

With the PEARL-FTS VMR profile optimized with respect to TROPOMI and its *a priori* profile, the former can be interpolated to the TROPOMI 50-layer retrieval grid and the partial column profile calculated using the right-hand portion of Eq. 4.1 and the TROPOMI pressure grid. The 'best estimate' of the PEARL-FTS total column $\hat{c}^{\mathrm{fts}}$ is determined by smoothing the partial column profile by the TROPOMI column averaging kernel following the method of Rodgers and Connor (2003):

$$\hat{c}_{\mathrm{smooth}}^{\mathrm{fts}} = c_{a}^{\mathrm{s5p}} + \mathbf{A}_{\mathrm{col}}(\rho_{\mathrm{op}}^{\mathrm{fts}} - \rho_{a}^{\mathrm{s5p}}), \tag{4.6}$$

where c_{a}^{s5p} is the TROPOMI *a priori* total column, $\mathbf{A}_{\mathrm{col}}$ is the TROPOMI column averaging kernel, $\rho_{\mathrm{op}}^{\mathrm{fts}}$ is the optimized PEARL-FTS partial column profile interpolated to the TROPOMI retrieval grid, and ρ_{a}^{s5p} is the TROPOMI *a priori* partial column profile. In theory, this operation can be done in the opposite direction by bringing the scaled TROPOMI profile to the PEARL-FTS retrieval grid, to then be smoothed by the PEARL-FTS averaging kernel. However, these two approaches are not symmetrical, and one way is expected to produce a better result than the other. This is because

the higher resolution will more realistically reproduce the lower resolution measurement, rather than the other way around (Rodgers and Connor, 2003). Since TROPOMI is the lower vertical resolution measurement in this particular instance, we chose to bring the PEARL-FTS profiles to the TROPOMI retrieval grid.

Once the best estimate of the PEARL-FTS column with respect to TROPOMI is obtained, the bias in the retrieved TROPOMI total columns relative to the PEARL-FTS as well as the standard deviations and the standard errors of the means are computed in the same manner as was done for the ACE-FTS and TROPOMI comparison described in Sect. 4.3.2.

4.3.4 ACE-FTS versus PEARL-FTS

As discussed in Sect. 4.2.3, earlier versions of the ACE-FTS CO data product have been validated against the PEARL-FTS and other ground-based FTSs in NDACC, namely by Clerbaux et al. (2008) and Griffin et al. (2017). Both of these studies showed generally good agreement between ACE-FTS and the ground-based instruments. Since ACE-FTS profiles do not extend to the surface, these previous studies primarily focused on comparisons of partial column abundances instead of total columns. In this work, we employ a similar approach, which is described below.

Firstly, since we aim to compare the partial column abundances of ACE-FTS and the PEARL-FTS, we must determine the optimal altitude range for the PEARL-FTS in which to perform this comparison. This step is crucial because if the selected range is too wide, then *a priori* information may dominate the partial column comparisons, and the true vertical information coming from the PEARL-FTS may be limited. On the other hand, if the selected altitude range is too small, then the comparison will essentially be reduced to a single layer. To achieve this, the sensitivity of the retrievals (as defined by Rodgers (2000)) at each level k was first computed by summing the corresponding rows of the averaging kernel matrix, $\sum_i \mathbf{A}_{ki}$, following the method of Vigouroux et al. (2008). The sensitivity density (i.e., the fraction of retrievals with sensitivity at a given altitude) of the PEARL-FTS retrievals was then investigated for all collocated ACE-FTS measurements (Fig. 4.1). From an analysis of the sensitivity density, an optimal altitude range of 9.33–66.58 km was selected for the comparison of the partial columns. This chosen range is similar to the the altitude range of 9.0–48.5 km used by Griffin et al. (2017), albeit slightly broader to encompass the secondary peak in the retrieval sensitivity in the approximate range of 40–70 km. However, the SFIT4 CO retrieval has been modified in the meantime due to an NDACC-wide harmonization initiative, and the range used by Griffin et al. (2017) may no longer be ideal. A smaller altitude region with high

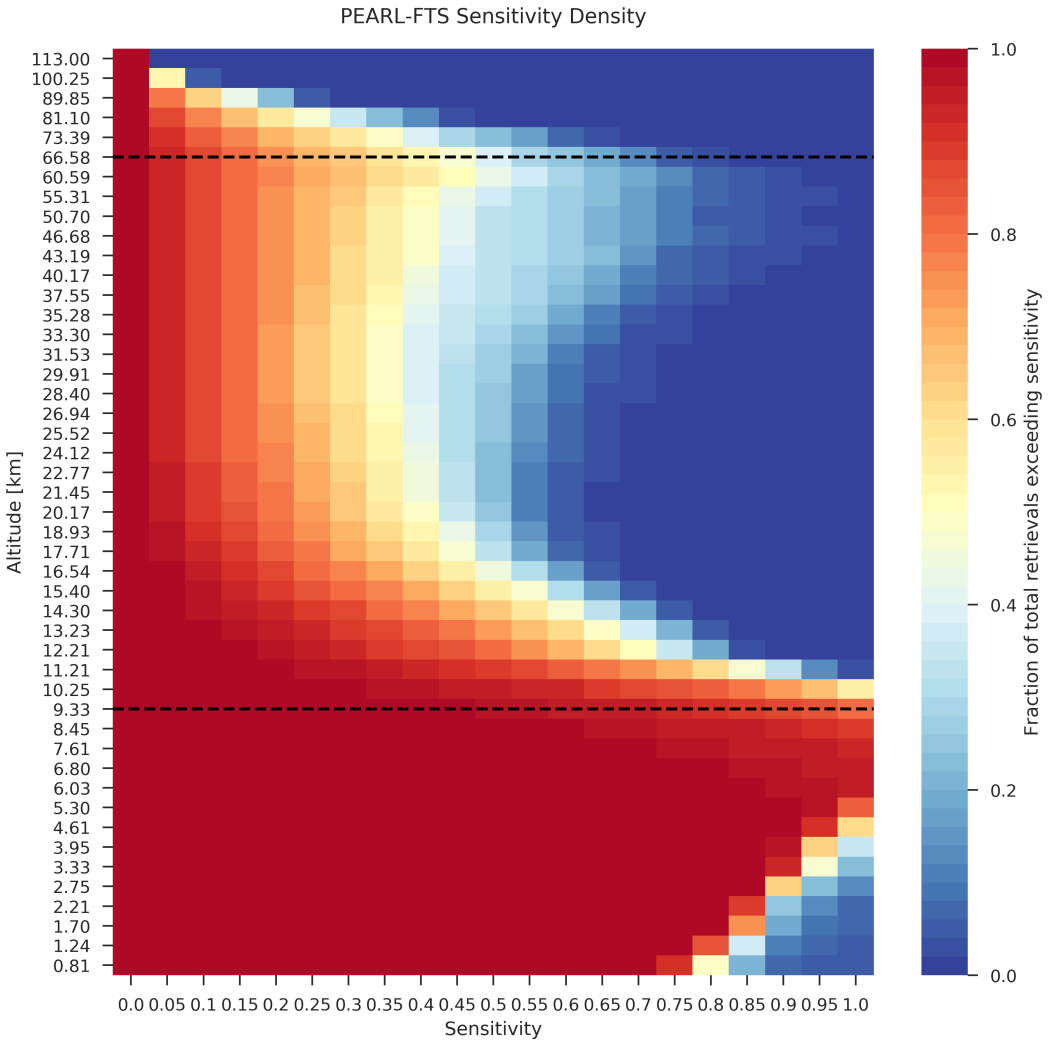

Figure 4.1: The mean sensitivity density of the PEARL-FTS CO retrieval for all collocated ACE-FTS measurements. The y-axis altitudes correspond to the mid-points of the PEARL-FTS retrieval layers, and the black dashed lines denote the selected altitude range for the partial column comparisons of 9.33 to 66.58 km.

sensitivity can be seen from 0.61–2.21 km, however ACE-FTS retrieved profiles do not typically extend this close to the surface, and as a result this region was not used. Again drawing from Rodgers and Connor (2003), since the PEARL-FTS is of a lower vertical resolution than ACE-FTS, the retrieved ACE VMR profiles must be interpolated to the coarser altitude grid of the PEARL-FTS. However, since the retrieval grid of the PEARL-FTS (0.61 km to 120 km) extends further towards the surface than ACE-FTS, the bottom-most altitudes of each coincident ACE-FTS VMR profile beneath the lowest measurement must first be filled in using the nearest value from the PEARL-FTS *a priori* profile. In this case, since it is assumed that ACE-FTS has a sensitivity of

1 at each measured altitude, and no *a priori* information is provided with the ACE data, we do not perform any prior substitution step here. ACE-FTS VMR profiles are then smoothed using the VMR/VMR averaging kernel $\mathbf{A}$ of the PEARL-FTS using a similar form to Eq. 4.6 (Rodgers and Connor, 2003):

$$\mathbf{x}^{\text{ace}}_{\text{smooth}} = \mathbf{x}^{\text{fts}}_{a} + \mathbf{A}(\mathbf{x}^{\text{ace}} - \mathbf{x}^{\text{fts}}_{a}), \tag{4.7}$$

where $\mathbf{x}^{\text{ace}}_{\text{smooth}}$ is the smoothed ACE-FTS VMR profile, $\mathbf{x}^{\text{fts}}_{a}$ is the PEARL-FTS *a priori*, and $\mathbf{x}^{\text{ace}}$ is the original ACE-FTS profile that has been interpolated to the PEARL-FTS retrieval grid. The partial column profile for ACE-FTS is calculated using Eq. 4.2, and then the partial columns from 9.33–66.58 km are summed. The difference between the ACE-FTS and the PEARL-FTS partial columns, δc_{pc}, is found by:

$$\delta c_{\text{pc}} = c^{\text{ace}}_{\text{pc}} - c^{\text{fts}}_{\text{pc}}, \tag{4.8}$$

where $c^{\text{ace}}_{\text{pc}}$ and $c^{\text{fts}}_{\text{pc}}$ are the ACE-FTS and PEARL-FTS partial columns respectively, between 9.33 and 66.58 km.

4.4 Results and Discussion

4.4.1 TROPOMI versus ACE-FTS: Global Comparison of CO

A global comparison of ACE-FTS and TROPOMI CO partial columns was performed for the period from 28 November 2017 to 31 May 2020. During this period, there were a total of 5955 unique collocations, spanning 82° N to 81° S and broadly encompassing all longitudinal meridians. Due to the nature of the overlap between the ACE-FTS and TROPOMI orbits, a higher density of collocations occurred at the higher latitudes (both north and south) than towards the equator.

Linear regressions were performed and the mean biases and standard deviations of the differences were computed for the global comparison, as well as in five latitude bands; the north Polar region (60° N to 90° N), northern Mid-latitudes (20° N to 60° N), the Equatorial region (20° S to 20° N), southern Mid-latitudes (60° S to 20° S), and the south Polar region (90° S to 60° S). Figure 4.2 and Table 4.2 show the results of these comparisons. Globally, there is very strong correlation between the measurements from both instruments ($R = 0.93$), with a small mean bias of $-4.35 \pm 1.42 \times 10^{15}$ molec. cm^{-2} (-0.79 ± 0.26 %; bias $\pm$ standard error of the mean), and a standard deviation of the differences of 1.09×10^{17} molec. cm^{-2} (19.99 %). The observed global mean bias

between ACE-FTS and TROPOMI is well within the mission accuracy requirement of ± 15 % (Landgraf et al., 2016), and is consistent with global comparisons of the CO product to the ECMWF Integrated Forecasting System (IFS) by Borsdorff et al. (2018) who found a global mean relative bias of 3.2 ± 5.5 % (bias ± standard deviation).

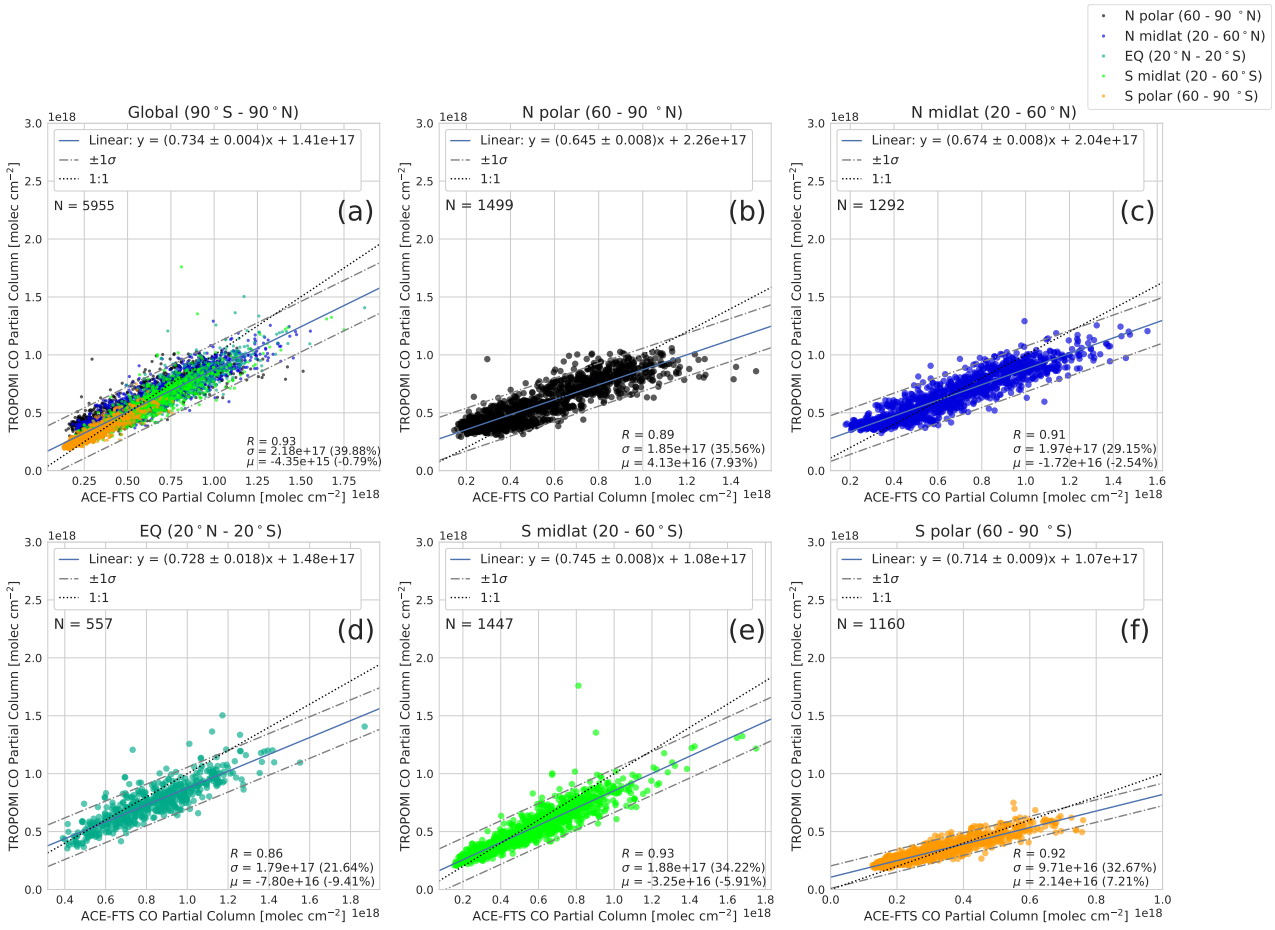

Figure 4.2: Correlation plots of collocated ACE-FTS and TROPOMI partial columns in the following latitude bands: **(a)** Global (90° S to 90° N), **(b)** northern Polar (60° N to 90° N), **(c)** northern Mid-latitudes (20° N to 60° N), **(d)** Equatorial (20° S to 20° N), **(e)** southern Mid-latitudes (20° S to 60° S), and **(f)** southern Polar (60° S to 90° S). In panel **(a)**, the color of the data points corresponds to the respective latitude regions. Values of the Pearson correlation coefficient R, the standard deviation of the TROPOMI columns σ, and the mean bias μ of the respective latitude band are displayed in the lower right of each panel.

Table 4.2: Summary of the number of collocations, the mean partial column differences, and the standard deviations of the differences between ACE-FTS and TROPOMI globally, and in each latitude region. The relative bias and standard deviation values are computed with respect to ACE-FTS (i.e., 100 ×(TROPOMI−ACE-FTS)/ACE-FTS). The uncertainties provided for the absolute and relative biases are the standard errors on the means.

Region (latitude)	$N_{\text{collocations}}$	R	Mean abs. bias (molec. cm^{-2})	σ_{bias} (molec. cm^{-2})	Mean rel. bias (%)	Rel. σ_{bias} (%)
Global (90° S to 90° N)	5955	0.93	$-4.35 \pm 1.42 \times 10^{15}$	1.09×10^{17}	-0.79 ± 0.26 %	19.99 %
N Polar (60° N to 90° N)	1499	0.89	$4.13 \pm 0.32 \times 10^{16}$	1.23×10^{17}	7.93 ± 0.61 %	23.70 %
N Mid-lat (20° N to 60° N)	1292	0.91	$-1.72 \pm 0.33 \times 10^{16}$	1.18×10^{17}	-2.54 ± 0.49 %	17.50 %
Equator (20° S to 20° N)	557	0.86	$-7.81 \pm 0.46 \times 10^{16}$	1.08×10^{17}	-9.41 ± 0.55 %	13.07 %
S Mid-lat (20° S to 60° S)	1447	0.93	$-3.25 \pm 0.24 \times 10^{16}$	9.17×10^{16}	-5.91 ± 0.44 %	16.68 %
S Polar (60° S to 90° S)	1160	0.91	$2.14 \pm 0.16 \times 10^{16}$	5.27×10^{16}	7.21 ± 0.52 %	17.73 %

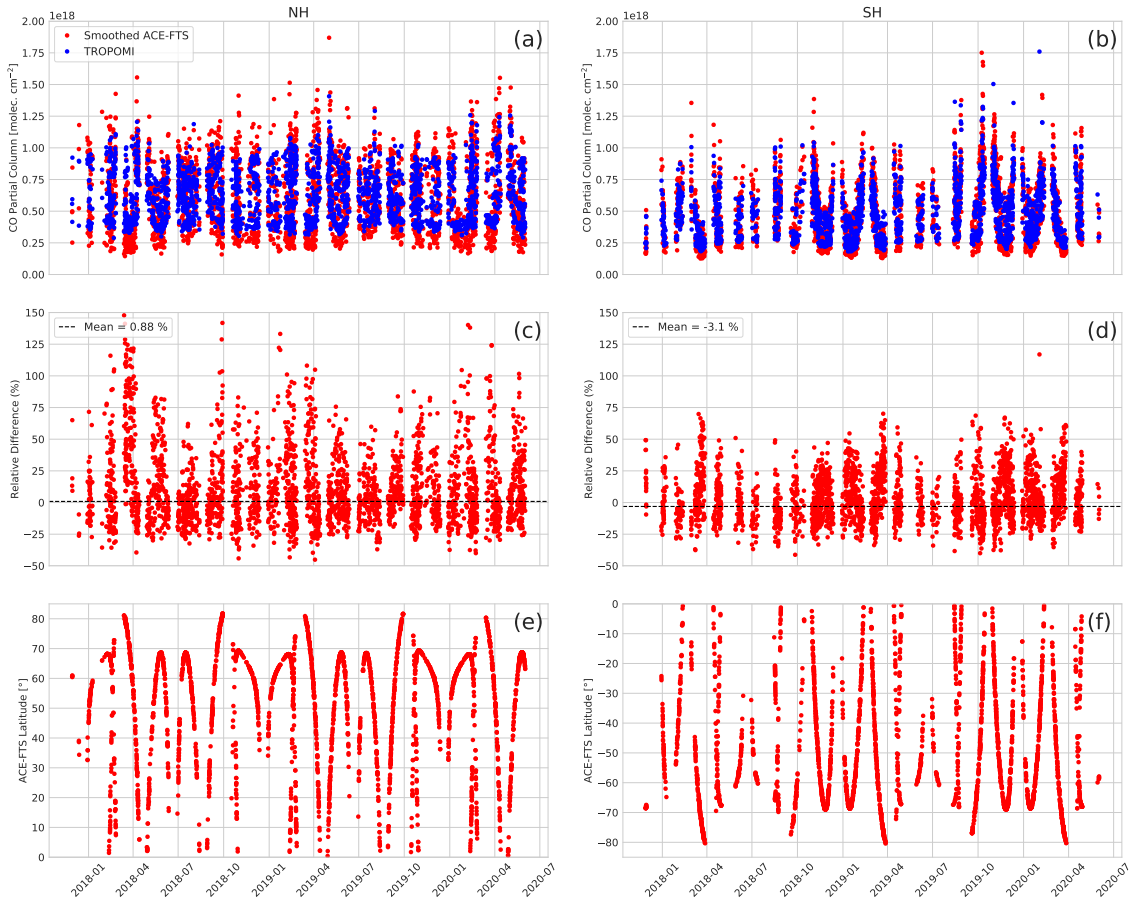

Figure 4.3: **(a)** and **(b)** Time-series of smoothed ACE-FTS and TROPOMI partial columns, **(c)** and **(d)** the relative differences between the instruments, and **(e)** and **(f)** the latitude of the coincident ACE-FTS measurement for both the northern hemisphere (left column) and the southern hemisphere (right column). The black dashed horizontal lines in panels **(c)** and **(d)** denote the mean of the differences.

From the latitudinal comparisons between ACE-FTS and TROPOMI shown in Fig. 4.2 and summarized in Table 4.2, it can be seen that the magnitude (as well as the sign) of the biases varies by latitude band. The largest positive relative biases are observed in the north and south Polar regions, with mean differences of $4.13 \pm 0.32 \times 10^{16}$ molec. cm^{-2} and $2.14 \pm 0.16 \times 10^{16}$ molec. cm^{-2} (7.93 ± 0.61 % and 7.21 ± 0.52 %) respectively, indicative of high TROPOMI column values in the Polar regions relative to ACE-FTS. The largest negative relative bias was found in the Equatorial region, with a mean difference of $-7.81 \pm 0.46 \times 10^{16}$ molec. cm^{-2} (-9.41 ± 0.55 %). Smaller negative biases of $-1.72 \pm 0.33 \times 10^{16}$ molec. cm^{-2} (-2.54 ± 0.49 %) and $-3.25 \pm 0.24 \times 10^{16}$ molec. cm^{-2} (-5.91 ± 0.44 %) are seen in the northern and southern Mid-latitude regions respectively. The standard deviations of the mean relative differences range between 13.07 % (Equatorial region) and 23.70 % (north Polar region). Despite the variability in the mean of the differences with respect

to latitude, generally strong correlations between ACE-FTS and TROPOMI are observed across all latitude bands, with the weakest correlation occurring in the Equatorial region ($R = 0.86$), which may be due in part to the smaller overall number of collocations ($N = 557$) in this latitude band relative to all others.

Overall, these observed correlations suggest that both instruments measure similar temporal trends in CO partial columns globally. Time-series of the TROPOMI and smoothed ACE-FTS partial columns, their relative differences, and the latitude of the coincident ACE-FTS measurements are shown for both the northern and southern hemispheres (NH and SH) in Fig. 4.3. From this, it is clear that both instruments do observe similar seasonal cycles in the CO columns, particularly in the SH where anthropogenic CO sources are less influential, and overall no clear seasonal dependence of the biases is apparent. The aforementioned latitudinal variability in the biases, however, can still be

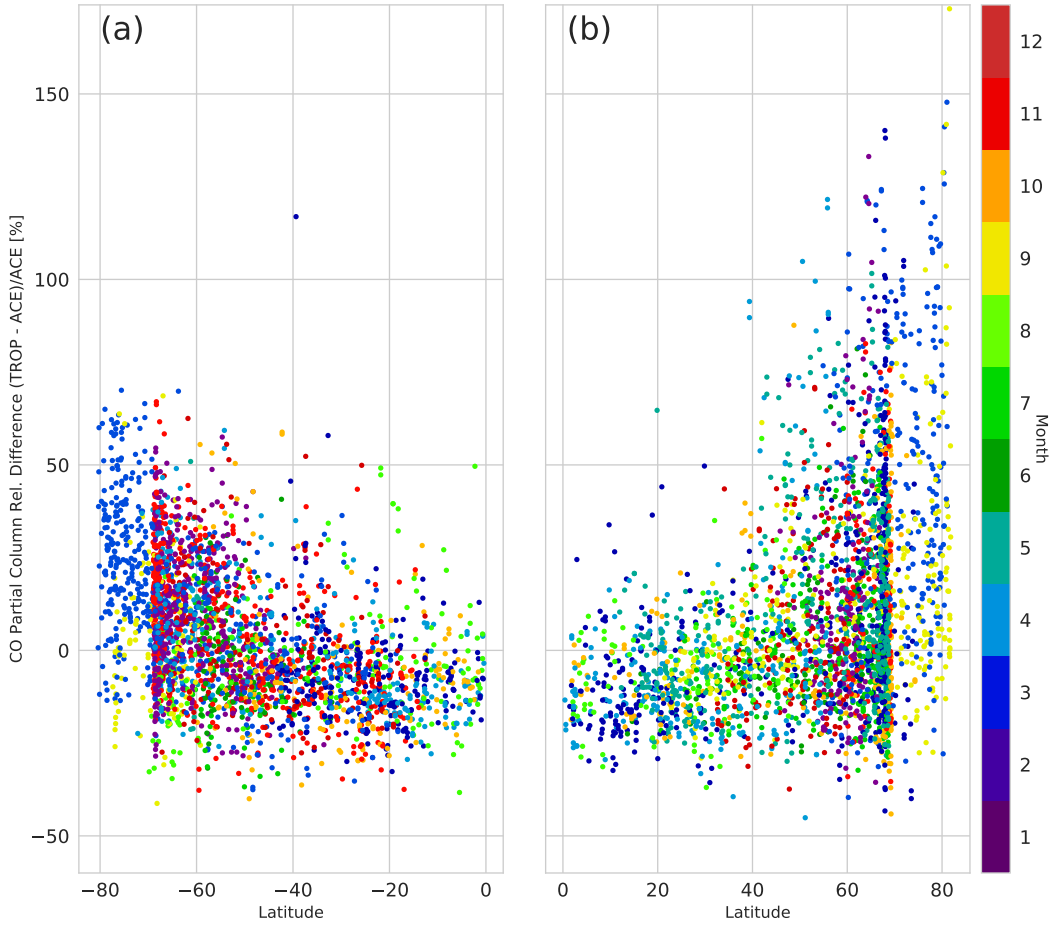

Figure 4.4: Relative difference between TROPOMI and ACE-FTS versus latitude in **(a)** the southern hemisphere and **(b)** the northern hemisphere for the period from 28 November 2017 to 31 May 2020. The data points are binned by color depending on the month in which the collocation occurred.

observed in Fig. 4.3c and Fig. 4.3d. The largest relative differences between the two instruments can be seen during March and September of each year when collocations are occurring at high latitudes in both hemispheres (i.e., towards the polar regions), while generally smaller relative differences, conversely, are observed for collocations occurring at lower latitudes (i.e., nearer to the equator). It can also be noted that the dynamic range of ACE-FTS partial column values is noticeably larger than TROPOMI in both hemispheres.

To examine the relationship between the partial column differences and latitude, the differences versus the latitude of each collocation are shown in Fig. 4.4. On average, larger differences occur at the higher latitudes (most notably in the northern hemisphere), with smaller or negative differences present towards the equator. A similar pattern in the biases of the TROPOMI CO product was observed in comparisons with the ECMWF-IFS model in Borsdorff et al. (2018), which displayed negative biases near the equator, and higher positive biases on the order of 10 % towards the poles. Comparisons of the TROPOMI CO product to ATom-4 in-situ aircraft profiles in Martínez-Alonso et al. (2020) displayed no latitudinal dependence in the biases, however, these comparisons were limited to only 103 collocated profiles over a smaller geographical and latitudinal range (60° S to 85° N).

To assess whether any differences are introduced by the TROPOMI retrievals over cloudless versus cloud-covered scenes, the mean differences between ACE-FTS and TROPOMI were independently investigated for clear-sky and cloudy scenes (in addition to all scenes), and are shown in Fig. 4.5 for both the unsmoothed and smoothed cases. In general, smoothing ACE-FTS by the TROPOMI column averaging kernels reduces the mean relative bias by a significant margin both in the global comparison as well as in all distinct latitude bands, but yields slightly poorer correlations in some regions (maximum difference of 0.03 in the Pearson correlation coefficients). The smoothing operation has a noticeably larger effect in the cloud-covered scenes than for the clear-sky pixels, and it shifts the mean biases in the Equatorial and Mid-latitude regions from positive to slightly negative. Furthermore, in both the unsmoothed and smoothed cases, the clear-sky-only scenes tend to be biased higher than the clear+cloudy scenes and cloud-covered scenes only. It should also be noted that particularly in the unsmoothed case, there is consistently better correlation between ACE-FTS and TROPOMI for cloud-covered vs. clear-sky scenes. This observed tendency is related to the aforementioned changes in the shape of the TROPOMI column averaging kernels over clear versus cloudy scenes. As outlined in Sect. 4.2.1, the shape of the TROPOMI column averaging kernels varies based on the cloud fraction of the measurement to reflect a reduction in sensitivity of the retrieval due to cloud contamination. For observations over clear-sky scenes, the values of the

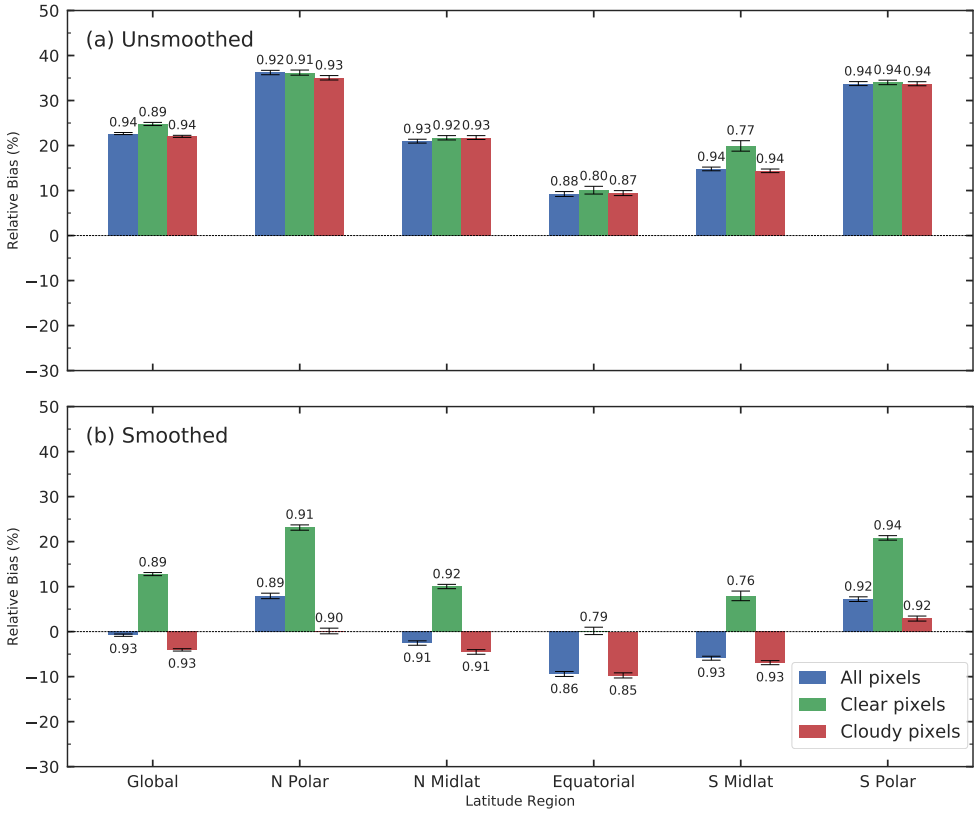

Figure 4.5: Summary of the relative differences between TROPOMI and ACE-FTS for **(a)** the unsmoothed and **(b)** smoothed comparisons for all TROPOMI pixels (qa_value $\geq$ 0.5; blue bars), clear pixels only (qa_value = 1.0; green bars), and cloud-covered pixels only (0.5 $\leq$ qa_value $\leq$ 0.7; red bars). The error bars correspond to the standard errors of the mean and the values above/below the error bars are the Pearson correlation coefficients for that particular case and latitude region.

column averaging kernel will be close to one at all levels, and the influence of the reference profile on the computation of the scaling factor will be minimal. However, for measurements made over cloud-covered scenes, the column averaging kernel values rapidly decrease towards zero below the height of the cloud, while simultaneously increasing above the cloud. Because of this, in cloudy scenes, the above-cloud column (which is in the same approximate altitude range that ACE-FTS measures) is used to estimate the total column, and a greater reliance is placed on the TM5 reference profiles. If the reference profiles are underestimating the CO column below the height of the cloud, then the resulting retrieved total column value will be biased lower, which is broadly consistent with the observed relationship. Despite the differences between the unsmoothed and smoothed comparisons, both cases still display a latitudinal bias, with the largest mean differences occurring in the north and south polar regions.

As discussed in Sect. 4.3.2, the smoothing error $e_{\text{smoothing}}$ can be helpful in diagnosing the error

associated with the choice of the *a priori* profile shape on the retrieved CO column in a profile-scaling approach, particularly for measurements made over cloudy scenes. The smoothing error was computed for all collocated cloudy pixels ($0.5 \leq$ qa_value ≤ 0.7) relative to the true (unsmoothed) ACE-FTS profiles, as shown in Fig. 4.6. The values of the relative smoothing errors are almost entirely negative across all latitudes, with a global mean of -28.63 ± 10.03 % (bias $\pm$ standard deviation). Furthermore, a pattern in the relative smoothing error with respect to latitude can also be observed, with the most strongly negative values occurring between 60° to 90° in both the NH and SH. The larger observed difference in this latitude band may be due to differing cloud properties relative to lower-latitude regions, such as cloud height and optical thickness. This implies that the magnitude of the error associated with this choice of reference profile is on average larger in these high-latitude regions.

The correlation between the relative differences and the relative smoothing errors was also investigated in the same latitude bands as the partial column comparisons, and this is shown in Fig. 4.7. In Fig. 4.7a, no clear relationship between the relative smoothing errors ($R = 0.04$) can be seen in the global comparison. However, within the latitude bands, weak correlations between the smoothing error and the partial column differences can be observed. In particular, in the northern Polar, Equatorial, and southern Polar regions, the relative partial column differences increase with relative smoothing errors, with Pearson correlation coefficients of $R = 0.22$, $R = 0.41$, and $R = 0.19$, respectively. The north and south Polar regions display the most strongly negative mean relative smoothing errors, with -33.55 ± 10.78 % and -29.96 ± 8.06 %, respectively, while the Equatorial region has the least negative mean smoothing error with -23.46 ± 8.04 %. In the northern and southern Mid-latitude regions, no notable correlation between the relative smoothing error and the relative partial column differences is observed, with $R = 0.09$ and $R = -0.11$, respectively. Overall, the observed pattern in the mean relative smoothing errors suggests that relative to retrieved ACE-FTS columns, the error associated with the choice of the TM5 reference profiles is largest in the northern and southern Polar regions, and lowest in the Equatorial region.

4.4.2 High-Arctic Ground-based Comparisons

TROPOMI versus PEARL-FTS

A total of 1875 collocations between TROPOMI and the PEARL-FTS at Eureka, Nunavut were found from 3 March 2018 to 27 March 2020. Correlation plots of TROPOMI total columns versus both the unsmoothed and smoothed PEARL-FTS total columns are displayed in Fig. 4.8a and

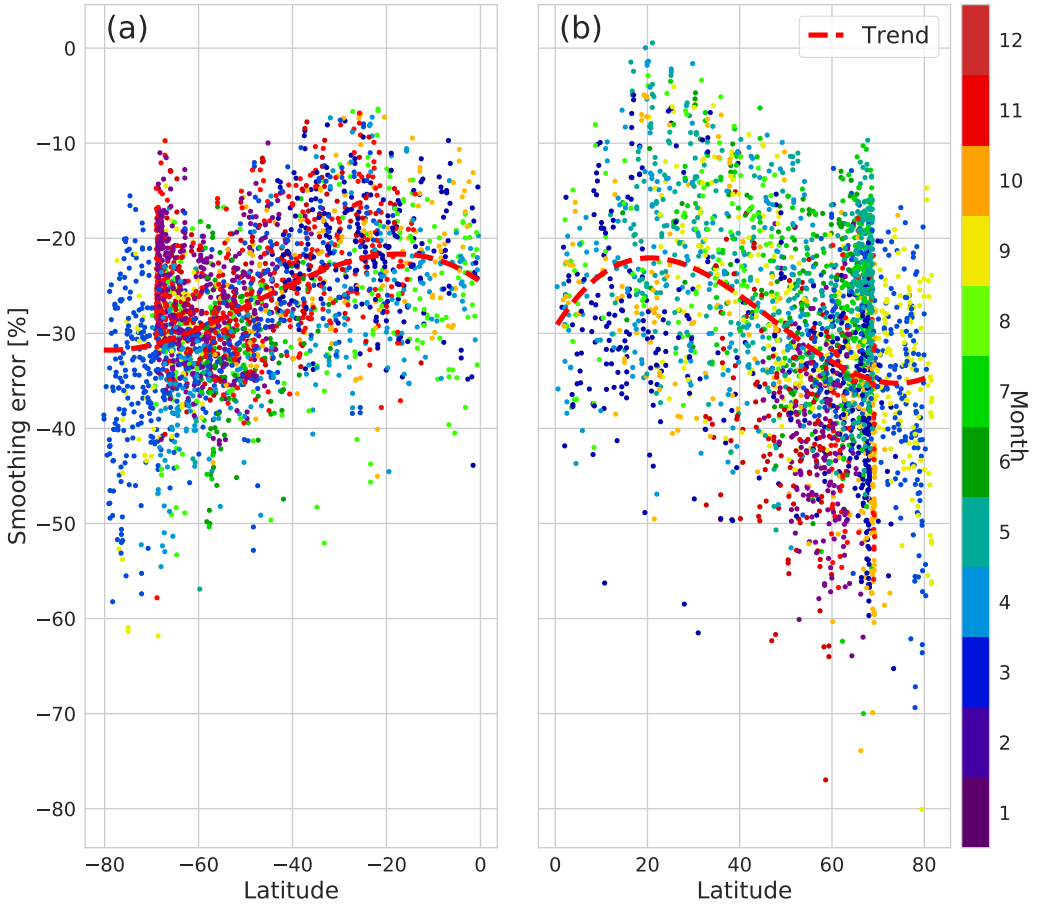

Figure 4.6: The relative smoothing error of TROPOMI pixels over cloudy scenes in **(a)** the southern hemisphere and **(b)** the northern hemisphere with respect to the true (unsmoothed) ACE-FTS partial columns versus latitude for the period from 28 November 2017 to 31 May 2020. A 3rd-order polynomial fit (denoted by the dashed red line) was applied to the data to better highlight the underlying pattern.

Fig. 4.8b, respectively. Smoothing the PEARL-FTS profiles by the TROPOMI column averaging kernels has a significant effect on the agreement between the two instruments. In the unsmoothed comparison, a correlation is observed between the two instruments ($R = 0.84$), but the slope of the linear fit is 1.75 and there is a large mean positive bias of $8.89 \pm 0.04 \times 10^{17}$ molec. cm^{-2} (73.7 ± 0.33 %) with a standard deviation of the differences of 1.70×10^{17} molec. cm^{-2} (14.1 %). The correlation with smoothed PEARL-FTS columns is improved ($R = 0.88$, slope of linear fit = 1.07), and the mean bias was reduced to $2.66 \pm 0.03 \times 10^{17}$ molec. cm^{-2} (14.7 ± 0.16 %), with a standard deviation of 1.24×10^{17} molec. cm^{-2} (6.76 %). While smoothing the PEARL-FTS retrievals by the TROPOMI column averaging kernels reduced the mean bias by approximately 60 %, a systematic bias of 14.7 % is still present. The observed positive mean bias is consistent with the recent ground-

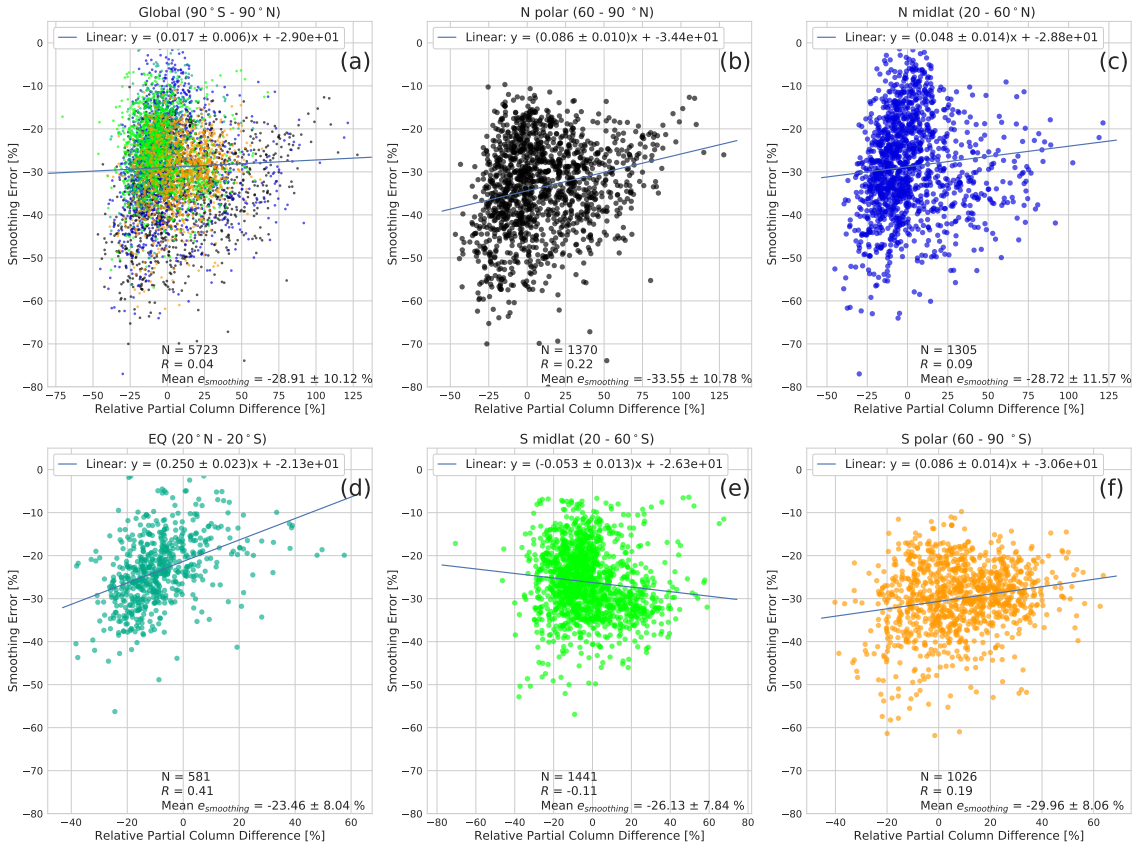

Figure 4.7: Correlation plots of the relative smoothing error of the TROPOMI retrievals for cloudy scenes versus the relative partial column differences between ACE-FTS and TROPOMI in the same latitude bins as Fig. 4.2. See the caption of Fig. 4.2 for more details.

based validation efforts of Sha et al. (2021), who found a bias of 12.96 ± 4.56 % for TROPOMI versus the PEARL-FTS while using a stricter collocation criterion of 50 km in space and 3 hours in time, and is also generally consistent with the positive biases observed between ACE-FTS and TROPOMI over the north Polar region.

To ascertain whether there is a seasonal dependence in the biases between TROPOMI and the PEARL-FTS, the time-series of the TROPOMI and smoothed PEARL-FTS total columns is shown in Fig. 4.9a, along with the total column and relative differences. From Fig. 4.9, it can be seen that with the exception of a few collocations during the late spring and early summer of 2018 and 2019, a positive systematic bias is present in the TROPOMI CO total columns with respect to the smoothed PEARL-FTS CO total columns. Furthermore, the differences display some seasonal variability, with the largest differences typically present during the spring, and the lowest differences occurring in the summer months. The larger CO column biases in the early spring may be a result of polar vortex conditions accompanied by the descent of mesospheric air masses containing high concentrations of

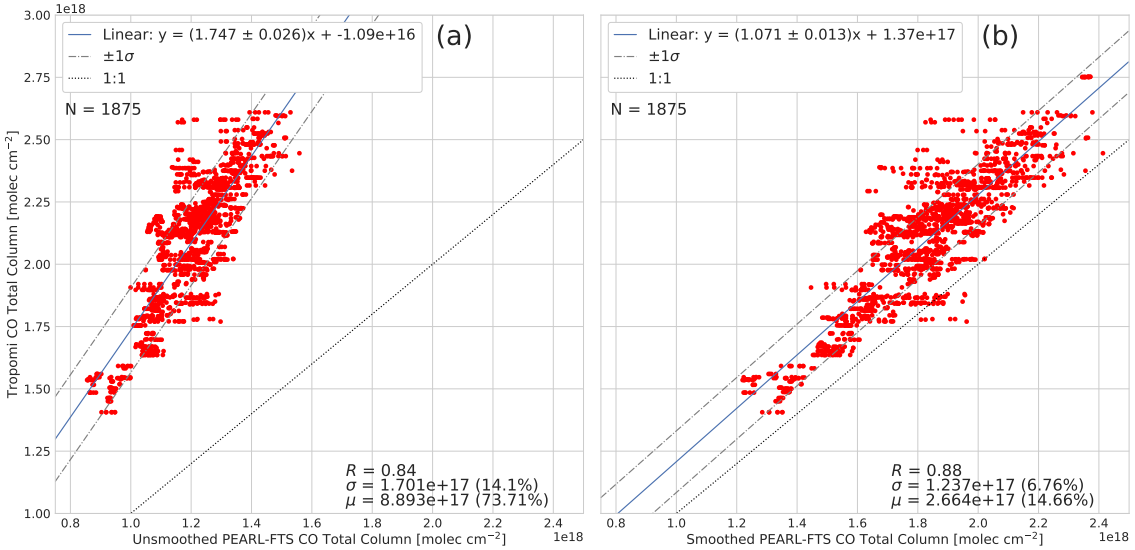

Figure 4.8: Correlation plots of TROPOMI CO total columns with **(a)** unsmoothed and **(b)** smoothed PEARL-FTS CO columns.

CO as the vortex begins to dissipate, an event previously observed over Eureka in Manney et al. (2008). Furthermore, larger differences may arise during the spring months from a mismatch in the TROPOMI footprint and the broader spatial extent of the PEARL-FTS measurements at high solar zenith angles (i.e., the slant-path of the PEARL-FTS covers a greater horizontal distance in high SZA conditions). In general, both instruments capture the same temporal patterns in the CO total columns across all months for which comparisons were possible, however TROPOMI displays a consistent systematic high bias in the high-Arctic region within 500 km of Eureka.

ACE-FTS versus PEARL-FTS

Comparison of ACE-FTS and PEARL-FTS CO partial columns provides additional context for the TROPOMI results presented above. Here, a total of 3015 unique collocations between ACE-FTS and the PEARL-FTS were analyzed spanning the period from 25 February 2007 to 18 March 2020. As outlined in Sect. 4.3.4, partial columns in the altitude range of 9.33 to 66.58 km are compared. The vertical information content of the PEARL-FTS is given by the DOFS which is calculated from the trace of the averaging kernels. The collocated PEARL-FTS retrievals have a mean total DOFS of 2.2 ± 0.37, while in the range of 9.33 to 66.58 km the mean DOFS is 0.72 ± 0.31. A DOFS of 1 or greater in the selected altitude range would be ideal, however a DOFS of 0.72 implies that there is approximately one third of the total vertical information coming from the measurement in this range.

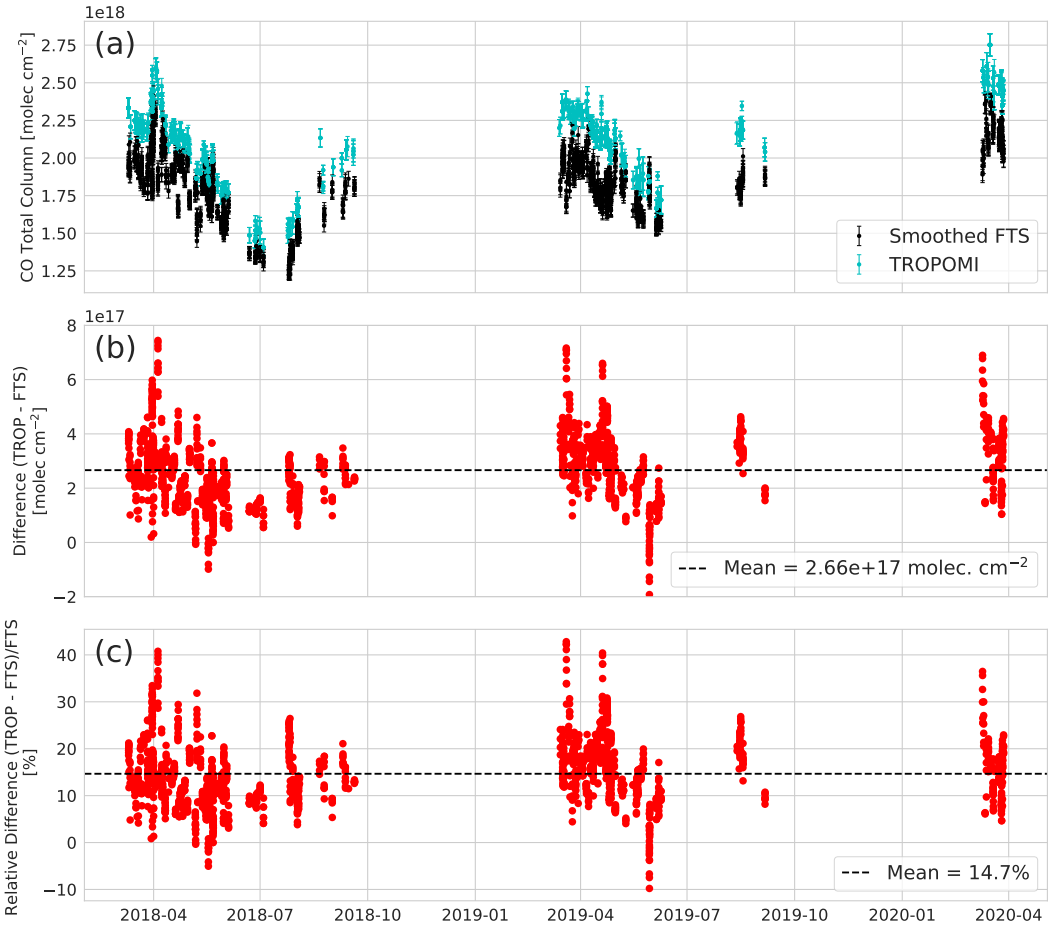

Figure 4.9: Time-series of **(a)** TROPOMI and smoothed PEARL-FTS total columns, **(b)** absolute column differences (in molec. cm^{-2}), and **(c)** relative differences (in %). The error bars in panel **(a)** represent the measurement uncertainties of both the PEARL-FTS and TROPOMI.

The correlation plot for ACE-FTS and PEARL-FTS partial columns in the range of 9.33 – 66.58 km is shown in Fig. 4.10. Good agreement is observed between ACE-FTS and the PEARL-FTS ($R = 0.79$, slope of linear fit = 0.84), with a mean difference of $1.53 \pm 0.04 \times 10^{16}$ molec. cm^{-2} (7.89 ± 0.21 %) with a standard deviation of 2.42×10^{16} molec. cm^{-2} (11.39 %). This observed relative bias is similar to the findings of Griffin et al. (2017), who obtained a mean relative difference of 7.1 ± 1.8 % with a correlation of $R = 0.80$ and slope of linear fit of 0.86 between ACE-FTS and the PEARL-FTS for an earlier version of the ACE CO data product (v3.5). Although the ACE-FTS and PEARL-FTS retrievals have each been updated since this earlier study, the findings presented here are within the range of the standard errors on the mean of those from Griffin et al. (2017) indicating reasonable agreement. Both TROPOMI and ACE-FTS display high systematic biases relative to the PEARL-FTS, however the observed mean relative bias in ACE-FTS relative to the

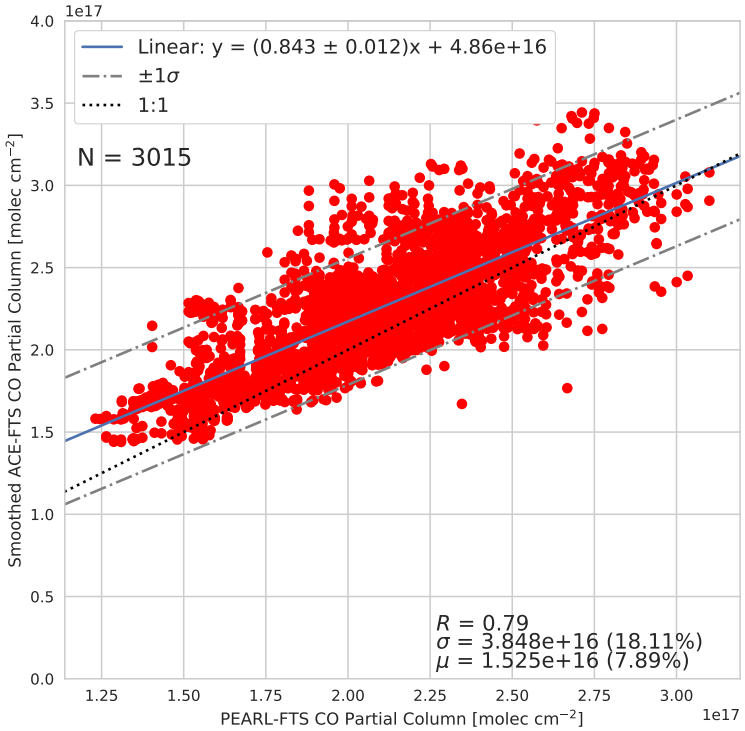

Figure 4.10: Correlation plot for ACE-FTS vs. PEARL-FTS CO partial columns in the range of 9.33 to 66.58 km for the period from 25 February 2007 to 18 March 2020. R, σ, and μ are defined as in Fig. 4.2.

PEARL-FTS is lower than for TROPOMI (7.89 % versus 14.7 %, respectively). In general, this result is consistent with the two previous comparisons performed in this work (i.e., both TROPOMI and ACE-FTS are biased high relative to the PEARL-FTS, but TROPOMI is biased higher relative to the PEARL-FTS than to ACE-FTS), which suggests that the observed high bias in TROPOMI over the high Arctic is a genuine feature in the TROPOMI CO product.

4.5 Conclusions

The TROPOMI instrument provides a highly spatially-resolved global dataset of CO columns. However, the validity and accuracy of TROPOMI's CO product in remote regions such as the high Arctic has previously not been well characterized. In this work, we have compared TROPOMI, ACE-FTS and a high-Arctic ground-based FTS located in Eureka, Nunavut. A global comparison of TROPOMI with ACE-FTS CO partial columns was performed for the period from 28 November 2017 to 31 May 2020, resulting in excellent agreement, with a Pearson correlation coefficient of $R = 0.93$, and a mean relative difference of -0.79 ± 0.26 % globally. The agreement between

TROPOMI and ACE-FTS was also investigated in five latitude bands including: the north Polar region (60° N to 90° N), the northern Mid-latitudes (20° N to 60° N), the Equatorial region (20° S to 20° N), the southern Mid-latitudes (20° S to 60° S), and the south Polar region (60°S to 90° S). A latitudinal dependence on the mean differences was observed, with positive mean relative biases of 7.93 ± 0.61 % and 7.21 ± 0.52 % in the north and south Polar regions, respectively, while a negative bias of −9.41 ± 0.55 % was found in the Equatorial region. This observed trend is generally consistent with earlier comparisons of the TROPOMI CO product with the ECMWF-IFS model in Borsdorff et al. (2018). Furthermore, to highlight any differences introduced by cloud contamination in the TROPOMI CO measurements, the latitudinal comparisons were repeated independently for cloud-covered and clear scenes only, and for the unsmoothed and smoothed cases. Clear-sky pixels were found to be biased higher, with slightly poorer correlations on average than clear+cloudy scenes and cloud-covered scenes only, which suggests that the TM5 reference profile shape used in the retrieval can have a measurable effect on the TROPOMI columns in the comparisons. Additionally, the latitudinal dependence of the biases is present in both the unsmoothed and smoothed cases, and the magnitude of the observed biases exceeds the ACE-FTS retrieval uncertainties of 5% in all latitude regions except the northern Mid-latitudes, indicating that the observed differences are significant. Despite the observed variability in the magnitude and direction of the mean biases, strong correlations ranging from $R = 0.93$ (SH mid-latitude region) to $R = 0.86$ (Equatorial region) were found between TROPOMI and ACE-FTS across all latitude bands.

To provide additional context to the global comparison of TROPOMI with ACE-FTS in the Arctic, both satellite data products were compared against NDACC measurements from the PEARL-FTS in Eureka, Nunavut (80.05° N, 86.42° W). Comparisons of TROPOMI with smoothed PEARL-FTS total columns in the period from 3 March 2018 to 27 March 2020 showed that the datasets were strongly correlated ($R = 0.88$, slope of linear fit = 1.07), however a systematic mean positive bias of 14.7 ± 0.16 % was also observed. These results are consistent with recent ground-based validation efforts by Sha et al. (2021) who found a comparable mean bias of 12.96 ± 4.56 % (bias ± standard deviation) for the PEARL-FTS while using stricter collocation criterion than in this study. A small degree of seasonal variability in the differences was found, with larger mean biases on average occurring during the spring months, and the lowest biases present during the summer months. However, with the exception of a few collocations during the late spring and early summer of 2018 and 2019, TROPOMI was consistently biased higher than the PEARL-FTS. Lastly, a partial column comparison between ACE-FTS and the PEARL-FTS was performed for the period from 25 February 2007 to 18 March 2020. These comparisons were performed in the optimal altitude

range of $9.33 - 66.58$ km, which was determined from an analysis of the sensitivity density of all PEARL-FTS retrievals that were collocated with ACE-FTS measurements. These partial column comparisons showed good agreement ($R = 0.79$, slope of linear fit $= 0.84$), and a mean positive bias of 7.89 ± 0.21 % in ACE-FTS with respect to the ground-based FTS. These findings are similar to previous validation results in Griffin et al. (2017), who found a mean relative difference of 7.1 ± 1.8 % between ACE-FTS and the PEARL-FTS for an earlier version of the ACE-FTS CO data product (v3.5).

In general, the magnitude and sign of the mean relative differences are consistent across all inter-comparisons presented in this work, suggesting that the version 1 TROPOMI CO product exhibits a high bias in the Arctic in the vicinity of Eureka that is consistent with the recent ground-based validation results of Sha et al. (2021). The observed mean differences fall within the TROPOMI mission accuracy requirement of $\pm$ 15 %, indicating that the data quality of the CO product in these high-latitude regions meets the specifications. Updates to the TROPOMI CO retrieval spectroscopy and de-striping methods described in Borsdorff et al. (2019) are expected to improve the latitudinal bias that is present in the version 1 operational product. It is suggested that a similar validation exercise be repeated on the version 2 TROPOMI CO product to verify that the observed latitudinal bias has been corrected.

Chapter 5

The August 2017 Canadian Wildfires

5.1 Introduction

This chapter summarizes the results of a study which investigated the enhancements of CO, C_2H_4, CH_3OH, HCOOH, and PAN over the high Arctic region resulting from the August 2017 Canadian wildfires in British Columbia and the Northwest Territories. This work builds upon a previous study by Lutsch et al. (2019) that investigated enhancements in CO, NH_3, HCN, and C_2H_6 total columns at Eureka from the August 2017 wildfires. This study is published as: Wizenberg et al., Exceptional Wildfire Enhancements of PAN, C_2H_4, CH_3OH, and HCOOH Over the Canadian High Arctic During August 2017, *J. Geophys. Res. Atmos.*, 2023 (Wizenberg et al., 2023).

In this study, we use a combination of ground-based FTIR measurements from Eureka, IASI satellite observations, and global simulations from the GEOS-Chem CTM to investigate the influence of two independent fires which occurred in British Columbia (BC) and the Northwest Territories (NWT) of Canada during August 2017. The BC wildfires were exacerbated by persistent warm and dry conditions brought on by climate change, and affected a record 1.2×10^6 hectares while displacing approximately 65,000 people (BC Wildfire Service, 2017; Kirchmeier-Young et al., 2019). These fires resulted in a volcano-like stratospheric smoke plume that encircled the tropical and extra-tropical northern hemisphere and lingered for several months (Fromm et al., 2021; Khaykin et al., 2018; Kloss et al., 2019; Peterson et al., 2018). Due to the far-reaching effects of anthropogenic climate change, wildfires are predicted to continue to increase in frequency and severity (Flannigan et al.,

2005; Halofsky et al., 2020; Hope et al., 2016), and extreme pyroCb events are expected to become more commonplace (Peterson et al., 2021). As a result, the 2017 wildfires may serve as a bellwether for future biomass burning events, and may forecast a substantial increase in wildfire-related VOC concentrations in the high Arctic, which has significant implications for the sensitive climate and environment of the region.

5.2 Methods

5.2.1 The PEARL-FTS

A detailed description of the PEARL-FTS instrument in Eureka, Nunavut is provided in Chapter 2 and in Batchelor et al. (2009). The PEARL-FTS retrievals are described in detail in Chapter 3, however, those for CO, C_2H_4, CH_3OH, HCOOH, and PAN are summarized in the context of this study below.

The spectral fitting microwindows, the interfering species, and corresponding references for each of the PEARL-FTS retrievals are summarized in Table 5.1. CO is a standard NDACC product, and is retrieved from PEARL-FTS measurements following NDACC-IRWG recommendations and the harmonized microwindows provided by Lutsch et al. (2016), Viatte et al. (2014) and references therein. PAN, C_2H_4, CH_3OH, HCOOH are non-standard products but are retrieved and processed in a similar manner. Three microwindows are used to retrieve CO: a strong line at 2157.50–2159.15 cm^{-1}, and two weak lines 2057.70–2058.00 cm^{-1}, and 2069.56–2069.76 cm^{-1} (Notholt et al., 2000; Viatte et al., 2014; Zhao et al., 2002). For CH_3OH, two windows were used: 992.00–998.70 cm^{-1} and 1029.00-1037.00 cm^{-1} (Bader et al., 2014; Viatte et al., 2014; Vigouroux et al., 2012). For the retrieval of HCOOH, two windows were also used: a primary window spanning 1102.00–1109.00 cm^{-1} that encompasses the ν_6 Q-branch absorption feature, and a small secondary window at 1178.40–1178.80 cm^{-1} to improve the fitting of the interfering species HDO, N_2O, CH_4, and O_3 (Paton-Walsh et al., 2005; Yamanouchi et al., 2020; Vigouroux et al., 2012; Zander et al., 2010). The ground-based FTIR retrieval of PAN is novel and was first described by Mahieu et al. (2021). Here, only a single broad window was used for PAN: 779.90–811.37 cm^{-1} (Mahieu et al., 2021). As discussed in Mahieu et al. (2021), the second PAN retrieval window spanning 1150.57–1178.83cm^{-1} yielded inconsistent and often unphysical retrieved columns at the Polar sites, and a lower signal-to-noise ratio on average. Lastly, C_2H_4 has previously been retrieved from ground-based FTIR instruments using the older SFIT2 algorithm (e.g., Paton-Walsh et al., 2005; Rinsland et al., 2005),

Table 5.1: Spectral fitting microwindows and the interfering species used for the PEARL-FTS retrievals and corresponding references.

Target species	Microwindows (cm^{-1})	Interfering species	References
CO	2057.70–2058.00, 2069.56–2069.76, 2157.50–2159.15	CO_2, H_2O, N_2O, O_3, OCS	Notholt et al. (2000), Zhao et al. (2002), Viatte et al. (2014)
PAN	779.90–811.37	CO_2, CCl_4, CHF_2Cl, $ClONO_2$, CFC-113, H_2O, O_3	Mahieu et al. (2021)
C_2H_4	948.80–952.40	CO_2, COF_2, H_2O, N_2O, NH_3, O_3, SF_6	Paton-Walsh et al. (2005), Rinsland et al. (2005), Toon et al. (2018), Vander Auwera et al. (2014)
CH_3OH	992.00–998.70, 1029.00–1037.00	CO_2, H_2O, O_3, O_3^{686}, O_3^{676}, O_3^{668}, O_3^{667}	Vigouroux et al. (2012), Viatte et al. (2014), Bader et al. (2014)
HCOOH	1102.00–1109.00, 1178.40–1178.80	CCl_2F_2, CH_4 CHF_2Cl, H_2O, HDO, N_2O, NH_3, O_3	Zander et al. (2010), Vigouroux et al. (2012), Yamanouchi et al. (2020)

but to our knowledge we are the first to implement these retrievals in SFIT4 and present a long-term time-series of C_2H_4 total columns at an Arctic FTIR site. For the retrievals of C_2H_4, we use a single spectral window at 948.80–952.40 cm^{-1} which encompasses the Q-branch absorption feature of the ν_7 band centered around 949 cm^{-1} (Paton-Walsh et al., 2005; Rinsland et al., 2005; Toon et al., 2018).

A full error analysis is performed for all retrievals following the approach of Rodgers (2000). The error budget includes forward model parameter errors, spectroscopic uncertainties and measurement noise error. The mean random, systematic, and total uncertainties, and the average DOFS are tabulated in Table 5.2. Adding the total random and systematic error components in quadrature gives mean retrieval uncertainties for the total columns of CO, PAN, C_2H_4, CH_3OH, and HCOOH of 2.75%, 25.6%, 67.3%, 11.8%, and 13.2%. The relative uncertainty associated with the C_2H_4 total columns appears very large, however this is primarily due to the extremely low ambient concentrations of C_2H_4 in the Arctic in the absence of biomass burning pollution. During the 17–23 August 2017 fire period, the mean relative uncertainty in the retrieved C_2H_4 columns was 7.9%. The DOFS for CO, PAN, C_2H_4, CH_3OH, and HCOOH are 2.17, 1.02, 1.01, 1.04, and 1.12, respectively. For the retrievals of CO and CH_3OH, we use an empirically tuned *a priori* covariance matrix to constrain

the retrieved profiles, while in the case of the retrievals of PAN, C_2H_4, and HCOOH, Tikhonov regularization was employed (Tikhonov, 1963). A plot of the mean VMR averaging kernels for all species is shown in Fig. 3.1, and the mean total column averaging kernels and the corresponding retrieval sensitivity calculated over the 2006–2020 time-series for each species is plotted in Fig. 3.2. A sensitivity of 1 indicates that a retrieval is independent of the a priori, while a sensitivity of 0 indicates that the *a priori* profile is the retrieved state. The CO retrieval has broad sensitivity in the troposphere and stratosphere, with a sensitivity greater than 0.5 between 0–55 km. The PAN, C_2H_4, and CH_3OH retrievals are primarily sensitive to the troposphere and lower stratosphere, with sensitivities greater than 0.5 in the range of 0–12 km for PAN and C_2H_4, and 0–13 km for CH_3OH species. The HCOOH retrieval displays slightly broader sensitivity to the lower to mid stratosphere in comparison to PAN, C_2H_4, and CH_3OH, with a sensitivity greater than 0.5 between 0–21 km. In general, the retrievals of CO, PAN, C_2H_4, CH_3OH, and HCOOH display good sensitivity to the troposphere and lower stratosphere where biomass burning plumes are likely to be located. Example SFIT4 spectral fits of C_2H_4 and PAN from during the August 2017 fire period are shown in Figs. 3.5 and 3.7, while similar fits of CO, CH_3OH, and HCOOH are provided in the appendix as Figs. A.1, A.2, and A.3.

Table 5.2: Mean total column retrieval uncertainties and DOFS of the PEARL-FTS retrievals calculated over the period of 2006–2020.

Species	Random uncertainty (%)	Systematic uncertainty (%)	Total uncertainty (%)	Mean DOFS
CO	1.56	2.26	2.75	2.17
PAN	22.4	8.00	25.6	1.02
C_2H_4	64.0	17.9	67.3	1.01
CH_3OH	4.66	10.5	11.8	1.04
HCOOH	5.28	11.3	13.2	1.12

5.2.2 IASI Observations

Measurements of CO, PAN, C_2H_4, CH_3OH, and HCOOH retrieved from the IASI-A and IASI-B instruments aboard the MetOp-A and MetOp-B satellites, respectively, were used. The MetOp platforms provide twice-daily global coverage (∼9:30 morning and evening), with a swath width of approximately 2200 km, and with a circular footprint of ∼12 km in diameter at nadir (Clerbaux et al., 2009). These properties provide an advantage over other nadir-sounding satellite instruments that can retrieve VOCs, such as TES, due to denser sampling and global coverage. To maximize the available data and the likelihood of coincident measurements with the PEARL-FTS, observations from both the a.m. and p.m. overpasses were used in the analysis. IASI data has been extensively

used to investigate the emissions and enhancement ratios of reactive VOC species and NH_3 within fire plumes around the world (Coheur et al., 2009; Franco et al., 2020; Paulot et al., 2017; Pommier et al., 2017; R'Honi et al., 2013; Rosanka et al., 2021; Whitburn et al., 2015, 2016, 2017).

Total column concentrations of CO are retrieved using the FORLI algorithm, which is based upon the optimal estimation method (George et al., 2015; Hurtmans et al., 2012). The IASI CO product has previously been validated against ground-based FTIR measurements from NDACC by Kerzenmacher et al. (2012), who found no notable biases in the collocated measurements. The vertical abundances of PAN, C_2H_4, CH_3OH, and HCOOH are obtained using the ANNI retrieval algorithm Version 3 (Franco et al., 2018). The HCOOH ANNI product was validated against ground-based NDACC instruments (including the PEARL-FTS) in Franco et al. (2020), and was found to have generally good agreement (i.e., correlation coefficients greater than 0.6) at most FTIR sites, but a positive bias at high latitudes. The PAN ANNI product was compared against ground-based FTIR measurements at the Jungfraujoch station in Switzerland by Mahieu et al. (2021), who found good agreement (correlation coefficient of 0.77) with no significant bias for the altitude-corrected IASI observations. The PAN ANNI product was also qualitatively compared against the PEARL-FTS PAN retrieval by Mahieu et al. (2021), however, due to the poor observational conditions for IASI in the absence of strong enhancements (i.e., low thermal contrast), observations were only made during a few summer months, and a general high bias relative to the ground-based measurements was seen. The C_2H_4 ANNI retrieval is new and is described in Franco et al. (2022).

The CH_3OH, HCOOH and PAN columns from IASI presented in this study were retrieved using a neural network that assumed a vertical distribution of each target species in an averaged transport regime, peaking in the free troposphere (see Franco et al., 2018). These vertical assumptions are unfortunately not fully representative for a concentrated fire plume at high altitude, such as observed in the fire event studied here (the altitude of the plume is discussed in Sect. 5.3.1). As a result, the retrieved columns of CH_3OH, HCOOH and PAN are likely overestimated. In contrast, the more recent ANNI C_2H_4 retrievals from IASI allow accounting specifically for the high altitude of the fire plume (Franco et al., 2022). Using the flexibility of these retrievals, we assess that the other retrieved VOC columns can be overestimated by up to 60% in the fire plume due to the assumption on the fire plume altitude. However, the same type of overestimation affects also the retrieved CO column measurements from IASI. As FORLI retrievals are strongly constrained, they do not allow retrieval of the altitude of the fire plume and the typical retrieved profile of CO is mixed vertically, even in the fire plume (George et al., 2015; Hurtmans et al., 2012). As a result, most of these high biases likely cancel in the IASI VOC:CO ratios that are calculated further in this study, however

some residual bias may persist.

5.2.3 GEOS-Chem Chemical Transport Model

The GEOS-Chem CTM (www.geos-chem.org; Bey et al., 2001), version 13.3.2, with detailed tropospheric and stratospheric chemistry was used. All model simulations in this study were performed using a horizontal resolution of 2°×2.5°, with 47 vertical hybrid levels from the surface to 0.01 hPa. The model is driven by assimilated meteorological fields from the Modern-Era Retrospective analysis for Research and Applications, Version 2 (MERRA-2; Gelaro et al., 2017), which is provided by the Global Modeling and Assimilation Office (GMAO) at NASA Goddard Space Flight Center. A model spin-up was performed from the beginning of January 2016 to the end of December 2016, before running the full year of 2017, with the last year used for the analysis presented here. Transport and chemical operator time steps of 10 and 20 minutes, respectively, were selected to minimize simulation errors (Philip et al., 2016).

Starting with GEOS-Chem version 13.1.0, all emissions in the model are configured at run-time using the Harmonized Emissions Component 3.0 (HEMCO; Lin et al., 2021) and various inventories. Global anthropogenic trace gas and aerosol emissions are sourced from the Community Emissions Data System (CEDS; Hoesly et al., 2018) version 2, while biogenic emissions are provided by the Model of Emissions of Gasses and Aerosols from Nature (MEGAN; Guenther et al., 2012) version 2.1. Biomass burning emissions from the Global Fire Assimilation System (GFAS; Kaiser et al., 2012) version 1.2 were used. GFAS provides global emissions for open fires on a 0.1° × 0.1° grid at 3-hourly resolution, which are derived from assimilated measurements of fire radiative power (FRP) from the Moderate Resolution Imaging Spectroradiometer (MODIS) onboard the NASA Aqua and Terra satellites. All emissions are re-gridded internally from their native resolutions to the 2° × 2.5° model resolution by the HEMCO module. GFAS was selected rather than the Global Fire Emissions Database, version 4.1 (GFEDv4.1) because it better represented the spatial and temporal patterns of the emissions from the 2017 fires when compared with IASI observations (i.e., the onset of emissions in GFED began much earlier in August than GFAS). Emissions of HCOOH are not included in the current version of GFAS, so in order to approximate these emissions, we scaled the GFAS CO emissions by the ratio of the emissions factors (i.e., EF_{HCOOH}/EF_{CO}, in molar units) taken for boreal forests from Andreae (2019), and then assigned these emissions to HCOOH for the August 2017 fire period. Additionally, C_2H_4 was recently added to GEOS-Chem chemical mechanism in version 13.3.0, and this is possibly the first application of this new simulation to wildfire studies,

providing an opportunity to compare the performance of the model against ground- and space-based observations.

5.3 Results and Discussion

5.3.1 Observed Enhancements

PEARL-FTS Time-series

The total column time series for CO, PAN, C_2H_4, CH_3OH, and HCOOH retrieved from the PEARL-FTS for the 2006-2020 period at Eureka are shown in Fig. 5.1, along with monthly means. A similar figure to Fig. 5.1 but with measurements from each year differentiated to better highlight previous enhancements is provided as Fig. A.4 in the appendix. The largest mean CO columns typically occur during February and March, with minima during July, as seen in Fig. 5.1a. The main sources of CO are fossil fuel combustion and the oxidation of VOCs and CH_4, and it is primarily transported to the Arctic from mid-latitude sources, with biomass burning being a significant secondary source during the summer months (Yurganov, 1997; Holloway et al., 2000). The main sink of CO in the Arctic is the oxidation reaction with OH. Due to the absence of sunlight during the Polar night, no OH is produced and the atmospheric lifetime of CO is extended significantly (Holloway et al., 2000). This allows transported mid-latitude CO emissions to accumulate in high concentrations, and leads to the large observed total columns in the spring months (Holloway et al., 2000; Stohl, 2006). With the return of sunlight and the resumption of OH photolysis at the end of Polar night, CO columns gradually decrease towards the summer months. The mean column increases in August, when the influence of biomass burning is most prominent.

From Fig. 5.1b, the largest mean PAN total columns are observed in the springtime, with a maximum in April and a minimum in July. The main source of PAN to the Arctic is long-range transport from polluted mid-latitude regions where it is formed via the reaction of NMVOCs with NO_x (Beine and Krognes, 2000). The primary sink of PAN is thermal decomposition (Fischer et al., 2014; Tuazon et al., 1991), with a smaller secondary sink due to photolysis that is thought to dominate in the upper troposphere above 7 km (Talukdar et al., 1995). The cold and stable atmosphere during the Polar night coupled with the lack of removal processes can lead to an accumulation of transported PAN, resulting in the large total columns observed in the spring months, as seen in Fig. 5.1b, which coincides with the 'Arctic haze' pollution phenomenon (Beine and Krognes, 2000; Law and Stohl, 2007; Law et al., 2014). Once the atmosphere begins to warm in the spring, PAN concen-

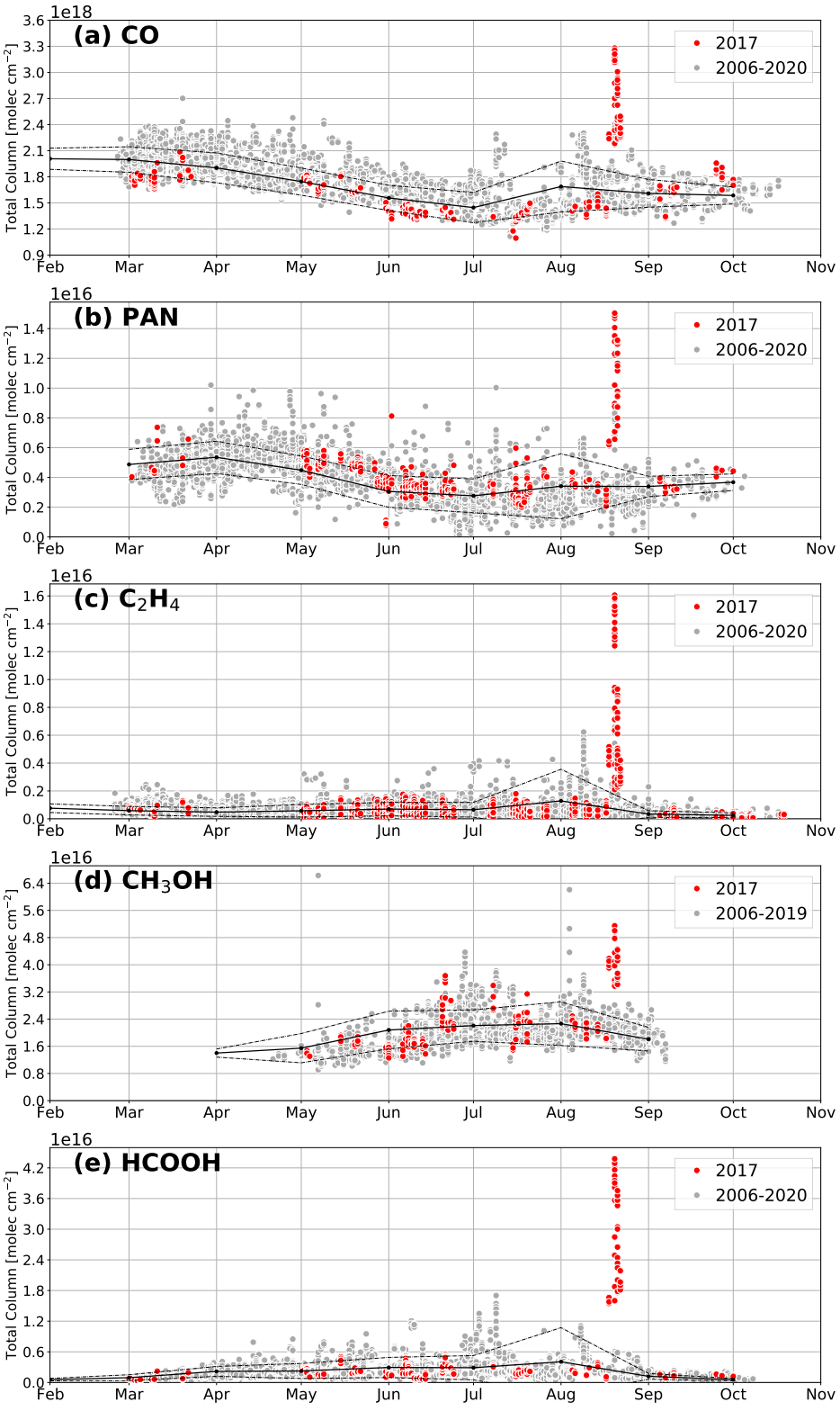

Figure 5.1: Total column time series of **(a)** CO, **(b)** PAN, **(c)** C_2H_4, **(d)** CH_3OH, and **(e)** HCOOH retrieved from the PEARL-FTS at Eureka for the period of 2006-2020. All years are plotted in light grey, while 2017 is highlighted in red. The solid black line denotes the monthly mean total columns calculated over all years and the dashed black line indicates $\pm 1\sigma$ from the monthly mean.

trations begin to decrease, leading to smaller measured columns in the summer months. Biomass burning presents a significant contribution to Arctic PAN columns during the summertime, leading to an increase in the mean columns in August that is reflected in the time-series in Fig. 5.1b (Fischer et al., 2014; Tereszchuk et al., 2013). As a result, although it has differing sources and sinks, PAN presents a similar seasonal cycle at Eureka as CO.

Fig. 5.1c shows that there is no detectable seasonal cycle for C_2H_4 columns at Eureka. In general, the column abundances of C_2H_4 at Eureka are extremely low, with mean total columns of 6.45×10^{14} molec. cm^{-2} calculated over all years. Globally, the primary sources of C_2H_4 are biomass burning (approximately 50% of global emissions), anthropogenic emissions from the petrochemical industry, automotive emissions, garbage incineration, and a smaller component from biogenic emissions (Sawada and Totsuka, 1986; Folberth et al., 2006; Gentner et al., 2013). In the Arctic region, there are very few local sources of C_2H_4, and due to its extremely short lifetime (approximately 14-35 hours in the Arctic summer atmosphere) resulting from its high reactivity with OH and O_3, transported mid-latitude anthropogenic emissions present a negligible contribution to Arctic C_2H_4 concentrations (Alvarado et al., 2011; Dolan et al., 2016). Transported biomass burning emissions appear to be the largest driver of the observed annual cycle of C_2H_4 at Eureka, with notable enhancements above the baseline visible in the time-series in Fig. 5.1c from previously detected Canadian and Siberian fires in 2014 and 2016, respectively (Lutsch et al., 2016, 2020).

At Eureka, a clear seasonal cycle of CH_3OH total columns can be seen in Fig. 5.1d, with the smallest total columns during the springtime and the largest columns in July and August, which is in agreement with ACE-FTS observations in Dufour et al. (2007). However, the exact nature of local sources and sinks of CH_3OH in the Arctic are not currently well understood. CH_3OH is primarily emitted biogenically from plants during their growth and decay phase (Ashworth et al., 2016; Fall and Benson, 1996; Hüve et al., 2007; MacDonald and Fall, 1993), with smaller sources including the reaction of methylperoxy radicals (CH_3O_2) with themselves and other organic peroxy radicals, oceanic emissions (Bates et al., 2021), as well as biomass burning (Akagi et al., 2013; Dufour et al., 2006). Its primary sinks are the reaction with OH, surface deposition, and uptake by the ocean (Bates et al., 2021; Stavrakou et al., 2011). A recent model study by Bates et al. (2021) indicates that atmospheric production via the reaction of CH_3O_2 + CH_3O_2/RO_2 and biogenic emissions are a significant driver of the seasonal cycle, resulting in a peak in the observed total columns in July and August. Despite this, chemical transport models have been shown to consistently underestimate CH_3OH concentrations, with the largest biases present at high latitudes, suggesting a significant and ubiquitous unknown source (Bates et al., 2021; Chen et al., 2019). Transported biomass burning

emissions also influence the Arctic CH_3OH budget during the summer months, although to a lesser degree than biogenic emissions (Dufour et al., 2007).

In the case of HCOOH, the seasonal cycle at Eureka is relatively weak as seen in Fig. 5.1e, however, some seasonality is apparent in the time-series, with smaller total columns in the spring and fall, and larger total columns during the summer. The sinks of HCOOH are believed to be well understood, with dry/wet deposition being the primary sink, however the sources of HCOOH in the Arctic are not particularly well understood (Paulot et al., 2011; Mungall et al., 2018). Similar to CH_3OH, previous comparisons of HCOOH observations with models (including GEOS-Chem) show significant underestimations in HCOOH abundances particularly at high northern latitudes, which suggests missing chemistry or unknown sources (Franco et al., 2021; Paulot et al., 2011; Schobesberger et al., 2016; Stavrakou et al., 2012). In situ measurements of HCOOH concentrations by Mungall et al. (2018) at Alert, Nunavut (82.30° N, 62.22° W) showed a high degree of diurnal variability and suggest a complex variety of regional sources in the Arctic that vary with meteorological conditions including snow melt emissions, soil emissions, and plant/vegetation emissions. The Eureka time-series demonstrates that biomass burning is a significant source of HCOOH to the high Arctic and a clear driver of the annual cycle, with the largest short-term perturbations in the total columns being the result of biomass-burning-related enhancements. The impact that these transient injections of high HCOOH concentrations to the Arctic atmosphere might have on soil and rainwater acidity should be investigated in future studies.

Enhancements in CO, CH_3OH and HCOOH columns resulting from biomass burning have been observed in the past by the PEARL-FTS at Eureka, with notable events including the August 2010 Russian fires (Viatte et al., 2013, 2015), the August 2014 NWT wildfires (Lutsch et al., 2016), and the July 2015 Alaskan wildfires (Lutsch et al., 2020). Lutsch et al. (2019) found that the August 2017 Canadian wildfires led to the greatest observed enhancements of CO, NH_3, HCN and C_2H_6 at Eureka in the 2006-2017 time-series. Importantly, it should be noted that all of the largest wildfire-driven enhancements observed at Eureka have occurred in the latter half of the time-series (evident in Fig. A.4), suggesting that biomass burning is becoming an increasingly significant source of these reactive trace gases to the high Arctic during the summer months. During the August 2017 fire period, with the exception of CH_3OH, all of the VOC species along with CO exhibited the largest enhancements in their total columns over the whole 2006-2020 Eureka time-series. The observed enhancement reaches a peak on 19 August 2017, with maximum total column values of $3.28 \pm 0.09 \times 10^{18}$ molec. cm^{-2}, $1.50 \pm 0.13 \times 10^{16}$ molec. cm^{-2}, $1.61 \pm 0.12 \times 10^{16}$ molec. cm^{-2}, $5.15 \pm 0.56 \times 10^{16}$ molec. cm^{-2}, and $4.38 \pm 0.33 \times 10^{16}$ molec. cm^{-2} (total column $\pm$ measurement

uncertainty) for CO, PAN, C_2H_4, CH_3OH, and HCOOH, respectively. It should be noted that no measurements were available on 18 August 2017 due to poor weather conditions, and it is possible that the PEARL-FTS did not capture the full extent of this enhancement event. These peak column values represent a perturbation on the order of approximately 2–12 times above the mean August total columns for these species at Eureka. In the case of CH_3OH, the total columns resulting from the 2017 fires are dwarfed by an un-attributed short-term enhancement that occurred in early May 2009, as well as an enhancement that is linked to boreal North American fires in August 2009 (Lutsch et al., 2020). In the following section, we will discuss the IASI observations over the Arctic during the August 2017 fire period.

IASI Observations

Under typical measurement conditions, retrievals of reactive VOCs from IASI over the high Arctic are difficult due to the low or even negative thermal contrast between the surface and the air directly above it, resulting in weaker signals in the recorded radiances, and hence in larger retrieval errors (Franco et al., 2018). Despite this, elevated concentrations of the target gases and the altitude of the transported plumes from the August 2017 fires provided sufficient sensitivity during the fire-affected period to allow for low-noise observations of these species over the Canadian Arctic region. Daily averages of CO, PAN, C_2H_4, CH_3OH, and HCOOH observations from IASI-A and IASI-B over the Arctic region on 19 August 2017 (the day of the peak measured enhancement of the PEARL-FTS) are shown in Fig. 5.2. IASI-A and IASI-B observations display strong enhancements in each species in the vicinity of Eureka, and capture the full spatial extent of the plume as it was transported from the Canadian fires northward to the Arctic region. IASI measurements show the plume passing directly over Eureka on 18 and 19 August 2017, corresponding with the peak in the PEARL-FTS total column measurements. The maximum hourly-mean columns observed by the IASI instruments of CO, PAN, C_2H_4, CH_3OH, and HCOOH on 19 August 2017 within 150 km of Eureka are $4.31 \pm 0.84 \times 10^{18}$ molec. cm^{-2}, $2.45 \pm 0.57 \times 10^{16}$ molec. cm^{-2}, $6.95 \pm 3.40 \times 10^{15}$ molec. cm^{-2}, $6.10 \pm 1.94 \times 10^{16}$ molec. cm^{-2}, and $2.57 \pm 0.58 \times 10^{16}$ molec. cm^{-2} respectively (mean total column $\pm$ standard deviation). These values broadly agree with the maximum total columns measured by the PEARL-FTS, although the total columns of the VOC species from IASI are on-average biased lower than those from the PEARL-FTS. In particular, the observed peak C_2H_4 columns from IASI are significantly smaller than those from the ground-based instrument ($6.95 \pm 3.40 \times 10^{15}$ molec. cm^{-2} versus $1.61 \pm 0.12 \times 10^{16}$ molec. cm^{-2} from the PEARL-FTS). Relative to ground-based FTIR measurements, the vertical sensitivity of the IASI VOC retrievals

may be reduced due to the aforementioned thermal contrast issues, potentially contributing to differences in the measured total columns. However, since ANNI retrievals do not employ an OEM-based approach, they do not produce averaging kernels, making it difficult to diagnose any differences in the vertical sensitivities between the instruments (Franco et al., 2018).

Additionally, the IASI observations shown in Fig. 5.2 provide a clear picture of the fragmentation of the biomass burning plume. A large portion of the plume can be seen passing over Eureka and the high Arctic, while another substantial fragment of the plume (centered around 60° N) is shown being lofted eastward towards the Atlantic Ocean and Europe, where it contributed to a stratospheric smoke layer and enhanced aerosol optical depth measurements over western Europe (Khaykin et al., 2018). The transported plumes from the BC and NWT fires resulted in the largest C_2H_4 total columns, and the second largest PAN total columns measured on 20 August 2017 by a Bruker 120HR ground-based FTIR at Jungfraujoch, Switzerland (46.55° N, 7.98° E, 3580 m a.s.l) which has been in operation since 1995. A time-series of C_2H_4 total columns measured at Jungfraujoch with the observations from 20 August 2017 highlighted is provided in the appendix as Fig. A.5. The

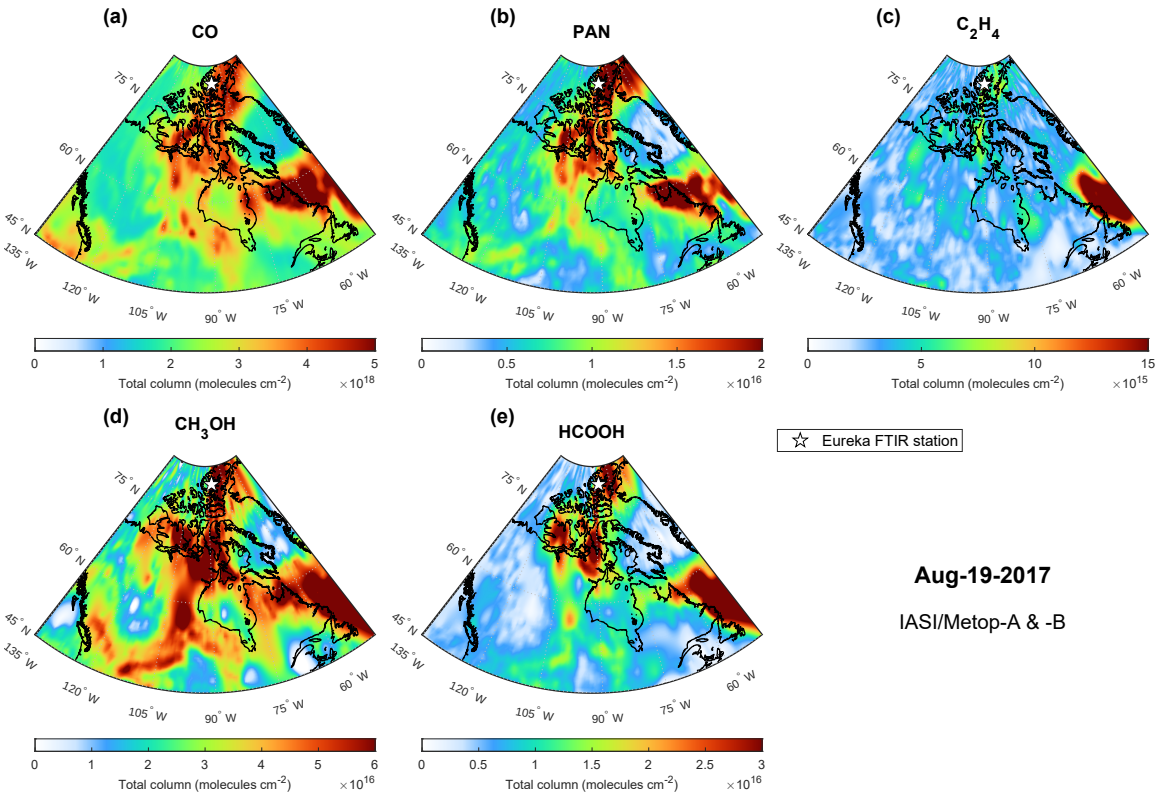

Figure 5.2: Daily average IASI-A and IASI-B total column measurements of **(a)** CO, **(b)** PAN, **(c)** C_2H_4, **(d)** CH_3OH, and **(e)** HCOOH over the mid- and high-latitude regions of North America on 19 August 2017. The location of Eureka, Nunavut is denoted by the white star in the top of each panel.

smoke from the August 2017 fires persisted in the stratosphere above Europe for several months, and the magnitude of the smoke injection has since been likened to that of a moderate volcanic eruption, demonstrating the exceptional nature of this particular fire event (Khaykin et al., 2018; Yu et al., 2019). In the following section, we will discuss the trace gas correlations, emission ratios, and emission factors that have been derived from PEARL-FTS and IASI measurements, as well as contrast them with the values provided in the literature.

5.3.2 Emissions Estimates

Trace Gas Correlations

The enhancement ratio (EnhR) enables a quantification of trace-gas emissions from biomass burning during wildfire events. Fire-affected measurements were first identified by those which had total column amounts greater than 1σ standard deviation from the monthly mean of all measurements and over all years following the methods of Viatte et al. (2015) and Lutsch et al. (2016, 2019). Due to the fact that the FTIR measurements are made across various spectral regions using a series of optical filters (i.e., CO and the VOCs may not be measured simultaneously), we only pair CO and VOC measurements made within 1 hr of each other, with each CO measurement only being used once. The 1-hr window was selected following the approach of Lutsch et al. (2019) to maximize the number of measurement pairs, while simultaneously minimizing the effects of plume aging between paired observations. On average, the difference in measurement times for each species and the coincident CO measurement is approximately 20 minutes. The EnhR (in units of molec. cm^{-2}/molec. cm^{-2}) is then given by the slope of a linear least-squares regression between the target species and CO for all fire-affected measurements. Bootstrap resampling (with 5000 ensemble members) was used to determine the 95% confidence intervals as the uncertainties for the fitted slopes. Bootstrap resampling such as this allows for a robust treatment of non-normally distributed datasets (Gatz and Smith, 1995). This process was repeated using IASI-A and IASI-B measurements within 150 km of Eureka to provide a second set of EnhRs for comparison with the values derived from the PEARL-FTS. The trace-gas correlations for each VOC species versus CO for the PEARL-FTS are shown in Fig. 5.3, and the resulting enhancement ratios are provided in the fourth column of Table 5.3. A similar figure as Fig. 5.3 but for IASI is shown in Fig. A.6 in the appendix. Enhancement ratios are sensitive to plume travel times, fuel types, combustion phases, and transport trajectories particularly for short-lived species (Viatte et al., 2015). As a result, comparisons with previously reported EnhRs from the literature can be challenging. However, for completeness we have included

values from previous studies in Table 5.3 wherever they were available.

PAN, C_2H_4, CH_3OH, and HCOOH display strong correlations with CO during the fire-affected period of 17–23 August 2017, with Pearson correlation coefficients of $R = 0.91$, $R = 0.97$, $R = 0.73$, and $R = 0.96$, respectively. In the case of CH_3OH, the smaller correlation coefficient may be due in part to the smaller number of observations during the fire period and the weaker overall enhancement relative to the other VOC species. However, this is consistent with Viatte et al. (2015) who found CH_3OH to have generally weaker correlations with CO than most other biomass burning tracer species at Eureka. The linear regressions obtained from IASI measurements for PAN, C_2H_4, CH_3OH, and HCOOH display good to moderate correlations with CO with $R = 0.87$, $R = 0.68$, $R = 0.47$, and $R = 0.79$, respectively. IASI measurements show the weakest correlation for CH_3OH with CO, which is consistent with the correlations derived from the PEARL-FTS measurements. The calculated enhancement ratios from the PEARL-FTS for PAN, C_2H_4, CH_3OH, and HCOOH relative to CO are $(6.36 \pm 0.65) \times 10^{-3}$, $(10.6 \pm 0.72) \times 10^{-3}$, $(10.6 \pm 2.64) \times 10^{-3}$, and $(24.3 \pm 1.43) \times 10^{-3}$, respectively. These values can be compared with the enhancement ratios derived from IASI-A and IASI-B measurements (shown in Fig. A.6 in the appendix) which are $(5.86 \pm 0.66) \times 10^{-3}$, $(1.60 \pm 0.37) \times 10^{-3}$, $(10.7 \pm 4.60) \times 10^{-3}$, and $(9.47 \pm 1.78) \times 10^{-3}$ for PAN, C_2H_4, CH_3OH, and HCOOH relative to CO, respectively. For CH_3OH and PAN, the PEARL-FTS and IASI measurements yield the same enhancement ratios within combined uncertainties. The CH_3OH enhancement ratios can be roughly compared with Viatte et al. (2015), who obtained a mean CH_3OH:CO ratio of $(25.9 \pm 20.6) \times 10^{-3}$ across all fire events detected at Eureka between 2008 and 2012. The mean value from Viatte et al. (2015) is more than double the values from the PEARL-FTS and IASI in this study, however our values fall within their bounds of uncertainty.

Since ground-based FTIR retrievals of PAN are new, there were no ground-based studies available for comparison. However, ACE-FTS measurements over aged Canadian and Alaskan plumes by Tereszchuk et al. (2013) yielded a PAN enhancement ratio of $(3.61 \pm 0.54) \times 10^{-3}$, and while this value is quite close to the enhancement ratios in this study, they fall just outside of the bounds of error. Aircraft measurements of aged Canadian boreal plumes during the ARCTAS-B campaign by Alvarado et al. (2010) yielded a mean PAN enhancement ratio of $(3.50 \pm 2.60) \times 10^{-3}$, with a range of individual PAN:CO enhancement ratios between 1.10×10^{-3} to 8.70×10^{-3}. While their reported mean value is smaller than the ones measured in this study as well as those reported by Tereszchuk et al. (2013), our values from the PEARL-FTS and IASI fall inside their range of reported enhancement ratios, and the upper bound of their mean value when accounting for the uncertainty.

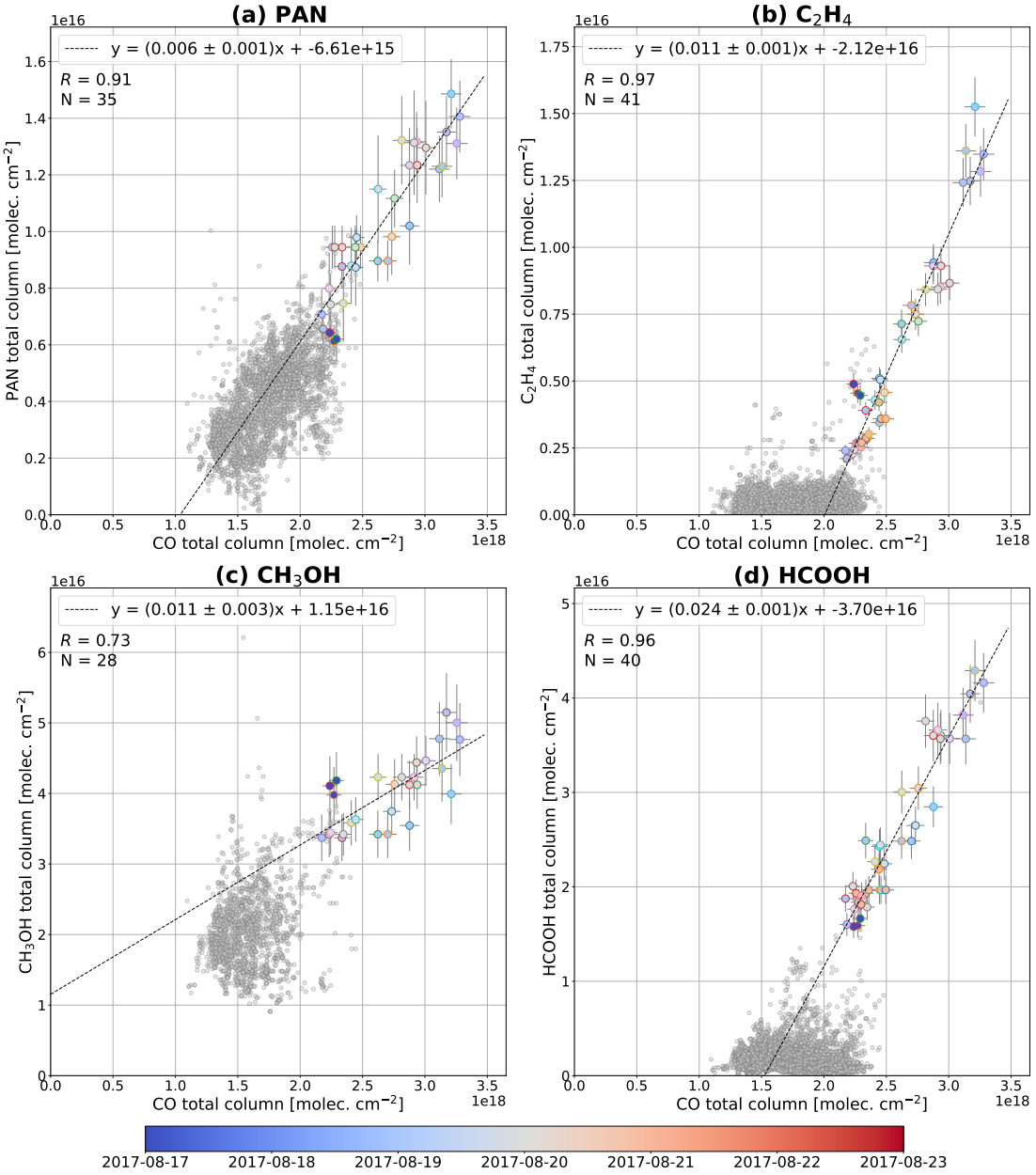

Figure 5.3: Enhancement ratios derived from PEARL-FTS measurements of **(a)** PAN, **(b)** C_2H_4, **(c)** CH_3OH, and **(d)** HCOOH relative to CO during the fire-affected period of 17 to 23 August 2017. Data points from the fire period are colored based on the day on which the measurements were made, and all other measurements (from 2006–2020) are plotted in light grey. The equation for the linear fit, the Pearson correlation coefficient R, and the number of fire-affected measurements are shown in the upper left of each panel.

For C_2H_4 and HCOOH, there are large differences in the EnhRs from the PEARL-FTS and IASI. The C_2H_4 EnhR from PEARL-FTS measurements is an order of magnitude larger than the one derived from IASI ($(10.6 \pm 0.72) \times 10^{-3}$ versus $(1.60 \pm 0.37) \times 10^{-3}$, respectively). The difference in the HCOOH EnhRs is smaller, but the FTIR-derived value is more than twice the IASI-derived EnhR ($(24.3 \pm 1.43) \times 10^{-3}$ versus $(9.47 \pm 1.78) \times 10^{-3}$, respectively). It should be noted however, that the IASI-derived EnhR for HCOOH of $(9.47 \pm 1.78) \times 10^{-3}$ is independently larger than the mean EnhR of $(8.08 \pm 5.87) \times 10^{-3}$ derived from ground-based FTIR measurements for all fires detected at Eureka between 2008 and 2012 provided by Viatte et al. (2015). The low bias in the IASI EnhRs for C_2H_4 and HCOOH is related to the smaller retrieved mean total columns for these species relative to the PEARL-FTS, which is likely a result of the generally lower sensitivity of the IASI retrievals and the poor observational conditions for IASI.

Calculation of emission ratios and emission factors

Since the FTIR and IASI measurements at Eureka are being made at a significant distance from the fire sources, the transported biomass burning plumes have undergone chemical aging, which leads to some loss of each species. We can estimate the emission ratio (ER) at the fire source by adjusting the EnhRs to account for the plume travel time and the subsequent chemical aging. The ER is given by (Lutsch et al., 2016; Viatte et al., 2015):

$$\mathrm{ER}_X = \mathrm{EnhR}_X \cdot \left(\frac{\exp(\frac{t}{\tau_x})}{\exp(\frac{t}{\tau_{\mathrm{co}}})} \right), \tag{5.1}$$

where τ_x is the lifetime of the target species, and t is the travel time of the plume. For CO, an atmospheric lifetime of 30 days was chosen based on Viatte et al. (2015), who performed model comparisons with FTIR measurements at Eureka. For C_2H_4, CH_3OH, and HCOOH, atmospheric lifetimes of 2, 5.8 and 4 days were chosen based on Toon et al. (2018), Stavrakou et al. (2011), and Stavrakou et al. (2012), respectively. For the calculation of the ERs, a plume travel time of 5 days was selected based on the FLEXPART model back-trajectories described in Lutsch et al. (2020). The ERs presented here are only rough estimates and the true uncertainties on the ERs are likely larger than those quoted in this study. There are additional uncertainties that are difficult to quantify such as the atmospheric lifetimes of each species inside of the smoke plumes which can be highly variable relative to the mean lifetimes used here, as well as uncertainties in the plume travel time resulting from the fact that the smoke originated from two distinct fires.

Additionally, biomass burning emissions are often characterized using the emission factor (EF),

which quantifies the amount of a given trace-gas species emitted per kg of dry biomass combusted (in units of g kg^{-1}). Emission factors are commonly reported in the literature, allowing for direct comparisons with the values derived in this study. The emission factor is defined as (Andreae and Merlet, 2001; Andreae, 2019):

$$\mathrm{EF}_X = \mathrm{EF}_{\mathrm{co}} \cdot \mathrm{ER}_X \cdot \left(\frac{\mathrm{MW}_X}{\mathrm{MW}_{\mathrm{co}}} \right), \tag{5.2}$$

where MW is the molecular weight of a given species (in units of g mol^{-1}). To convert from the calculated emission ratios to emission factors, we use the emission factor for CO of 121 ± 47 g kg^{-1} for boreal forests from the most recent compilation study by Andreae (2019). The uncertainty in the calculated emission factors is determined by adding the relative uncertainty contributions from the emission ratio of each respective species and the CO emission factor. The calculated emission ratios and emission factors for the PEARL-FTS and IASI, as well as those collected from previous studies are provided in columns 5 and 6 of Table 5.3, respectively. Additionally, the emission factors of CO used in the calculations of the emission ratios and emission factors are provided in column 3 of Table 5.3 where available. For PAN, since it only results from secondary formation, we do not calculate the emission ratio or emission factor.

From the measured C_2H_4 enhancement ratio, we obtain emission ratios of (109 ± 7.40) × 10^{-3} and (16.5 ± 3.87) × 10^{-3} for the PEARL-FTS and IASI, respectively. The derived emission factors are 13.2 ± 6.02 g kg^{-1} from the PEARL-FTS, and 1.99 ± 1.25 g kg^{-1} from IASI, reflecting a difference of approximately 560% in the emission factors. The emission factor computed from the FTIR is an order of magnitude larger than those provided by the compilation studies by Andreae (2019) and Akagi et al. (2011), as well as the value used in GFASv1.2, which give emission factors of 1.54 ± 0.66 g kg^{-1}, 1.42 ± 0.43 g kg^{-1}, and 1.18 ± 0.55 g kg^{-1}, respectively. Furthermore, aircraft measurements by Simpson et al. (2011) over Canadian boreal fires during the 2008 ARCTAS-B campaign yielded an emission factor for C_2H_4 of 0.82 ± 0.09 g kg^{-1}, while aircraft measurements over Alaskan fires by Goode et al. (2000) yielded an emission factor of 3.28 (with no uncertainty reported), both of which are significantly smaller than the value obtained from the FTIR in this study. The C_2H_4 emission factor of 1.99 ± 1.25 obtained from IASI measurements in this study is larger than all previous studies with the exception of Goode et al. (2000), and only overlaps within the bounds of uncertainty of the reported value of Andreae (2019). As previously discussed in Sect. 5.2.2, limitations in the measurement sensitivity of the IASI retrievals over the high Arctic compared to the ground-based FTIR may lead to the satellite measurements not capturing the full magnitude

Table 5.3: Comparison of calculated enhancement ratios, emission ratios, and emission factors for PAN, C_2H_4, CH_3OH, HCOOH at Eureka. The reported uncertainties are provided in parentheses.

Source	Type	EF_{CO}(g kg^{-1})	EnhR $\times 10^{-3}$	ER $\times 10^{-3}$	EF (g kg^{-1})
		PAN			
This study - PEARL-FTS	Ground-based	-	6.36 (0.65)	-	-
This study - IASI	Satellite	-	5.86 (0.66)	-	-
Tereszchuk et al. (2013)[a]	Satellite	-	3.61 (0.54)	-	-
Alvarado et al. (2010)[b]	Aircraft	-	3.50 (2.60)	-	-
		C_2H_4			
This study - PEARL-FTS	Ground-based	121 (47)[c]	10.6 (0.72)	109 (7.40)	13.2 (6.02)
This study - IASI	Satellite	121 (47)[c]	1.60 (0.37)	16.5 (3.87)	1.99 (1.25)
GFASv1.2[d]	Compilation	106 (37)	-	-	1.18 (0.55)
Andreae (2019)[e]	Compilation	121 (47)	-	-	1.54 (0.66)
Akagi et al. (2011)	Compilation	127 (45)	-	-	1.42 (0.43)
Simpson et al. (2011)[f]	Aircraft	113 (72)	-	7.30 (0.10)	0.82 (0.09)
Goode et al. (2000)[h]	Aircraft	88.8	-	38.4	3.28
		CH_3OH			
This study - PEARL-FTS	Ground-based	121 (47)[c]	10.6 (2.64)	21.2 (5.43)	2.94 (1.89)
This study - IASI	Satellite	121 (47)[c]	10.7 (4.60)	21.4 (9.52)	2.96 (2.47)
GFASv1.2[d]	Compilation	106 (37)	-	-	1.89 (1.40)
Andreae (2019)[e]	Compilation	121 (47)	-	-	2.33 (1.45)
Akagi et al. (2011)	Compilation	127 (45)	-	-	2.82 (1.62)
Viatte et al. (2015)[h]	Ground-based	127 (45)	25.9 (20.6)	28.1 (12.5)	3.44 (1.68)
Tereszchuk et al. (2013)[a]	Satellite	-	1.99 (0.40)	-	-
Rinsland et al. (2007)[i]	Satellite	86 (17)	-	27.8 (4.56)	2.73 (0.71)
Simpson et al. (2011)[f]	Aircraft	113 (72)	-	9.60 (1.90)	1.20 (0.30)
Goode et al. (2000)[g]	Aircraft	88.8	-	15.3	1.45
		HCOOH			
This study - PEARL-FTS	Ground-based	121 (47)[c]	24.3 (1.43)	71.7 (4.23)	14.3 (6.38)
This study - IASI	Satellite	121 (47)[c]	9.47 (1.78)	28.0 (5.33)	5.56 (3.22)
Andreae (2019)[e]	Compilation	121 (47)	-	-	1.04 (0.89)
Akagi et al. (2011)	Compilation	127 (45)	-	-	0.57 (0.46)
Viatte et al. (2015)[h]	Ground-based	127 (45)	8.08 (5.87)	15.3 (4.03)	2.69 (1.14)
Pommier et al. (2017)[j]	Satellite	-	4.40 (0.09)	-	-
R'Honi et al. (2013)[k]	Satellite	-	11.0	47.0	-
Tereszchuk et al. (2013)[a]	Satellite	-	1.46 (0.49)	-	-
Rinsland et al. (2007)[i]	Satellite	86 (17)	-	4.63 (0.67)	0.65 (0.16)
Goode et al. (2000)[g]	Aircraft	88.8	-	11.6	1.57

[a] ACE-FTS observations of Canadian and Alaskan plumes aged by 120-144 h.
[b] NASA DC-8 measurements of aged Canadian boreal plumes during the 2008 ARCTAS-B campaign.
[c] To convert from ER to EF in this work, we use the EF_{CO} for boreal forests from Andreae (2019).
[d] Emission factors for boreal forests based on Andreae and Merlet (2001) with updates by M.O. Andreae.
[e] Values reported for boreal forests.
[f] Measurements of Canadian boreal fires during the 2008 ARCTAS-B campaign.
[g] Measurements of Alaskan fires.
[h] Mean values derived from ground-based FTIR measurements at Eureka, Nunavut between 2008 and 2012.
[i] Also ACE-FTS observations of Canadian and Alaskan fires.
[j] IASI observations of Siberian boreal fires.
[k] IASI measurements of plumes from the 2010 central Russian fires. The EnhR is an average over all days of the fires.

of the enhancement in the total column abundances, and may contribute to the observed difference in the derived emission factors and emission ratios compared to the FTIR results.

In the case of CH_3OH, there is extremely good agreement between the derived emission ratios and emission factors from the PEARL-FTS and IASI. The emission ratios are $(21.2 \pm 5.43) \times 10^{-3}$ and $(21.4 \pm 9.52) \times 10^{-3}$ for the PEARL-FTS and IASI, respectively. These emission ratios yield emission factors of 2.94 ± 1.89 g kg^{-1} for the PEARL-FTS, and 2.96 ± 2.47 g kg^{-1} for IASI. The derived emission factors in this study agree well with the values from the two most recent compilation studies by Andreae (2019) and Akagi et al. (2011), who reported values of 2.33 ± 1.45 g kg^{-1} and 2.81 ± 1.62 g kg^{-1}, respectively. PEARL-FTS and IASI emission factors are both larger than the GFASv1.2 emission factor of 1.89 ± 1.40 g kg^{-1}, which falls towards the lower end of the literature values, however, this value is based on Andreae and Merlet (2001) and is likely out-dated in comparison to the newer study by Andreae (2019). Viatte et al. (2015) reported a mean CH_3OH emission factor of 3.44 ± 1.68 g kg^{-1} across all fires at Eureka between 2008-2012, which is larger than the values derived in this study, but still agrees within the combined bounds of uncertainty. A study by Rinsland et al. (2007) that used ACE-FTS satellite observations of Canadian and Alaskan fires provides an emission factor of 2.73 ± 0.71 g kg^{-1}, which is in agreement with our values, and falls between the values provided in the compilation studies by Andreae (2019) and Akagi et al. (2011). Lastly, studies by Simpson et al. (2011) and Goode et al. (2000) using aircraft measurements reported smaller emission factors of 1.2 ± 0.3 g kg^{-1} and 1.45 g kg^{-1}, respectively, which do not agree within the bounds of uncertainty of our values. In general, our CH_3OH emission factors fall towards the upper end of the values reported in the literature, but show excellent agreement with recent studies.

For HCOOH, the calculated emission ratio from the PEARL-FTS is $(71.7 \pm 4.23) \times 10^{-3}$, which is notably larger than the emission ratio of $(28.0 \pm 5.33) \times 10^{-3}$ determined from IASI measurements. The resulting emission factors display similar differences, with values of 14.3 ± 6.38 g kg^{-1} and 5.56 ± 3.22 g kg^{-1} for the PEARL-FTS and IASI, respectively, reflecting a difference of approximately 150%. In comparison to the HCOOH emission ratios and factors previously reported in the literature, both of the values derived in this study are significantly larger. One exception to this is R'Honi et al. (2013) who obtained a mean emission ratio for HCOOH of 47.0×10^{-3} using IASI measurements over plumes from the 2010 central Russian wildfires, which falls in between the values derived from PEARL-FTS and IASI in this study. The compilation studies by Andreae (2019) and Akagi et al. (2011) provide emission factors of 1.04 ± 0.89 g kg^{-1} and 0.57 ± 0.46, respectively, which are roughly 1/10th and 1/20th of the emission factor from the FTIR, and 1/5th and 1/10th

of the emission factor from IASI in this study. The ground-based study by Viatte et al. (2015) reported a mean emission factor for HCOOH of 2.69 ± 1.14, which is larger than the aforementioned compilation studies, but is still significantly smaller than the values in this study. It should be noted, however, that for one particularly large enhancement event in August 2010 resulting from fires in Russia, Viatte et al. (2015) obtained an emission ratio of 40.9×10^{-3}, which falls between the range of the values derived from the PEARL-FTS and IASI in this work. Rinsland et al. (2007) provide an emission factor of 0.65 ± 0.16 g kg^{-1}, which is in-line with Akagi et al. (2011), but is smaller than this study and the other previous studies listed in Table 5.3. Lastly, aircraft measurements by Goode et al. (2000) in Alaskan fire plumes yielded an emission factor for HCOOH of 1.57 g kg^{-1}, which is larger than the values from the studies by Akagi et al. (2011), Andreae (2019), and Rinsland et al. (2007), but is still significantly smaller than the derived emission factors from IASI and the PEARL-FTS in this study. The high emission ratio and emission factor calculated for HCOOH may indicate that significant secondary production of this species occurred in the plumes. This will be investigated further using GEOS-Chem sensitivity tests in Section 5.3.3.

5.3.3 GEOS-Chem Comparisons to Observations

Simulated plume transport and enhancement

Since measurements of reactive VOC species are sparse in the high-Arctic region, global chemical transport models such as GEOS-Chem can provide an additional perspective on the transport and enhancements resulting from wildfires in these remote regions. Furthermore, PEARL-FTS and IASI measurements of these reactive species can serve as a means for evaluating the performance of the model during this fire event, in particular, for the new C_2H_4 simulation that was recently added to GEOS-Chem version 13.3.0. In this study, we use CO as a tracer of the wildfire emissions and the subsequent transport since due to its long atmospheric lifetime of approximately 30 days, it is relatively unaffected by chemical aging in the plume over the span of a several days. In comparison, C_2H_4, CH_3OH, and HCOOH all have lifetimes on the order of a few days, and while the lifetime of PAN is highly temperature dependent, its lifetime due to thermal decomposition is generally shorter than that of CO in the troposphere (Jacob, 2000; Moxim et al., 1996).

Comparisons of GEOS-Chem simulations with IASI and the PEARL-FTS were performed as follows. For comparisons with IASI, the IASI data was re-gridded onto the 2°×2.5° spatial grid used by the model. Since the IASI ANNI retrievals do not produce averaging kernels, we do not apply averaging kernel smoothing in these comparisons. When performing direct comparisons between

GEOS-Chem and the PEARL-FTS, we first select the nearest grid-box of the model to PEARL, and then pair the GEOS-Chem simulated profiles (which are outputted at a two-hour frequency) with FTIR observations within ±1 h of the time of the FTIR measurement, allowing multiple FTIR measurements to pair with a single GEOS-Chem profile. The GEOS-Chem profiles are interpolated to the FTIR vertical grid, and then smoothed by the mean FTIR total column averaging kernel calculated over all years for the respective species following Rodgers and Connor (2003). The application of averaging kernel smoothing such as this minimizes any biases introduced by the *a priori* profile and the sensitivity of the instrument, allowing for an optimized comparison between the model and the FTIR measurements. When qualitatively inter-comparing both the PEARL-FTS and IASI with GEOS-Chem, no smoothing or re-gridding was applied to the GEOS-Chem data.

We first performed a baseline GEOS-Chem simulation for the period of August 2017 with no modifications made to the GFAS emissions or the method through which the emissions were being injected. By default, in version 13 of the model, biomass burning emissions from GFAS are distributed evenly between the surface and the "mean altitude of maximum injection" (MAMI), which is determined using a simple 1-D plume-rise model as described in Freitas et al. (2006) and Rémy et al. (2017). The mean MAMI values during the period of peak fire activity between 10 to 15 August 2017 for the BC and NWT fires were approximately 1500 m and 1100 m, respectively. However, in the case of wildfires such as the 2017 BC fires where strong pyroCb events occurred, this injection scheme may not properly reflect reality as pyroCb smoke plumes can rise to extreme altitudes before they are transported laterally. Peterson et al. (2018) and Fromm et al. (2021) termed the BC pyroCb event the Pacific Northwest Event (PNE), and demonstrated that the smoke from these fires was injected directly into the lower stratosphere at an altitude of approximately 12-13 km before being lofted northwards, which represents a significant disparity with the values provided by GFAS.

The baseline simulation displays a severe model discrepancy with respect to IASI observations whereby the plume is diverted around Eureka almost entirely, resulting in much smaller enhancements in the total column abundances of CO and the VOC species than was observed by the PEARL-FTS and IASI. To exclude the possibility that the model error was being introduced by the choice of meteorology, an identical baseline simulation was performed using GEOS-FP meteorology in place of MERRA-2, however both simulations exhibited a nearly identical model error. This model error was determined to be a direct result of the method through which the biomass burning emissions are injected into the vertical model grid. The injection height of the BC fires has been examined in detail in the literature (e.g., Bourassa et al., 2019; Fromm et al., 2021; Peterson et al., 2018; Torres et al., 2020), and it is generally understood that the plume was injected into the UTLS

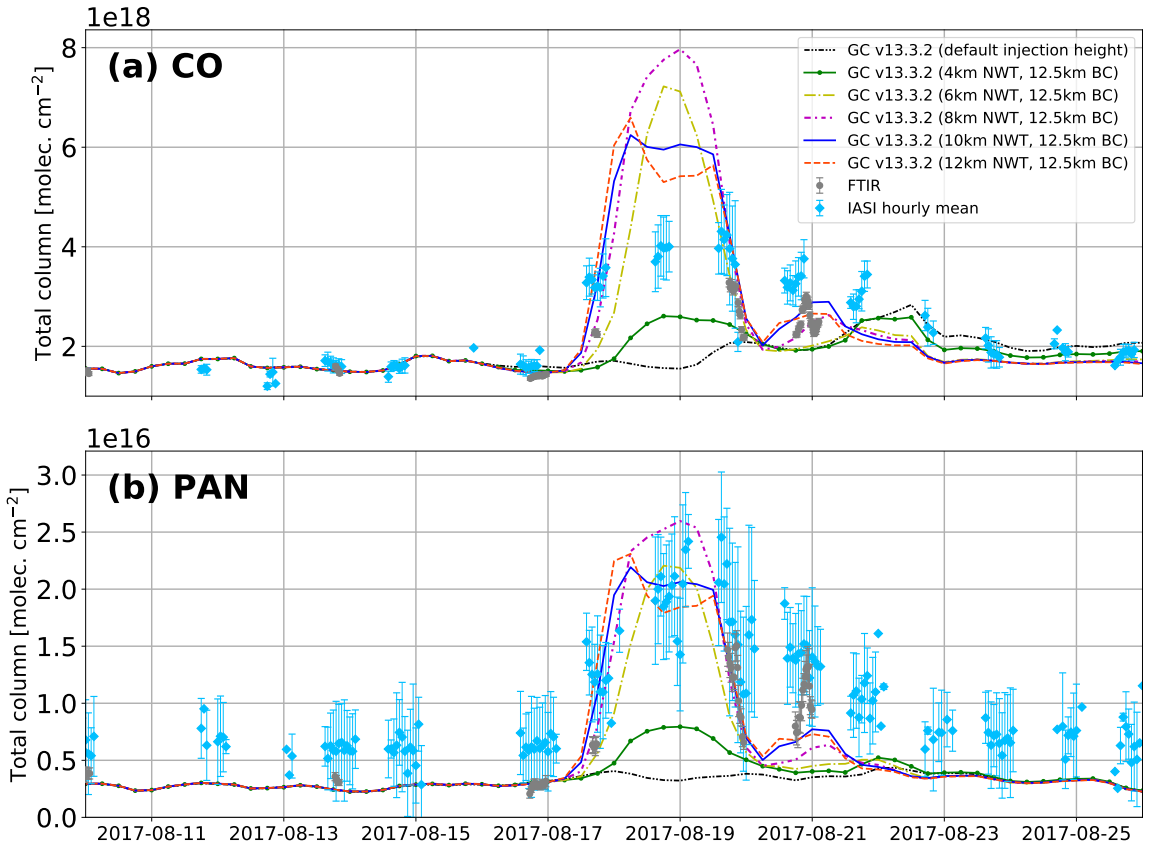

Figure 5.4: Time-series of un-smoothed GEOS-Chem columns of **(a)** CO, and **(b)** PAN for simulations with varying emission injection heights for the NWT wildfires. PEARL-FTS measurements are shown in grey, and IASI-A and IASI-B hourly averages within 150 km of Eureka are shown in cyan. The error bars on the FTIR data points indicate the measurement uncertainties and the error bars on the IASI data points correspond to the standard deviations.

with a mean altitude of 12–13 km above the fires, with the top of the injected plume reaching as high as 13.7 km. However, the injection and plume height of the NWT fires has not been examined in the same depth, and is not well constrained.

To ascertain an appropriate injection height for the NWT fires, we performed a series of simulations with variable injection heights for the NWT fires, while using a fixed injection height of 12.5 km for the BC fires based on Peterson et al. (2018) and Fromm et al. (2021), and we used both CO and PAN as tracers for the plume transport. CO was chosen because its long atmospheric lifetime means that it will be minimally affected by chemical aging over the course of a few days, and PAN was selected as a secondary tracer since it is highly sensitive to the transport altitude as a result of the strong temperature dependence of its atmospheric lifetime. To quantitatively assess the performance of each simulation, we calculated the correlations of the smoothed GEOS-Chem columns with those observed by the PEARL-FTS. A time-series of GEOS-Chem simulated columns

of CO and PAN for the various injection height simulations, along with PEARL-FTS observations and hourly-averaged IASI measurements are shown in Fig. 5.4, and correlation plots of GEOS-Chem with the PEARL-FTS for CO and PAN for each simulation are provided as Figures A.7 and A.8 in the appendix. For both CO and PAN, it can be seen from Fig. 5.4 that the simulation using the default GFAS injection height scheme fails to produce a noticeable enhancement in the total columns on 18 and 19 August 2017 when IASI and the PEARL-FTS observed the peak enhancement. Setting the injection height for the BC fires to 12.5 km and increasing the injection height for the NWT fires to 4 km starts to produce a stronger simulated enhancement at Eureka, however, the magnitude of the resulting enhancement is still smaller than that from both IASI and FTIR observations. Further increasing the NWT injection height leads to a larger subsequent enhancement at Eureka up to a value of approximately 8 km, after which the magnitude of the peak enhancement begins to decrease again. The simulation with a 5 km injection height for NWT matches the magnitude of the peak CO enhancement of IASI most closely, however, this simulation has only a moderate correlation with the PEARL-FTS measurements of $R = 0.74$ for CO, and $R = 0.70$ for PAN. The strongest correlation between GEOS-Chem and the PEARL-FTS for both CO and PAN is seen with an injection height for the NWT fires of 10 km, with Pearson correlation coefficients of $R = 0.85$ and $R = 0.77$, respectively. Furthermore, the simulation using a 10 km injection height for the NWT fires reproduces the secondary peak observed in the FTIR measurements on 21 August 2017 most effectively. Although an injection height of 10 km for the NWT fires may be higher than in reality, injecting the emissions at a higher altitude such as this may compensate for the slower vertical transport in the troposhere of the GEOS-Chem model which has previously been highlighted by Yu et al. (2018) and Stanevich et al. (2020). For the remainder of the comparisons with observations, we use an injection height of 12.5 km for the BC fires, and 10 km for the NWT fires, and this is referred to as the"modified injection height" simulation.

Fig. 5.5 shows daily-averaged IASI-A and IASI-B measurements re-gridded onto the 2°×2.5° GEOS-Chem model grid in addition to the simulated columns from the modified injection height simulation for CO, PAN, C_2H_4, CH_3OH, and HCOOH on 19 August 2017. The modified injection height simulation appears to capture the shape and spatial distribution of the plume extremely well in comparison to IASI observations. Furthermore, the GEOS-Chem simulation shown in Fig. 5.5 exhibits a similar pattern of the fragmentation of the plume as seen in IASI observations as discussed in Section 5.3.1. GEOS-Chem shows one fragment being transported northwards towards Eureka, and the other (centered around 60° N, 55° W) that was transported eastwards towards Europe. IASI daily means display larger columns than the model in the eastern plume fragment,

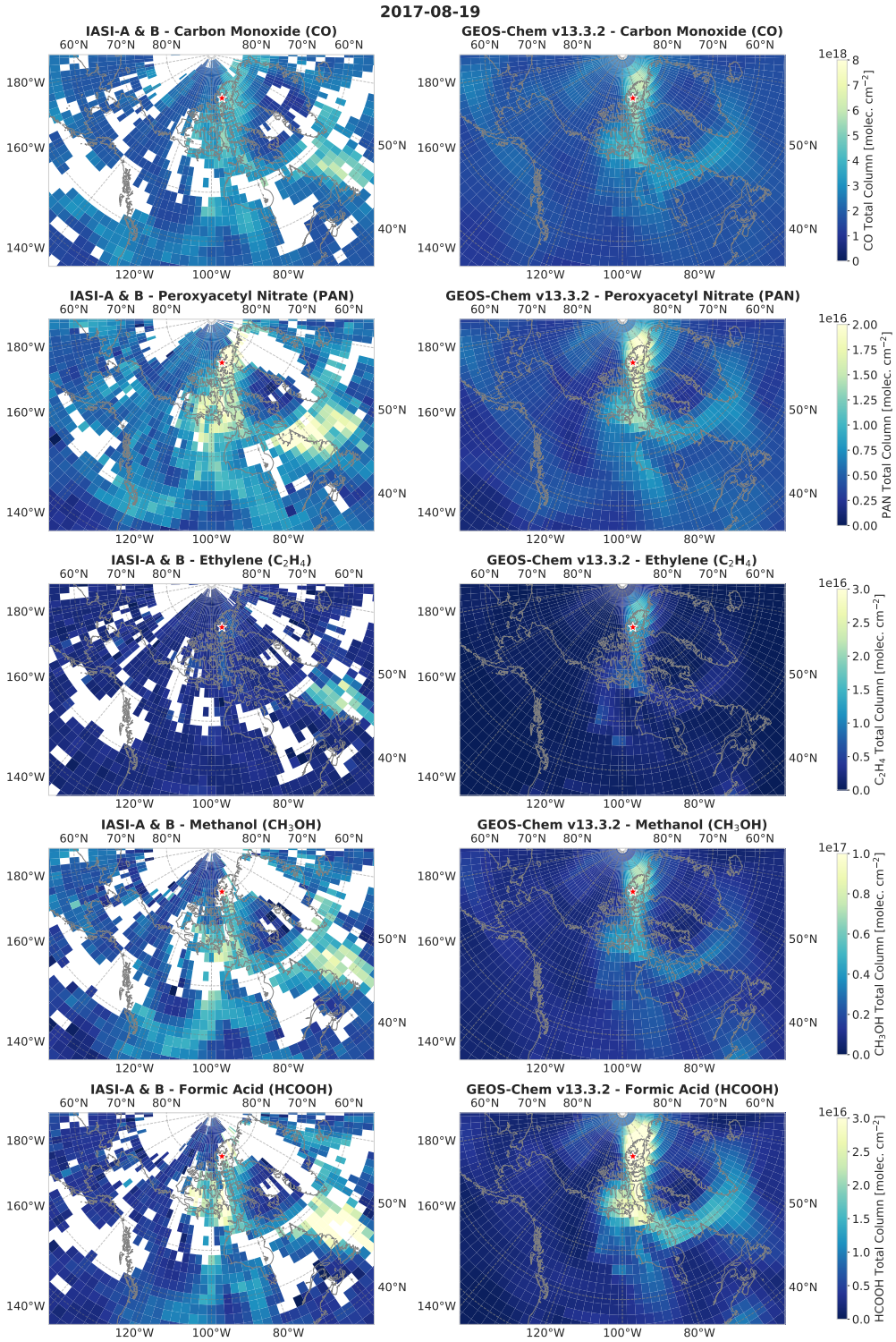

Figure 5.5: (left column) Daily averaged IASI-A and IASI-B total columns of CO, PAN, C_2H_4, CH_3OH, and HCOOH on 19 August 2017 re-gridded to the 2°×2.5° model grid. (Right column) GEOS-Chem total columns of CO, PAN, C_2H_4, CH_3OH, and HCOOH on 19 August 2017 taken from the simulation with modified injection heights for the BC and NWT fires. The location of Eureka is shown by a red star.

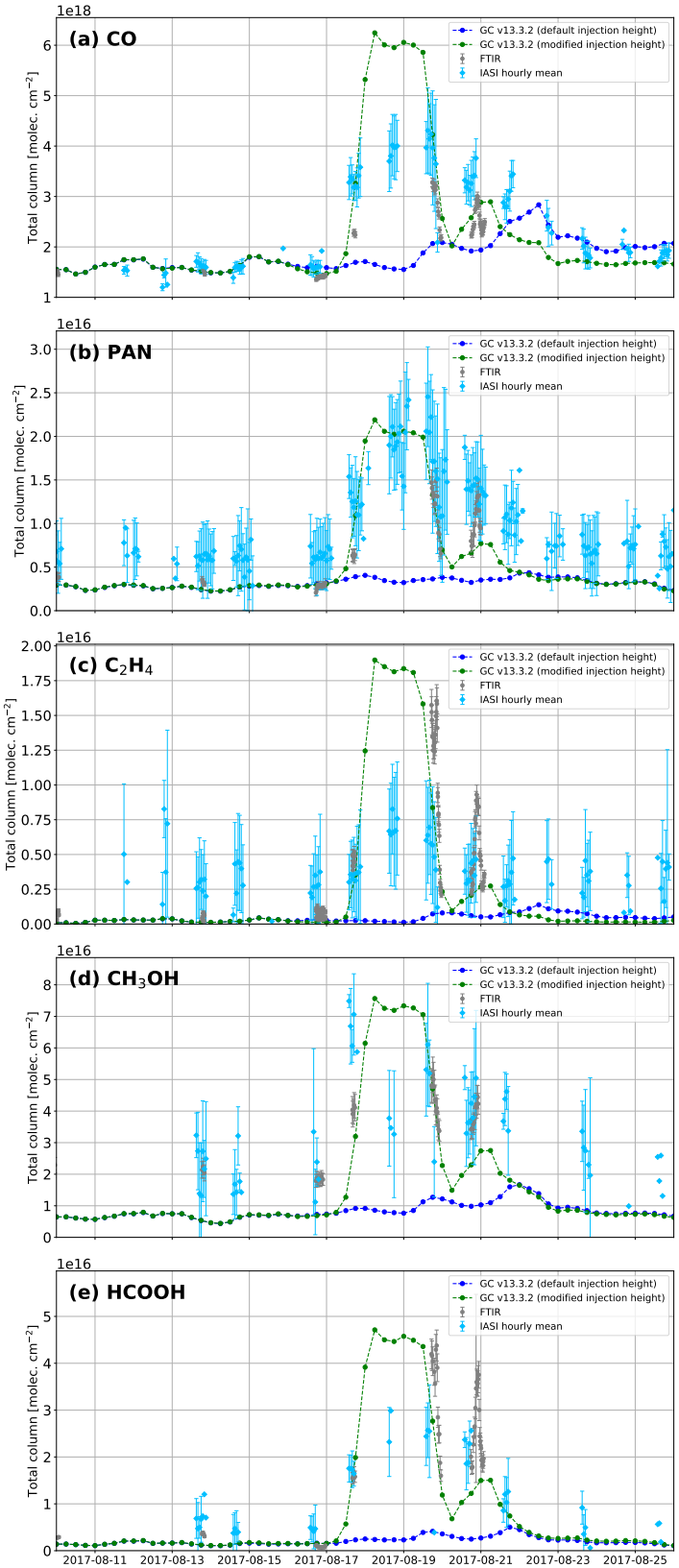

Figure 5.6: Time-series of un-smoothed GEOS-Chem columns of **(a)** CO, **(b)** PAN, **(c)** C_2H_4, **(d)** CH_3OH, and **(e)** HCOOH for the baseline simulation (blue), and the modified injection height simulation (green). PEARL-FTS measurements are shown in grey, and IASI-A and IASI-B hourly averages within 150 km of Eureka are shown in cyan.

which may be a result of numerical diffusion of the plume that has previously been identified as a source of transport errors at coarser horizontal resolutions in the GEOS-Chem model, particularly in the free troposphere (Eastham and Jacob, 2017). The magnitude of the columns in the northern fragment of the plume in GEOS-Chem is in closer agreement with IASI observations, particularly for PAN and CH_3OH. Some differences in the total columns are seen for CO, HCOOH, and C_2H_4, which are overall smaller in the IASI observations than in GEOS-Chem, however this may also be impacted by the lower density of IASI measurements at these high latitudes. Despite this, the GEOS-Chem simulation with the modified injection heights successfully reproduces the spatial and temporal pattern of the plume that is observed by IASI.

The time-series for each species of GEOS-Chem simulated columns, as well as PEARL-FTS measurements and IASI observations near Eureka are shown in Fig. 5.6. In the vicinity of Eureka, IASI and GEOS-Chem display comparable PAN total columns, but for all other species, IASI observes smaller total columns than are predicted by GEOS-Chem, particularly during the peak enhancement on 18–19 August 2017. The largest measurement-model difference is seen for C_2H_4, of which only a very small enhancement is seen by IASI near Eureka on 19 August 2017. The observed differences between IASI and the model are likely again related to the reduced sensitivity of the IASI instrument and retrievals over high-latitude regions such as the Arctic. In comparison to the PEARL-FTS, the GEOS-Chem columns of all species in the baseline simulation are severely underestimated relative to the ground-based measurements, and this simulation fails to capture the temporal pattern of the enhancement. In contrast, the simulated total columns of all species in the modified injection height simulation broadly agree with the magnitude of the columns observed by the PEARL-FTS on 19 August 2017, the day following peak enhancement observed by IASI. Since no FTIR measurements were taken on 18 August 2017, we lack a third point of comparison, and it is difficult to assess whether the magnitude of the enhancement on that day is being simulated accurately.

More specifically, the GEOS-Chem CO columns on 18 August are approximately 2×10^{18} molec cm^{-2} ($\sim$+50%) larger than the IASI daily mean, and approximately 4×10^{18} molec cm^{-2} ($\sim$+100%) larger than those measured with the PEARL-FTS on the following day. Between 19 and 21 August 2017, there is general agreement across the PEARL-FTS and IASI observations, and the simulated GEOS-Chem CO columns. GEOS-Chem PAN columns agree well with the PEARL-FTS measurements on 19 August, but are biased low relative to the ground-based measurements on 20 and 21 August. A similar pattern to that for PAN between GEOS-Chem and the PEARL-FTS is seen for C_2H_4, CH_3OH, and HCOOH, which are all biased low in the model on 20 and 21 August. The general agreement between the GEOS-Chem simulated columns and the PEARL-FTS measurements

near the peak enhancement on 19 August suggests that the large retrieved columns from the FTIR (particularly for C_2H_4 and HCOOH) are not unrealistic.

Lastly, we investigated the vertical localization of the GEOS-Chem simulated biomass burning plumes in the vicinity of Eureka in the modified injection height simulation. A plot of daily mean un-smoothed GEOS-Chem CO VMR and partial column profiles during the fire period of 17 to 23 August 2017 are provided as Fig. A.9 in the appendix, along with the mean FTIR profiles in the same period. A clear peak representing the biomass burning plume can be seen in the GEOS-Chem CO profiles on 17 and 18 August in the range of 4–6 km, broadly agreeing with location of the peak in the mean retrieved FTIR CO profiles. A study of the 2017 smoke plumes using a ground-based lidar at Eureka and the Navy Aerosol Analysis and Prediction System (NAAPS) model by Ranjbar et al. (2019) found that the BC and NWT plumes were vertically distinct, and that the BC plume was located at an altitude of approximately 7 km above PEARL, while the smoke from the NWT fires was located at an approximate altitude of 4 km. While the model profiles show some layering, the FTIR measurements are not able to vertically resolve the two distinct biomass burning plumes in the profiles, resulting in a single wide peak in the FTIR CO profiles at Eureka. However, the general altitude of the plume is consistent across the PEARL-FTS and GEOS-Chem profiles in this work, and the findings of Ranjbar et al. (2019).

Estimating Secondary VOC Production

To determine whether the values of our derived emission ratios and emission factors for CH_3OH and HCOOH are being influenced by secondary production of these species as the plume was transported, we use GEOS-Chem to obtain an estimate of the fraction of the total columns observed at Eureka that are a result of secondary in-plume production. To accomplish this, we performed a set of independent simulations with the GFAS emissions of each species switched off. We then compared the simulated columns on 18 and 19 August 2017, the days of the peak observed enhancement, with the simulations with the GFAS fire emissions switched on. To negate any influence from ambient column abundances of each species, we calculated the mean pre-fire total columns in the period of 1–15 August 2017, and then subtracted this from the fire-affected total columns of each simulation.

The time series of these simulations is shown in Fig. 5.7. For both CH_3OH and HCOOH, the simulations without direct fire emissions lead to a significant decrease in the resulting columns at Eureka on 18 and 19 August. For CH_3OH, there is a very small enhancement, and the mean peak columns in the no-emission simulation are approximately 3% of the those in the simulation with direct fire emissions, suggesting a very small in-plume secondary production component. This indicates that

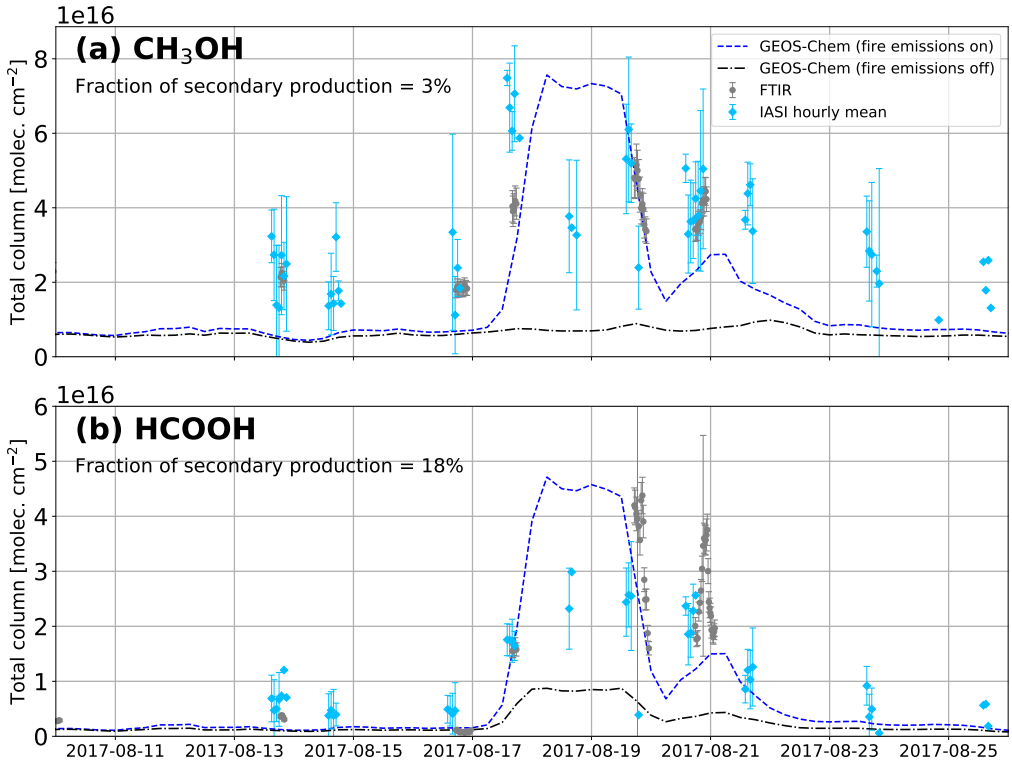

Figure 5.7: Time-series of un-smoothed GEOS-Chem columns of **(a)** CH_3OH, and **(b)** HCOOH for the modified injection height simulation (blue dashed line), and simulations where direct GFAS fire emissions of each species were turned off (black dashed line). The fraction of secondary production was determined as the mean relative difference (i.e., $100 \times \frac{x_{\text{on}} - x_{\text{off}}}{x_{\text{on}}}$) between the two simulations during the peak enhancement on 18 and 19 August, after correcting for the background pre-fire column abundances.

the derived emission ratio and emission factor for CH_3OH is likely not overestimated due to secondary production. For HCOOH in the no-emissions scenario, there is still a notable enhancement at Eureka that is approximately 18% of the peak columns in the original simulation, indicating that there is a non-negligible secondary in-plume production component in the resulting enhancement at Eureka. This finding is consistent with a recent study by Chen et al. (2021) who used airborne measurements from the ATom missions and GEOS-Chem to highlight a significant secondary production component of HCOOH in aged biomass burning plumes, leading to CO:HCOOH enhancement ratios that broadly increase with plume age. It should be noted, however, that due to the effects of numerical diffusion on transported plumes in global Eulerian models (Eastham and Jacob, 2017) and the fact that precursor species within these plumes are diluted over the model grid-boxes, these estimates of secondary production should likely be viewed as a lower limit. In addition, missing chemical pathways in the model could contribute to discrepancies in the model simulation. Reducing the HCOOH emission factors from the PEARL-FTS and IASI by 18% to account for this secondary production, we arrive

at values of 11.69 g ± 4.78 g kg^{-1} and 4.56 ± 2.06 g kg^{-1}, respectively. These corrected emission factors are still significantly larger than the values provided in all previous studies, suggesting that the emissions of HCOOH from the NWT and BC fires were much larger than previously reported.

5.4 Conclusions

The August 2017 BC and NWT wildfires led to the largest observed short-term perturbations in the budgets of CO, PAN, C_2H_4, and HCOOH in the 2006–2020 time-series of measurements by the PEARL-FTS at Eureka. In general, IASI observed a similar temporal pattern in the enhancements but smaller columns of most species in comparison to the PEARL-FTS, which can likely be attributed to the reduced sensitivity of the IASI retrievals at high latitudes as a result of low thermal contrast in the region. We have derived enhancement and emission ratios, as well as emission factors for all species relative to CO from both PEARL-FTS and IASI measurements. The derived emission factors for PAN and CH_3OH are in good agreement between the PEARL-FTS, IASI, and previous studies, while those for C_2H_4 and HCOOH, particularly those from the PEARL-FTS, are significantly larger than previously reported in the literature.

The GEOS-Chem CTM was used to simulate the transport of the wildfire plumes and the subsequent enhancements of each species at Eureka. Using the default biomass burning injection scheme of GFAS in the model produces a severe transport error leading to unrealistically small enhancements, and poor correlations with PEARL-FTS and IASI measurements in the vicinity of Eureka. By modifying the injection height scheme, and injecting the emissions directly at higher model levels, GEOS-Chem reproduces the transport and the observed enhancements much more accurately. Using CO and PAN as tracer species for the fire plumes, we performed model sensitivity tests to determine the appropriate injection heights for the fires, finding that injection heights of 12.5 km for the BC fires, based on Peterson et al. (2018) and Fromm et al. (2021), and 10 km for the NWT fires, produced the strongest correlations with ground-based FTIR observations at Eureka for CO and PAN. Lastly, we used GEOS-Chem to approximate the portions of the observed total columns at Eureka which resulted from secondary in-plume production. It was found that for CH_3OH, there was minimal secondary production (approximately 3% of the observed total columns). However, for HCOOH, secondary production was a more significant component (approximately 18%) of the peak observed columns at Eureka. After applying a correction to the calculated HCOOH emission factors from the PEARL-FTS and IASI, there is still a significant discrepancy with the values previously reported in the literature, which suggests unusually large HCOOH emissions from the August 2017

fires.

In general, the August 2017 wildfires were a major biomass burning event, one that demonstrates how resulting biomass burning plumes can lead to significant transient perturbations far above baseline concentrations of short-lived VOCs in the high Arctic. It is expected that as wildfires increase in frequency and severity due to anthropogenic climate change, events such as these will continue to occur and may grow in magnitude and scale. Biomass burning is expected to become an increasingly large component of the budgets and annual cycles of reactive VOCs at high latitudes; the climatic and environmental impacts of these VOCs on the highly sensitive Arctic region thus deserve further investigation.

Chapter 6

Long-term Trends in Arctic Tropospheric Pollutants

6.1 Introduction

In this chapter, we investigate the observed seasonal variability and long-term trends of CO, C_2H_2, C_2H_4, C_2H_6, CH_3OH, HCOOH, H_2CO, and PAN in the total column time-series of two North American high-Arctic FTIR sites; PEARL at Eureka, Nunavut (2006–2020), and PSB in Thule, Greenland (1999–2022). Additionally, we perform a long-term simulation using the GEOS-Chem High Performance (GCHP) CTM which covers the period of 2003–2021. We examine the modeled seasonal and inter-annual variability in these eight tropospheric trace gas species, and evaluate the performance of the model against the ground-based FTIR observations at the two high-Arctic sites. A manuscript on this work is being prepared for submission to *Journal of Geophysical Research: Atmospheres*.

6.2 Methods

6.2.1 Ground-Based FTIR Measurements

FTIR Sites

In this study, measurements from two high-Arctic ground-based FTIRs were used. The first instrument is located at PEARL at Eureka, Nunavut (80.05° N, 86.42° W, 610m a.s.l) on Ellesmere

Island in the Canadian Arctic. The instrument is a Bruker IFS 125HR FTIR spectrometer, and was installed at PEARL in July 2006. Measurements are made during sunlit clear-sky conditions using a custom-built heliostat. At present, the time-series of PEARL-FTS measurements extends from August 2006 until March 2020, when the COVID-19 pandemic halted nominal operations. A detailed description of the PEARL-FTS is provided in Sect. 2.3.

The second ground-based instrument is located at PSB in Thule, Greenland (76.53° N, 68.74° W, 225m a.s.l.). A Bruker IFS 120M FTIR was installed at PSB in mid 1999, with measurements beginning in Fall 1999. The Thule FTIR is also equipped with a computer-controlled heliostat, and an automated liquid nitrogen fill-system to cool the detectors, allowing the instrument to be operated semi-autonomously. In 2015, the Bruker IFS 120M was replaced by a Bruker IFS 125HR, and an improved heliostat system was also installed. The time-series of Thule FTIR measurements covers the period of October 1999 to October 2022, although some trace-gas species are not retrieved over the full time-series. A detailed description of the Thule FTIR and the semi-autonomous measurement station is provided in Hannigan et al. (2009).

Measurements at both Eureka and Thule are made in the mid-infrared at a spectral resolution of 0.0035 cm^{-1} using a KBr beamsplitter that covers the spectral range of 700–5000 cm^{-1}, a series of optical filters, and two photovoltaic detectors; an InSb detector (1850–10,000 cm^{-1}), and a HgCdTe detector (600–6000 cm^{-1}). Trace gas profiles and total column concentrations are retrieved from the measured spectra, and the data are regularly contributed to NDACC. In the following subsection, we describe the retrieval methods for estimating the trace-gas column concentrations from the measured solar-absorption spectra.

FTIR Retrieval Methods

The FTIR retrieval methods are described in detail in Chapter 2 and Chapter 3, however we briefly re-summarize the methodology here. The measured solar-absorption spectra from the Eureka and Thule FTIRs are processed using the SFIT4 retrieval algorithm (`https://wiki.ucar.edu/display/sfit4/`) that is based upon the OEM described in Rodgers (2000). The trace gas VMR profiles are iteratively adjusted until the difference between the calculated and measured solar-absorption spectra is minimized. The SFIT4 forward model is a line-by-line radiative transfer model that assumes a Voigt line shape profile and encompasses multiple atmospheric layers spanning the altitude of the instrument to 120 km above the surface (Notholt et al., 2006).

For the retrievals of C_2H_2, C_2H_6, CH_3OH, and HCOOH, spectroscopic parameters from the HITRAN 2008 line list database (Rothman et al., 2009) are used for the target gas and all interfering

species. In the retrieval of PAN, pseudo-lines generated by G. C. Toon (Jet Propulsion Laboratory, California Institute of Technology, Pasadena, CA; available from https://mark4sun.jpl.nasa.gov/pseudo.html) are used for the spectral features of PAN, while H_2O lines from the HITRAN 2016 line list database Gordon et al. (2017) were used based on the recommendations in Mahieu et al. (2021), and HITRAN 2008 was used for all other interfering species. For the retrieval of CO, the ATM12 linelist is used for the CO spectroscopy, while HITRAN 2008 is used for all interfering species. For the retrieval of H_2CO, the ATM16 line list is used (Toon et al., 2016), while in the retrieval of C_2H_4, the more recent ATM20 line list is used (Toon, 2022). In these retrievals, pseudo-linelists were used to supplement the spectroscopic databases in the case of any unresolved interfering features, namely those of CCl_4, $ClONO_2$, CCl_2F_2, $CHClF_2$, CHF_3, and CCl_2FCClF_2. Additionally, atmospheric temperature and pressure profiles are daily averages provided by NCEP, and the *a priori* profiles of each species are taken from a 40-year average (1980-2020) of a WACCM version 4 simulation (Marsh et al., 2013).

The SFIT4 spectral microwindows, the interfering trace-gas species, and the corresponding references for each of the retrievals are provided in Table 3.1. CO and C_2H_6 are standard NDACC products, and are retrieved using specified NDACC-IRWG recommendations and harmonized spectral microwindows (i.e., the same microwindows and retrieval approach are used for all sites in the network). C_2H_2, C_2H_4, CH_3OH, H_2CO, HCOOH, and PAN are non-standard species, meaning that not all NDACC sites retrieve these products, however, these species are processed and retrieved in a similar manner as the standard products. For detailed descriptions of each retrieval, refer to Chapter 3.

For all retrievals, a full error analysis is performed following Rodgers (2000) and which is described in depth in Sect. 3.9. The total error budgets include contributions from forward model parameter errors, spectroscopic uncertainties, and measurement errors. The mean random and systematic uncertainties, as well as the DOFS for the Eureka and Thule FTIR retrievals are summarized in Table 6.1. The mean VMR averaging kernels for Eureka are provided in Fig. 3.1, while the mean Eureka total column averaging kernels and the retrieval sensitivity are shown in Fig. 3.2. The mean VMR averaging kernels for Thule are provided in the appendix as Fig. B.1, and the mean total column averaging kernels and retrieval sensitivity for Thule are plotted in Fig. B.2. All of the trace gas retrievals display good vertical sensitivity throughout the troposphere, while CO and H_2CO display additional sensitivity to the mid- and lower-stratosphere. All retrievals have a DOFS of 1 or greater indicating that total column concentrations can be retrieved, while the retrieval of CO displays a higher DOFS of 2–3 on average, meaning that there is sufficient vertical information to

Table 6.1: Mean retrieval uncertainties and DOFS of the Eureka and Thule FTIR retrievals.

Species	Random uncertainty	Systematic uncertainty	DOFS
CO	1%	3%	2–3
C_2H_2	5%	1%	1–1.5
C_2H_4	50%	25%	1
C_2H_6	2.5%	6%	1.5–2
CH_3OH	4.5%	12%	1
H_2CO	10%	13%	1–1.5
HCOOH	3%	9%	1
PAN	20%	10%	1

derive partial columns from the retrievals.

6.2.2 GEOS-Chem Chemical Transport Model

The GCHP CTM (Eastham et al., 2018; Martin et al., 2022), version 14.1.1 was used in this study. GCHP is a new and highly parallelizable version of the GEOS-Chem model, allowing simulations to be completed in a much shorter duration when utilizing a high number of CPU cores. GCHP uses a equidistant gnomonic cubed-sphere grid, a type of map projection where all great-circles are straight lines, which differs from the standard rectilinear latitude-longitude grid used in GEOS-Chem Classic. The equidistant gnomonic projection divides each cube edge into N equally sized segments that are connected with the opposite cube edge by great circle arcs to generate a mesh grid (Eastham et al., 2018). As a result, the model grid resolution in GCHP is referred to as CN, where a C48 grid will have 48×48 grid cells on each of the six cube faces, and the mean spatial resolution is approximated by $10000/N$ km (Eastham et al., 2018).

The model simulation in this work was performed at a horizontal resolution of C48 (∼2° × 2.5°), with 72 vertical layers from the surface to 0.01 hPa (approximately 80 km). The simulation is driven by assimilated meteorological fields from MERRA-2 provided by GMAO at the NASA Goddard Space Flight Center. The simulation covers the period of 1 January 2003 to 31 December 2021, with a 2-hourly output frequency. A model spin-up was performed for the full year of 2002 to provide the initial conditions for the simulation. Based on the recommendations provided in Philip et al. (2016), model transport and chemical operator time steps of 10 and 20 minutes, respectively, were selected to minimize simulation errors.

The emissions in the model are configured at run-time using HEMCO (Lin et al., 2021), taking into account various inventories. All emission fields are re-gridded by HEMCO from their native resolutions to the C48 cubed-sphere grid. Global anthropogenic emissions for the period of 1980–2019 are provided by CEDSv2, a comprehensive bottom-up inventory developed for use in Earth system

models that utilizes regional and country-specific inventories to scale base emissions to produce trends over recent decades while maintaining a consistent methodology (Hoesly et al., 2018). These regional and country-scale inventories include the US EPA National Emissions Inventory (NEI) for the United States, the European Monitoring and Evaluation Programme inventory (EMEP) for Europe, and the Emissions Database for Global Atmospheric Research (EDGAR) for countries where national inventories are not available (Hoesly et al., 2018). For the years in the simulation which extend beyond the end of the CEDSv2 inventory (i.e., 2020 and 2021), the 2019 emissions are applied. In the case of C_2H_6, in the default configuration of the model anthropogenic emissions are sourced from the emissions inventory of Tzompa-Sosa et al. (2017) instead of CEDSv2, as other anthropogenic inventories were found to underestimate C_2H_6 emissions by approximately 40%. Additionally, biogenic emissions in the model are sourced from MEGAN version 2.1 (Guenther et al., 2012), and biomass burning emissions are provided by GFAS version 1.2 (Kaiser et al., 2012). The GFASv1.2 inventory provides global fire emissions at a 3-hourly frequency on a $0.1^\circ \times 0.1^\circ$ grid for the period of 2003–2021. The GFASv1.2 inventory was selected over the default Global Fire Emissions Database, version 4.1 inventory (GFEDv4.1; Van Der Werf et al., 2017) as it was found that northern mid- and high-latitude fires were better represented by GFAS when compared against satellite observations as discussed in Sect. 5.2.3.

Emissions of C_2H_2 and HCOOH are absent from the current version of the GFAS inventory, so to approximate the emissions of these species we follow the approach described in Sect. 5.2.3 and calculate the ERs relative to CO (in molar units) using values from Andreae (2019) for various biomass types (i.e., boreal forests, temperate forests, tropical forests, and grasslands). The GFEDv4.1 basis region map (shown in Fig. B.3 in the appendix) was then used to allocate and apply the emissions globally in the model by scaling the existing GFAS CO emissions fields by the pre-determined molar ERs in each region via the HEMCO module. An example of the resulting mean monthly HCOOH emission flux and a map of the scaling ratios for August 2017 are shown in Fig. B.4 in the appendix. It should be noted that the GFEDv4.1 inventory was used for the biomass burning emissions during the model spin-up year of 2002, since the earliest year available for the GFASv1.2 inventory is 2003.

6.2.3 Trend Analysis

The Eureka and Thule ground-based FTIR time-series span 14 years (2006–2020) and 23 years (1999–2022), respectively, allowing long-term trends to be assessed. Since the time-series of each trace-gas species contains both intra-annual variability (seasonal cycles) and inter-annual variability

(long-term trends), we apply Fourier series fitting of multiple orders to daily means of the total column time-series data from the two Arctic FTIRs, and the simulated total columns from GCHP following the method of Gardiner et al. (2008) and Friedrich et al. (2020). We apply a least-squares fit to the data with a function F of the form (Gardiner et al., 2008):

$$F(t, a, \boldsymbol{b}) = at + V(t, \boldsymbol{b}), \tag{6.1}$$

where a is the annual trend in the data, t is the time measured in years, and $V(t, \boldsymbol{b})$ is the Fourier series component that is given by:

$$V(t, \boldsymbol{b}) = b_0 + b_1 \cos 2\pi t + b_2 \sin 2\pi t + b_3 \cos 4\pi t + b_4 \sin 4\pi t + ..., \tag{6.2}$$

where b_0 to b_n are the Fourier series parameters contained in the vector $\boldsymbol{b}$. Fourier series models of this type allow for the underlying periodicity of the data to be captured while also reducing the impact of sparse data. This method also allows for regular gaps in the data, such as during the polar night, to be accounted for without causing a discontinuity in the intra-annual fit function (Gardiner et al., 2008). In this study, a Fourier series of order 3 was used for all fits, with the exception of CH_3OH at Eureka where a Fourier series of order 2 was used because an appropriate fit to the FTIR data could not be established with order 3 as a result of the sparser nature of the data set and prominent data gap between 2012–2013. To derive the confidence intervals for the fitted trends, we apply bootstrap resampling with $Q = 5000$ (the number of bootstrapping ensemble members). Bootstrap resampling allows for a statistically robust treatment of non-normally distributed datasets, and this approach has been widely used to evaluate the confidence intervals of trends derived from FTIR measurements (Franco et al., 2016a; Friedrich et al., 2020; Gatz and Smith, 1995; Gardiner et al., 2008; Yamanouchi et al., 2021).

Since the FTIR and GEOS-Chem total column time-series contain transient events such as biomass burning enhancements, we identify these events using Fourier fitting following Lutsch et al. (2020) and Zellweger et al. (2009). The fitted Fourier series function is first subtracted from the data to obtain the residuals, and then assuming a normal distribution of the residuals about zero, the negative residuals are mirrored into positive values (by taking the absolute value). A cutoff threshold of 2σ is then applied to the data based on the standard deviation of the absolute residuals, and another Fourier series fit is performed with the identified enhancements removed. The trend analysis was performed twice; first on the full data set, and then on time-series with the enhance-

ments removed. The trends derived from the "enhancement-removed" Fourier fit are likely more representative of the true long-term variability in the background concentrations of each trace-gas species, however, comparing the differences between the Fourier fits (i.e., with and without enhancements) may highlight how significantly each time-series is impacted by wildfires and other transient events.

6.3 Results and Discussion

6.3.1 FTIR-derived Seasonal Cycles

In this section, we evaluate the seasonal cycles of CO, C_2H_2, C_2H_4, C_2H_6, CH_3OH, HCOOH, H_2CO, and PAN derived from the ground-based FTIR measurements at Eureka and Thule. The retrieved total column time-series of these eight tropospheric species and the corresponding monthly means calculated across all years are shown for Eureka and Thule in Fig. 6.1 and Fig. 6.2, respectively.

CO

The seasonal cycle of CO is shown for Eureka in Fig. 6.1a, and for Thule in Fig. 6.2a. CO displays a strong seasonal cycle that is consistent at both Arctic sites, with the largest mean CO columns observed during the late winter and early spring (February to April), and a minimum during the summer in July. The mean maximum total columns are approximately 2.0×10^{18} molec. cm^{-2} and 2.1×10^{18} molec. cm^{-2}, while the mean minimum total columns are around 1.5×10^{18} molec. cm^{-2} and 1.6×10^{18} molec. cm^{-2} at Eureka and Thule, respectively. The primary sources of CO are fossil fuel combustion and the oxidation of VOCs and CH_4, which is transported to the Arctic from mid-latitude sources, with biomass burning being a significant periodic source during the late summer months (Holloway et al., 2000; Lutsch et al., 2020; Yurganov, 1997). CO is primarily removed from the atmosphere through oxidation by OH, which consumes OH and yields CO_2, making CO an indirect greenhouse gas. During polar night, no OH is present in the Arctic troposphere and the atmospheric lifetime of CO can be on the order of several months (Holloway et al., 2000). As a consequence, transported mid-latitude CO tends to accumulate in high concentrations, resulting in the peak in the observed total columns in the late winter and early spring months (Holloway et al., 2000; Stohl, 2006). As polar night ends and sunlight gradually returns to the high Arctic, the observed CO total columns rapidly decrease, leading to a minimum in July. Periodic enhancements in the CO total columns can be seen in August at both Eureka and Thule, resulting from the

influence of transported biomass burning plumes.

C_2H_2

The total column time-series and monthly means for C_2H_2 are shown for Eureka and Thule in Figs. 6.1b and 6.2b, respectively. C_2H_2 presents a very similar seasonal cycle to CO at both Eureka and Thule, with a maxima in the observed total columns in February and March, and a minima in the total columns during June. The mean maximum columns are approximately 4.5×10^{15} molec. cm^{-2} at both sites, while the mean minimum total columns are 2.5×10^{15} molec. cm^{-2} and 1.8×10^{15} molec. cm^{-2} at Eureka and Thule, respectively. C_2H_2 is primarily emitted from biofuel and fossil fuel combustion, and is co-emitted with CO in many cases. Biomass burning is also a notable source of C_2H_2 to the high Arctic, which is clearly seen at both sites during August in Figs. 6.1b and 6.2b (Viatte et al., 2014, 2015). Like CO, the primary atmospheric sink of C_2H_2 is oxidation by OH, which is a crucial driver of its strong seasonality at high latitudes. As a result, C_2H_2 is strongly correlated with CO in the atmosphere as they share very similar sources and sinks which is evidenced in the seasonal cycles at both Arctic sites (Duflot et al., 2015; Xiao et al., 2007).

C_2H_4

The C_2H_4 time-series and monthly means are plotted for Eureka and Thule in Fig. 6.1c and 6.2c, respectively. The observed C_2H_4 total columns at Eureka and Thule do not vary significantly over the course of the year, with mean columns over all months of 6.2×10^{14} molec. cm^{-2} and 1.2×10^{15} molec. cm^{-2}, respectively. C_2H_4 is one of the most abundant atmospheric unsaturated hydrocarbons in the global atmosphere, with annual emissions on the order of 20 Tg, half of which is estimated to be the product of biomass burning (Folberth et al., 2006; Herbin et al., 2009; Horowitz et al., 2003). The atmospheric lifetime of C_2H_4 is short, at approximately 1 to 3 days due to its high reactivity with OH and O_3. C_2H_4 is directly emitted from anthropogenic sources such as motor vehicle exhaust and petrochemical production, waste burning, and natural sources including direct emissions from plants and soils, and forest fires (Folberth et al., 2006; Morgott, 2015; Sawada and Totsuka, 1986). C_2H_4 is only emitted directly, and there are currently no known secondary production pathways of C_2H_4 in the atmosphere. In the high Arctic, there are very few known local sources of C_2H_4, and the extremely short lifetime of 1–3 days broadly inhibits long-range transport from mid-latitude anthropogenic sources. As a result, there is no discernible seasonal cycle in the high Arctic. As discussed in Chapter 5, competition for reactants within transported biomass burning plumes can significantly extend the lifetime of C_2H_4, leading to large observed enhancements in the

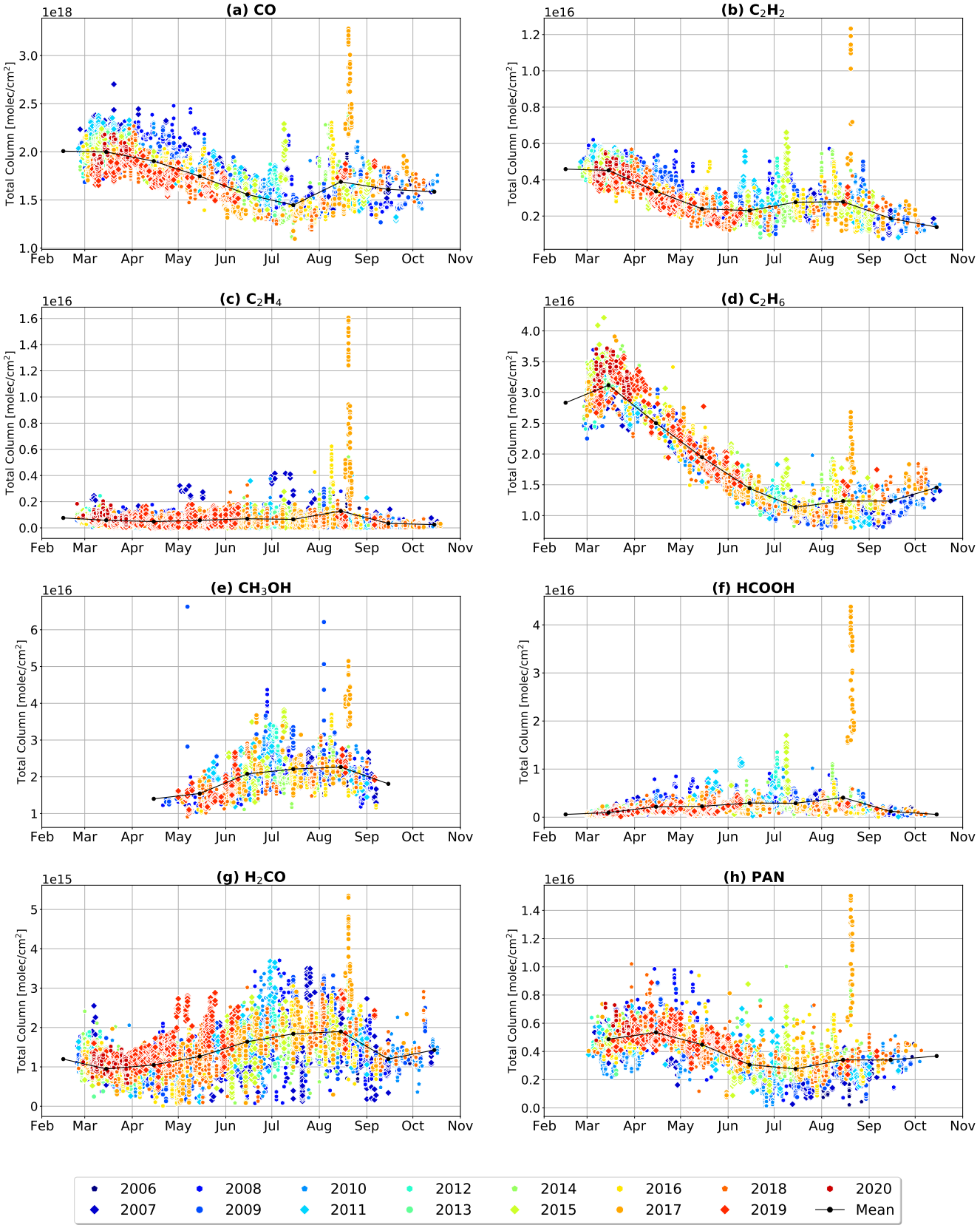

Figure 6.1: Total column time series of **(a)** CO, **(b)** C_2H_2, **(c)** C_2H_4, **(d)** C_2H_6, **(e)** CH_3OH, **(f)** HCOOH, **(g)** H_2CO, and **(h)** PAN retrieved from PEARL-FTS measurements at Eureka for the period of 2006–2020. Measurements from each year are plotted in differing colors and marker styles to better highlight enhancements and anomalies. The monthly means across all years are denoted by the black line.

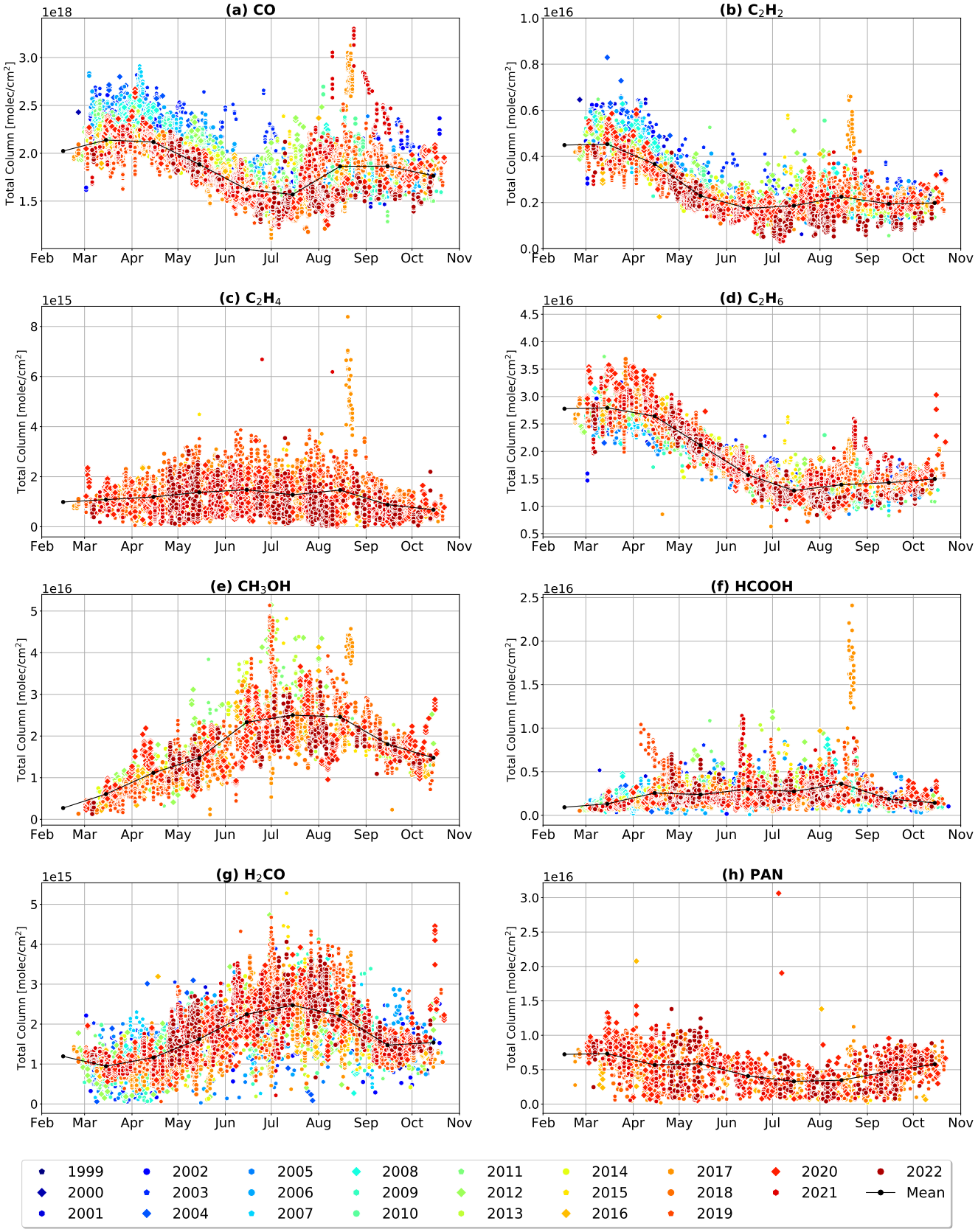

Figure 6.2: Total column time series of **(a)** CO, **(b)** C_2H_2, **(c)** C_2H_4, **(d)** C_2H_6, **(e)** CH_3OH, **(f)** HCOOH, **(g)** H_2CO, and **(h)** PAN retrieved from the Bruker 120M (1999–2015) and Bruker 125HR (2015–2022) measurements at Thule. Measurements from each year are plotted in differing colors and marker styles to better highlight enhancements and anomalies. The monthly means across all years are denoted by the black line.

total columns relative to ambient levels at the high Arctic FTIR sites as a result of these wildfire emissions. Consequentially, biomass burning appears to be the most significant source of C_2H_4 at Eureka and Thule.

C_2H_6

The seasonal cycle and monthly means of C_2H_6 are plotted for Eureka and Thule in Figs. 6.1d and 6.2d, respectively. C_2H_6 displays a strong seasonal cycle at both sites akin to that of CO and C_2H_2, with the largest observed total columns in February and March, and the smallest columns in July. The mean maximum columns are 3.1×10^{16} molec. cm^{-2} and 2.8×10^{16} molec. cm^{-2}, while the mean minimum total columns are 1.1×10^{16} molec. cm^{-2} and 1.3×10^{16} molec. cm^{-2} at Eureka and Thule, respectively. C_2H_6 is the most abundant NMHC in the atmosphere, and is an important precursor to tropospheric ozone and PAN through its oxidation in the presence of NO_x in polluted airmasses (Fischer et al., 2014; Franco et al., 2016a). C_2H_6 also acts as an indirect greenhouse gas through its influence on the global lifetime of CH_4 as a result of its removal from the atmosphere by OH. In contrast to CO and C_2H_2, C_2H_6 differs in that it is primarily emitted from the various stages of natural gas production and distribution as opposed to the direct combustion of fossil fuels (Franco et al., 2016a; Friedrich et al., 2020; Xiao et al., 2008). The main sources of C_2H_6 to the high Arctic are biomass burning and transported mid-latitude pollution, and it is primarily removed from the Arctic troposphere through oxidation by OH which strongly modulates the observed seasonal cycles at Eureka and Thule.

CH_3OH

The total column time-series and the corresponding monthly means of CH_3OH calculated across all years are shown in Fig. 6.1e and Fig. 6.2e for Eureka and Thule, respectively. CH_3OH displays a clear seasonal cycle at Eureka and Thule, with the smallest total columns in the spring and fall months, and the largest observed columns in the summertime between June and August. The mean maximum columns are 2.3×10^{16} molec. cm^{-2} and 2.5×10^{16} molec. cm^{-2}, and the mean minimum columns are 1.4×10^{16} and 2.7×10^{15} molec. cm^{-2} at Eureka and Thule, respectively. It should be noted that CH_3OH measurements at Thule extend earlier into the year than at Eureka, with measurements available beginning in February at Thule and April at Eureka. Retrievals during the early year often fail to converge at Eureka due to the low abundance of CH_3OH and strong interference from O_3 in the early spring. The mean columns in April at Thule are approximately 1.1×10^{16} molec. cm^{-2}, which is broadly consistent with the mean minimum columns at Eureka.

CH_3OH is the second-most abundant organic gas (after CH_4) found in the global remote atmosphere (Stavrakou et al., 2011). It is primarily emitted biogenically from plants during their growth stage (and to a lesser extent when they decay), however, it is also emitted from biomass burning (Fall and Benson, 1996; Holzinger et al., 1999; MacDonald and Fall, 1993; Wells et al., 2014). The oceans can also serve as a source of CH_3OH, however, globally they are thought to represent a small net sink (Bates et al., 2021). Through its oxidation, CH_3OH influences global OH concentrations, producing the hydroperoxyl radical (HO_2) and H_2CO, and it can influence the budget of tropospheric O_3 (Folberth et al., 2006; Tie et al., 2003). As a result, the seasonal cycle at both Eureka and Thule is largely correlated with the growth cycle of plants and vegetation, leading to the highest observed columns during the summer months, and lower columns during the early spring and fall. Biomass burning enhancements are visible in the time-series at Eureka and Thule in Figs. 6.1e and Fig. 6.2e, however, these enhancements tend to be more moderate than for some of the other biomass burning tracer species such as CO, C_2H_2, and C_2H_4.

HCOOH

The seasonal cycle and monthly means of HCOOH are shown in Fig. 6.1f and Fig. 6.2f for Eureka and Thule, respectively. HCOOH displays a similar seasonal cycle as CH_3OH albeit less pronounced at the two Arctic sites, with smaller total columns seen in the spring and fall, and larger columns on average during the summer. The mean maximum columns across all years at Eureka and Thule are 4.1×10^{15} molec. cm^{-2} and 3.6×10^{15} molec. cm^{-2}, and the mean minimum columns are 5.6×10^{14} and 9.3×10^{14} molec. cm^{-2}, respectively. HCOOH is the most abundant carboxylic acid in the global troposphere, with a relatively short lifetime typically on the order of four days (Stavrakou et al., 2012). Sources of HCOOH include anthropogenic emissions, direct emissions from plant leaves, and biomass burning, while the main sinks of HCOOH are oxidation by OH, as well as dry and wet deposition (Chameides and Davis, 1983; Chen et al., 2021). As a result of its removal from the atmosphere by dry and wet deposition, HCOOH directly contributes to soil and rainwater acidity in remote regions such as the Arctic (Paulot et al., 2011; Stavrakou et al., 2012). As with CH_3OH, emissions from plants are an important driver of the seasonal cycle at Eureka and Thule. Additionally, a study of ground-level HCOOH concentrations at Alert, Nunavut by Mungall et al. (2018) suggests that there may be a complex system of local photochemical sources of HCOOH in the Arctic, however these are currently not well quantified, and the magnitude of their influence on the overall budget is unclear. Very large enhancements in the total columns resulting from transported biomass burning plumes can also be seen in the late summer months at both Eureka and Thule in

Figs. 6.1f and 6.2f, respectively.

H_2CO

The total columns and monthly means of H_2CO are shown in Fig. 6.1g and Fig. 6.2g for Eureka and Thule, respectively. H_2CO displays a distinct seasonal cycle at both FTIR sites, with lower total columns in the spring and fall, and higher total columns on average during the summer months. The mean maximum columns across all years at Eureka and Thule are 1.9×10^{15} molec. cm^{-2} and 2.5×10^{15} molec. cm^{-2}, respectively, and mean minimum columns of approximately 9.5×10^{14} molec. cm^{-2} observed at both sites. H_2CO is one of the most abundant VOCs in the atmosphere, and it plays an important role in atmospheric photochemistry and air quality (Luecken et al., 2012). H_2CO is directly emitted from a variety of anthropogenic and natural sources including fossil fuel combustion, biomass burning, and biogenic emissions from plants and soil, but it is also produced in large quantities via secondary formation in the atmosphere through the oxidation of CH_4 and NMVOCs (Holzinger et al., 1999; Luecken et al., 2012, 2018; Wittrock et al., 2006). It is primarily removed via its reaction with OH yielding HO_2 radicals, which can subsequently be converted back into OH, meaning that OH plays an important role in both the formation and removal of H_2CO from the atmosphere (Mahajan et al., 2010; Nussbaumer et al., 2021; Wittrock et al., 2006). As a result, the seasonal cycle of H_2CO at Eureka and Thule is largely driven by the availability of sunlight and OH in the Arctic atmosphere. Biogenic emissions of H_2CO from high latitude boreal forests also contribute to the observed seasonal maxima in the summertime (Zhao et al., 2022). Some biomass burning enhancements are visible in the time-series at Eureka and Thule between June to August. However, the influence of wildfires on the overall H_2CO columns during the summertime appears to be relatively small, particularly at Thule.

PAN

The seasonal cycle and monthly means of PAN are shown for Eureka and Thule in Figs. 6.1h and 6.2h, respectively. PAN exhibits a seasonal cycle similar in appearance to CO and C_2H_2, with the largest columns observed between February and March which corresponds with the peak in the Arctic Haze pollution phenomena (Law and Stohl, 2007), and the smallest total columns during June to July. The mean maximum columns across all years are 5.4×10^{15} molec. cm^{-2} and 7.3×10^{15} molec. cm^{-2}, and the mean minimum columns are 2.8×10^{15} and 3.3×10^{15} molec. cm^{-2} at Eureka and Thule, respectively. PAN's atmospheric lifetime is highly variable, ranging from approximately one hour at 298 K to several months at the colder temperatures found in the UTLS (Bridier et al., 1991;

Jacob, 2000; Moxim et al., 1996; Orlando et al., 1992; Talukdar et al., 1995). PAN is not directly emitted, but rather it results from secondary formation through the oxidation of NMVOCs such as acetone (C_3H_6O), acetaldehyde (CH_3CHO), and methylglyoxal ($C_3H_4O_2$) in the presence of NO_x. These PAN precursors have both anthropogenic and natural sources including direct emissions from human activities and industry, and biomass burning (Akagi et al., 2011; Coheur et al., 2009; Fischer et al., 2014; Jacob, 2000; Juncosa Calahorrano et al., 2020; Liu et al., 2016). As a result, PAN is primarily formed in polluted mid-latitude regions, particularly during the springtime, and then it undergoes long-range transport to the high-Arctic region (Fischer et al., 2014; Moxim et al., 1996). Consequently, this leads to an accumulation of high concentrations of PAN during polar night and the early spring (visible in Figs. 6.1h and 6.2h). The temperature dependence of PAN's atmospheric lifetime is a major driver of the observed seasonal cycle at the two Arctic sites, leading to a steady decrease in the observed PAN columns at both sites beginning in April and reaching a minimum in July. Biomass burning enhancements can be seen to some extent at both Eureka and Thule, however, the influence of wildfires on the PAN total columns in the late summer months appears to be more significant at Eureka.

6.3.2 FTIR-derived Trends

The Fourier series fitting approach described in Sect. 6.2.3 was applied to the daily-mean total columns of all species at each site. The fitted trends and 95% confidence intervals (CIs) in % yr^{-1} are summarized in Table 6.2, and are plotted in Fig. 6.3 and Fig. 6.4 for Eureka and Thule, respectively. In the text, we provide the trend values in relative units. A version of Table 6.2 in absolute units (i.e., molec. cm^{-2} yr^{-1}) is included in the appendix as Table B.1, and the reader can refer to this table for the absolute values of the trends. Additionally, the residuals of the first Fourier series fit (i.e., with all data included) used to identify enhancement events at Eureka and Thule are provided in the appendix as Fig. B.5 and Fig. B.6, respectively.

CO

CO at Eureka was found to have a clear decreasing trend of −0.84 [−1.07, −0.62] % yr^{-1} (slope [lower 95% CI, upper 95% CI]) over the period of 2006–2020 (see Fig. 6.3a). Similarly, at Thule a decreasing trend of −0.76 [−0.94, −0.58] % yr^{-1} is found for the period of 1999–2022 (see Fig. 6.4a). If enhancement events are excluded from the time-series, we obtain slightly more negative trends of −1.10 [−1.23, −0.97] % yr^{-1} and −0.89% [−0.99, −0.79] % yr^{-1} at Eureka and Thule, respectively.

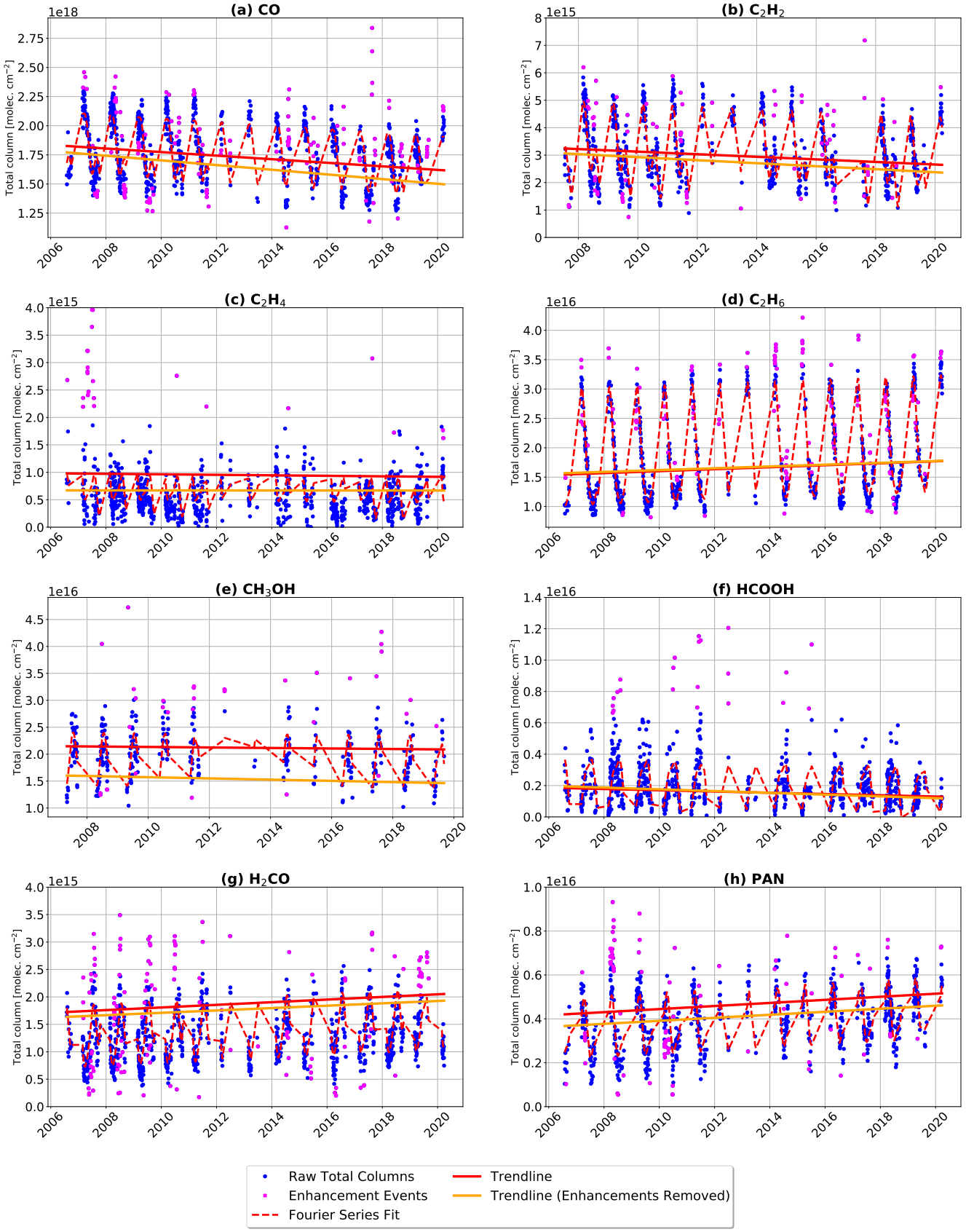

Figure 6.3: Fourier series fit and the corresponding trendlines plotted over the total column time-series of **(a)** CO, **(b)** C_2H_2, **(c)** C_2H_4, **(d)** C_2H_6, **(e)** CH_3OH, **(f)** HCOOH, **(g)** H_2CO, and **(h)** PAN retrieved from PEARL-FTS measurements at Eureka. Note that the y-axis limits of some panels have been adjusted for increased visibility of the fitted trends. Note that the y-axis limits of some panels have been adjusted relative to Fig. 6.1 for increased visibility of the fitted trends.

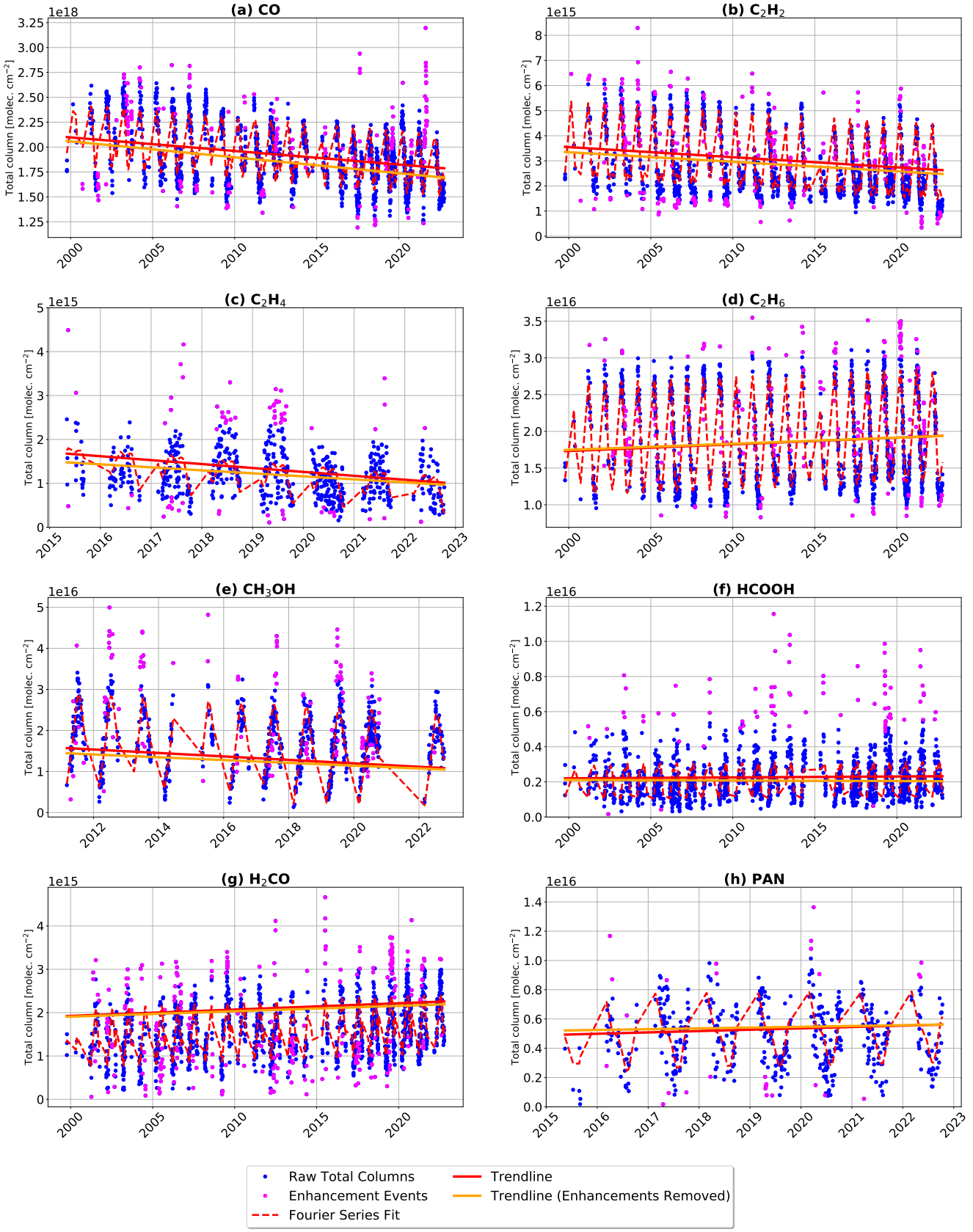

Figure 6.4: Fourier series fit and the corresponding trendlines plotted over the total column time-series of **(a)** CO, **(b)** C_2H_2, **(c)** C_2H_4, **(d)** C_2H_6, **(e)** CH_3OH, **(f)** H_2CO, **(g)** HCOOH, and **(h)** PAN retrieved from the Bruker 120M (1999–2015) and Bruker 125HR (2015–2022) measurements at Thule. Note that the y-axis limits of some panels have been adjusted relative to Fig. 6.2 for increased visibility of the fitted trends.

Table 6.2: Fitted trends derived from daily-mean FTIR total columns at Eureka and Thule in relative units (% yr^{-1}). The 95% confidence intervals calculated from bootstrap resampling with $Q = 5000$ ensemble members are provided below each value in parentheses. Trends that are considered statistically significant (i.e., the 95% confidence intervals do not overlap with zero) are in bold.

Species	Eureka, Nunavut (2006–2020)		Thule, Greenland (1999–2022)	
	Trend (% yr^{-1})	Trend w/o enhancements (% yr^{-1})	Trend (% yr^{-1})	Trend w/o enhancements (% yr^{-1})
CO	**−0.84**	**−1.10**	**−0.76**	**−0.89**
	(−1.07, −0.62)	(−1.23, −0.97)	(−0.93, −0.58)	(−0.99, −0.79)
C_2H_2	**−2.20**[a]	**−2.57**[a]	**−1.71**	**−1.61**
	(−3.03, −1.34)	(−3.14, −1.96)	(−2.03, −1.38)	(−1.83, −1.39)
C_2H_4	−0.43	−0.02	**−6.69**[b]	**−5.13**[b]
	(−2.05, 1.30)	(−0.65, 0.61)	(−9.34, −4.02)	(−6.62, −3.66)
C_2H_6	**1.07**	**0.98**	**0.61**	**0.56**
	(0.76, 1.38)	(0.77, 1.18)	(0.39, 0.84)	(0.42, 0.70)
CH_3OH	−0.24[c]	**−0.57**[c]	**−2.02**[d]	**−1.64**[d]
	(−1.01, 0.51)	(−1.07, −0.08)	(−2.73, −1.30)	(−2.09, −1.20)
HCOOH	−2.14	**−2.98**	0.26	−0.17
	(−5.09, 0.82)	(−4.13, −1.82)	(−0.58, 1.08)	(−0.68, 0.35)
H_2CO	**2.00**	**1.80**	**1.15**	**0.98**
	(1.21, 2.79)	(1.34, 2.25)	(0.64, 1.65)	(0.67, 1.29)
PAN	**2.17**	**2.13**	2.20[b]	1.29[b]
	(1.28, 3.05)	(1.64, 2.62)	(−0.31, 4.61)	(−0.59, 3.22)

[a] The time-series of C_2H_2 at Eureka begins in July 2007.
[b] The time-series of C_2H_4 and PAN at Thule begins in May 2015.
[c] Only one day of CH_3OH total columns was available at Eureka in 2020, so this data is excluded from the analysis.
[d] The time-series of CH_3OH at Thule begins in March 2011.

The decrease in the fitted trends when removing enhancement events suggests that larger and more frequent enhancement events are occurring in the latter portion of the data record at Eureka and Thule, and this can be seen to some extent in Figs. 6.3a and 6.4a.

The observed trends at Eureka and Thule are consistent with recent satellite-derived CO trends over the last two decades, which are generally in the range of −0.5% yr^{-1} to −1% yr^{-1} in the northern hemisphere depending on the period of study (Buchholz et al., 2021; Worden et al., 2013; Zhang et al., 2020). A recent trend study using ground-based FTIR data at Toronto by Yamanouchi et al. (2021) found a CO trend of -0.90 ± 0.07% yr^{-1} over the period of 2002–2019, and an older study by Angelbratt et al. (2011) derived CO trends of -0.45 ± 0.16% yr^{-1}, -1.00 ± 0.24% yr^{-1}, -0.62 ± 0.19% yr^{-1}, and -0.61 ± 0.16% yr^{-1} from NDACC FTIR measurements in Europe at Jungfraujoch, Zugspitze, Harestua and Kiruna over the period of 1996–2006, respectively. The observed downward trend in CO is believed to be largely driven by reductions in fossil fuel-based emissions resulting from the increased efficiency of internal combustion engines in recent years (Buchholz et al., 2021; Worden et al., 2013; Yamanouchi et al., 2021).

C_2H_2

A decreasing trend of −2.20 [−3.03, −1.34] % yr^{-1} over the period of 2007–2020 was found for C_2H_2 at Eureka (Fig. 6.3b). At Thule, a decreasing C_2H_2 trend of −1.71 [−2.03, −1.38] % yr^{-1} is seen during the period of 1999–2022 (Fig. 6.4b). Excluding enhancement events, we obtain a stronger negative trend at Eureka of −2.57 [−3.14, −1.96] % yr^{-1} but the trend at Thule becomes slightly less negative with a value of −1.61 [−1.83, −1.39] % yr^{-1}. At Eureka, the largest enhancement events occur in the latter half of the 2007–2020 time-series, while at Thule a very large C_2H_2 enhancement event occurred in 2004 (shown in Fig. 6.4b), leading to the slight difference in the trends with and without enhancements at the two sites.

Since CO and C_2H_2 are co-emitted from fossil fuel combustion and are highly correlated in the atmosphere (Xiao et al., 2007), the observed negative trends at Eureka and Thule are anticipated, and are broadly consistent with recent studies. Yamanouchi et al. (2021) reported a C_2H_2 trend of $-1.12 \pm 0.30\%$ yr^{-1} derived from FTIR measurements at Toronto in the period of 2002–2019. Similarly, Bernath et al. (2020) report a trend of $-1.70 \pm 0.38\%$ yr^{-1} derived from ACE-FTS measurements between 30° N–90° N in the period of 2004–2020.

C_2H_4

The retrieved C_2H_4 total columns at Eureka show no statistically significant trend in the period of 2006–2020, with a fitted slope of −0.43 [−2.05, 1.30] % yr^{-1} (see Fig. 6.3c). With enhancement events removed, the C_2H_4 trend at Eureka remains statistically insignificant, with a fitted slope of −0.02 [−0.65, 0.61] % yr^{-1}. At Thule, a significant negative trend of −6.69 [−9.34, −4.02] % yr^{-1} was found for the period of 2015–2022 (see Fig. 6.4c). Without enhancement events, a slightly less negative trend of −5.13 [−6.62, −3.66] % yr^{-1} is found. Although the trends at Thule can be considered statistically significant in the context of the Fourier series fitting, they are not robust due to the small number of years (2015–2022) used to derive the trend, and the high year-to-year variability in the retrieved C_2H_4 total columns at the site. Since the atmospheric lifetime of C_2H_4 is extremely short and there no local sources in the high Arctic, the absence of a statistically significant trend is expected as is the case with Eureka, particularly when enhancement events caused by biomass burning are removed from the total column time-series.

C_2H_6

An increasing trend in C_2H_6 is observed at both high Arctic sites. At Eureka, a trend of 1.07 [0.76, 1.38] % yr^{-1} in the period of 2006–2020 was found (Fig. 6.3d). At Thule, a trend of 0.61 [0.39, 0.84] % yr^{-1} is observed between 1999–2022 (Fig. 6.4d). If a fit is performed on the Thule time-series over the same period as the Eureka dataset (August 2006 to March 2020), a more strongly positive trend of 1.66 [1.26, 2.06] % yr^{-1} is found. When excluding enhancement events, the positive trends at both sites decrease slightly to 0.98 [0.77, 1.18] % yr^{-1} and 0.56 [0.42, 0.70] % yr^{-1} at Eureka and Thule, respectively. An apparent brief decline in C_2H_6 can be seen in the Eureka time-series between 2015–2018 before returning to higher levels in 2019, however this feature is not discernible in the Thule time-series and the cause is unclear.

Positive trends in atmospheric C_2H_6 concentrations in the Northern Hemisphere after 2009 have been widely reported in recent studies (e.g., Bernath et al., 2020; Franco et al., 2015, 2016a; Friedrich et al., 2020; Maddanu and Proietti, 2023; Yamanouchi et al., 2021), and this has been linked to significant increases in oil and natural gas production and distribution in the United States (Franco et al., 2016a; Helmig et al., 2016; Monks et al., 2018; Tzompa-Sosa et al., 2017). Franco et al. (2016a) obtained positive trends of approximately 3% yr^{-1} at Eureka and Thule between 2009–2014, and if the methodology presented here is used for the same time period, we obtain consistent trends of 3.63 [2.53, 4.74] % yr^{-1} and 2.93 [1.72, 4.08] % yr^{-1} at Eureka and Thule, respectively. Yamanouchi et al. (2021) report a positive trend of 1.19 ± 0.27% yr^{-1} determined from FTIR measurements at Toronto between 2009–2019, which is broadly consistent with the trends presented here for Eureka and Thule. Lastly, Bernath et al. (2020) found a positive C_2H_6 trend of 1.26 ± 0.30% yr^{-1} in the northern hemisphere between 30° N–90° N using ACE-FTS data in the period of 2004–2020, which falls within the range of uncertainty of the fitted trend at Eureka.

CH_3OH

The measured CH_3OH total columns at Eureka show no statistically significant trend in the period of 2006–2019, with a fitted slope of −0.24 [−1.01, 0.51] % yr^{-1} (see Fig. 6.3e). At Thule, a significant negative trend of −2.02 [−2.73, −1.30] % yr^{-1} was obtained for 2011–2022 (shown in Fig. 6.4e). If the Eureka time-series is truncated to 2011–2020, a more strongly negative slope of −1.04 [−2.71, 0.49] % yr^{-1} is obtained, however the trend is still not considered statistically significant. When enhancement events are excluded from the Fourier series fit, a statistically significant negative trend is found at Eureka of −0.57 [−1.07, −0.08] % yr^{-1} between 2006–2020. At Thule, the trend becomes

slightly less negative when enhancements are removed, with a slope of −1.64 [−2.09, −1.20] % yr^{-1}.

It is currently uncertain what factors might drive a negative trend in CH_3OH in the Arctic region, as the general understanding of the local sources and sinks at these high latitudes is relatively limited. Bernath et al. (2020) found no trend in CH_3OH in ACE-FTS measurements between 2004–2020, however, their trend analysis was limited to the region of −60° S to 60° N. Their results also indicate high concentrations of CH_3OH between 80°–90° N, but this was not included in their discussion. Similarly, Yamanouchi et al. (2021) found no statistically significant trend in CH_3OH at Toronto over the period of 2002–2019. In remote regions such as the Arctic, the ocean serves as a net sink of atmospheric CH_3OH due to deposition on the sea surface and subsequent uptake by marine bacteria (Bates et al., 2021; Yang et al., 2013). A recent study by Wohl et al. (2022) that measured dissolved concentrations of CH_3OH and other VOCs in regions of varying ice coverage in the Canadian Arctic ocean suggests a complex interplay between sea ice coverage and the strength of the ocean as a sink for CH_3OH. It is believed that as sea ice coverage decreases and the air-to-sea flux in the Arctic increases, the ocean will become a stronger sink of oxygenated VOCs, causing a reduction in their atmospheric concentrations (Wohl et al., 2022). It is possible that this may be a driver of the observed CH_3OH trends at Eureka and Thule, however further study is needed.

HCOOH

No statistically significant trend is found in the measured HCOOH total columns at Eureka when all data are included, with a fitted slope of −2.14 [−5.09, 0.82] % yr^{-1} (see Fig. 6.3f). When enhancement events are excluded from the Fourier series fit at Eureka, a significant negative trend of −2.98 [−4.13, −1.82] % yr^{-1} is found between 2006–2020. At Thule, no statistically significant trends are found with or without enhancement events, with slopes of 0.26 [−0.58, 1.08] % yr^{-1} and −0.17 [−0.68, 0.35] % yr^{-1}, respectively (shown in Fig. 6.4f).

To our knowledge, no studies have reported long-term HCOOH trends in the high Arctic. Yamanouchi et al. (2021) found negative HCOOH trends of $-2.15 \pm 0.64\%$ yr^{-1} with enhancements and $-0.73 \pm 0.53\%$ yr^{-1} without enhancements at Toronto in the period of 2002–2019, which are more negative than the trend derived from ACE-FTS measurements of $-0.51 \pm 0.28\%$ yr^{-1} in the range of 60° S to 60° N between 2004–2020 reported by Bernath et al. (2020). These reported negative trends broadly agree with the observations at Eureka, but they may not be fully representative of trends in the Arctic. Several studies in the Arctic have found that snowpack photochemistry is an important local source of HCOOH in the region, and that the high measured concentrations could not be sustained by transport alone (Dibb and Arsenault, 2002; Mungall et al., 2018; Paulot et al.,

2011). Mungall et al. (2018) found that surface HCOOH concentrations measured during early summer 2016 at Alert, Nunavut displayed occasional excursions to extremely high values and a strong diurnal cycle during sunny conditions, indicating a notable photochemical source near the ground and highlighting the complex nature of local HCOOH sources. The extent to which these local sources may influence the measured atmospheric concentrations and trends at Eureka and Thule is currently not well quantified.

H_2CO

Increasing trends were found for H_2CO at Eureka and Thule. At Eureka, a trend of 2.00 [1.21, 2.79] % yr^{-1} was found for the period of 2006–2020 (see Fig. 6.3g). At Thule, a trend of 1.15 [0.64, 1.65] % yr^{-1} was found between 1999–2022 (Fig. 6.4g). If enhancement events are excluded, the slope of the trends decrease slightly to 1.80 [1.34, 2.25] % yr^{-1} and 0.98 [0.67, 1.29] % yr^{-1} at Eureka and Thule, respectively.

Both positive and negative H_2CO trends have been reported in the literature, and the direction of the trends appears to vary based on region. Vigouroux et al. (2018) found no statistically significant trends at Eureka or Thule, but obtained negative trends at mid-latitude FTIR sites, with trends of $-0.39 \pm 0.33\%$ yr^{-1} and $-0.96 \pm 0.51\%$ yr^{-1} at St. Petersburg and Mexico City, respectively, and strong positive trends of $1.73 \pm 1.52\%$ yr^{-1} and $1.58 \pm 0.52\%$ yr^{-1} the tropical sites of Izana (2005–2016) and Saint-Denis (2004–2013), respectively. Yamanouchi et al. (2021) found a slightly negative trend at Toronto of $-0.43 \pm 0.25\%$ yr^{-1} only after removing enhancement events. Franco et al. (2016b) found a positive trend at Jungfraujoch of $0.81 \pm 0.62\%$ yr^{-1} using FTIR data between 2003–2015, which they suggest is likely related to increases in atmospheric CH_4 concentrations. Bernath et al. (2020) found a positive but non-significant trend in stratospheric H_2CO of $0.18 \pm 0.18\%$ yr^{-1} between 30° S and 30° N with ACE-FTS, but a positive significant trend in the troposphere in the same region. Lastly, De Smedt et al. (2015) found strongly positive trends over Asia driven by greater emissions, but negative trends over Europe and North America using measurements from the Ozone Monitoring Instrument (OMI) and the Global Ozone Monitoring Experiment-2 (GOME-2) between 2004–2014. The observed positive trends at Eureka and Thule may be driven in-part by greater emissions from Asia coupled with steadily rising CH_4 concentrations, however a broader study of these observed trends at high northern latitudes may be needed.

PAN

A clear upwards trend of 2.17 [1.28, 3.05] % yr^{-1} is seen in the observed PAN total columns at Eureka between 2006–2020. When enhancement events are removed, the slope of the trend at Eureka is largely unchanged with a value of 2.13 [1.64, 2.62] % yr^{-1}, however the range of the 95% CIs decreases, indicating a higher confidence in the observed positive trend. At Thule, PAN measurements are only available between 2015–2022, and positive but non-significant trends are found, with values of 2.20 [−0.31, 4.61] % yr^{-1} with all measurements, and 1.29 [−0.59, 3.22] % yr^{-1} when enhancement events are excluded from the time-series. The magnitude of the slope at Thule is generally consistent with the observations at Eureka, however more years of measurements at the site are likely needed to derive a statistically significant trend.

Relatively few studies are available that report long-term trends in PAN. Bernath et al. (2020) report no statistically significant trend between 2004–2012, and then a strongly decreasing trend of $-11.7 \pm 2.3\%$ yr^{-1} averaged over 60° S to 60° N between 2004–2020. Fadnavis et al. (2014) found positive annual PAN trends ranging from 0.4 ± 1.3 to 3.2 ± 0.49 ppt yr^{-1} over India, and 1.0 ± 0.25 to 3.4 ± 1.3 ppt yr^{-1} over China (no relative trend values provided). Additionally, several studies have demonstrated that PAN production is highly spatially heterogeneous, and that Asian emissions of O_3 and PAN precursors have been steadily rising, leading to increased export of PAN particularly during the springtime (Cooper et al., 2010; Fadnavis et al., 2014; Fischer et al., 2011, 2014; Jiang et al., 2016; Zhang et al., 2008). Since Asian anthropogenic emissions are a dominant source of transported pollution at Eureka (Lutsch et al., 2020) (see Fig. 1.3), the upward trend at Eureka is likely influenced by greater PAN export from Asia in recent decades.

6.3.3 GEOS-Chem Simulation and Comparison with Observations

Since measurements of CO, C_2H_2, C_2H_4, C_2H_6, CH_3OH, HCOOH, H_2CO, and PAN are sparse in the high-Arctic region, global chemical transport models such as GEOS-Chem can provide an additional perspective on the transport, distribution, and temporal variability and evolution of these trace gases. Ground-based FTIR measurements of these gases can serve as a means for evaluating the performance of the model and can help to identify biases or potential areas of improvement. In the following subsections, we compare the modeled intra- and inter-annual variability of CO, C_2H_2, C_2H_4, C_2H_6, CH_3OH, HCOOH, H_2CO, and PAN with the ground-based FTIR measurements at Eureka and Thule.

Seasonal Cycles

The monthly mean simulated total columns from GCHP of all eight tropospheric species are plotted along with the FTIR monthly mean total columns in Fig. 6.5 and Fig. 6.6 for Eureka and Thule, respectively. It should be noted that in Fig. 6.5 the GEOS-Chem time-series was truncated to 2006–2020 before calculating the monthly means to more accurately correspond to the Eureka FTIR time-series, while in Fig. 6.6 the Thule FTIR time-series was truncated to 2003–2021 prior to calculating the monthly means for easier comparison with the GEOS-Chem simulation. Additionally, correlation plots comparing the daily mean simulated total columns with the daily mean FTIR-retrieved total columns at Eureka and Thule are included in the appendix as Figs. B.7 and B.8, providing a more quantitative means of evaluating the model against the FTIR measurements at both sites.

CO

The seasonal cycle of CO is well captured by GEOS-Chem at both Arctic FTIR sites, and is shown in Fig. 6.5a and Fig. 6.6a for Eureka and Thule, respectively. The model reflects the observed springtime maximum in February to April and low total columns in July at both sites, with a strong correlation of $R = 0.78$ and a mean relative bias of -5.5% at Eureka, and a correlation coefficient of $R = 0.84$ and mean relative bias of -14.1% at Thule (see appendix Figs. B.7a and B.8a). The closest agreement between the modeled and FTIR-observed mean total columns is seen during the period of May to July, and larger differences are found during the early spring months and the late summer and into early fall. The observed springtime low bias at Eureka and Thule is consistent with previous modeling studies using GEOS-Chem, which have shown that northern mid-latitude CO emissions during the wintertime are broadly underestimated in many anthropogenic emissions inventories due to underestimated vehicle combustion and residential heating emissions (Jiang et al., 2015; Kopacz et al., 2010; Whaley et al., 2022). The GEOS-Chem CO simulation captures biomass burning enhancement events at both Arctic sites in August, however, the magnitude of these enhancements appears to be underestimated in the model, particularly at Thule where a larger measurement-model difference is seen in August compared to Eureka. The observed discrepancy in the simulated versus observed biomass burning enhancements is due in-part to the rudimentary default biomass burning injection height scheme as discussed in Chapter 5, which can negatively impact the transport of the plumes and the subsequent enhancements at the Arctic FTIR sites. However, despite this GEOS-Chem generally performs quite well in simulating the annual CO cycle in the region and is highly correlated with the FTIR observations at Eureka and Thule.

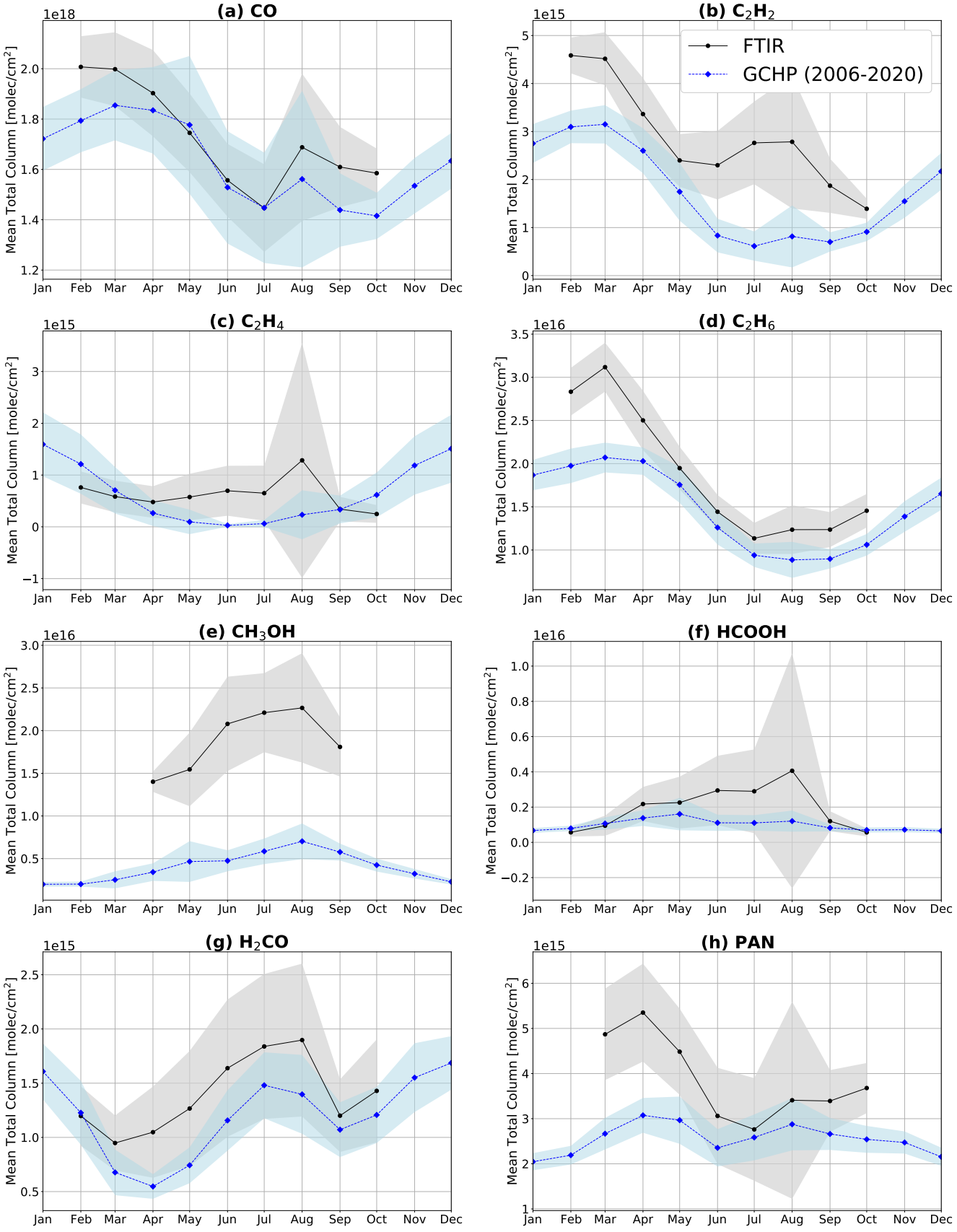

Figure 6.5: FTIR and GCHP-simulated seasonal cycles at Eureka for **(a)** CO, **(b)** C_2H_2, **(c)** C_2H_4, **(d)** C_2H_6, **(e)** CH_3OH, **(f)** HCOOH, **(g)** H_2CO, and **(h)**. The shaded regions denote 1σ from the monthly means. Note that the GCHP monthly means presented here were calculated over 2006-2020 to correspond with the Eureka FTIR time-series.

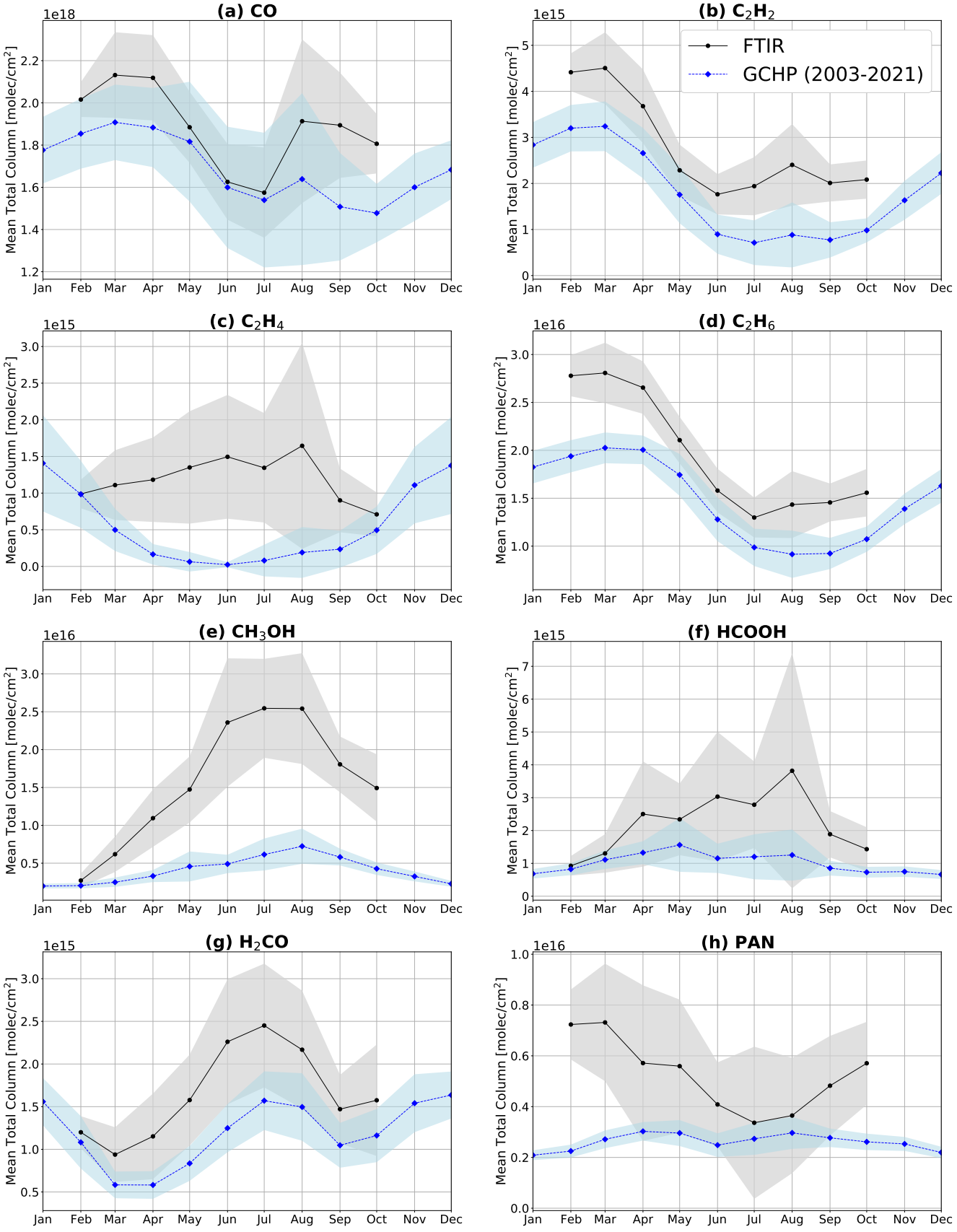

Figure 6.6: FTIR and GCHP-simulated seasonal cycles at Thule for **(a)** CO, **(b)** C_2H_2, **(c)** C_2H_4, **(d)** C_2H_6, **(e)** CH_3OH, **(f)** HCOOH, **(g)** H_2CO, and **(h)** PAN. The shaded regions denote 1σ from the monthly means. Note that the Thule FTIR monthly means presented here were calculated over 2003-2021 to correspond with the time range of the GCHP simulation.

C_2H_2

The addition of a full-chemistry simulation of C_2H_2 to the GEOS-Chem model is a relatively recent development (added in version 13.3 in November 2021), and to our knowledge this is the first study to evaluate this simulation against FTIR observations. The monthly mean GEOS-Chem C_2H_2 total columns for Eureka and Thule are shown in Fig. 6.5b and Fig. 6.6b, respectively. The GEOS-Chem simulation displays an intra-annual cycle that is largely consistent with the monthly mean FTIR-observed total columns at both Arctic sites, however a consistent low bias is seen in the model across all months. The modeled C_2H_2 daily-mean total columns display a good correlation of $R = 0.75$ with the FTIR daily-mean total columns at Eureka, however, a mean measurement-model bias of -43.4% was found in the period of 2006–2020 (Fig. B.7b). Similarly, at Thule the GEOS-Chem C_2H_2 total columns are well-correlated with the FTIR measurements ($R = 0.88$), but a mean negative relative bias of -47.6% was found for the period 2003–2021 (Fig. B.8b). The strong correlations but large negative model versus measurement biases at both Arctic FTIR sites suggest that the emissions of C_2H_2 in the model should be increased by approximately 40–50%. Additionally, at Eureka larger biomass burning enhancements of C_2H_2 are observed in comparison to Thule, however, GEOS-Chem shows a relatively small influence of wildfires in the month of August. This effect can also be observed in the correlation plot for Eureka (Fig. B.7b), where the distribution of the data points displays a bifurcation, and some large daily mean FTIR total columns can be seen that correspond to smaller GEOS-Chem simulated total columns.

C_2H_4

As with C_2H_2, a full-chemistry simulation of C_2H_4 was only recently added to the GEOS-Chem model (version 13.3 in November 2021). The C_2H_4 simulation was evaluated at Eureka during the August 2017 biomass burning event in Chapter 5, however no studies have evaluated this simulation on a broader scale yet. The monthly mean GEOS-Chem C_2H_4 total columns at Eureka and Thule are shown in Fig. 6.5c and Fig. 6.6c, respectively. The GEOS-Chem and FTIR monthly means broadly agree during February to March and September to October at Eureka, however during the summer months, the model and FTIR measurements diverge more significantly. GEOS-Chem indicates near-zero C_2H_4 total columns at Eureka in June and July, while the FTIR monthly means reflect higher ambient concentrations. Similarly, at Thule the GEOS-Chem simulation agrees closely with FTIR observations in February and October, however between this period there is a notable low bias in the model with respect to the measurements. Interestingly, GEOS-Chem displays a significant

accumulation of C_2H_4 in the Arctic atmosphere over the wintertime possibly as a result of the absence of OH, but FTIR measurements are not available during this period to verify this phenomenon. The GEOS-Chem daily mean C_2H_4 columns are poorly correlated with FTIR observations, with Pearson correlation coefficients of $R = 0.08$ and $R = 0.21$, and with mean relative biases of -16.9% and -82.1% at Eureka and Thule, respectively (see Figs. B.7c and B.8c in the appendix). The larger mean negative bias at Thule relative to Eureka is related to the larger retrieved mean total columns at that site (discussed in Sect. 6.3.1), however the comparison at Thule only covers 2015–2021 and is less statistically robust than the comparison at Eureka. The GEOS-Chem simulation does show some influence from biomass burning at both sites during the month of August but the magnitude of these enhancements appears to be underestimated relative to FTIR observations, which may be related to the simplistic default biomass burning injection height scheme in the model as discussed in Chapter 5.

C_2H_6

The monthly mean model and FTIR C_2H_6 total columns are plotted in Fig. 6.5d and Fig. 6.6d for Eureka and Thule, respectively. GEOS-Chem and the measured total columns generally display a similar seasonal cycle, with a maxima in the total columns occurring in February and March, and a minima in the total columns occurring in July. The simulated C_2H_6 columns are strongly correlated with the FTIR total columns, with correlation coefficients of $R = 0.90$ and $R = 0.91$ and mean relative biases of -20.8% and -25.1% at Eureka and Thule, respectively (see Figs. B.7d and B.7d in the appendix). A seasonally-dependent bias can be seen at both Arctic sites, with larger mean differences during the early spring months and closer agreement during the late spring and early summer months (May to July). In the default configuration of the model, the Tzompa-Sosa et al. (2017) emissions inventory was selected by the GEOS-Chem Emissions Working Group because the CEDS inventory tended to underestimate C_2H_6 emissions in the Northern Hemisphere relative to observations (e.g., Dalsøren et al., 2018). However, a drawback of the Tzompa-Sosa inventory is that it only includes emissions for 2010 (which are applied to all years in the simulation) and it does not exhibit intra-annual variability in the emissions outside of North America. To investigate whether the springtime model bias is related to the choice of anthropogenic emissions, we repeated a GCHP simulation for 2019 using the CEDSv2 C_2H_6 emission inventory in place of the Tzompa-Sosa C_2H_6 inventory, while all other model parameters were kept the same. We compare the monthly means for these simulations in Fig. 6.7, and we provide correlation plots for each scenario for Eureka and Thule in the appendix as Figs. B.9 and B.10, respectively. In these figures, we also include an additional

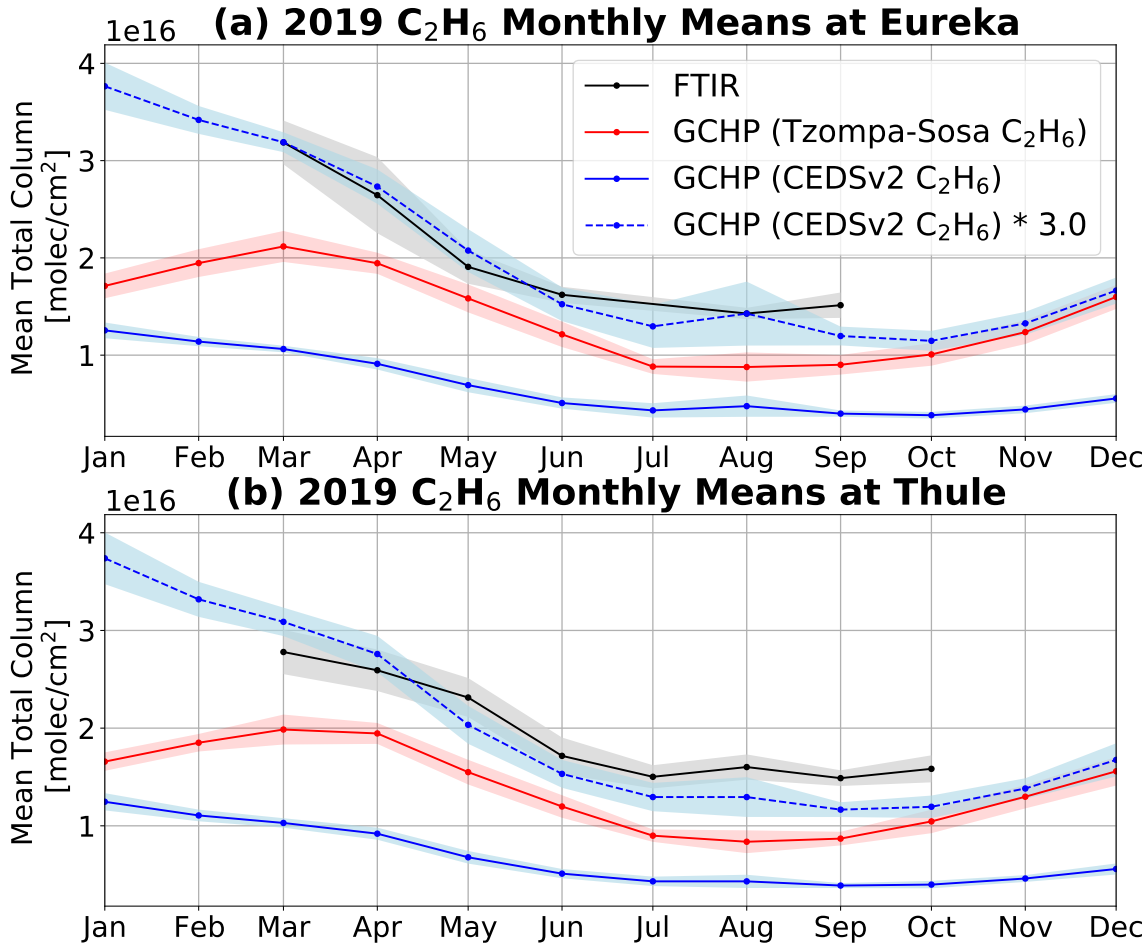

Figure 6.7: FTIR and GCHP-simulated monthly mean total columns of C_2H_6 for 2019 at **(a)** Eureka, and **(b)** Thule for three scenarios; the default simulation using the Tzompa-Sosa et al. (2017) emissions inventory (red solid line), a simulation using CEDSv2 emissions (blue solid line), and the CEDSv2 simulation with the total columns scaled up by a factor of 3.0 (blue dashed line). The shaded regions denote 1σ from the means.

scenario whereby the GEOS-Chem C_2H_6 total columns are scaled up by a factor of 3 to account for the observed measurement-model bias. The new simulation using CEDSv2 displays improved correlations of $R = 0.93$ versus $R = 0.88$ and $R = 0.96$ versus $R = 0.94$, but larger biases of -66.6% versus -28.3% and -69.6% versus -34.8% during 2019 at Eureka and Thule, respectively. This observed low bias in the CEDSv2 simulation is consistent with a recent study by Adedeji et al. (2023), who evaluated the CEDS inventory using GEOS-Chem against in-situ measurements on the Japanese island of Hateruma, and found that the Asian C_2H_6 emissions needed to be increased by a factor of 2.22 in order to reproduce their observations. Similar low biases have also previously been observed in the Hemispheric Transport of Air Pollutants, Phase II (HTAPv2) inventory using CAM-Chem simulations in Franco et al. (2016a). In Fig. 6.7 and Figs. B.9c and B.10c, we show that

when the modeled C_2H_6 total columns in our simulation using CEDSv2 are increased by a factor of 3.0, we find improved slopes in the linear regressions and much closer agreement with the FTIR measurements at Eureka and Thule. Although this is only an ad hoc analysis, it indicates that by using a scaled version of the CEDSv2 C_2H_6 emissions in place of the default Tzompa-Sosa inventory, the simulation could be improved relative to observations and would better capture the intra-annual variability of C_2H_6 in the Arctic region.

CH_3OH

Fig. 6.5e and 6.6e show the monthly mean simulated and observed CH_3OH total columns at Eureka and Thule, respectively. The GEOS-Chem total columns display a seasonal cycle similar to the FTIR observations, with smaller columns on average during the spring and fall, and larger columns during the summer months of July to September, however a very large bias can be seen at both Arctic sites. Regression plots comparing the GEOS-Chem and FTIR CH_3OH daily-means are shown in Fig. B.7e for Eureka and B.8e for Thule. Consistent negative biases relative to the FTIR measurements on the order of approximately -70% are found at both Eureka and Thule, suggesting that there may be a large source of CH_3OH or unknown chemical pathways which are not accounted for in the model. We find a relatively weak correlation of $R = 0.28$ between the model and measurements at Eureka, but a stronger correlation of $R = 0.69$ at Thule, which is related to the fact that the FTIR CH_3OH measurements at Thule cover a larger portion of the year (February to October at Thule, and April to September at Eureka) and exhibit a higher dynamic range than at Eureka. The observed model bias in CH_3OH is generally consistent with recent GEOS-Chem modeling studies by Chen et al. (2019) and Bates et al. (2021), who found that the modeled CH_3OH concentrations over North America are broadly underestimated relative to observations, with the largest biases at high latitudes. Improvements were made to the CH_3OH simulation in GEOS-Chem version 13.3.0 in November 2021 through the addition of a new aromatic VOC oxidation scheme and the inclusion of a CH_3O_2 + OH reaction into the chemistry scheme, which generally reduced the observed biases, however, it is evident that more improvements are needed to remediate the large measurement-model biases in the Arctic.

HCOOH

The modeled and observed seasonal cycles of HCOOH are shown in Fig. 6.5f and 6.6f for Eureka and Thule, respectively. The GEOS-Chem simulation displays seasonality which is mostly consistent with the FTIR observations at both sites, with smaller mean columns early and late in the year,

and larger columns on average during the late spring and summer. However, the model presents a maximum in May, while the FTIR measurements show a peak in August that is related to the large wildfire enhancements that can occur during the mid to late summer, but which may not be properly captured in the model due to the injection height scheme. Correlation plots comparing the daily mean GEOS-Chem HCOOH total columns and the FTIR daily means are shown in Figs. B.7f and B.8f in the appendix. These figures show moderate correlations of $R = 0.43$ and $R = 0.53$ between the model and measurements, with mean relative biases of -7.9% and -36.7% at Eureka and Thule, respectively. The observed biases are generally in-line with previous comparisons of models with observations that found underestimations in HCOOH abundances, particularly at high northern latitudes, suggesting missing chemistry or unknown local sources (Paulot et al., 2011; Schobesberger et al., 2016; Stavrakou et al., 2012). The inclusion of a surface-level source of HCOOH in the Arctic from the snow-pack based on the observations of Mungall et al. (2018) may help bridge the gap of the observed biases in the late spring to some extent, however the nature of this local source of HCOOH is still highly uncertain and requires further investigation. Furthermore, an improved parameterization of the biomass burning injection height in the model would help to improve agreement with observations in the late summer months as demonstrated in Chapter 5.

H_2CO

Figs. 6.5g and 6.6g show the simulated and observed H_2CO monthly means at Eureka and Thule, respectively. GEOS-Chem is able to reproduce the distinct seasonality in the total columns observed by the FTIRs at both sites, and shows the largest total columns occurring during the winter months of November to January, however no FTIR measurements are available during this period for comparison. The simulated H_2CO columns reach a minimum at both sites in April and then increase until July before decreasing again, which is generally consistent with the observed seasonal cycle at Eureka and Thule but a low model bias can be seen across all months relative to the FTIR monthly means. The correlations between the daily-mean GEOS-Chem and FTIR H_2CO total columns are shown in Fig. B.7g for Eureka and B.8g for Thule. The GEOS-Chem columns are generally well-correlated with the FTIR observations, with a correlation coefficient of $R = 0.69$ at Eureka, and $R = 0.76$ at Thule. Moderate relative biases of -20.5% and -26.7% calculated across all years were found for Eureka and Thule, respectively. These mean biases are consistent with the study by Vigouroux et al. (2018), who found similar measurement-model biases of -20% and -28% with the IMAGES CTM at Eureka and Thule in the periods of 2006–2017 and 2002–2017, respectively.

PAN

The simulated and observed monthly mean PAN total columns are shown in Fig. 6.5h at Eureka and Fig. 6.6h at Thule. GEOS-Chem does capture some seasonal cycle, with the lowest mean total columns in December and January, and a springtime peak in April, with some large columns occurring in August as the result of transported wildfire plumes. However, a very large negative bias in the model can be seen from February to May. Correlation plots comparing the GEOS-Chem daily mean PAN columns with those retrieved from the Arctic FTIRs are shown in Figs. B.7h and B.8h. A moderate correlation of $R = 0.43$ is found at Eureka, while no correlation ($R = -0.01$) is found at Thule, however the comparison at Thule covers a shorter time period (2015–2021) compared to Eureka (2007–2020). Mean relative biases of -18.6% and -17.5% were found for Eureka and Thule, respectively, indicating a similar underestimation in the model at both Arctic sites. The observed springtime bias in the total columns is likely related to lower than expected wintertime outflows of PAN from China, which is attributed partly to missing or underestimated NMVOC emissions in the region as highlighted by Fu et al. (2007) and Fischer et al. (2014). Additionally, currently no emissions of methylglyoxal are included in GEOS-Chem, which is an important PAN precursor (contributing approximately 30% to global PAN production) and may be an additional factor in the observed springtime bias in the model (Fischer et al., 2014; Liu et al., 2010). Increasing the Asian NMVOC emissions and including direct emissions of methylglyoxal in the model would likely enhance the simulation of PAN in the Arctic region relative to the FTIR observations.

Simulated Trends

To further evaluate the performance of the model and its ability to reproduce the observed trends, the Fourier series fitting approach that was described in Sect. 6.2.3 and applied to the FTIR daily-mean total columns in Sect. 6.3.2 was also applied to the GEOS-Chem simulated daily mean total columns. To increase the inter-comparability of the observed and modeled trends, the GCHP-simulated trends at Eureka were calculated over the same approximate time range as where the Eureka FTIR measurements are available (July 2006 to March 2020). At Thule, since the FTIR time-series extends slightly beyond the time range of the GCHP simulation, we calculate the GCHP-simulated trends over the full simulation period (January 2003 to December 2021). The daily-mean simulated total columns of all species at each site, and the fitted trends and 95% CIs in % yr^{-1} are summarized in Table 6.3, and are plotted in Fig. 6.8 and Fig. 6.9 for Eureka and Thule, respectively. A version of Table 6.3 in total column units is included in the appendix as Table B.2. The residuals

Table 6.3: Fitted trends derived from daily-mean GEOS-Chem total columns at Eureka and Thule in relative units (% yr^{-1}). The 95% confidence intervals calculated from bootstrap resampling with $Q = 5000$ ensemble members are provided below each value in parentheses. Trends that are considered statistically significant (i.e., the 95% confidence intervals do not overlap with zero) are in bold.

Species	Eureka, Nunavut (2006–2020)		Thule, Greenland (2003–2021)	
	Trend (% yr^{-1})	Trend w/o enhancements (% yr^{-1})	Trend (% yr^{-1})	Trend w/o enhancements (% yr^{-1})
CO	**−0.88** (−1.09, −0.67)	**−0.85** (−0.98, −0.72)	**−0.79** (−0.98, −0.61)	**−0.86** (−0.94, −0.77)
C_2H_2	**−2.03** (−2.46, −1.61)	**−1.95** (−2.22, −1.68)	**−1.63** (−1.91, −1.35)	**−1.71** (−1.85, −1.55)
C_2H_4	−0.20 (−1.11, 0.68)	−0.11 (−0.56, 0.34)	0.49 (−0.28, 1.25)	**0.40** (0.02, 0.76)
C_2H_6	−0.19 (−0.38, 0.01)	**−0.16** (−0.27, −0.05)	**−0.26** (−0.42, −0.11)	**−0.28** (−0.34, −0.21)
CH_3OH	−0.45 (−0.90, 0.02)	**−0.43** (−0.63, −0.24)	−0.24 (−0.52, 0.05)	**−0.20** (−0.33, −0.07)
HCOOH	**−1.17** (−1.97, −0.36)	**−1.09** (−1.41, −0.77)	**−0.71** (−1.11, −0.32)	**−0.59** (−0.78, −0.41)
H_2CO	−0.18 (−0.47, 0.13)	−0.13 (−0.29, 0.03)	0.08 (−0.16, 0.16)	0.02 (−0.11, 0.16)
PAN	**−0.80** (−1.00, −0.60)	**−0.83** (−0.94, −0.71)	**−0.61** (−0.75, −0.48)	**−0.58** (−0.66, −0.50)

of the first Fourier series fit used to identify enhancement events at Eureka and Thule are provided in the appendix as Fig. B.11 and Fig. B.12, respectively.

CO

The fitted trends in the GEOS-Chem simulated CO columns are shown in Fig. 6.8a and Fig. 6.9a for Eureka and Thule, respectively. From GEOS-Chem, we obtain a negative trend in the CO total columns of −0.88 [−1.09, −0.67] % yr^{-1} at Eureka between 2006–2020, and −0.79 [−0.98, −0.61] % yr^{-1} at Thule between 2003–2021. When enhancement events are excluded from the Fourier series fit, we find a slightly less negative trend at Eureka of −0.85 [−0.98, −0.72] % yr^{-1}, and a slightly more negative trend at Thule of −0.86 [−0.94, −0.77] % yr^{-1}. This effect appears to be caused by the fact that some larger enhancement events occur earlier in the simulation at Eureka, while at Thule, the largest identified enhancements occur towards the end of the simulated time-series. These trends can be contrasted with the FTIR-derived trends of −0.84 [−1.07, −0.62] and −0.76 [−0.94, −0.58] (with enhancements), and −1.10 [−1.23, −0.97] and −0.89 [−0.99, −0.79] (without enhancements) at Eureka and Thule, respectively. The measured and modeled trends are

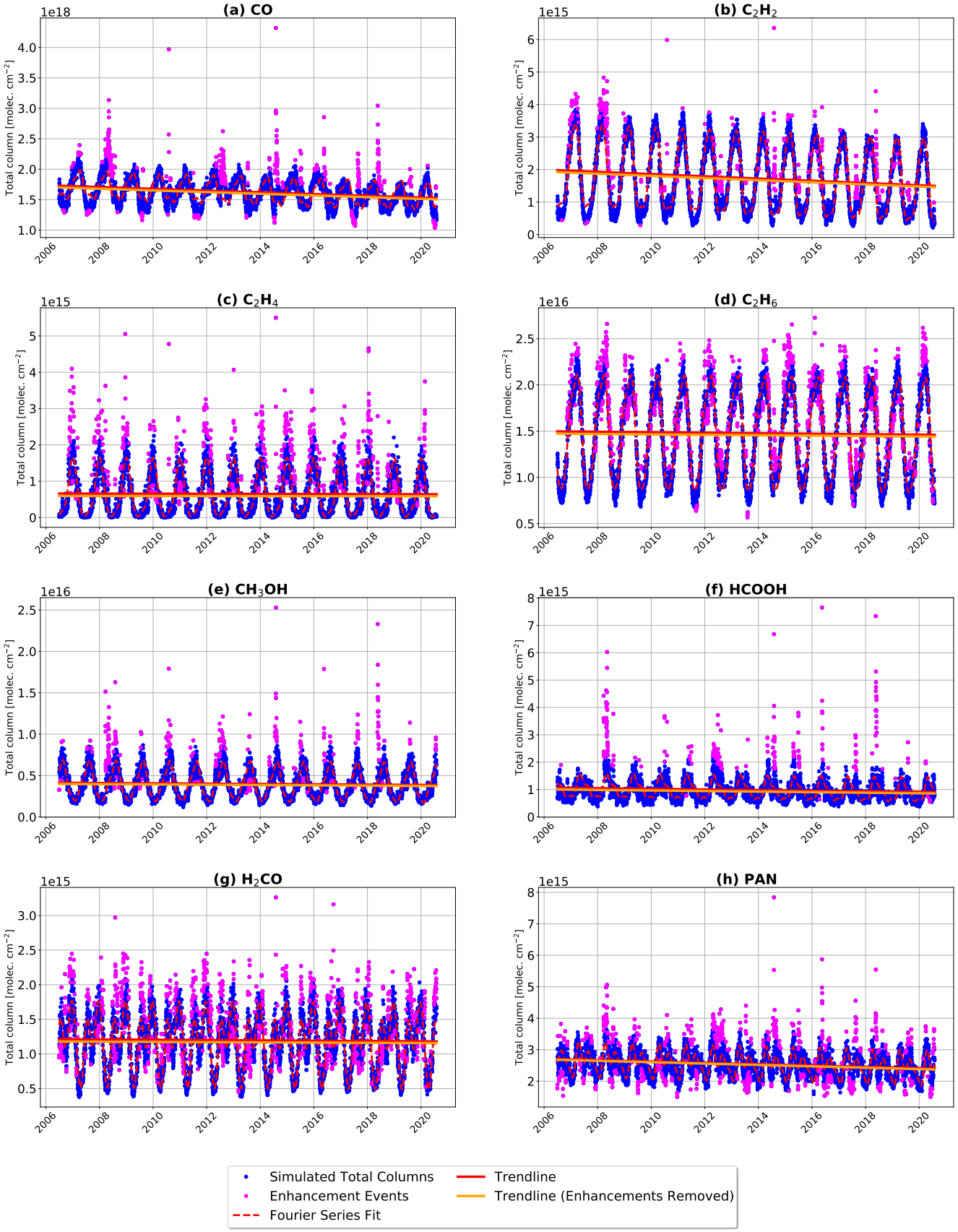

Figure 6.8: Fourier series fit and the corresponding trendlines plotted over the GCHP simulated total column time-series of **(a)** CO, **(b)** C_2H_2, **(c)** C_2H_4, **(d)** C_2H_6, **(e)** CH_3OH, **(f)** HCOOH, **(g)** H_2CO, and **(h)** PAN at Eureka.

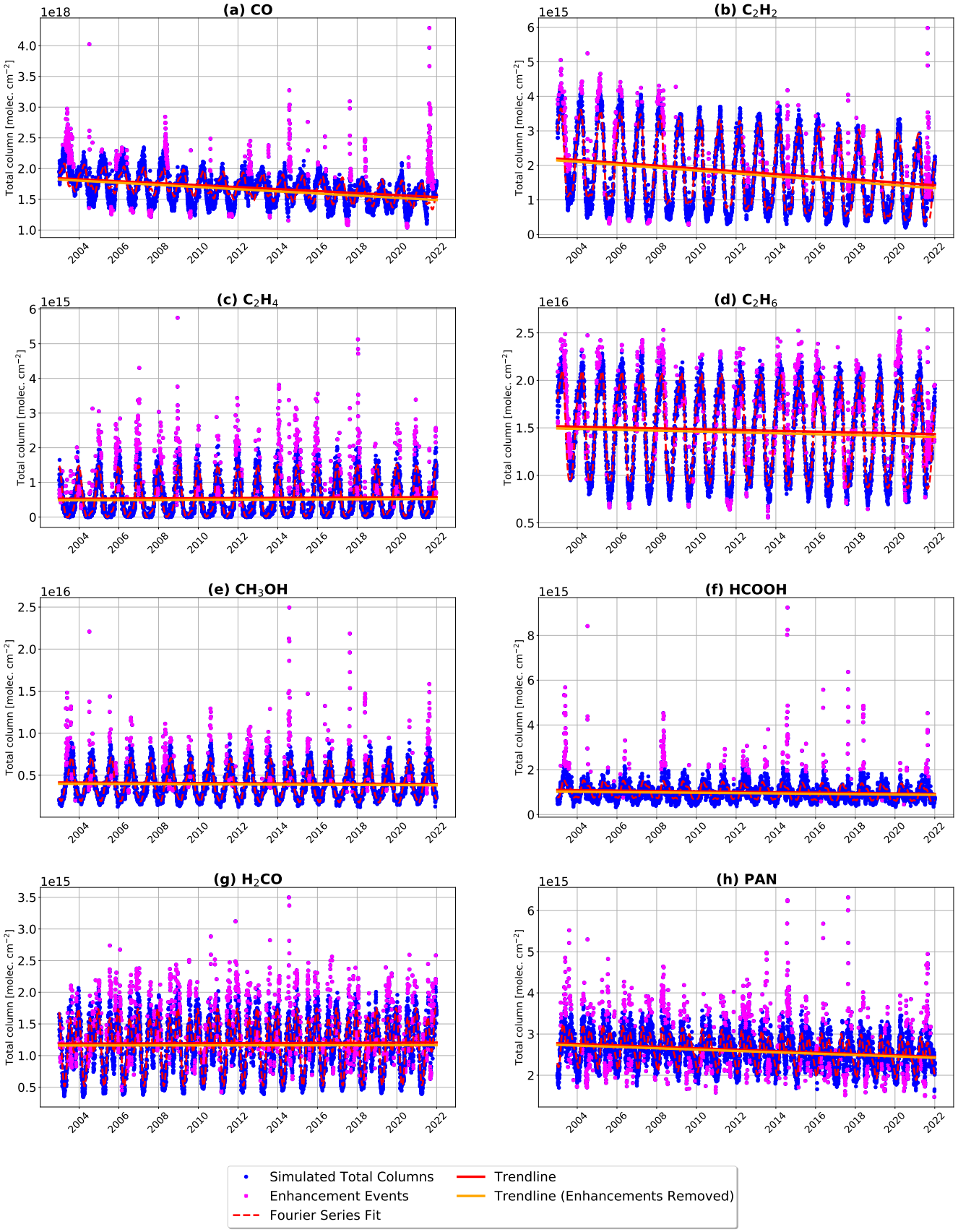

Figure 6.9: Fourier series fit and the corresponding trendlines plotted over the GCHP simulated total column time-series of **(a)** CO, **(b)** C_2H_2, **(c)** C_2H_4, **(d)** C_2H_6, **(e)** CH_3OH, **(f)** HCOOH, **(g)** H_2CO, and **(h)** at Thule.

broadly consistent, and fall within the bounds of the 95% confidence intervals with the exception of the enhancement-removed FTIR-derived trend at Eureka which is more strongly negative than that estimated from GEOS-Chem. In general, CO appears to be well-modeled in GCHP at both Arctic FTIR sites, showing good consistency in the inter-annual variability when compared with the FTIR observations.

C_2H_2

For C_2H_2, we derive negative trends from the daily-mean GEOS-Chem total columns of −2.03 [−2.46, −1.95] % yr^{-1} at Eureka (Fig. 6.8b), and −1.63 [−1.91, −1.35] % yr^{-1} at Thule (Fig. 6.9b). If enhancement events are removed, we obtain a slightly less negative trend of −1.95 [−2.22, −1.68] % yr^{-1} at Eureka, and −1.71 [−1.85, −1.55] % yr^{-1} at Thule. The tendency of the C_2H_2 trend to become more strongly negative at Thule when removing the identified enhancement events is consistent with the modeled CO trends at this site, and appears to be influenced by a particularly large wildfire enhancement that occurred in August 2021 but which is not included when fitting the trends at Eureka. We can compare these modeled trends with the FTIR-derived trends of −2.20 [−3.03, −1.34] % yr^{-1} and −1.71 [−2.03, −1.38] % yr^{-1} when all measurements are included, and −2.57 [−3.14, −1.96] % yr^{-1} and −1.61 [−1.83, −1.39] % yr^{-1} when enhancements are removed for Eureka and Thule, respectively. Consistent with the modeled CO trends, we find that there is generally good agreement between the FTIR-derived and GEOS-Chem simulated C_2H_2 trends at both sites, with all trends overlapping within the bounds of the 95% CIs except for the enhancement-removed trend at Eureka, which is more strongly negative than the GEOS-Chem derived trend.

C_2H_4

When all data are included, GEOS-Chem shows no statistically significant trends in C_2H_4 at Eureka or Thule with slopes of −0.20 [−1.11, −0.68] % yr^{-1} and 0.49 [−0.28, 1.25] % yr^{-1}, respectively (see Fig. 6.8c and Fig. 6.9c). When enhancements are removed from the GEOS-Chem time-series the trend at Eureka remains statistically insignificant with a slope of −0.11 [−0.56, 0.34] % yr^{-1}, but we find a slightly positive significant trend at Thule of 0.40 [0.02, 0.76] % yr^{-1}. No statistically significant trends were found in the C_2H_4 FTIR time-series at Eureka over the period of 2006–2020, while negative trends of −6.69 [−9.34, −4.02] % yr^{-1} (with all data) and −5.13 [−6.62, −5.13] % yr^{-1} (with enhancements removed) were found at Thule in the limited period of 2015–2022, however these trends are not robust due to the few number of years used in the Fourier series fitting and the high year-to-year variability in the columns. The slight upward trend found in the enhancement-removed

simulated C_2H_4 time-series at Thule is almost statistically insignificant (the lower CI is 0.02 and almost overlaps with zero), and without more years of FTIR data at this site it is difficult to discern whether there is a real detectable trend.

C_2H_6

The Fourier series fits to the GEOS-Chem C_2H_6 daily-mean total columns are shown in Fig. 6.8d and Fig. 6.9d for Eureka and Thule, respectively. We find no significant trend at Eureka when fitting the full simulated time-series with a slope of −0.19 [−0.38, 0.01] % yr^{-1}, but a small negative trend when enhancements are removed of −0.16 [−0.27, −0.05] % yr^{-1}. At Thule, slight negative trends are also found in the GEOS-Chem C_2H_6 time-series with values of −0.26 [−0.42, −0.11] % yr^{-1} with all data and −0.28 [−0.34, −0.21] % yr^{-1} when enhancements are removed. These simulated trends can be contrasted with the positive trends derived from the Arctic FTIR measurements of 1.07 [0.76, 1.38] % yr^{-1} and 0.61 [0.39, 0.84] % yr^{-1} (all data), and 0.98 [0.77, 1.18] % yr^{-1} and 0.56 [0.42, 0.70] % yr^{-1} (enhancements excluded) at Eureka and Thule, respectively. The difference in the observed versus modeled trends can be attributed to the use of the Tzompa-Sosa et al. (2017) emissions inventory which is the default option for the anthropogenic C_2H_6 emissions in the current version of GEOS-Chem. As briefly discussed in Sect. 6.3.3, the Tzompa-Sosa emissions inventory only contains data for the year of 2010, which is applied to all years in the simulation, and thus does not exhibit any inter-annual variability in the global C_2H_6 emissions. To further investigate the long-term temporal variability in the Tzompa-Sosa and CEDSv2 C_2H_6 inventories, the HEMCO Standalone module (`https://hemco.readthedocs.io/en/stable/`) version 3.6.2 was used to generate the time-series of emissions over the same period as the GCHP simulation (2003–2021). Time-series of C_2H_6 emissions over Asia and North America using both the Tzompa-Sosa and CEDSv2 emissions inventories are shown in Fig. B.13 in the appendix. When comparing the time-series from the two inventories, a clear discrepancy can be seen in the magnitude of the emissions, with CEDSv2 being significantly lower than the Tzompa-Sosa inventory in both regions. However, while there is seasonality in the Tzompa-Sosa emissions over North America, there is no seasonal variability in the emissions over Asia (and all other regions) and they are constant throughout the simulation period. In addition, the Tzompa-Sosa inventory shows no inter-annual variability in the emissions, while with the CEDSv2 inventory there is a clear evolution of the emissions over the period of 2003–2021. As a simple ad hoc solution to reconcile the differences between these two inventories, we suggest that the CEDSv2 emissions time-series be scaled up to match the magnitude of the Tzompa-Sosa emissions during the year of 2010, with the scaling factors being calculated

on a by-region basis. This could yield an inventory that better captures both the magnitude and the temporal variability of the emissions, and would improve the simulation of C_2H_6 in the model relative to observations.

CH_3OH

For CH_3OH, no statistically significant trends are found when fitting the full time-series of GEOS-Chem daily-mean total columns, with slopes of -0.45 [-0.90, 0.01] % yr^{-1} at Eureka (Fig. 6.8e) and -0.24 [-0.52, 0.05] % yr^{-1} at Thule (Fig. 6.9e). When enhancements are excluded from the fit, we find small but statistically significant decreasing trends at both locations with values of -0.43 [-0.63, -0.24] % yr^{-1} and -0.20 [-0.33, -0.07] % yr^{-1} at Eureka and Thule, respectively. At Eureka, no statistically significant trend was detected in the FTIR time-series when all data were fitted, but a negative trend on the order of -0.57 [-1.07, -0.08] % yr^{-1} was found for the period of 2007–2019 when enhancement events were removed from the time-series. At Thule, statistically significant negative trends were found in both cases with relative values of -2.02 [-2.73, -1.30] % yr^{-1} (all measurements) and -1.64 [-2.09, -1.20] % yr^{-1} (enhancements excluded). There is general consistency in the direction of the observed and modeled CH_3OH trends, and the enhancement-removed GEOS-Chem trend at Eureka falls within the range of the 95% CIs of the fitted FTIR trend, but the FTIR-derived trend at Thule is more strongly negative than the one derived from GEOS-Chem and the confidence intervals do not overlap. Further study is required to identify the source of the decreasing CH_3OH trends in the Arctic region.

HCOOH

Statistically significant decreasing trends in the modeled daily-mean total columns of HCOOH were found at Eureka and Thule with values of -1.17 [-1.97, -0.36] % yr^{-1} and -0.71 [-1.11, -0.32] % yr^{-1}, respectively (shown in Fig. 6.8f and Fig. 6.9f). If enhancement events are excluded from the GEOS-Chem time-series, we obtain slightly less negative trends of -1.09 [-1.41, -0.77] % yr^{-1} and -0.59 [-0.78, -0.41] % yr^{-1}. From the FTIR data sets, a trend of -2.98 [-4.13, -1.82] % yr^{-1} was found at Eureka between 2006–2020 when enhancements were excluded from the Fourier series fit, but no statistically significant trends were found when fitting the full Eureka time-series, and at Thule with or without enhancements. The decreasing trends simulated by GEOS-Chem appear to be driven by broad reductions in Northern Hemisphere anthropogenic emissions of HCOOH between 2003 and 2021, particularly in North America and Asia, which is shown in Fig. B.14 in the appendix. The values of the fitted slopes from GEOS-Chem fall in between the negative

trends reported by Yamanouchi et al. (2021) (-2.15 ± 0.64 % yr^{-1}) at Toronto and Bernath et al. (2020) (-0.51 ± 0.28 % yr^{-1}) in the range of 60° S to 60° N.

H_2CO

No statistically significant trends could be derived from the GEOS-Chem simulated H_2CO total columns at either Arctic FTIR site (Fig. 6.8g and Fig. 6.9g). At Eureka, a slope of -0.18 [-0.47, 0.13] % yr^{-1} when all data are included in the Fourier series fit, and -0.13 [-0.29, 0.03] % yr^{-1} when enhancements are excluded from the fit. At Thule, we find slopes of 0.08 [-0.16, 0.16] % yr^{-1} with all data, and 0.02 [-0.11, 0.16] % yr^{-1} without enhancement events. In comparison, statistically significant positive trends were derived from the FTIR measurements at both Arctic sites, with values at Eureka of 2.00 [1.21, 2.79] % yr^{-1} (all measurements) and 1.80 [1.34, 2.25] % yr^{-1} (enhancements removed), and 1.15 [0.64, 1.65] % yr^{-1} (all measurements) and 0.98 [0.67, 1.29] % yr^{-1} (enhancements removed) at Thule. To investigate whether increasing CH_4 concentrations have an influence on the simulated H_2CO columns in the Arctic, we repeated the Fourier series fitting on the modeled H_2CO partial columns at both sites. We apply separate Fourier fits to the lower troposphere (defined here as the surface to the model planetary boundary layer), free troposphere (planetary boundary layer to the model tropopause), the whole troposphere (surface to tropopause), as well as the stratosphere to TOA (tropopause to the top of the model grid) where the formation of H_2CO via CH_4 oxidation is expected to play the largest role. The fits to the partial columns are shown in Fig. B.15 and Fig. B.16 in the appendix for Eureka and Thule, respectively. At Eureka, we find no statistically significant trends in the simulated H_2CO partial columns in the troposphere, but a negative trend on the order of -0.69 [-1.00, -0.38] % yr^{-1} in the stratospheric partial columns (enhancements excluded). At Thule, we observe a decreasing trend in the lower troposphere of -0.66 [-0.86, -0.46] % yr^{-1}, a slight increasing trend in the free troposphere of 0.23 [0.05, 0.40] % yr^{-1}, and a decreasing trend in the stratosphere of -0.23 [-0.44, -0.02] % yr^{-1}, but no trend when fitting the full-troposphere partial columns. The presence of decreasing H_2CO trends in the stratosphere of the model at both Arctic sites is surprising because the modeled CH_4 total columns were found to be steadily increasing by 0.36 [0.347, 0.368] % yr^{-1} and 0.32 [0.316, 0.331] % yr^{-1} at Eureka and Thule, respectively (not shown). The source of the observed downward trend in H_2CO in the stratosphere of the model is currently unclear.

PAN

The simulated PAN daily-mean total columns are plotted along with the fitted trendlines in Fig. 6.8h and Fig. 6.9h and show statistically significant decreasing trends at both Arctic FTIR sites. At Eureka, we obtain trends of −0.80 [−1.00, −0.60] % yr^{-1} (-2.12×10^{13} [-2.66×10^{13}, -1.59×10^{13}] molec. cm^{-2} yr^{-1}) when all data are included, and −0.83 [−0.94, −0.71] % yr^{-1} (-2.19×10^{13} [-2.50×10^{13}, -1.88×10^{13}] molec. cm^{-2} yr^{-1}) when enhancements are excluded for the period of 2006–2020. At Thule, we derive trends from GEOS-Chem of −0.61 [−0.75, −0.48] % yr^{-1} (-1.72×10^{13} [-2.10×10^{13}, -1.35×10^{13}] molec. cm^{-2} yr^{-1}) and −0.58 [−0.66, −0.50] % yr^{-1} (-1.64×10^{13} [-1.87×10^{12}, -1.41×10^{13}] molec. cm^{-2} yr^{-1}) between 2003–2021 for all data and the enhancement-removed cases, respectively. These simulated trends are in disagreement with the positive trends derived from the FTIR at Eureka of 2.17 [1.28, 3.05] % yr^{-1} (all data) and 2.13 [1.64, 2.62] % yr^{-1} (enhancements excluded). As discussed earlier, this discrepancy between the modeled and observed trend in PAN can most likely be attributed to missing or underestimated emissions of precursor NMVOCs in Asia, as well as the absence of direct emissions of methylglyoxal in the model which is an substantial source of PAN in the global budget (Fischer et al., 2014; Fu et al., 2007).

6.4 Conclusions

This chapter presented the first long-term study of the trends and seasonal variability of eight tropospheric pollutant species: CO, C_2H_2, C_2H_4, C_2H_6, CH_3OH, HCOOH, H_2CO, and PAN in the North American high-Arctic region. The intra- and inter-annual variability of these eight trace gases was derived from the total column time-series measured by two high-resolution ground-based FTIR instruments located at Eureka, Nunavut (2006–2020) and Thule, Greenland (1999–2022). Strong consistency in the measured seasonal cycles was found across the two sites for all gases, and the influence of transported mid-latitude biomass burning plumes was observed to varying degrees in the time-series of all gases at Eureka and Thule. Decreasing trends consistent with past studies were found for CO and C_2H_2 with relative values of −1.10 [−1.23, −0.97] % yr^{-1} and −2.57 [−3.14, −1.96] % yr^{-1} at Eureka, and −0.89 [−0.99, −0.79] % yr^{-1} and −1.61 [−1.83, −1.39] % yr^{-1} at Thule, respectively (enhancement-excluded trends). Decreasing trends were also observed in the measured CH_3OH total columns with slopes of −0.57 [−1.07, −0.08] % yr^{-1} at Eureka and −1.64 [−2.09, −1.20] % yr^{-1} at Thule. A decreasing trend in HCOOH was found at Eureka of −2.98 [−4.13, −1.82] % yr^{-1} when enhancements were excluded, but no trend was

observed at Thule. Increasing trends were detected for C_2H_6 and H_2CO of 0.98 [0.77, 1.18] % yr^{-1} and 1.80 [1.34, 2.25] % yr^{-1} at Eureka, and 0.61 [0.39, 0.84] % yr^{-1} and 0.98 [0.67, 1.29] % yr^{-1} at Thule, respectively. A positive trend in PAN of 2.13 [1.64, 2.62] % yr^{-1} was also detected in the Eureka time-series, while at Thule the time-series of PAN only spans the period of 2015–2022 and was too short to reliably discern a trend. The time-series of C_2H_4 displayed no statistically significant trend at Eureka, but is strongly influenced by transported mid-latitude biomass burning plumes, while at Thule there were too few years (2015–2022) to establish the presence or absence of a statistically robust trend.

To provide an additional point of comparison and to assess the performance of the novel GCHP CTM in this high-latitude region, a global C48 simulation covering the period of 2003–2021 was performed using version 14.1.1 of the model. We evaluated the simulated intra- and inter-annual variability against the FTIR-derived seasonal cycles and trends at Eureka and Thule. GEOS-Chem was generally able to reproduce the shape of the FTIR-observed seasonal cycles, however significant measurement-model biases exist for some species, with the concentrations of all gases being biased low on average relative to the Arctic FTIRs. GCHP CO, C_2H_2, C_2H_6, and H_2CO were found to be well-correlated with the FTIR observations and with relative biases ranging from −5.5% (CO at Eureka) to −47.6% (C_2H_2 at Thule). GCHP HCOOH was moderately correlated with FTIR observations at both sites, with mean biases of −36.7% and −7.9% at Eureka and Thule, respectively. GCHP C_2H_4 and PAN show poor agreement with the FTIR at Thule, but improved agreement at Eureka which may be attributed to the shorter time-series of these species at Thule (2015–2022 versus 2006–2020 at Eureka). GCHP CH_3OH was found to have a very large bias on the order of −70% relative to the FTIR measurements at both Eureka and Thule, possibly indicating missing local sources or unknown chemistry that are not accounted for in the model. The modeled trends showed broad consistency with those derived from the FTIRs for CO (modeled trends of −0.85% yr^{-1} at Eureka, and −0.86% yr^{-1} at Thule), C_2H_2 (Eureka: −1.95% yr^{-1}, Thule: −1.71% yr^{-1}), and CH_3OH (Eureka: −0.43% yr^{-1}, Thule: −0.20% yr^{-1}). However, opposing trends in the model relative to the FTIRs were found for C_2H_6 (Eureka: −0.16% yr^{-1}, Thule: −0.28% yr^{-1}) and PAN (Eureka: −0.83% yr^{-1}, Thule: −0.58% yr^{-1}), and no trend was found in the modeled H_2CO columns despite positive trends being observed in the FTIR datasets at both sites.

Most discrepancies between the measured and modeled trends are believed to be attributed to errors or underestimations in the emissions of the model. In particular, the default configuration of the model uses the Tzompa-Sosa et al. (2017) inventory for C_2H_6 but it only contains emissions for the year of 2010 and does not exhibit seasonality in the emissions outside of North America,

resulting in large springtime biases at the Arctic sites and trends which disagree with observations. The modeling results of this study highlight the necessity for more frequent and rigorous model evaluation exercises over these high-latitude regions, which can be under-represented in the validation efforts for global chemical transport models such as GEOS-Chem.

Chapter 7

Conclusions and Future Work

There were three primary scientific objectives of this thesis work with a focus on improving our understanding and quantification of tropospheric pollution in the Arctic region. The first scientific objective of this thesis was to inter-compare and validate satellite observations of tropospheric pollutants over the high Arctic region with ground-based measurements and model simulations. To achieve this objective, we have performed a global inter-comparison of the CO product from the TROPOMI instrument on board the European Space Agency's Sentinel-5 Precursor satellite against solar occultation measurements from the ACE-FTS satellite instrument, as well as a targeted validation of both satellite datasets over the high Arctic against the ground-based PEARL-FTS CO time-series at Eureka, Nunavut. This was the focus of Chapter 4. Additionally, in support of this objective, I have developed and implemented two new retrievals of tropospheric pollutants for the PEARL-FTS; ethylene (C_2H_4) and peroxyacetyl nitrate (PAN). A total column time-series of both species was retrieved for 2006–2020, and has been contributed to the public NDACC archive for future use in satellite and model inter-comparisons. These new data products were also compared against the GEOS-Chem model and novel neural network retrievals of these species from the IASI instruments aboard the MetOp-A and MetOp-B satellite platforms during the August 2017 Canadian wildfire enhancement event, which was an important component of the work presented in Chapter 5 of this thesis.

The second scientific objective of this thesis was to investigate the enhancements of reactive tropospheric species in the Arctic due to the August 2017 Canadian wildfires, and to place this event in the context of previously studied fires. To address this objective, the observed enhancements in the measured total columns of CO, C_2H_4, CH_3OH, HCOOH and PAN from the PEARL-FTS, as well

as from the IASI satellite instruments have been evaluated. The wildfire emissions were estimated using the PEARL-FTS and IASI datasets in terms of the enhancement ratios, emission ratios, and emission factors and the derived values were compared against the literature. These wildfires and the subsequent plume transport were also simulated using the GEOS-Chem model, andthe plume injection heights as well as the secondary in-plume production of CH_3OH and HCOOH have been evaluated. This was the subject of Chapter 5.

The third scientific objective of this thesis was to investigate the inter- and intra-annual variability of tropospheric pollutants over the high Arctic region over long time-scales. To address this objective, the measured total column time-series of eight tropospheric pollutant species: CO, C_2H_2, C_2H_4, C_2H_6, CH_3OH, HCOOH, H_2CO, and PAN has been evaluated from the PEARL-FTS at Eureka, and an additional FTIR in Thule, Greenland. The seasonal variability and the long-term trends were analyzed and inter-compared with the literature where available. To complement the FTIR datasets and to assess the performance of the new GEOS-Chem High Performance model in the Arctic, a long simulation covering the period of 2003–2021 was performed. The inter- and intra-annual variability of these eight trace-gases were derived from the model simulation and compared these against the FTIR-derived trends and seasonality. This was the primary focus of Chapter 6. The key results of each of these studies, as well as their scientific significance in the context of the objectives of this thesis are discussed in the following subsections.

7.1 Validation of TROPOMI CO Measurements Over the High Arctic

7.1.1 Summary

Chapter 4 describes the global inter-comparisons of the TROPOMI CO product with ACE-FTS measurements, as well as the localized comparisons in the Arctic of both satellite instruments against the ground-based PEARL-FTS dataset. A methodology was developed enabling the comparisons of the TROPOMI CO column product against the measured ACE-FTS profiles, and a total of 5955 unique collocations between these two satellite instruments over the period of 28 November 2017 to 31 May 2020 were analyzed. The agreement between TROPOMI and ACE-FTS was investigated in five latitude bands: the north Polar region (60° N to 90° N), the northern Mid-latitudes (20° N to 60° N), the Equatorial region (20° S to 20° N), the southern Mid-latitudes (20° S to 60° S), and the south Polar region (60° S to 90° S). A latitudinal dependence on the mean biases was observed,

with the positive mean biases in the north and south Polar regions ($7.93 \pm 0.61\%$ and $7.21 \pm 0.52\%$, respectively), and a negative mean bias of $-9.41 \pm 0.55\%$ in the Equatorial region. The influence of cloud contamination in the TROPOMI CO dataset and the impacts of averaging kernel smoothing on the comparisons with ACE-FTS was also investigated. Clear-sky pixels were found to be biased higher, with poorer correlations on average than the clear+cloudy scenes and cloud-covered scenes, suggesting that the TM5 reference profile shape used in the TROPOMI CO retrieval can have a measurable impact on the TROPOMI columns in the comparisons. The latitudinal dependence of the biases was found to be present in both the unsmoothed and smoothed cases, and the magnitude of the observed mean biases exceeds the ACE-FTS retrieval uncertainties of 5% in all latitude regions except the northern Mid-latitudes. However, despite the observed biases, strong correlations in the range of $R = 0.93$ to $R = 0.86$ were found between the TROPOMI and ACE-FTS CO data products across all latitude bands indicating robust agreement between these two instruments.

To complement the global comparisons of TROPOMI and ACE-FTS and to provide additional context to the observed biases at high latitudes, both satellite data products were compared against smoothed CO measurements from the PEARL-FTS at Eureka. A total of 1875 collocations between the PEARL-FTS and TROPOMI were processed in the period of 3 March 2018 to 27 March 2020, and a strong correlation of $R = 0.88$ was found between the two datasets, however a mean positive bias of $14.7 \pm 0.16\%$ was also observed, which was consistent with the validation efforts of Sha et al. (2021). Lastly, a partial column comparison between the ACE-FTS and PEARL-FTS data products was performed, with a total of 3015 unique collocations analyzed between the period of 25 February 2007 to 18 March 2020. These partial column comparisons showed good agreement between the PEARL-FTS and ACE-FTS partial columns, with a correlation coefficient of $R = 0.79$, and a mean positive bias of $7.89 \pm 0.21\%$ in ACE-FTS with respect to the PEARL-FTS. These results were found to be consistent with the earlier validation results of Griffin et al. (2017). In general, the magnitude and direction of the mean biases was consistent across all intercomparisons, suggesting that the TROPOMI CO product exhibits a high bias in the high-Arctic region consistent with the results of Sha et al. (2021). However, the mean relative differences fall within the TROPOMI mission accuracy requirements for the CO product of $\pm 15\%$, indicating that the data quality of the CO product in these high-latitude regions meets the specifications.

7.1.2 Significance

The inter-comparisons of the TROPOMI CO product builds upon earlier satellite validation studies involving the PEARL-FTS by Holl et al. (2016) and Griffin et al. (2017). A methodology was developed based upon the work by Holl et al. (2016) enabling the comparison of the TROPOMI data product against the partial column product of ACE-FTS, and this methodology was employed to perform a global comparison of these data products. This study supports the results of the broader ground-based validation work by Sha et al. (2021), and demonstrates the superb data quality and accuracy of the TROPOMI instrument, and underscores the fact that this valuable dataset could be applied to studies of CO in the high-Arctic region. This study also serves to verify the previously observed agreement between the PEARL-FTS and ACE-FTS CO data products, which were validated for earlier versions of the data products by Griffin et al. (2017).

7.2 The August 2017 Canadian Wildfires

7.2.1 Summary

Chapter 5 investigates the enhancements of CO, C_2H_4, CH_3OH, HCOOH and PAN observed by the IASI satellite instruments and the ground-based PEARL-FTS resulting from the August 2017 Canadian wildfires in British Columbia and the Northwest Territories. The August 2017 wildfires led to the largest observed short-term perturbations in the total column concentrations of PAN, C_2H_4, and HCOOH in the 2006–2020 time-series of PEARL-FTS measurements. The IASI instruments were found to observe a similar temporal pattern in the measured enhancements at Eureka but smaller total columns of most species on average relative to the PEARL-FTS, which can likely be attributed to the lower overall sensitivity of the IASI retrievals at high latitudes as a result of the low thermal contrast in the region. Enhancement ratios, emission ratios, and emission factors for all species relative to CO were calculated from both PEARL-FTS and IASI measurements. The derived emission factors for PAN and CH_3OH were found to be in good agreement between the PEARL-FTS, IASI, and previous studies, while those for C_2H_4 and HCOOH, particularly those derived from the PEARL-FTS, are significantly larger than previously reported in the literature. These findings suggest higher than expected emissions of C_2H_4 and HCOOH from the British Columbia and Northwest Territories wildfires.

The wildfires and the subsequent plume transport to Eureka were simulated using the GEOS-Chem model. When using the default biomass burning emissions injection scheme, the model pro-

duces a severe transport error resulting in a poor representation of the observed enhancements and weak correlations with PEARL-FTS and IASI measurements in the vicinity of Eureka. It was found that by modifying the injection height scheme, and injecting the wildfire emissions directly into higher model levels, GEOS-Chem was able to reproduce the plume transport and the observed enhancements much more accurately, and displayed greatly improved correlations with observations at Eureka. CO and PAN were also used as tracer species for the fire plumes, and model sensitivity tests were performed to determine the appropriate injection heights for the fires, finding that injection heights of 12.5 km for the British Columbia fires (based on Peterson et al. (2018) and Fromm et al. (2021)), and 10 km for the Northwest Territories fires, produced the strongest correlations with PEARL-FTS measurements at Eureka for CO and PAN.

Additionally, GEOS-Chem was used to investigate the fraction of the enhanced CH_3OH and HCOOH total columns at Eureka that could be attributed to secondary in-plume production. It was found that the effect of secondary production was minimal for CH_3OH (approximately 3% of the enhanced total columns), however for HCOOH secondary production was a significant component (approximately 18%) of the maximum enhanced total columns at Eureka. The HCOOH emission factors derived from the PEARL-FTS and IASI were corrected to account for this secondary production component, however, a significant discrepancy with the values previously reported in the literature was still found. These findings further support the conclusions that there were unusually large emissions of HCOOH from the August 2017 Canadian wildfires.

7.2.2 Significance

The August 2017 Canadian wildfires were an exceptional biomass burning event, and led to the largest observed enhancements in the total columns of PAN, C_2H_4, and HCOOH over the 2006–2020 PEARL-FTS time-series. This study builds upon the earlier work by Lutsch et al. (2019), who investigated the enhancements of CO, C_2H_6, HCN and NH_3 at Eureka resulting from these same fires. The enhancement ratios, emission ratios, and emission factors of C_2H_4, CH_3OH, HCOOH, and PAN calculated from the PEARL-FTS and IASI datasets are a contribution to the relatively sparse literature of boreal wildfire emissions, and they highlight the unusually high emissions of C_2H_4 and HCOOH from these fires. Furthermore, this study was also the first to employ the new IASI neural network PAN and C_2H_4 products to investigate biomass burning enhancements. Lastly, areas for improvement in the GEOS-Chem model have been suggested, particularly with regards to the injection scheme for biomass burning emissions. A simple methodology for estimating and

modeling the biomass burning emissions of species which are absent from the GFAS inventory has also been outlined, an approach which was later applied on a larger scale in GCHP for the study in Chapter 6. In general, the results of this study emphasizes that biomass burning is likely to become an increasingly large component of the budgets and annual cycles of short-lived reactive VOCs at high northern latitudes. The impacts that these transient wildfire-driven reactive VOC injections may have on the high-Arctic environment and atmosphere should be investigated in further depth in future studies.

7.3 Long-term Trends in Arctic Tropospheric Pollutants

7.3.1 Summary

Chapter 6 presents the long-term trends and seasonality of CO, C_2H_2, C_2H_4, C_2H_6, CH_3OH, HCOOH, H_2CO, and PAN in the North American high-Arctic region estimated from the total column time-series of two Arctic ground-based FTIRs at Eureka, Nunavut (2006–2020) and Thule, Greenland (1999–2022). Good consistency in the measured seasonal cycles was found for all gases between the two Arctic FTIR sites, and the influence of transported biomass burning plumes is observed to varying degrees in all species. Decreasing trends consistent with the literature were found for CO and C_2H_2, with slopes of -1.10 % yr^{-1} and -2.57 % yr^{-1} at Eureka, and -0.89 % yr^{-1} and -1.61 % yr^{-1} at Thule (enhancement-removed trends). A decreasing trend in CH_3OH was detected of -0.57 % yr^{-1} and -1.64 % yr^{-1} at Eureka and Thule, respectively. A decreasing trend in HCOOH was found at Eureka of -2.98 % yr^{-1}, but no trend was seen at Thule. Increasing trends were detected for C_2H_6 and H_2CO of 0.98 % yr^{-1} and 1.80 % yr^{-1} at Eureka, and 0.61 % yr^{-1} and 0.98 % yr^{-1} at Thule. A clear increasing trend in PAN was found at Eureka of 2.13 % yr^{-1} and no trend was observed in C_2H_4 there, but the Thule PAN and C_2H_4 time-series were too short (2015–2022) to reliably discern trends in these gases at that site.

To complement the ground-based FTIR observations and to evaluate the capabilities of the novel GEOS-Chem High Performance CTM in the high Arctic, a global C48 (approximately 2°×2.5° horizontal resolution) simulation was performed covering the period of 2003–2021 using version 14.1.1 of the model. The seasonal cycles and long-term trends of CO, C_2H_2, C_2H_4, C_2H_6, CH_3OH, HCOOH, H_2CO, and PAN were calculated from the GEOS-Chem simulation applying the same methodology as for the FTIR datasets, and the simulated intra- and inter-annual variability were evaluated against the FTIR-derived seasonal cycles and trends at Eureka and Thule. GEOS-Chem

was found to generally reproduce the shape of the FTIR-observed seasonal cycles, however significant measurement-model biases were found for some of the trace gases, with the GEOS-Chem total column concentrations being biased low on average at the two sites relative to observations for all species.

CO, C_2H_2, C_2H_6, and H_2CO were found to be well-correlated with the FTIR observations with small to moderate biases ranging from -5.5% (CO at Eureka) to -47.6% (C_2H_2 at Thule). HCOOH was found to be moderately correlated with the FTIR observations at Eureka and Thule, with mean relative biases of -36.7% and -7.9%, respectively. The simulated C_2H_4 and PAN total columns were found to have poor agreement with the FTIR-measured columns at Thule, but better agreement at Eureka, which may be attributed to the shorter time-series of measurements at Thule (2015–2022 versus 2006–2020 at Eureka). GEOS-Chem simulated CH_3OH columns were found to display a very large bias on the order of -70% relative to the FTIR measurements at both Arctic sites, possibly suggesting that there are missing local sources or unknown chemical pathways which are not being captured in the model. The modeled trends show broad consistency with the FTIR-derived trends for CO (modeled trends of -0.85% yr^{-1} at Eureka, and -0.86% yr^{-1} at Thule), C_2H_2 (Eureka: -1.95% yr^{-1}, Thule: -1.71% yr^{-1}), and CH_3OH (Eureka: -0.43% yr^{-1}, Thule: -0.20% yr^{-1}). However, opposing trends were found in the model relative to the FTIRs for C_2H_6 (Eureka: -0.16% yr^{-1}, Thule: -0.28% yr^{-1}) and PAN (Eureka: -0.83% yr^{-1}, Thule: -0.58% yr^{-1}), and no statistically significant trend was found for H_2CO despite positive trends being observed in the FTIR total columns at Eureka and Thule. It was found that many of the discrepancies between the measured and modeled trends can be attributed to errors or underestimations in the emissions inventories used by the model.

7.3.2 Significance

As it stands, measurements of many of these reactive tropospheric trace gases are extremely sparse in the high-Arctic region, and very few studies have evaluated the trends of most of these species both globally and in the Arctic. Although satellite instruments exist that can be used to retrieve many of these gases (e.g., IASI, TES, and CrIS), they often encounter difficulties when measuring over these high-latitude regions due to issues with poor thermal contrast. As a result, ground-based FTIR observations are vital for the measurement and monitoring of these trace gases in the Arctic region over long time-scales. Understanding the long-term trends of these reactive tropospheric gases can aid in predicting future changes and impacts on the sensitive Arctic climate, environment, and

atmosphere. This study is the first to present long-term trends (> 10 years) of C_2H_2, C_2H_4, CH_3OH, HCOOH, and PAN derived from ground-based FTIR measurements in the high Arctic. Additionally, most global chemical transport models are not well-validated in the Arctic due to the dearth of reliable observations in the region. This study is the first to evaluate the performance of GCHP against Arctic ground-based observations, and in Chapter 6, several suggestions are provided for improvements that could be made in current or future versions of the model to improve the simulation of these reactive trace-gases and enhance agreement with the ground-based FTIR observations at high latitudes.

7.4 Future Work

Improving the quality and quantity of measurements from the PEARL-FTS is a continuous effort that has been carried out by a long line of graduate students since the instrument was installed at PEARL in July 2006. There are several suggestions on ways in which the FTIR measurements at PEARL could be improved, namely enhancing the automation of the measurement system to reduce the amount of input required from on-site operators. A few suggestions that could improve the operation of the instrument are:

1. Improvements to the solar tracker: Currently the sun-tracker camera is mounted below the 45° input mirror outside of the instrument. However, the current placement of the camera may be prone to tracking issues over time as it does not take into account the position of the solar beam on the input aperture. This exact issue had occurred in early 2023, when the physical position of the solar tracker itself had changed due to sag of the support base, leading to the solar beam no longer filling the first off-axis parabolic mirror and not being centered on the input aperture. Placing the sun-tracker camera inside the source compartment, and using position of the solar beam on the aperture as the center-point of the Sun would negate this issue. The Bruker-made solar trackers and CamTracker software currently use this approach with generally favorable results.

2. Enhancing the automation of the system: As it currently stands, a high degree of on-site support is required for mid-infrared measurements with the PEARL-FTS, including manually cooling the detectors with liquid nitrogen each day before measurements commence and swapping the beamsplitter for switching between mid- and near-infrared measurements. An automatic liquid nitrogen fill-system connected to a large LN_2 dewar could be installed, al-

lowing the detectors to be cooled remotely and greatly reducing the amount of input required from on-site operators. Additionally, extended range KBr beamsplitters have been undergoing testing recently within the NDACC-IRWG and TCCON networks, which would allow a single beamsplitter to be used for both NDACC and TCCON measurements. Example results of an extended range KBr beamsplitter were presented at the 2023 NDACC-COCCON-TCCON meeting in Spa, Belgium and it showed promise for both NDACC and TCCON solar measurements. The implementation of an automatic LN_2 fill-system and an extended range KBr beamsplitter would allow the PEARL-FTS to be run almost fully remotely in mid-infrared mode, only requiring personnel to refill the LN_2 dewar approximately once per week.

3. Improvements to the sun-tracker dome: The solar-tracker Robodome and suntracker system have been encountering a slew of mechanical and software issues in recent years, leading to a high degree of unreliability when operating the instrument and sun-tracker remotely. These issues include wear on the Robodome plastic tracks leading to issues opening and closing the dome, and unresponsiveness when issuing open/close commands (i.e., a dome open command will be issued from the Trax software and the software will report that the dome is open, but it is in-fact still closed). One issue with the current Robodome is that the open/close logic is extremely simple, and there is no feedback to the Trax software on whether the dome is physically open or closed. To aid in remote operation of the dome, we installed an upward-facing webcam in July 2023, allowing a remote operator to confirm the physical status of the dome. Ideally, the Robodome would be replaced with a more mechanically reliable system at some point in the future, but this would likely require a re-working of the Trax software which may be a large effort.

In addition to improvements to the PEARL-FTS measurement system, there are some suggestions for avenues of future work based on the work presented in the chapters of this thesis. In Chapter 3, new retrievals of C_2H_4 and PAN were presented, and although some unsuccessful efforts were made to implement and test the PAN retrievals for the University of Toronto Toronto Atmospheric Observatory (largely owing to the greater interference from water vapor there), the retrieval of C_2H_4 could possibly be tested and implemented for this site. Additionally, the full suite of Eureka FTIR retrievals will need to be re-processed using the new WACCMv7 *a priori* generated for the NDACC-IRWG (which is a 60-year average of the period of 1980–2040), and new spectroscopic line-lists (HITRAN 2020 or ATM20). This process has already started for several species, and the new line-lists and WACCM *a priori* have been tested for C_2H_6, $ClONO_2$, HCl, HF, and HNO_3 with generally

favorable results, however a future graduate student will need to complete the re-processing efforts.

The comparisons between the PEARL-FTS, ACE-FTS, and TROPOMI CO data products presented in Chapter 4 could be repeated for the new version 2 TROPOMI CO processor that is described in Borsdorff et al. (2019) to verify that the latitudinal dependence of the biases has been ameliorated. Additionally, there are potential avenues for applying the methodology to perform comparisons of ACE-FTS measurements with other TROPOMI data products, and possibly datasets from other nadir-sounding satellite instruments. Building upon the work presented in Chapter 5, FTIR measurements made during the August 2017 fire event from the TCCON site located at East Trout Lake, Saskatchewan (54.35° N, 104.98° W) could be incorporated into the analysis. The EnhRs, ERs, and EFs could be calculated from the measurements at East Trout Lake and compared with those derived at Eureka, possibly providing an interesting perspective on the aging of these wildfire smoke plumes and a more accurate quantification of the true ERs as these measurements were made much closer to the source of the fires.

Based on the GEOS-Chem results presented in Chapter 5 and Chapter 6, it is clear that there is room for improvement in certain aspects of the model. One area of the model in particular which could be improved is the biomass burning injection height scheme. An improved injection height scheme for GEOS-Chem was described by Zhu et al. (2018) which showed significant improvements relative to observations for CO and PAN, however this scheme was never implemented into the main branch of the GEOS-Chem model. Implementing an improved scheme similar to that described by Zhu et al. (2018) would likely greatly improve the representation of boreal wildfires in the model, which tend to inject smoke much higher into the atmosphere than fires at lower mid-latitudes and in the tropics. Furthermore, based on the findings in Chapter 6, it is a possibility that the emissions of many of the tropospheric species (most notably C_2H_2, CH_3OH and PAN precursors) are underestimated in the current emissions inventories. Further work could be done to determine appropriate scaling factors to reduce the measurement-model biases that were observed. This could be done using either forward model sensitivity tests, or an inverse modeling approach. Additionally, the emissions of C_2H_6 implemented in the model show room for improvement. The Tzompa-Sosa et al. (2017) emissions inventory (currently the default option) does not contain any seasonal variability outside of North America and no inter-annual variability in the emissions, meanwhile the alternative CEDSv2 inventory solves the problems of the Tzompa-Sosa inventory but displays a significant underestimation in terms of the magnitude of the C_2H_6 emissions. As a simple ad hoc solution, the CEDSv2 inventory could be regionally scaled up to match the magnitude of the Tzompa-Sosa inventory in the year of 2010, which would preserve the magnitude of the emissions but also capture

the appropriate intra- and inter-annual variability of the emissions. If improvements are made to the emissions in GEOS-Chem, another long GCHP simulation could be performed and the agreement with the FTIR observations at the Arctic sites could be re-evaluated.

Appendix A

Supplemental Figures for Chapter 5

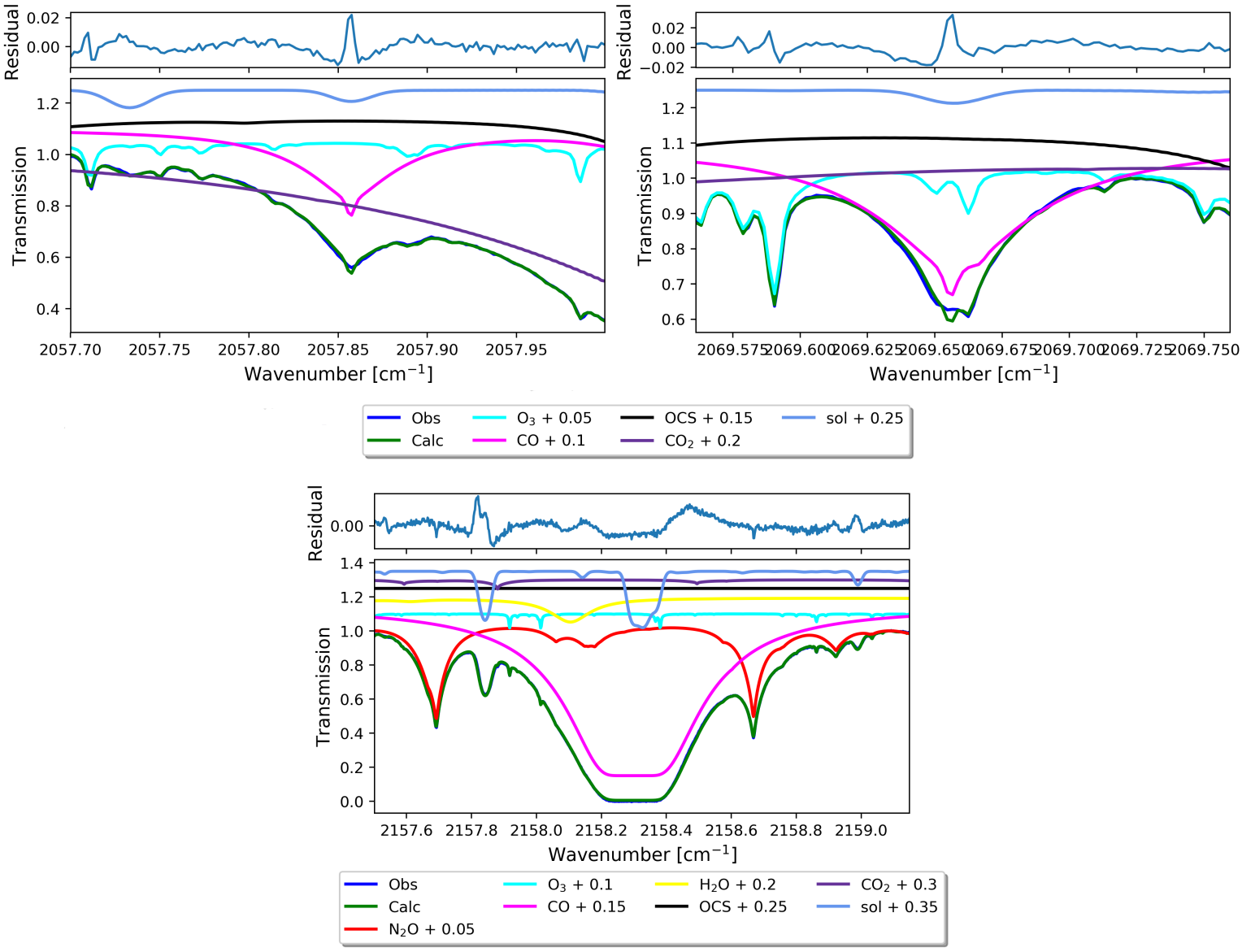

Figure A.1: An example spectral fit of CO and interfering species in the three fitting microwindows for a PEARL-FTS measurement taken during the wildfire enhancement event on 19 August 2017.

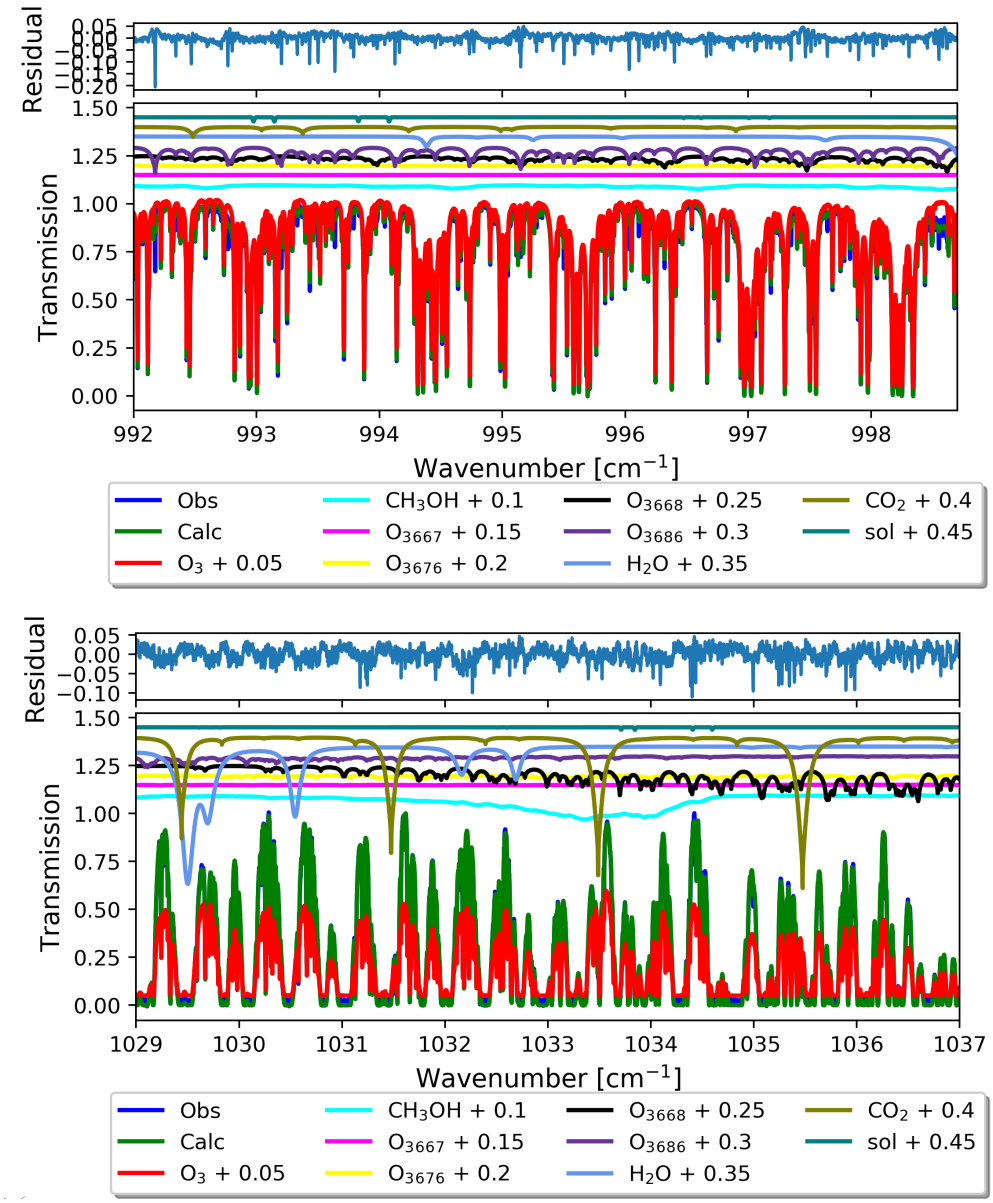

Figure A.2: An example spectral fit of CH_3OH and interfering species in the two fitting microwindows for a PEARL-FTS measurement taken during the wildfire enhancement event on 19 August 2017.

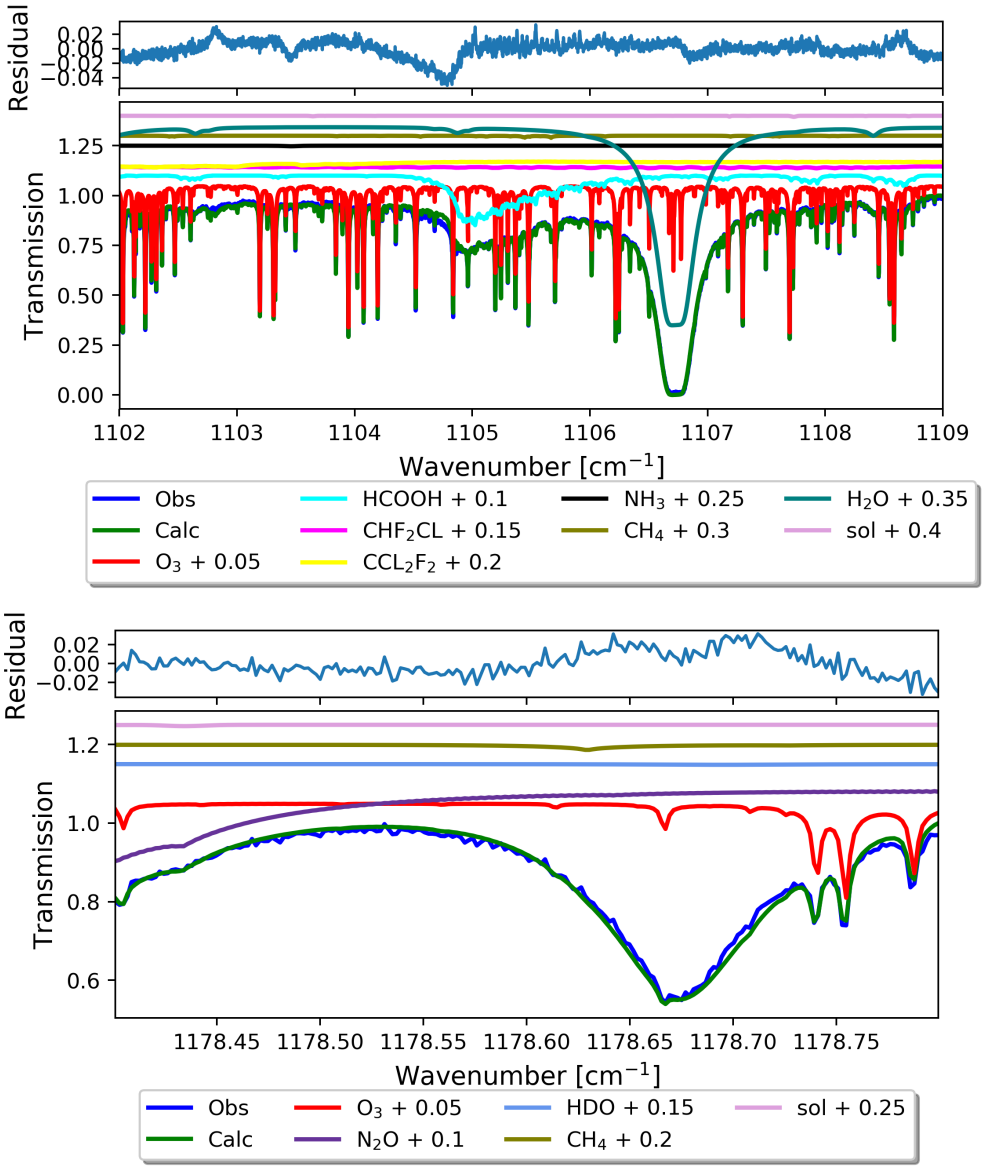

Figure A.3: An example spectral fit of HCOOH and interfering species in the two fitting microwindows for a PEARL-FTS measurement taken during the wildfire enhancement event on 19 August 2017.

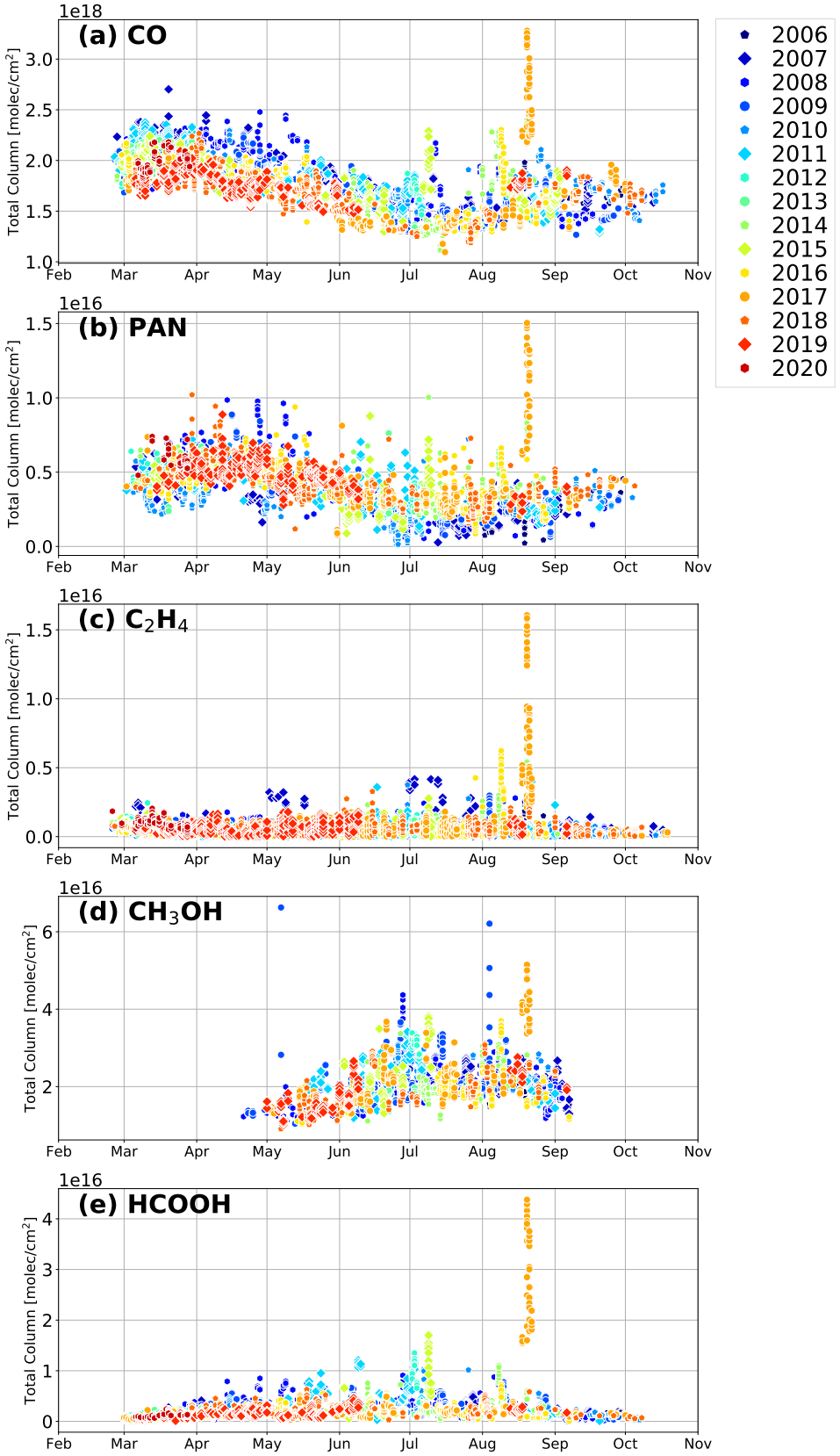

Figure A.4: Total column time series of **(a)** CO, **(b)** PAN, **(c)** C_2H_4, **(d)** CH_3OH, and **(e)** HCOOH retrieved from the PEARL-FTS at Eureka for the period of 2006–2020. Measurements from each year are plotted in differing colors and marker styles to better highlight previous enhancements and anomalies.

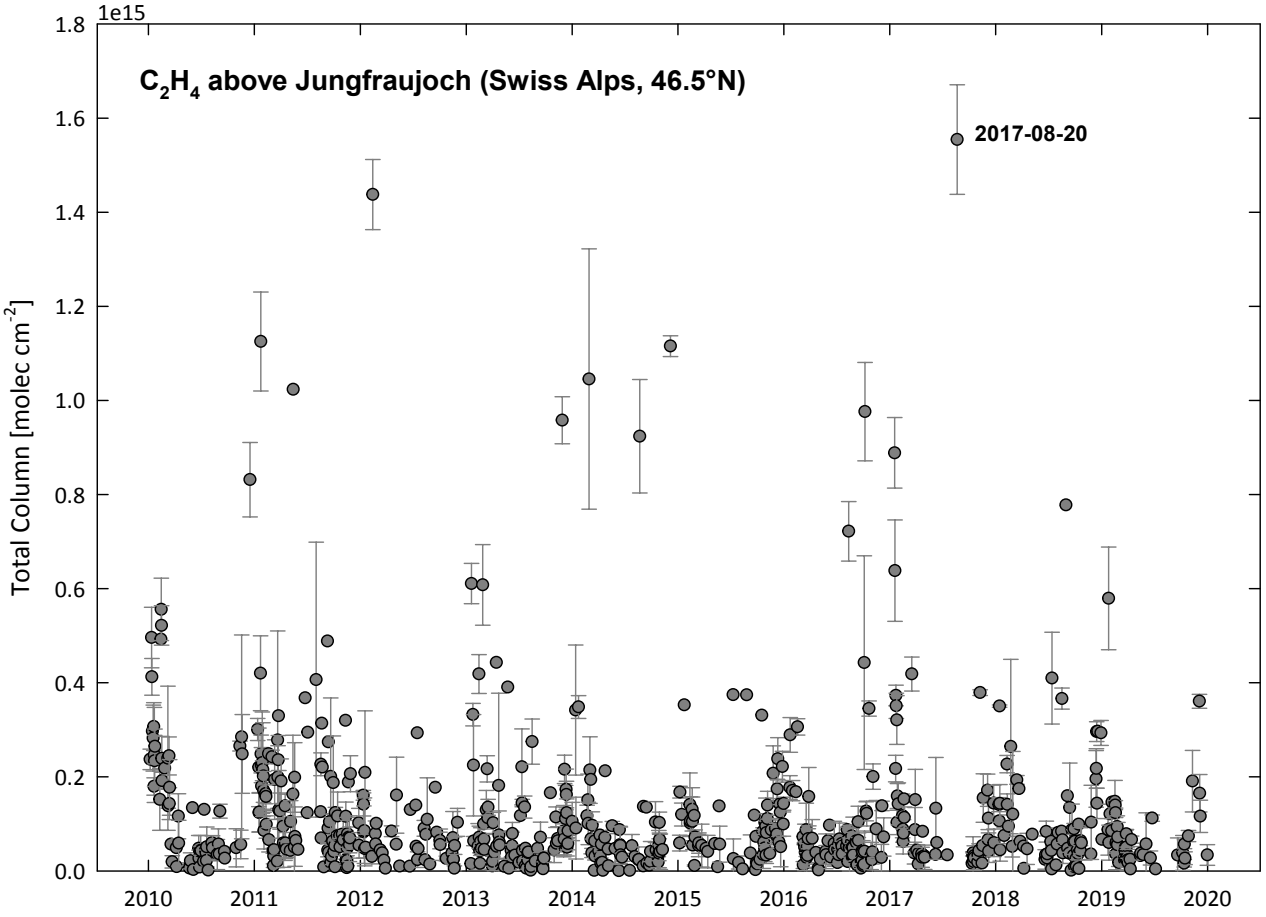

Figure A.5: Time series of daily-averaged C_2H_4 total columns retrieved from a ground-based Bruker 120HR FTIR at Jungfraujoch, Switzerland (46.55° N, 7.98° E, 3580 m a.s.l) for the period of 2010–2020. The daily mean corresponding to 20 August 2017 is highlighted. Data courtesy of Emmanuel Mahieu.

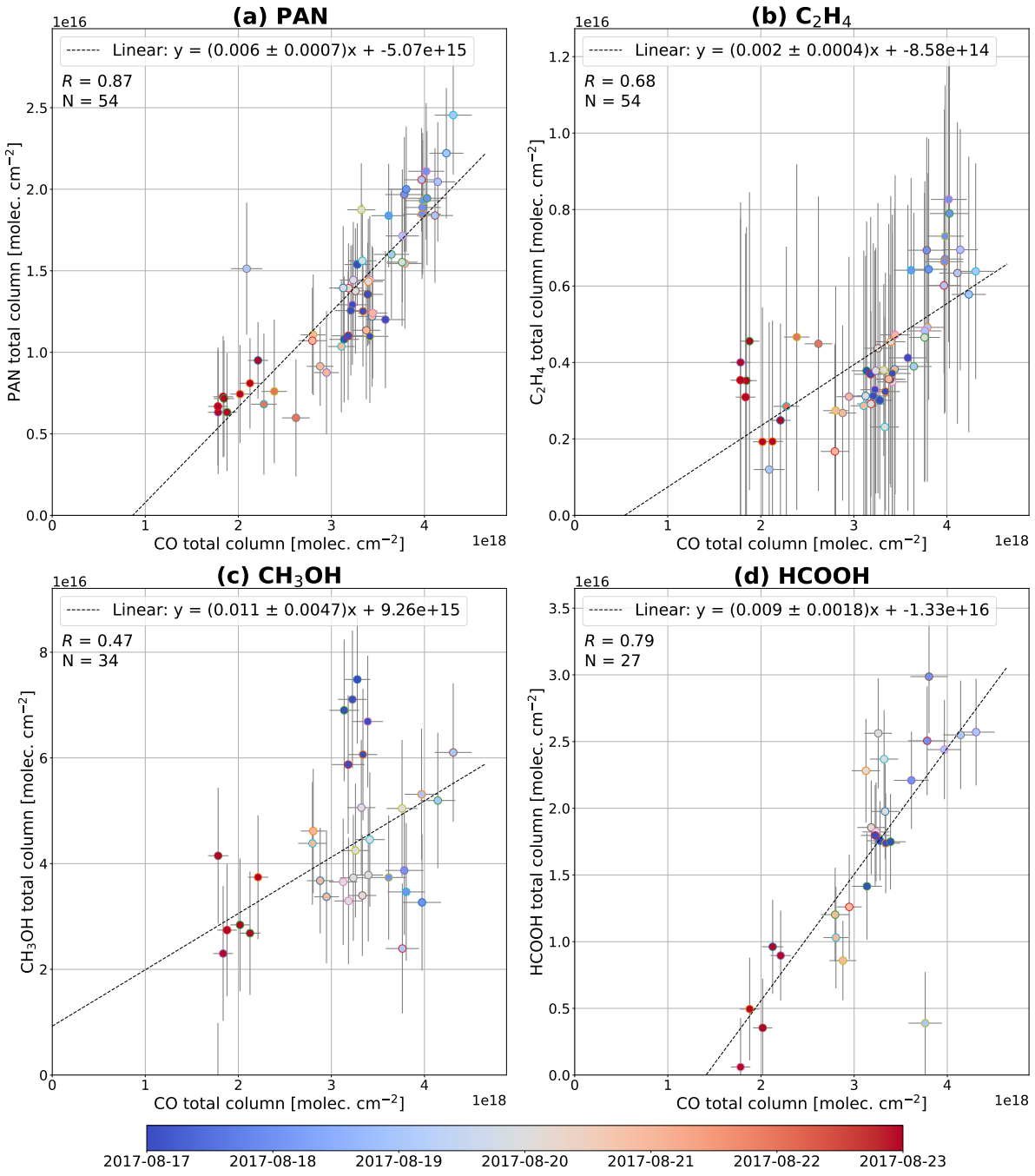

Figure A.6: Enhancement ratios derived from IASI-A and IASI-B hourly-averaged measurements near Eureka of PAN, C_2H_4, CH_3OH, and HCOOH relative to CO during the fire-affected period of 17 to 23 August 2017. Data points are colored based on the day on which the measurements were made. The equation for the linear fit, the Pearson correlation coefficient R, and the number of fire-affected measurements are shown in the upper left of each panel.

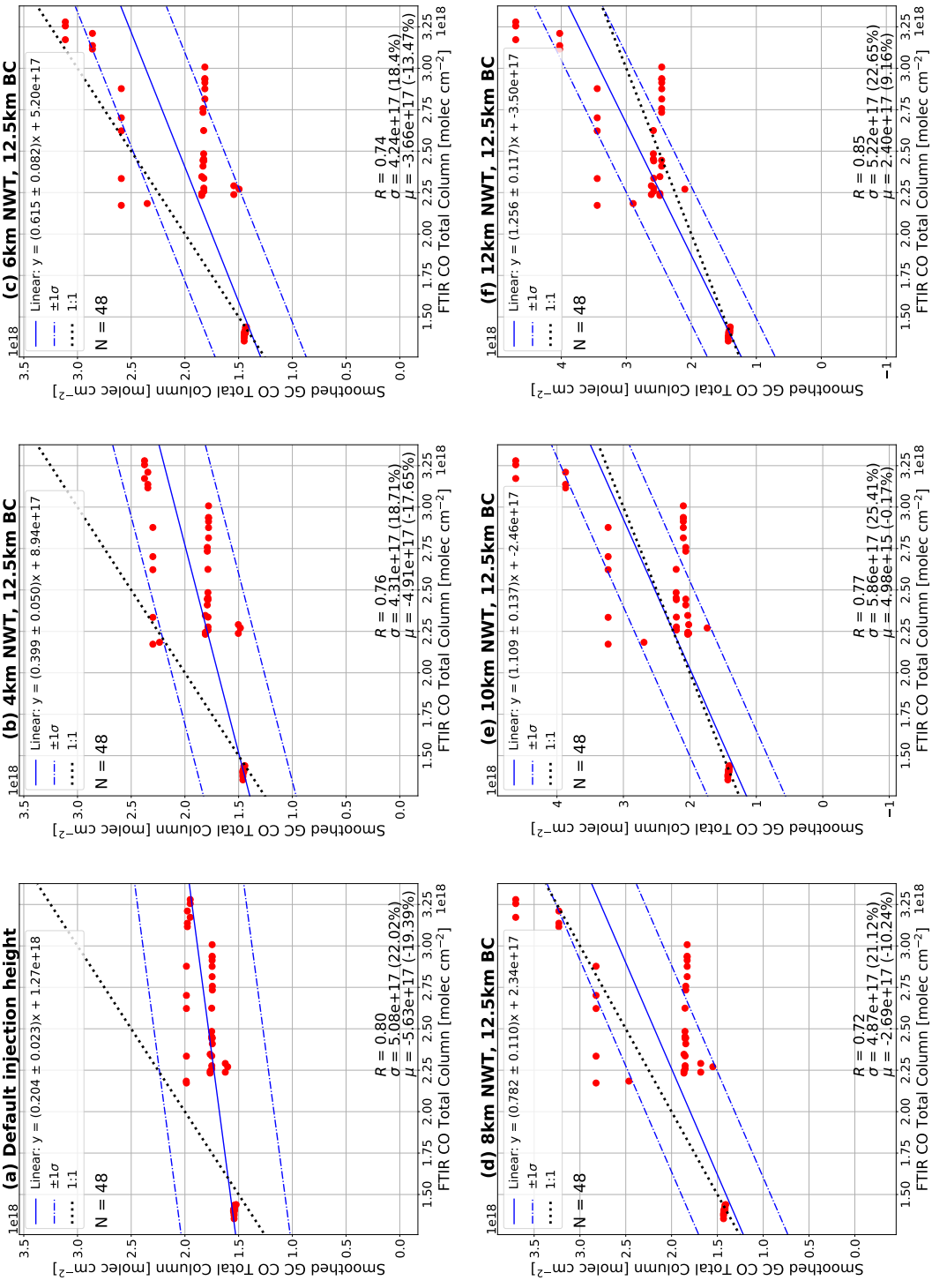

Figure A.7: Correlation plots of smoothed GEOS-Chem total columns of CO versus retrieved CO total columns from the PEARL-FTS for **(a)** the simulation using the default GFAS injection height scheme, **(b)** an injection height of 4 km for the NWT fires and 12.5 km for BC fires, **(c)** an injection height of 5 km for the NWT fires and 12.5 km for the BC fires, **(d)** an injection height of 6 km for the NWT fires and 12.5 km for the BC fires, **(e)** an injection height of 8 km for the NWT fires and 12.5 km for the BC fires, and **(f)** an injection height of 10 km for the NWT fires and 12.5 km for the BC fires.

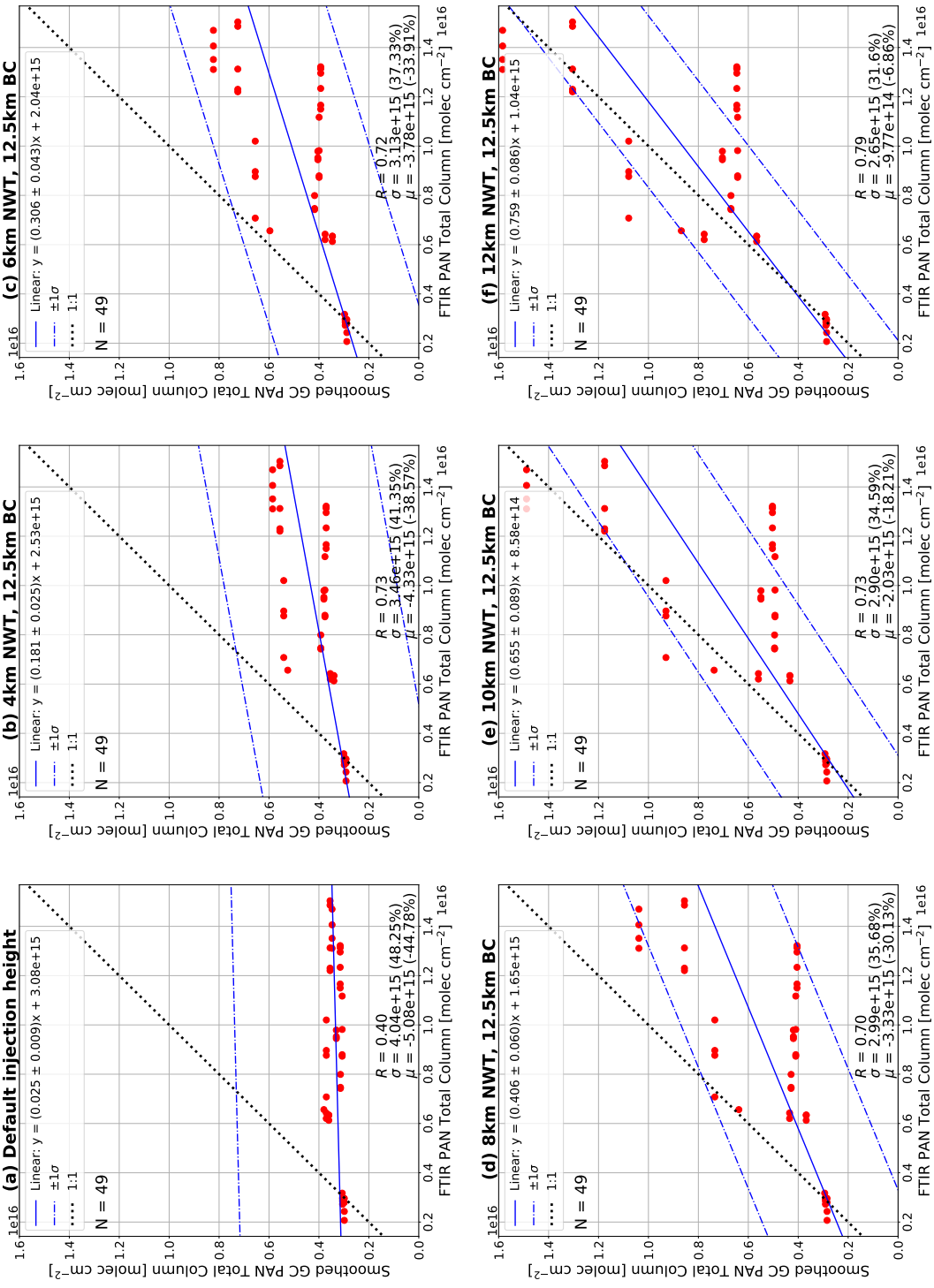

Figure A.8: Correlation plots of smoothed GEOS-Chem total columns of PAN versus retrieved PAN total columns from the PEARL-FTS for **(a)** the simulation using the default GFAS injection height scheme, **(b)** an injection height of 4 km for the NWT fires and 12.5 km for the BC fires, **(c)** an injection height of 5 km for the NWT fires and 12.5 km for the BC fires, **(d)** an injection height of 6 km for the NWT fires and 12.5 km for the BC fires, **(e)** an injection height of 8 km for the NWT fires and 12.5 km for the BC fires, and **(f)** an injection height of 10 km for the NWT fires and 12.5 km for the BC fires.

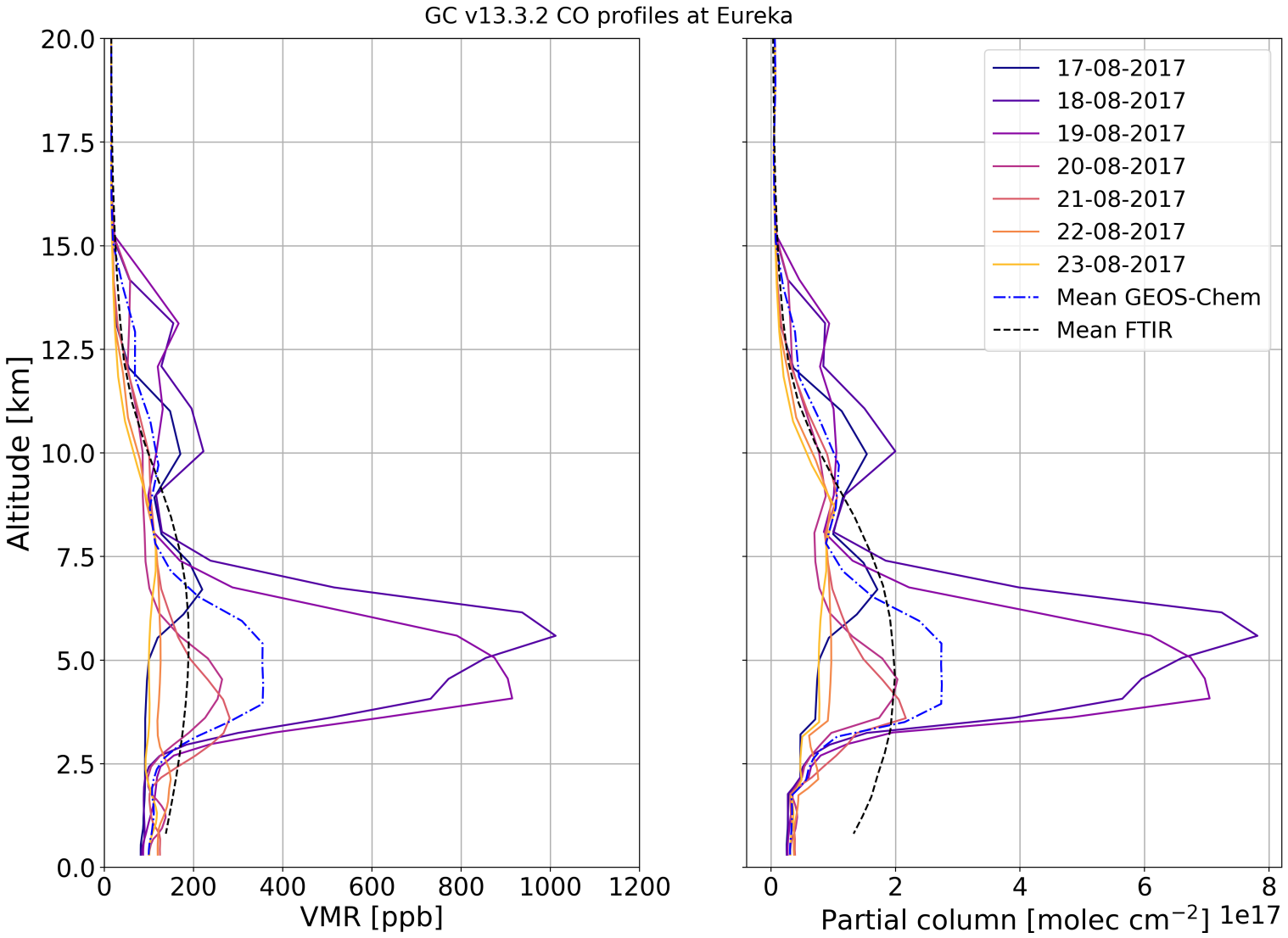

Figure A.9: Simulated GEOS-Chem CO (left) VMR profiles, and (right) partial column profiles at Eureka (i.e., within the 2°×2.5° gridbox encompassing the FTIR site) for each day during the August 2017 fire period from the simulation with a 10km injection height for the NWT fires and 12.5 km injection height for the BC fires. The mean of the GEOS-Chem profiles during the fire period is included as a blue dash-dotted line, and the mean FTIR CO profiles calculated over the same period are included as a black dashed line.

Appendix B

Supplemental Figures for Chapter 6

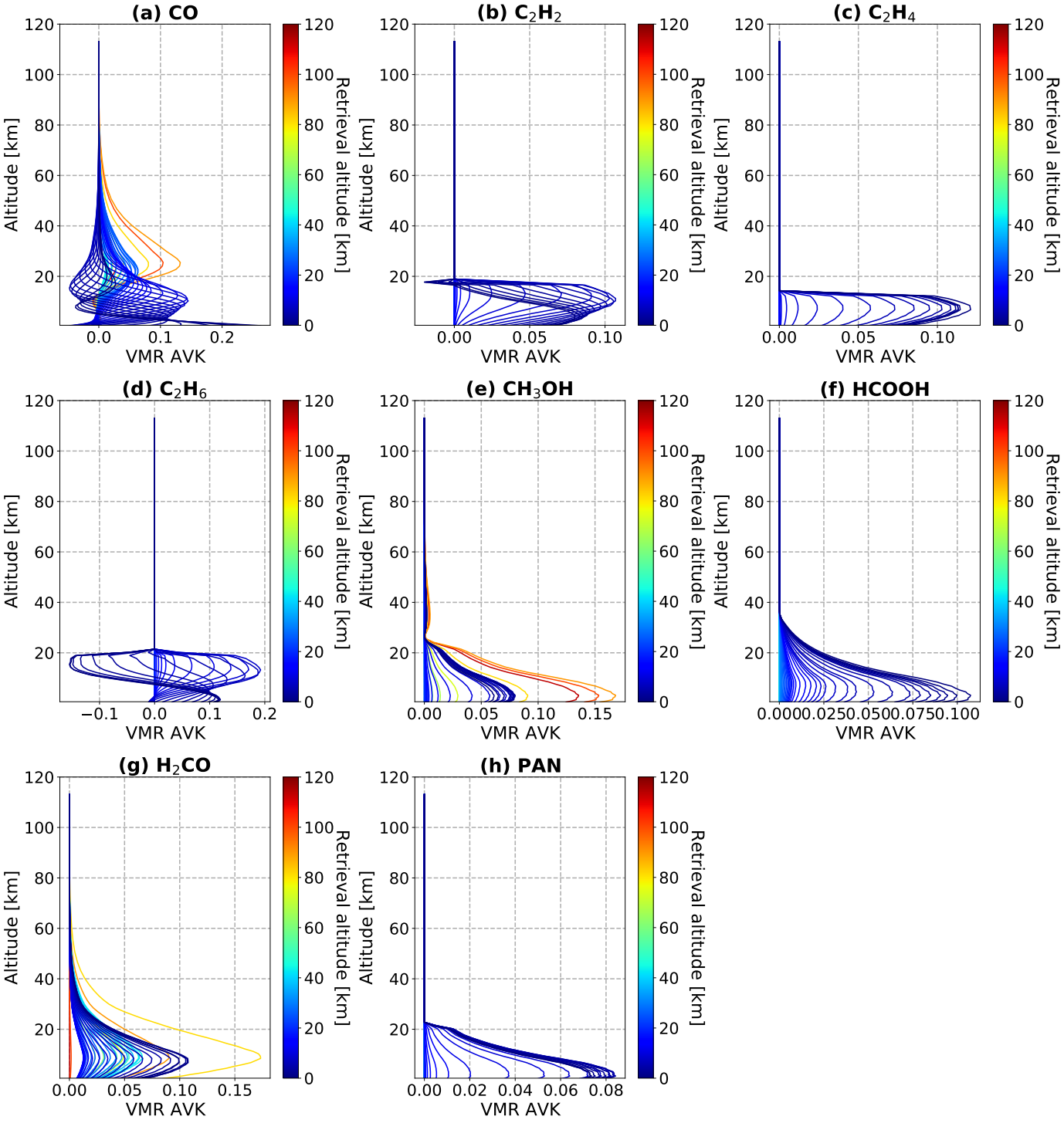

Figure B.1: Mean (1999–2022) Thule VMR averaging kernels for **(a)** CO, **(b)** C_2H_2, **(c)** C_2H_4, **(d)** C_2H_6, **(e)** CH_3OH, **(f)** HCOOH, **(g)** H_2CO, and **(h)** PAN. Note for CH_3OH these are means calculated over 2011–2022, and for C_2H_4 and PAN these are means calculated over 2015–2022.

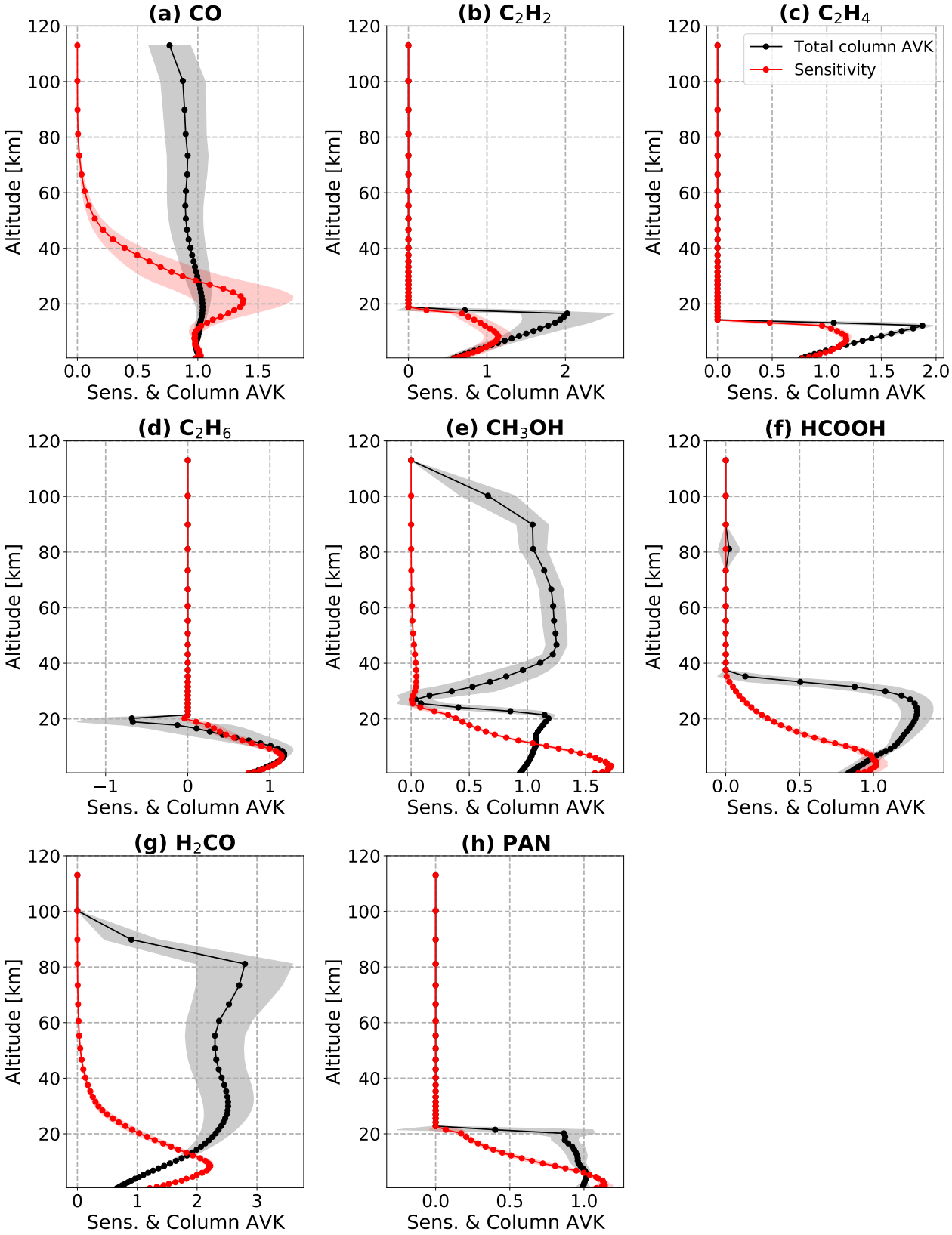

Figure B.2: Mean (1999–2022) Thule total column averaging kernels and retrieval sensitivity for **(a)** CO, **(b)** C_2H_2, **(c)** C_2H_4, **(d)** C_2H_6, **(e)** CH_3OH, **(f)** HCOOH, **(g)** H_2CO, and **(h)** PAN. The black and red shaded areas denote one standard deviation from the means. Note for CH_3OH these are means calculated over 2011–2022, and for C_2H_4 and PAN these are means calculated over 2015–2022.

BONA	Boreal North America	NHAF	Northern Hemisphere Africa
TENA	Temperate North America	SHAF	Southern Hemisphere Africa
CEAM	Central America	BOAS	Boreal Asia
NHSA	Northern Hemisphere South America	CEAS	Central Asia
SHSA	Southern Hemisphere South America	SEAS	Southeast Asia
EURO	Europe	EQAS	Equatorial Asia
MIDE	Middle East	AUST	Australia and New Zealand

Figure B.3: The Global Fire Emissions Database version 4.1 (GFASv4.1; Van Der Werf et al., 2017) basis region map used to distribute the emissions of C_2H_2 and HCOOH in GFASv1.2 as described in Sect. 6.2.2. Figure obtained from https://www.globalfiredata.org/data.html.

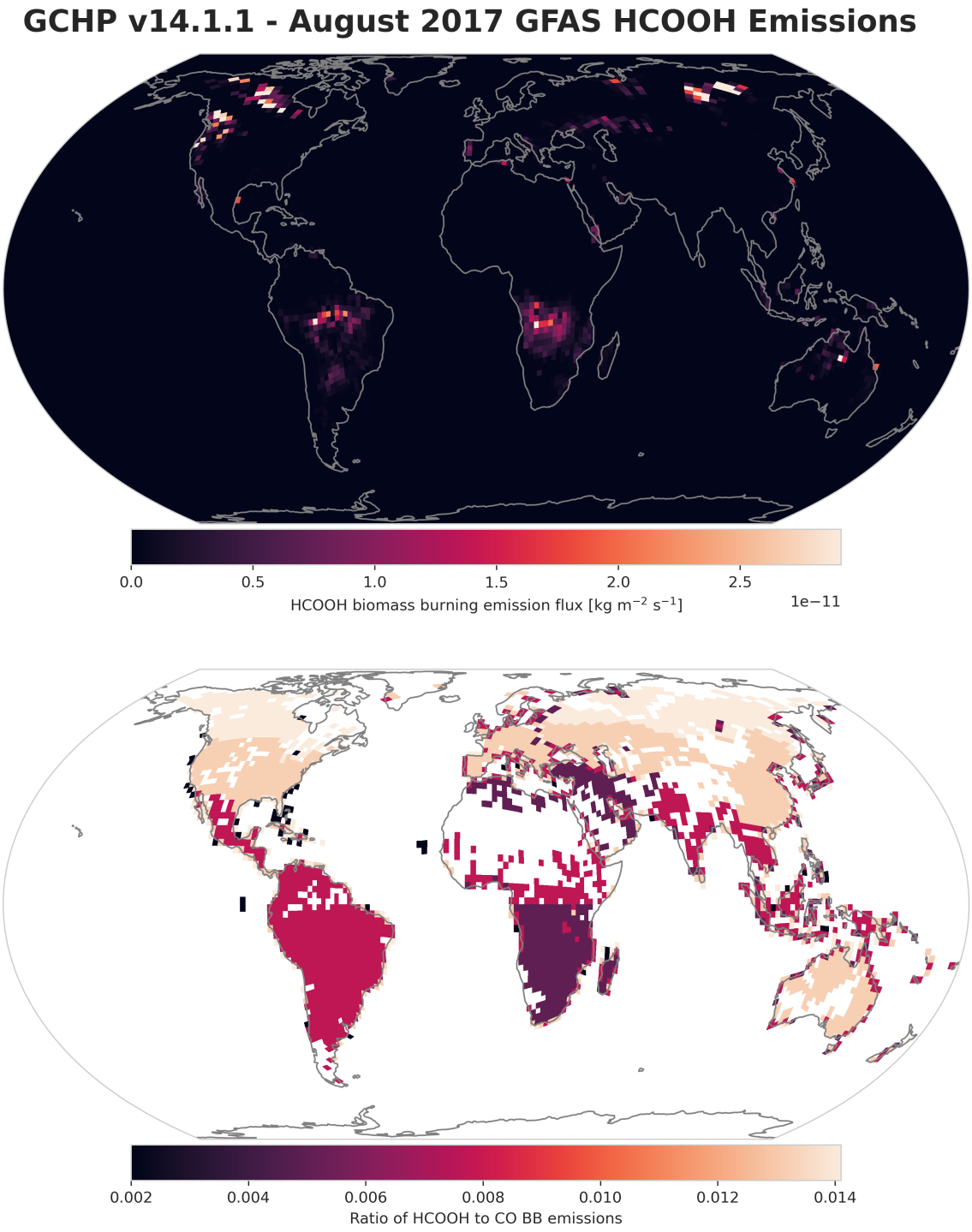

Figure B.4: (Top) A map of the estimated mean HCOOH emission flux for August 2017 derived using the method described in Sect. 6.2.2, and (bottom) a map of the scaling factors applied to the GFASv1.2 CO fields to estimate the HCOOH emissions.

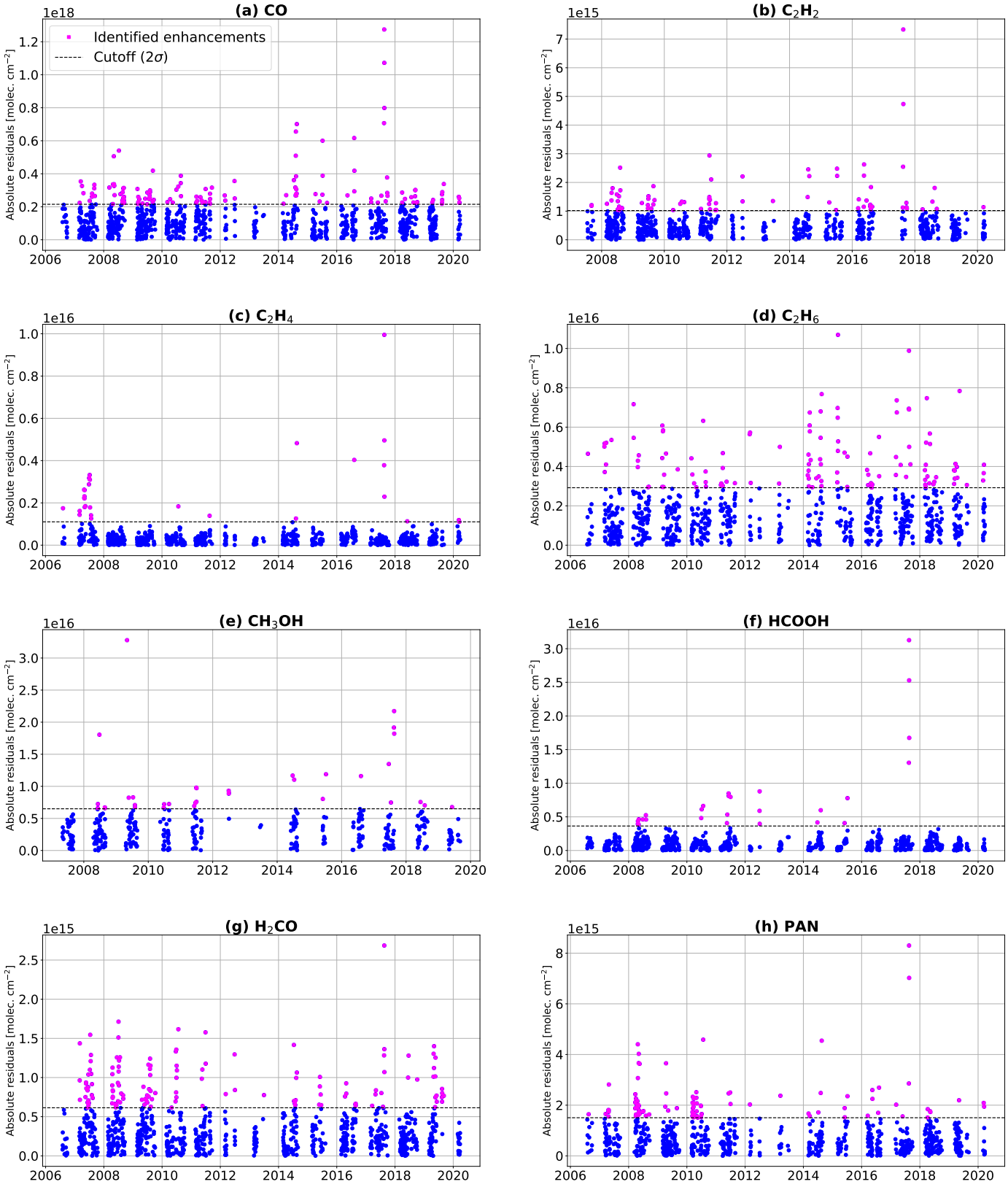

Figure B.5: Fourier series fit residuals of **(a)** CO, **(b)** C_2H_2, **(c)** C_2H_4, **(d)** C_2H_6, **(e)** CH_3OH, **(f)** H_2CO, **(g)** HCOOH, and **(h)** PAN for Eureka for the period of 2006–2020.

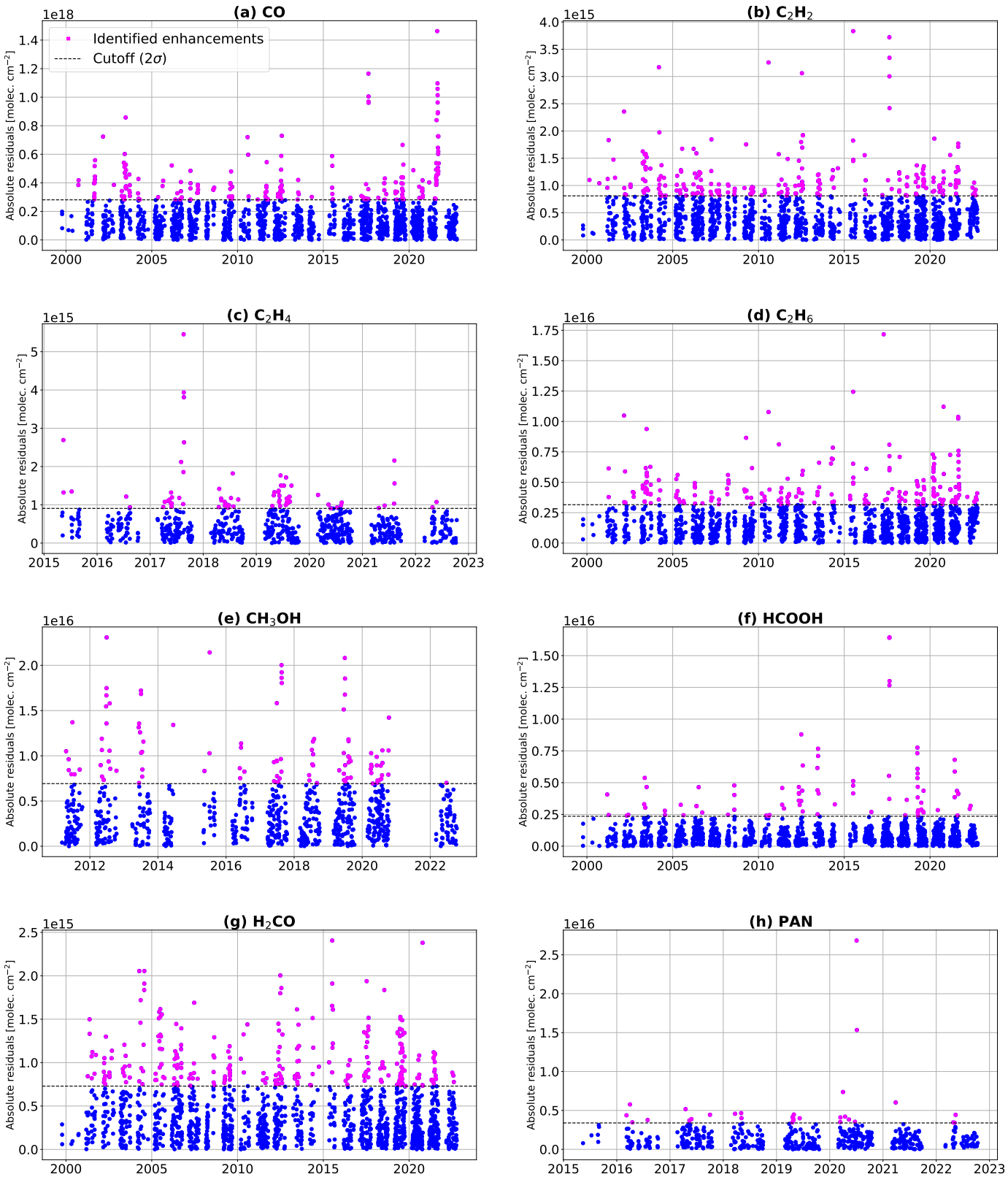

Figure B.6: Fourier series fit residuals of **(a)** CO, **(b)** C_2H_2, **(c)** C_2H_4, **(d)** C_2H_6, **(e)** CH_3OH, **(f)** H_2CO, **(g)** HCOOH, and **(h)** PAN for Thule for the period of 1999–2022.

Table B.1: Fitted trends derived from daily-mean FTIR total columns at Eureka and Thule. The 95% confidence intervals calculated from bootstrap resampling with $Q = 5000$ ensemble members are provided below each value in parentheses. Trends which are considered statistically significant (i.e., the 95% confidence intervals do not overlap with zero) are in bold.

Species	Eureka, Nunavut (2006–2020)		Thule, Greenland (1999–2022)	
	Trend (molec. cm^{-2} yr^{-1})	Trend w/o enhancements (molec. cm^{-2} yr^{-1})	Trend (molec. cm^{-2} yr^{-1})	Trend w/o enhancements (molec. cm^{-2} yr^{-1})
CO	$\mathbf{-1.53 \times 10^{16}}$	$\mathbf{-2.01 \times 10^{16}}$	$\mathbf{-1.36 \times 10^{16}}$	$\mathbf{-1.60 \times 10^{16}}$
	$(-1.93 \times 10^{16}, -1.12 \times 10^{16})$	$(-2.24 \times 10^{16}, -1.76 \times 10^{16})$	$(-1.67 \times 10^{16}, -1.04 \times 10^{16})$	$(-1.77 \times 10^{16}, -1.42 \times 10^{16})$
C_2H_2	$\mathbf{-4.70 \times 10^{13}}$[a]	$\mathbf{-5.49 \times 10^{13}}$[a]	$\mathbf{-4.03 \times 10^{13}}$	$\mathbf{-3.79 \times 10^{13}}$
	$(-6.49 \times 10^{13}, -2.83 \times 10^{13})$	$(-6.72 \times 10^{13}, -4.25 \times 10^{13})$	$(-4.81 \times 10^{13}, -3.25 \times 10^{13})$	$(-4.32 \times 10^{13}, -3.28 \times 10^{13})$
C_2H_4	-4.61×10^{12}	-2.39×10^{11}	$\mathbf{-8.93 \times 10^{13}}$[b]	$\mathbf{-6.84 \times 10^{13}}$[b]
	$(-2.27 \times 10^{13}, 1.36 \times 10^{13})$	$(-6.86 \times 10^{12}, 6.72 \times 10^{12})$	$(-1.25 \times 10^{14}, -5.53 \times 10^{13})$	$(-8.78 \times 10^{13}, -4.84 \times 10^{13})$
C_2H_6	$\mathbf{1.68 \times 10^{14}}$	$\mathbf{1.53 \times 10^{14}}$	$\mathbf{9.05 \times 10^{13}}$	$\mathbf{8.30 \times 10^{13}}$
	$(1.20 \times 10^{14}, 2.17 \times 10^{14})$	$(1.21 \times 10^{14}, 1.86 \times 10^{14})$	$(5.66 \times 10^{13}, 1.24 \times 10^{14})$	$(6.19 \times 10^{13}, 1.03 \times 10^{14})$
CH_3OH	-4.76×10^{13}[c]	$\mathbf{-1.13 \times 10^{14}}$[c]	$\mathbf{-4.21 \times 10^{14}}$[d]	$\mathbf{-3.41 \times 10^{14}}$[d]
	$(-1.99 \times 10^{14}, 1.07 \times 10^{14})$	$(-2.10 \times 10^{14}, -1.62 \times 10^{13})$	$(-5.63 \times 10^{14}, -2.70 \times 10^{14})$	$(-4.31 \times 10^{14}, -2.46 \times 10^{14})$
HCOOH	-4.03×10^{13}	$\mathbf{-5.62 \times 10^{13}}$	5.22×10^{12}	-3.39×10^{12}
	$(-9.53 \times 10^{13}, 1.59 \times 10^{13})$	$(-7.77 \times 10^{13}, -3.45 \times 10^{13})$	$(-1.18 \times 10^{13}, 2.20 \times 10^{13})$	$(-1.39 \times 10^{13}, 7.08 \times 10^{12})$
H_2CO	$\mathbf{2.40 \times 10^{13}}$	$\mathbf{2.16 \times 10^{13}}$	$\mathbf{1.46 \times 10^{13}}$	$\mathbf{1.25 \times 10^{13}}$
	$(1.44 \times 10^{13}, 3.36 \times 10^{13})$	$(1.60 \times 10^{13}, 2.70 \times 10^{13})$	$(8.41 \times 10^{12}, 2.12 \times 10^{13})$	$(8.58 \times 10^{12}, 1.64 \times 10^{13})$
PAN	$\mathbf{7.00 \times 10^{13}}$	$\mathbf{6.87 \times 10^{13}}$	9.25×10^{13}[b]	5.43×10^{13}[b]
	$(4.29 \times 10^{13}, 9.91 \times 10^{13})$	$(5.30 \times 10^{13}, 8.40 \times 10^{13})$	$(-9.87 \times 10^{12}, 1.93 \times 10^{14})$	$(-2.86 \times 10^{13}, 1.35 \times 10^{14})$

[a] The time-series of C_2H_2 at Eureka begins in July 2007.
[b] The time-series of C_2H_4 and PAN at Thule begins in May 2015.
[c] Only one day of CH_3OH total columns was available at Eureka in 2020, so this data is excluded from the analysis.
[d] The time-series of CH_3OH at Thule begins in March 2011.

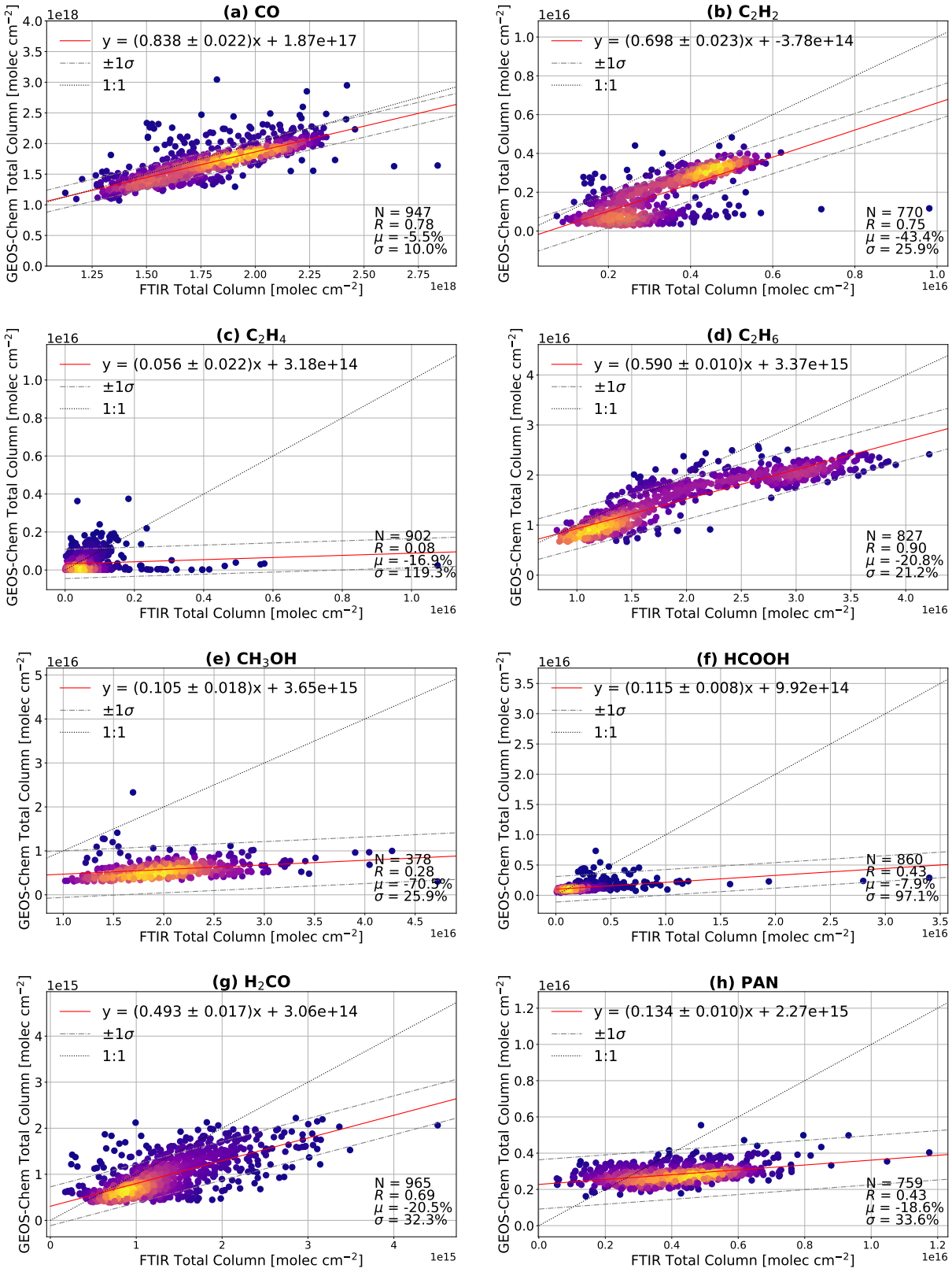

Figure B.7: Correlation plots comparing GCHP-simulated daily mean total columns with daily mean retrieved total columns for **(a)** CO, **(b)** C_2H_2, **(c)** C_2H_4, **(d)** C_2H_6, **(e)** CH_3OH, **(f)** HCOOH, **(g)** H_2CO, and **(h)** PAN at Eureka in the period of 2006–2020. The number of paired days (N), the Pearson correlation coefficient (R), the mean relative bias (μ), and the mean relative standard deviation of the GEOS-Chem columns (σ) are provided in the bottom right of each panel.

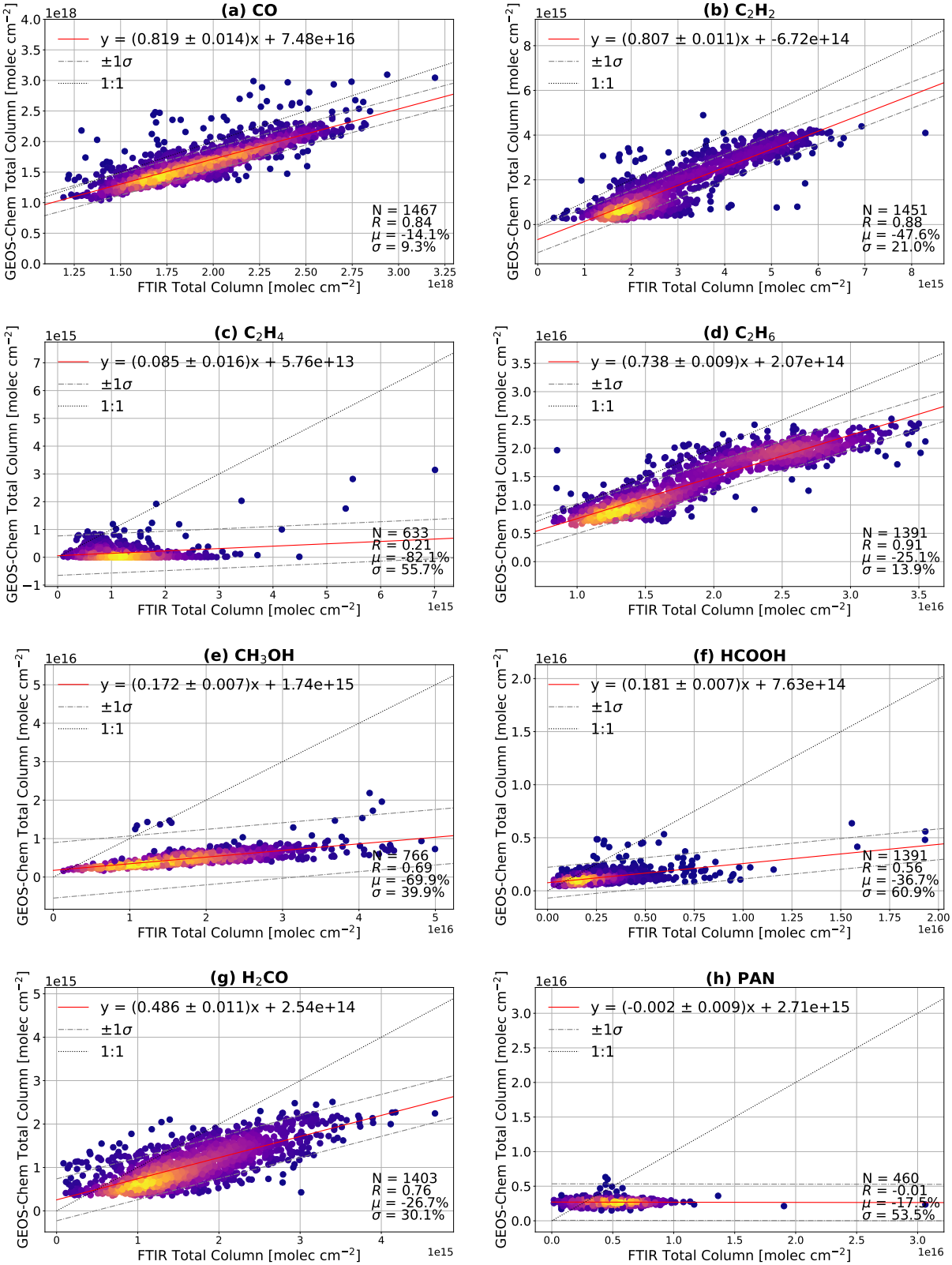

Figure B.8: Correlation plots comparing GCHP-simulated daily mean total columns with daily mean retrieved total columns for **(a)** CO, **(b)** C_2H_2, **(c)** C_2H_4, **(d)** C_2H_6, **(e)** CH_3OH, **(f)** HCOOH, **(g)** H_2CO, and **(h)** PAN at Thule in the period of 2003–2021. The number of paired days (N), the Pearson correlation coefficient (R), the mean relative bias (μ), and the mean relative standard deviation of the GEOS-Chem columns (σ) are provided in the bottom right of each panel.

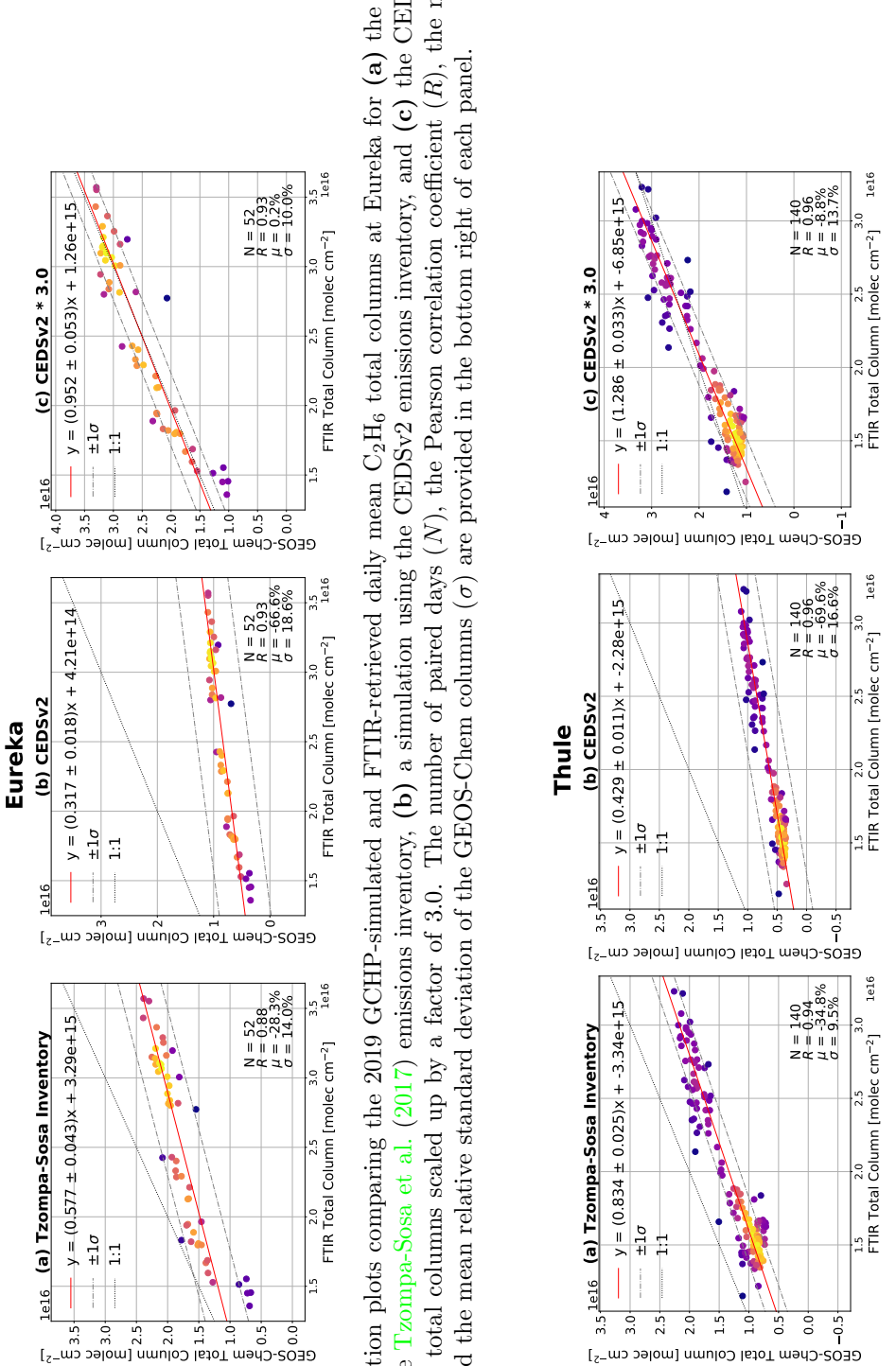

Figure B.9: Correlation plots comparing the 2019 GCHP-simulated and FTIR-retrieved daily mean C_2H_6 total columns at Eureka for **(a)** the base simulation using the Tzompa-Sosa et al. (2017) emissions inventory, **(b)** a simulation using the CEDSv2 emissions inventory, and **(c)** the CEDSv2 simulation with the total columns scaled up by a factor of 3.0. The number of paired days (N), the Pearson correlation coefficient (R), the mean relative bias (μ), and the mean relative standard deviation of the GEOS-Chem columns (σ) are provided in the bottom right of each panel.

Figure B.10: Correlation plots comparing the 2019 GCHP-simulated and FTIR-retrieved daily mean C_2H_6 total columns at Thule for **(a)** the base simulation using the Tzompa-Sosa et al. (2017) emissions inventory, **(b)** a simulation using the CEDSv2 emissions inventory, and **(c)** the CEDSv2 simulation with the total columns scaled up by a factor of 3.0. The number of paired days (N), the Pearson correlation coefficient (R), the mean relative bias (μ), and the mean relative standard deviation of the GEOS-Chem columns (σ) are provided in the bottom right of each panel.

Table B.2: Fitted trends derived from daily-mean GEOS-Chem total columns at Eureka and Thule. The 95% confidence intervals calculated from bootstrap resampling with $Q = 5000$ ensemble members are provided below each value in parentheses. Trends which are considered statistically significant (i.e., the 95% confidence intervals do not overlap with zero) are in bold.

Species	Eureka, Nunavut (2006–2020)		Thule, Greenland (2003–2021)	
	Trend (molec. cm^{-2} yr^{-1})	Trend w/o enhancements (molec. cm^{-2} yr^{-1})	Trend (molec. cm^{-2} yr^{-1})	Trend w/o enhancements (molec. cm^{-2} yr^{-1})
CO	$\mathbf{-1.44 \times 10^{16}}$	$\mathbf{-1.38 \times 10^{16}}$	$\mathbf{-1.61 \times 10^{16}}$	$\mathbf{-1.75 \times 10^{16}}$
	$(-1.78 \times 10^{16}, -1.10 \times 10^{16})$	$(-1.60 \times 10^{16}, -1.18 \times 10^{16})$	$(-2.00 \times 10^{16}, -1.25 \times 10^{16})$	$(-1.92 \times 10^{16}, -1.58 \times 10^{16})$
C_2H_2	$\mathbf{-3.43 \times 10^{13}}$	$\mathbf{-3.30 \times 10^{13}}$	$\mathbf{-4.05 \times 10^{13}}$	$\mathbf{-4.23 \times 10^{13}}$
	$(-4.15 \times 10^{13}, -2.72 \times 10^{13})$	$(-3.74 \times 10^{13}, -2.84 \times 10^{13})$	$(-4.73 \times 10^{13}, -3.35 \times 10^{13})$	$(-4.59 \times 10^{13}, -3.85 \times 10^{13})$
C_2H_4	-1.35×10^{12}	-7.35×10^{11}	2.36×10^{12}	$\mathbf{1.94 \times 10^{12}}$
	$(-7.46 \times 10^{12}, 4.58 \times 10^{12})$	$(-3.75 \times 10^{12}, 2.28 \times 10^{12})$	$(-1.35 \times 10^{12}, 6.00 \times 10^{12})$	$(1.11 \times 10^{11}, 3.66 \times 10^{12})$
C_2H_6	-2.63×10^{13}	$\mathbf{-2.22 \times 10^{13}}$	$\mathbf{-4.32 \times 10^{13}}$	$\mathbf{-4.66 \times 10^{13}}$
	$(-5.24 \times 10^{13}, 6.81 \times 10^{11})$	$(-3.70 \times 10^{13}, -7.20 \times 10^{12})$	$(-6.93 \times 10^{13}, -1.83 \times 10^{13})$	$(-5.79 \times 10^{13}, -3.51 \times 10^{13})$
CH_3OH	-1.90×10^{13}	$\mathbf{-1.80 \times 10^{13}}$	-1.08×10^{13}	$\mathbf{-9.27 \times 10^{12}}$
	$(-3.80 \times 10^{13}, 2.96 \times 10^{11})$	$(-2.64 \times 10^{13}, -9.95 \times 10^{12})$	$(-2.39 \times 10^{13}, 2.07 \times 10^{12})$	$(-1.52 \times 10^{13}, -3.35 \times 10^{12})$
HCOOH	$\mathbf{-1.08 \times 10^{13}}$	$\mathbf{-1.01 \times 10^{13}}$	$\mathbf{-9.29 \times 10^{12}}$	$\mathbf{-7.75 \times 10^{12}}$
	$(-1.82 \times 10^{13}, -3.37 \times 10^{12})$	$(-1.31 \times 10^{13}, -7.11 \times 10^{12})$	$(-1.45 \times 10^{13}, -4.16 \times 10^{12})$	$(-1.10 \times 10^{13}, -5.34 \times 10^{12})$
H_2CO	-2.24×10^{12}	-1.63×10^{12}	8.39×10^{11}	2.53×10^{11}
	$(-5.89 \times 10^{12}, 1.59 \times 10^{12})$	$(-3.64 \times 10^{12}, 3.90 \times 10^{11})$	$(-1.84 \times 10^{12}, 3.57 \times 10^{12})$	$(-1.26 \times 10^{12}, 1.78 \times 10^{12})$
PAN	$\mathbf{-2.12 \times 10^{13}}$	$\mathbf{-2.19 \times 10^{13}}$	$\mathbf{-1.72 \times 10^{13}}$	$\mathbf{-1.64 \times 10^{13}}$
	$(-2.66 \times 10^{13}, -1.59 \times 10^{13})$	$(-2.50 \times 10^{13}, -1.88 \times 10^{13})$	$(-2.10 \times 10^{13}, -1.35 \times 10^{13})$	$(-1.87 \times 10^{13}, -1.41 \times 10^{13})$

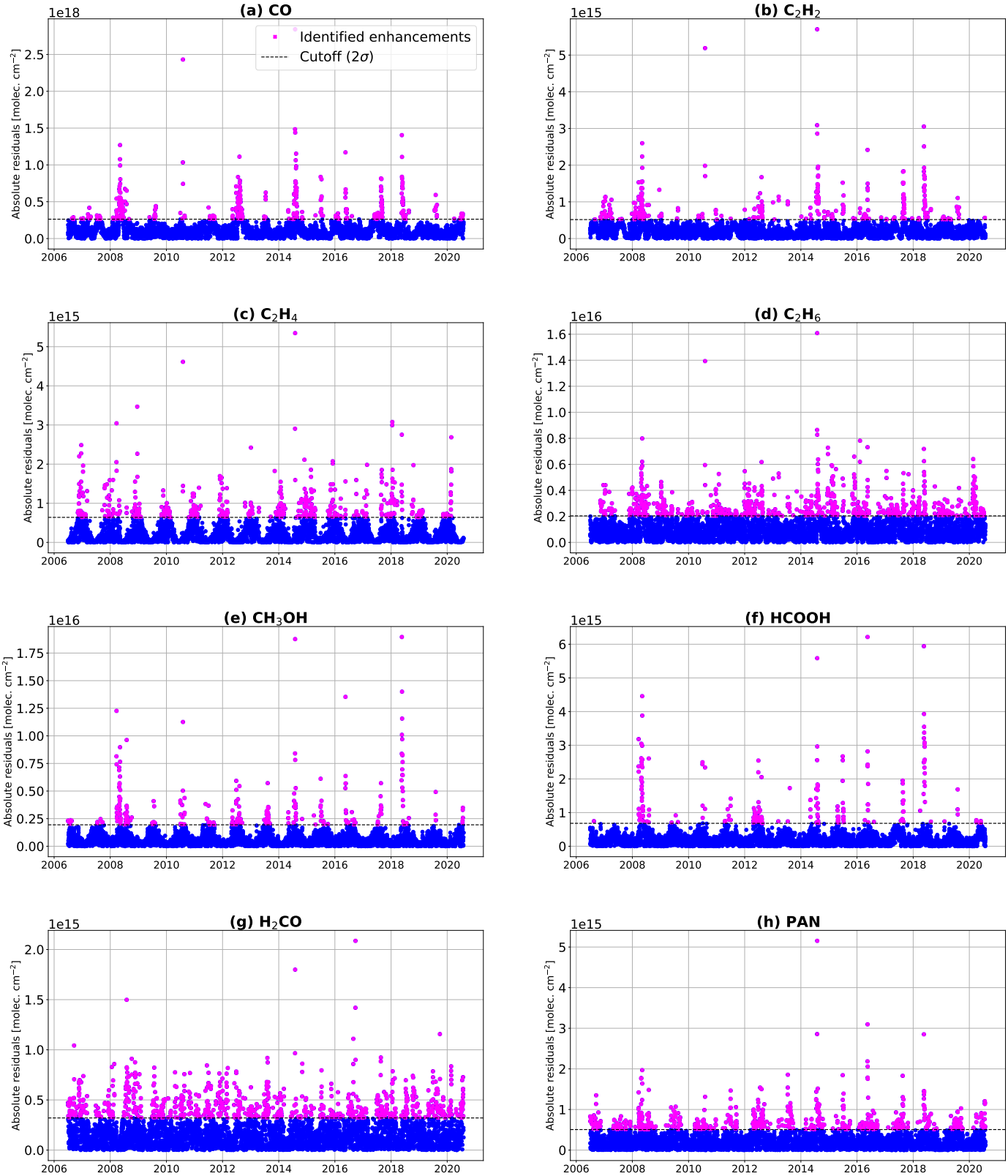

Figure B.11: Fourier series fit residuals of the GEOS-Chem simulated total columns of **(a)** CO, **(b)** C_2H_2, **(c)** C_2H_4, **(d)** C_2H_6, **(e)** CH_3OH, **(f)** H_2CO, **(g)** HCOOH, and **(h)** PAN for Eureka for the period of 2006–2020.

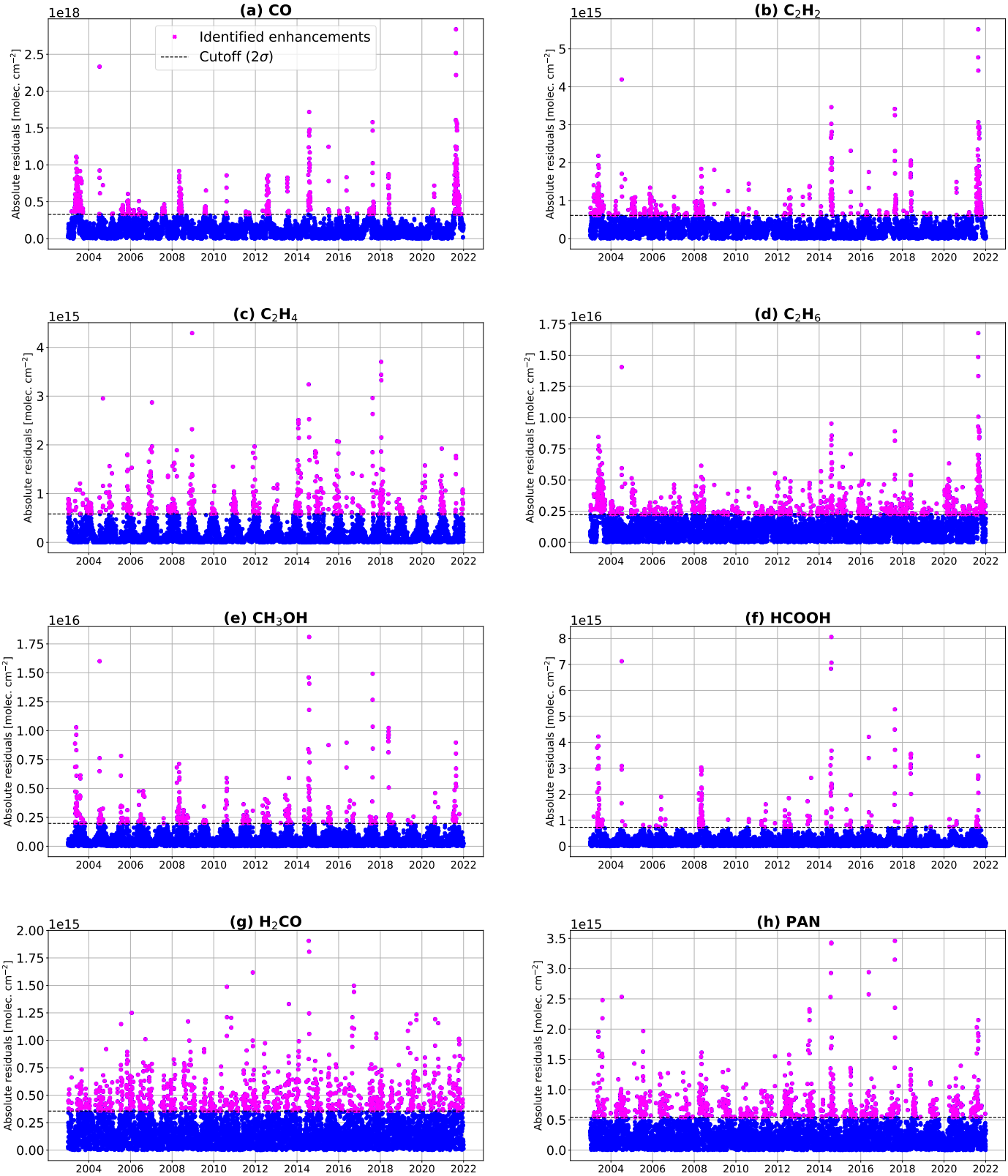

Figure B.12: Fourier series fit residuals of the GEOS-Chem simulated total columns of **(a)** CO, **(b)** C_2H_2, **(c)** C_2H_4, **(d)** C_2H_6, **(e)** CH_3OH, **(f)** H_2CO, **(g)** HCOOH, and **(h)** PAN for Thule for the period of 2003–2021.

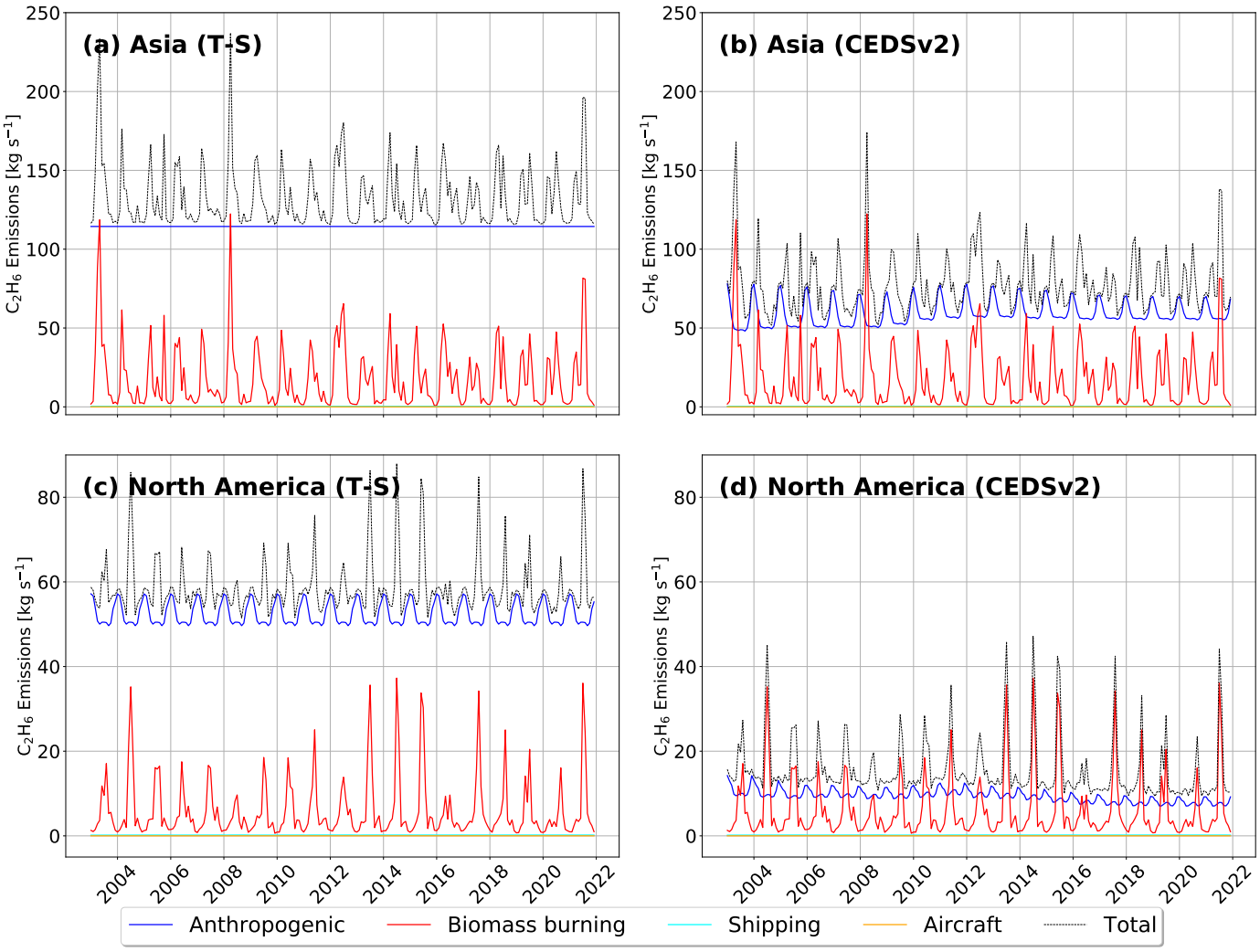

Figure B.13: Time-series plots of C_2H_6 emissions generated using the HEMCO Standalone module for **(a)** Asian emissions using the Tzompa-Sosa et al. (2017) (T-S) inventory, **(b)** Asian emissions using the CEDSv2 inventory, **(c)** North American emissions using the Tzompa-Sosa et al. (2017) inventory, **(d)** North American emissions using the CEDSv2 inventory. Here Asia is roughly defined as the region bounded by 20° N–70° N, 60° E–180° E, and North America as the region bounded by 20° N–70° N, 55° W–170° W.

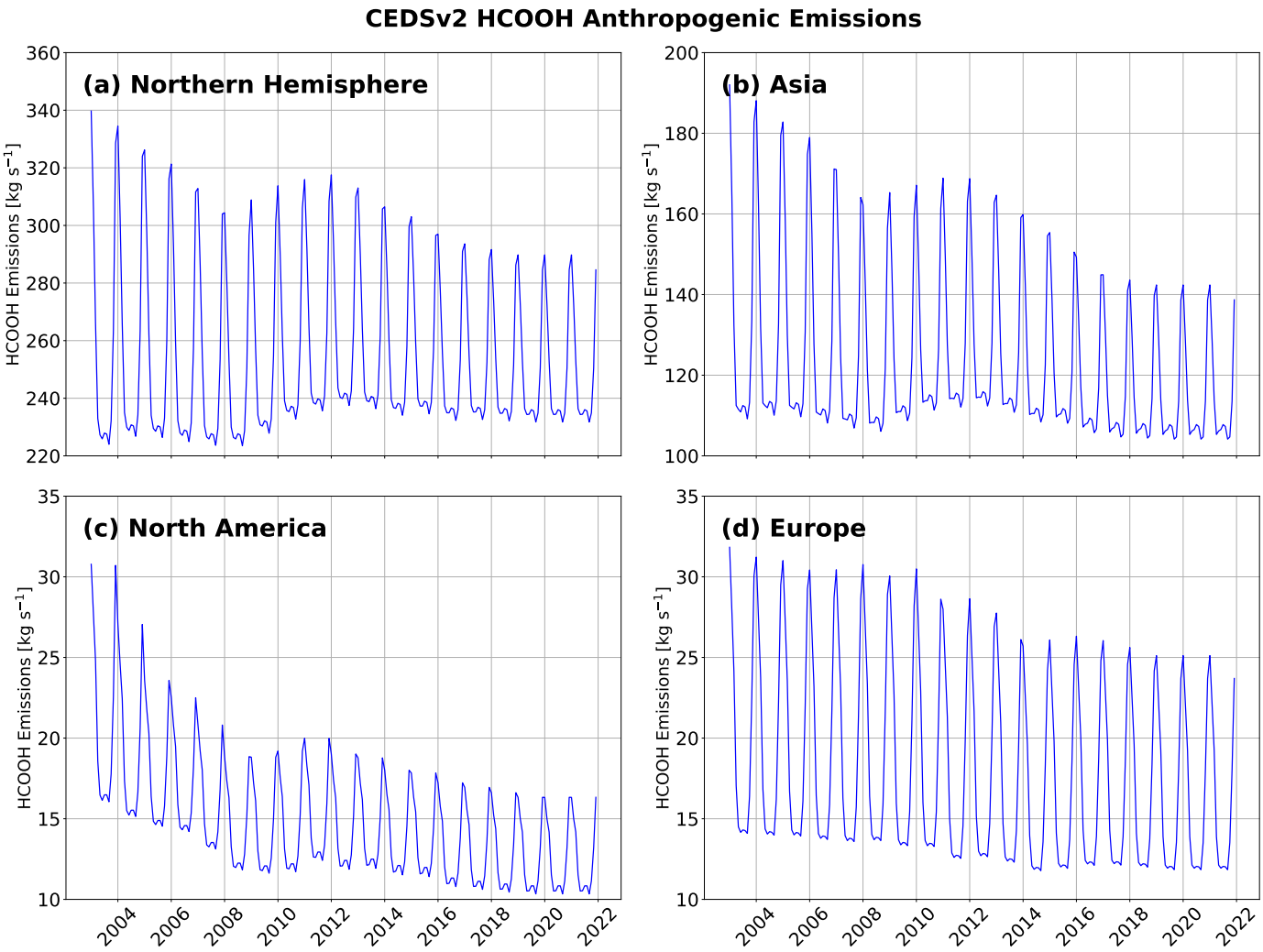

Figure B.14: Time-series plots of anthropogenic HCOOH CEDSv2 emissions generated using the HEMCO Standalone module for **(a)** the Northern Hemisphere, **(b)** Asia, **(c)** North America, **(d)** Europe. Here Asia is roughly defined as the region bounded by 20° N–70° N, 60° E–180° E, North America as the region bounded by 20° N–70° N, 55° W–170° W, and Europe as the region bounded by 35° N–70° N, 15° W–60° E.

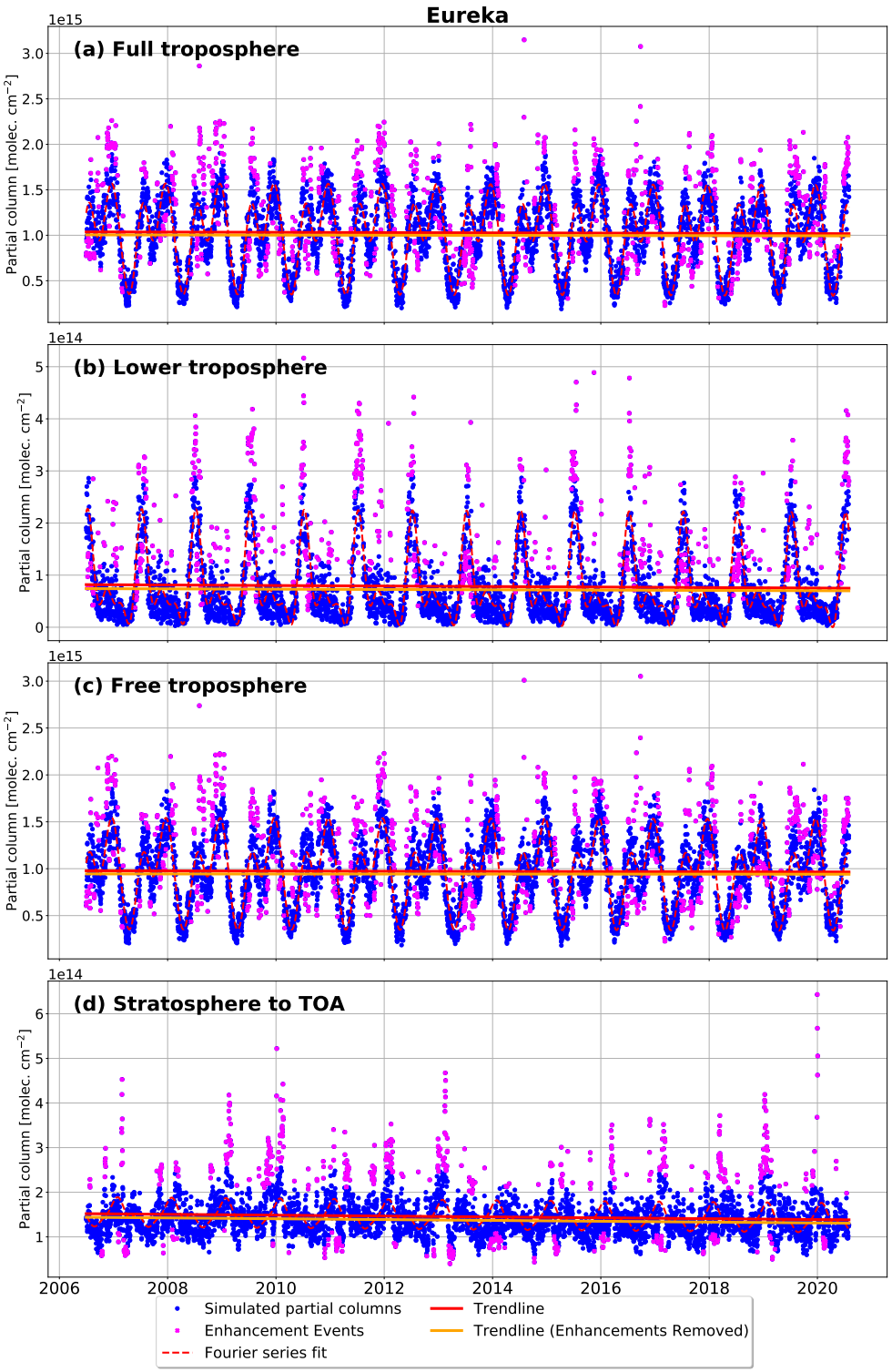

Figure B.15: Fourier series fit to GEOS-Chem simulated H_2CO partial columns and the corresponding trendlines for **(a)** the full troposphere, **(b)** the lower troposphere, **(c)** the free troposphere, and **(d)** the stratosphere to the top of the atmosphere (TOA) at Eureka. Here the full troposphere is defined as the surface to the tropopause, the lower troposphere as the surface to the planetary boundary layer, the upper troposphere as the planetary boundary layer to the tropopause, and the stratosphere to TOA as the tropopause to the top of the model grid.

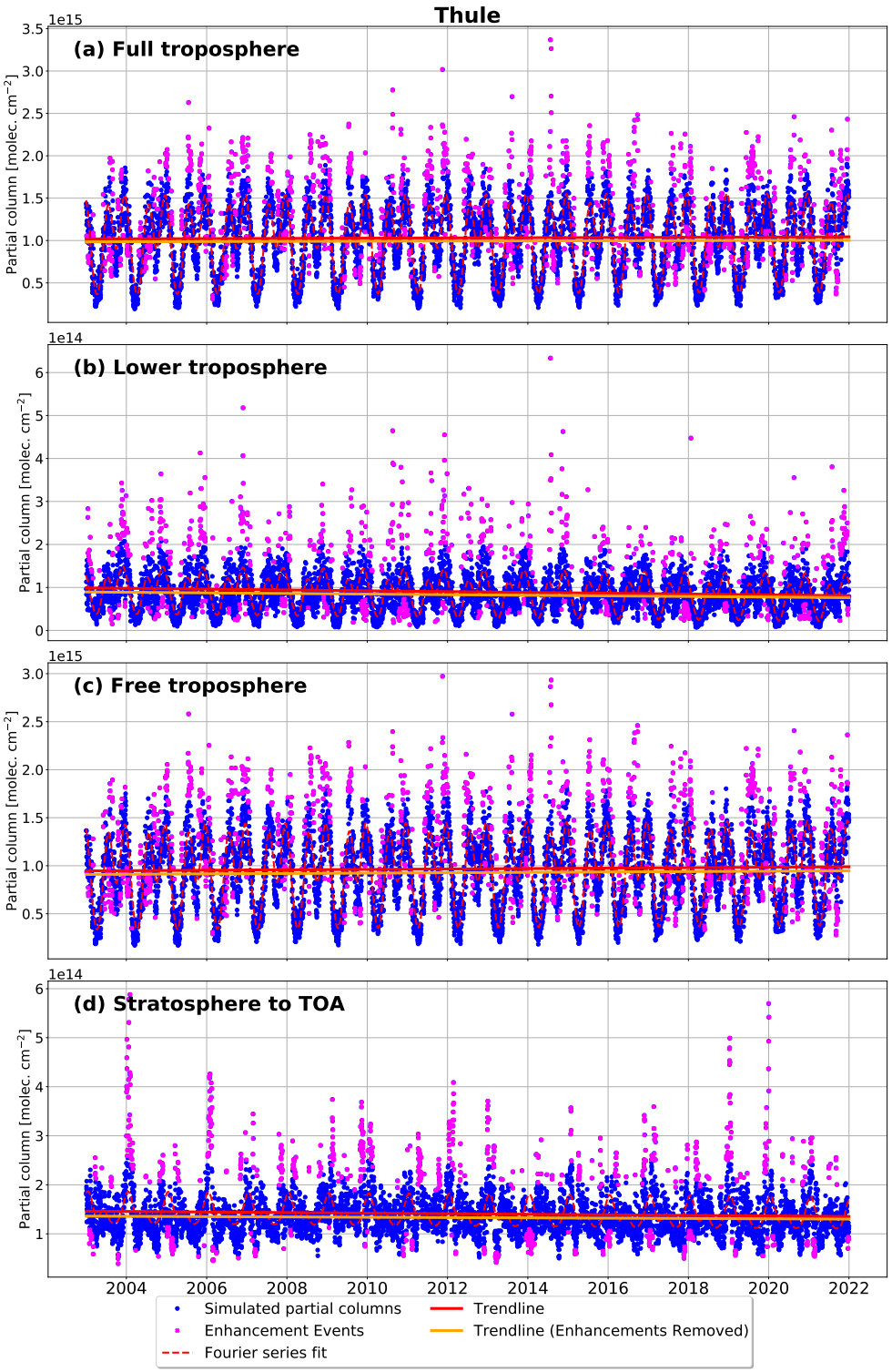

Figure B.16: Fourier series fit to GEOS-Chem simulated H_2CO partial columns and the corresponding trendlines for **(a)** the full troposphere, **(b)** the lower troposphere, **(c)** the free troposphere, and **(d)** the stratosphere to the top of the atmosphere (TOA) at Thule. Here the full troposphere is defined as the surface to the tropopause, the lower troposphere as the surface to the planetary boundary layer, the upper troposphere as the planetary boundary layer to the tropopause, and the stratosphere to TOA as the tropopause to the top of the model grid.

Bibliography

Adedeji, A. R., Andrews, S. J., Rowlinson, M. J., Evans, M. J., Lewis, A. C., Hashimoto, S., Mukai, H., Tanimoto, H., Tohjima, Y., and Saito, T. (2023). Measurement report: Assessment of Asian emissions of ethane and propane with a chemistry transport model based on observations from the island of Hateruma. *Atmospheric Chemistry and Physics*, 23(16):9229–9244.

Akagi, S. K., Yokelson, R. J., Burling, I. R., Meinardi, S., Simpson, I., Blake, D. R., McMeeking, G. R., Sullivan, A., Lee, T., Kreidenweis, S., Urbanski, S., Reardon, J., Griffith, D. W. T., Johnson, T. J., and Weise, D. R. (2013). Measurements of reactive trace gases and variable O_3 formation rates in some South Carolina biomass burning plumes. *Atmospheric Chemistry and Physics*, 13(3):1141–1165.

Akagi, S. K., Yokelson, R. J., Wiedinmyer, C., Alvarado, M. J., Reid, J. S., Karl, T., Crounse, J. D., and Wennberg, P. O. (2011). Emission factors for open and domestic biomass burning for use in atmospheric models. *Atmospheric Chemistry and Physics*, 11(9):4039–4072.

Allen, G., Remedios, J. J., Newnham, D. A., Smith, K. M., and Monks, P. S. (2005). Improved mid-infrared cross-sections for peroxyacetyl nitrate (PAN) vapour. *Atmospheric Chemistry and Physics*, 5(1):47–56.

Alvarado, M. J., Cady-Pereira, K. E., Xiao, Y., Millet, D. B., and Payne, V. H. (2011). Emission ratios for ammonia and formic acid and observations of peroxy acetyl nitrate (PAN) and ethylene in biomass burning smoke as seen by the Tropospheric Emission Spectrometer (TES). *Atmosphere*, 2(4):633–654.

Alvarado, M. J., Logan, J. A., Mao, J., Apel, E., Riemer, D., Blake, D., Cohen, R. C., Min, K.-E., Perring, A. E., Browne, E. C., Wooldridge, P. J., Diskin, G. S., Sachse, G. W., Fuelberg, H., Sessions, W. R., Harrigan, D. L., Huey, G., Liao, J., Case-Hanks, A., Jimenez, J. L., Cubison, M. J., Vay, S. A., Weinheimer, A. J., Knapp, D. J., Montzka, D. D., Flocke, F. M., Pollack, I. B.,

Wennberg, P. O., Kurten, A., Crounse, J., Clair, J. M. S., Wisthaler, A., Mikoviny, T., Yantosca, R. M., Carouge, C. C., and Le Sager, P. (2010). Nitrogen oxides and PAN in plumes from boreal fires during ARCTAS-B and their impact on ozone: An integrated analysis of aircraft and satellite observations. *Atmospheric Chemistry and Physics*, 10(20):9739–9760.

Alwe, H. D., Millet, D. B., Chen, X., Raff, J. D., Payne, Z. C., and Fledderman, K. (2019). Oxidation of volatile organic compounds as the major source of formic acid in a mixed forest canopy. *Geophysical Research Letters*, 46(5):2940–2948.

AMAP (2006). *AMAP assessment 2006: Acidifying pollutants, Arctic Haze, and acidification in the Arctic*. Arctic Monitoring and Assessment Programme.

Anand, S. S., Philip, B. K., and Mehendale, H. M. (2014). *Volatile Organic Compounds*, volume 4, page 450–455. Elsevier, Academic Press.

Andreae, M. O. (2019). Emission of trace gases and aerosols from biomass burning – An updated assessment. *Atmospheric Chemistry and Physics*, 19(13):8523–8546.

Andreae, M. O. and Merlet, P. (2001). Emission of trace gases and aerosols from biomass burning. *Global Biogeochemical Cycles*, 15(4):955–966.

Angelbratt, J., Mellqvist, J., Simpson, D., Jonson, J. E., Blumenstock, T., Borsdorff, T., Duchatelet, P., Forster, F., Hase, F., Mahieu, E., De Mazière, M., Notholt, J., Petersen, A. K., Raffalski, U., Servais, C., Sussmann, R., Warneke, T., and Vigouroux, C. (2011). Carbon monoxide (CO) and ethane (C_2H_6) trends from ground-based solar FTIR measurements at six European stations, comparison and sensitivity analysis with the EMEP model. *Atmospheric Chemistry and Physics*, 11(17):9253–9269.

Arnold, S., Law, K., Brock, C., Thomas, J., Starkweather, S., von Salzen, K., Stohl, A., Sharma, S., Lund, M., Flanner, M., Petäjä, T., Tanimoto, H., Gamble, J., Dibb, J., Melamed, M., Johnson, N., Fidel, M., Tynkkynen, V.-P., Baklanov, A., Eckhardt, S., Monks, S., Browse, J., and Bozem, H. (2016). Arctic air pollution: Challenges and opportunities for the next decade. *Elementa: Science of the Anthropocene*, 4:000104.

Ashworth, K., Chung, S. H., McKinney, K. A., Liu, Y., Munger, J. W., Martin, S. T., and Steiner, A. L. (2016). Modelling bidirectional fluxes of methanol and acetaldehyde with the FORCAsT canopy exchange model. *Atmospheric Chemistry and Physics*, 16(24):15461–15484.

Bader, W., Stavrakou, T., Muller, J.-F., Reimann, S., Boone, C. D., Harrison, J. J., Flock, O., Bovy, B., Franco, B., Lejeune, B., Servais, C., and Mahieu, E. (2014). Long-term evolution and seasonal modulation of methanol above Jungfraujoch (46.5° N, 8.0° E): Optimisation of the retrieval strategy, comparison with model simulations and independent observations. *Atmospheric Measurement Techniques*, 7(11):3861–3872.

Barret, B., De Mazière, M., and Mahieu, E. (2003). Ground-based FTIR measurements of CO from the Jungfraujoch: Characterisation and comparison with in situ surface and MOPITT data. *Atmospheric Chemistry and Physics*, 3(6):2217–2223.

Barrie, L. A. (1986). Arctic air pollution: An overview of current knowledge. *Atmospheric Environment (1967)*, 20(4):643–663.

Batchelor, R. L., Kolonjari, F., Lindenmaier, R., Mittermeier, R. L., Daffer, W., Fast, H., Manney, G., Strong, K., and Walker, K. A. (2010). Four Fourier transform spectrometers and the Arctic polar vortex: instrument intercomparison and ACE-FTS validation at Eureka during the IPY springs of 2007 and 2008. *Atmospheric Measurement Techniques*, 3(1):51–66.

Batchelor, R. L., Strong, K., Lindenmaier, R., Mittermeier, R. L., Fast, H., Drummond, J. R., and Fogal, P. F. (2009). A New Bruker IFS 125HR FTIR Spectrometer for the Polar Environment Atmospheric Research Laboratory at Eureka, Nunavut, Canada: Measurements and Comparison with the Existing Bomem DA8 Spectrometer. *Journal of Atmospheric and Oceanic Technology*, 26(7):1328–1340.

Bates, K. H., Jacob, D. J., Wang, S., Hornbrook, R. S., Apel, E. C., Kim, M. J., Millet, D. B., Wells, K. C., Chen, X., Brewer, J. F., Ray, E. A., Commane, R., Diskin, G. S., and Wofsy, S. C. (2021). The Global Budget of Atmospheric Methanol: New Constraints on Secondary, Oceanic, and Terrestrial Sources. *Journal of Geophysical Research: Atmospheres*, 126(4):e2020JD033439.

Bayes, T. (1763). Lii. an essay towards solving a problem in the doctrine of chances. by the late rev. mr. bayes, f. r. s. communicated by mr. price, in a letter to john canton, a. m. f. r. s. *Philosophical Transactions of the Royal Society of London*, 53:370–418.

BC Wildfire Service (2017). Wildfire season summary. https://www2.gov.bc.ca/gov/content/safety/wildfire-status/about-bcws/wildfire-history/wildfire-season-summary. Last accessed on 23 October 2023.

Beine, H. J. and Krognes, T. (2000). The seasonal cycle of peroxyacetyl nitrate (PAN) in the European Arctic. *Atmospheric Environment*, 34(6):933–940.

Bernath, P., Steffen, J., Crouse, J., and Boone, C. (2020). Sixteen-year trends in atmospheric trace gases from orbit. *Journal of Quantitative Spectroscopy and Radiative Transfer*, 253:107178.

Bernath, P. F., McElroy, C. T., Abrams, M. C., Boone, C. D., Butler, M., Camy-Peyret, C., Carleer, M., Clerbaux, C., Coheur, P.-F., Colin, R., DeCola, P., De Mazière, M., Drummond, J. R., Dufour, D., Evans, W. F. J., Fast, H., Fussen, D., Gilbert, K., Jennings, D. E., Llewellyn, E. J., Lowe, R. P., Mahieu, E., McConnell, J. C., McHugh, M., McLeod, S. D., Michaud, R., Midwinter, C., Nassar, R., Nichitiu, F., Nowlan, C., Rinsland, C. P., Rochon, Y. J., Rowlands, N., Semeniuk, K., Simon, P., Skelton, R., Sloan, J. J., Soucy, M.-A., Strong, K., Tremblay, P., Turnbull, D., Walker, K. A., Walkty, I., Wardle, D. A., Wehrle, V., Zander, R., and Zou, J. (2005). Atmospheric Chemistry Experiment (ACE): Mission overview. *Geophysical Research Letters*, 32(15):L15S01.

Bey, I., Jacob, D. J., Yantosca, R. M., Logan, J. A., Field, B. D., Fiore, A. M., Li, Q., Liu, H. Y., Mickley, L. J., and Schultz, M. G. (2001). Global modeling of tropospheric chemistry with assimilated meteorology: Model Description and Evaluation. *Journal of Geophysical Research: Atmospheres*, 106(D19):23073–23095.

Bognar, K., Zhao, X., Strong, K., Boone, C. D., Bourassa, A. E., Degenstein, D. A., Drummond, J. R., Duff, A., Goutail, F., Griffin, D., Jeffery, P. S., Lutsch, E., Manney, G. L., McElroy, C. T., Mclinden, C. A., Millán, L. F., Pazmino, A., Sioris, C. E., Walker, K. A., and Zou, J. (2019). Updated validation of ACE and OSIRIS ozone and NO_2 measurements in the Arctic using ground-based instruments at Eureka, Canada. *Journal of Quantitative Spectroscopy and Radiative Transfer*, 238:106571.

Boone, C. D., Bernath, P. F., Cok, D., Jones, S. C., and Steffen, J. (2020). Version 4 retrievals for the Atmospheric Chemistry Experiment Fourier Transform Spectrometer (ACE-FTS) and imagers. *Journal of Quantitative Spectroscopy and Radiative Transfer*, 247:106939.

Boone, C. D., Nassar, R., Walker, K. A., Rochon, Y., Mcleod, S. D., Rinsland, C. P., and Bernath, P. F. (2005). Retrievals for the Atmospheric Chemistry Experiment Fourier-Transform Spectrometer. *Applied Optics*, 44(33):7218.

Borsdorff, T., Aan De Brugh, J., Hu, H., Aben, I., Hasekamp, O., and Landgraf, J. (2018). Measuring

Carbon Monoxide With TROPOMI: First Results and a Comparison With ECMWF-IFS Analysis Data. *Geophysical Research Letters*, 45(6):2826–2832.

Borsdorff, T., Brugh, J., Schneider, A., Lorente, A., Birk, M., Wagner, G., Kivi, R., Hase, F., Feist, D. G., Sussmann, R., Rettinger, M., Wunch, D., Warneke, T., and Landgraf, J. (2019). Improving the TROPOMI CO data product: update of the spectroscopic database and destriping of single orbits. *Atmospheric Measurement Techniques*, 12(10):5443–5455.

Borsdorff, T., Hasekamp, O. P., Wassmann, A., and Landgraf, J. (2014). Insights into Tikhonov regularization: application to trace gas column retrieval and the efficient calculation of total column averaging kernels. *Atmospheric Measurement Techniques*, 7(2):523–535.

Boulanger, Y., Gauthier, S., and Burton, P. J. (2014). A refinement of models projecting future Canadian fire regimes using homogeneous fire regime zones. *Canadian Journal of Forest Research*, 44(4):365–376.

Bourassa, A. E., Rieger, L. A., Zawada, D. J., Khaykin, S., Thomason, L. W., and Degenstein, D. A. (2019). Satellite limb observations of unprecedented forest fire aerosol in the stratosphere. *Journal of Geophysical Research: Atmospheres*, 124(16):9510–9519.

Bozem, H., Hoor, P., Kunkel, D., Köllner, F., Schneider, J., Herber, A., Schulz, H., Leaitch, W. R., Aliabadi, A. A., Willis, M. D., Burkart, J., and Abbatt, J. P. D. (2019). Characterization of transport regimes and the polar dome during arctic spring and summer using in situ aircraft measurements. *Atmospheric Chemistry and Physics*, 19(23):15049–15071.

Bridier, I., Caralp, F., Loirat, H., Lesclaux, R., Veyret, B., Becker, K. H., Reimer, A., and Zabel, F. (1991). Kinetic and theoretical studies of the reactions acetylperoxy + nitrogen dioxide + M $\rightleftharpoons$ acetyl peroxynitrate + M between 248 and 393 K and between 30 and 760 Torr. *The Journal of Physical Chemistry*, 95(9):3594–3600.

Buchholz, R. R., Deeter, M. N., Worden, H. M., Gille, J., Edwards, D. P., Hannigan, J. W., Jones, N. B., Paton-Walsh, C., Griffith, D. W. T., Smale, D., Robinson, J., Strong, K., Conway, S., Sussmann, R., Hase, F., Blumenstock, T., Mahieu, E., and Langerock, B. (2017). Validation of MOPITT carbon monoxide using ground-based Fourier transform infrared spectrometer data from NDACC. *Atmospheric Measurement Techniques*, 10(5):1927–1956.

Buchholz, R. R., Worden, H. M., Park, M., Francis, G., Deeter, M. N., Edwards, D. P., Emmons, L. K., Gaubert, B., Gille, J., Martínez-Alonso, S., Tang, W., Kumar, R., Drummond, J. R.,

Clerbaux, C., George, M., Coheur, P.-F., Hurtmans, D., Bowman, K. W., Luo, M., Payne, V. H., Worden, J. R., Chin, M., Levy, R. C., Warner, J., Wei, Z., and Kulawik, S. S. (2021). Air Pollution Trends measured from Terra: CO and AOD over industrial, fire-prone, and background regions. *Remote Sensing of Environment*, 256:112275.

Cady-Pereira, K. E., Chaliyakunnel, S., Shephard, M. W., Millet, D. B., Luo, M., and Wells, K. C. (2014). HCOOH measurements from space: TES retrieval algorithm and observed global distribution. *Atmospheric Measurement Techniques*, 7(7):2297–2311.

Cady-Pereira, K. E., Shephard, M. W., Millet, D. B., Luo, M., Wells, K. C., Xiao, Y., Payne, V. H., and Worden, J. (2012). Methanol from TES global observations: Retrieval algorithm and seasonal and spatial variability. *Atmospheric Chemistry and Physics*, 12(17):8189–8203.

Chameides, W. L. and Davis, D. D. (1983). Aqueous-phase source of formic acid in clouds. *Nature*, 304(5925):427–429.

Chen, X., Millet, D. B., Neuman, J. A., Veres, P. R., Ray, E. A., Commane, R., Daube, B. C., McKain, K., Schwarz, J. P., Katich, J. M., Froyd, K. D., Schill, G. P., Kim, M. J., Crounse, J. D., Allen, H. M., Apel, E. C., Hornbrook, R. S., Blake, D. R., Nault, B. A., Campuzano-Jost, P., Jimenez, J. L., and Dibb, J. E. (2021). HCOOH in the remote atmosphere: Constraints from Atmospheric Tomography (ATom) airborne observations. *ACS Earth and Space Chemistry*, 5(6):1436–1454.

Chen, X., Millet, D. B., Singh, H. B., Wisthaler, A., Apel, E. C., Atlas, E. L., Blake, D. R., Bourgeois, I., Brown, S. S., Crounse, J. D., de Gouw, J. A., Flocke, F. M., Fried, A., Heikes, B. G., Hornbrook, R. S., Mikoviny, T., Min, K.-E., Müller, M., Neuman, J. A., O'Sullivan, D. W., Peischl, J., Pfister, G. G., Richter, D., Roberts, J. M., Ryerson, T. B., Shertz, S. R., Thompson, C. R., Treadaway, V., Veres, P. R., Walega, J., Warneke, C., Washenfelder, R. A., Weibring, P., and Yuan, B. (2019). On the sources and sinks of atmospheric VOCs: An integrated analysis of recent aircraft campaigns over North America. *Atmospheric Chemistry and Physics*, 19(14):9097–9123.

Clapeyron, E. (1834). Mémoire sur la puissance motrice de la chaleur. *Journal de l'École polytechnique (in French)*, Tome XIV:153–190.

Clerbaux, C., Boynard, A., Clarisse, L., George, M., Hadji-Lazaro, J., Herbin, H., Hurtmans, D., Pommier, M., Razavi, A., Turquety, S., Wespes, C., and Coheur, P.-F. (2009). Monitoring of

atmospheric composition using the thermal infrared IASI/MetOp sounder. *Atmospheric Chemistry and Physics*, 9(16):6041–6054.

Clerbaux, C., George, M., Turquety, S., Walker, K. A., Barret, B., Bernath, P., Boone, C., Borsdorff, T., Cammas, J. P., Catoire, V., Coffey, M., Coheur, P.-F., Deeter, M., De Mazière, M., Drummond, J., Duchatelet, P., Dupuy, E., de Zafra, R., Eddounia, F., Edwards, D. P., Emmons, L., Funke, B., Gille, J., Griffith, D. W. T., Hannigan, J., Hase, F., Höpfner, M., Jones, N., Kagawa, A., Kasai, Y., Kramer, I., Le Flochmoën, E., Livesey, N. J., López-Puertas, M., Luo, M., Mahieu, E., Murtagh, D., Nédélec, P., Pazmino, A., Pumphrey, H., Ricaud, P., Rinsland, C. P., Robert, C., Schneider, M., Senten, C., Stiller, G., Strandberg, A., Strong, K., Sussmann, R., Thouret, V., Urban, J., and Wiacek, A. (2008). CO measurements from the ACE-FTS satellite instrument: data analysis and validation using ground-based, airborne and spaceborne observations. *Atmospheric Chemistry and Physics*, 8(9):2569–2594.

Coffey, M., Goldman, A., Hannigan, J., Mankin, W., Schoenfeld, W., Rinsland, C., Bernardo, C., and Griffith, D. (1998). Improved vibration–rotation (0–1) hbr line parameters for validating high resolution infrared atmospheric spectra measurements. *Journal of Quantitative Spectroscopy and Radiative Transfer*, 60(5):863–867.

Coheur, P.-F., Clarisse, L., Turquety, S., Hurtmans, D., and Clerbaux, C. (2009). IASI measurements of reactive trace species in biomass burning plumes. *Atmospheric Chemistry and Physics*, 9(15):5655–5667.

Coheur, P.-F., Herbin, H., Clerbaux, C., Hurtmans, D., Wespes, C., Carleer, M., Turquety, S., Rinsland, C. P., Remedios, J., Hauglustaine, D., Boone, C. D., and Bernath, P. F. (2007). ACE-FTS observation of a young biomass burning plume: First reported measurements of C_2H_4, C_3H_6O, H_2CO, and PAN by infrared occultation from space. *Atmospheric Chemistry and Physics*, 7(20):5437–5446.

Cooper, O. R., Parrish, D. D., Stohl, A., Trainer, M., Nédélec, P., Thouret, V., Cammas, J. P., Oltmans, S. J., Johnson, B. J., Tarasick, D., Leblanc, T., McDermid, I. S., Jaffe, D., Gao, R., Stith, J., Ryerson, T., Aikin, K., Campos, T., Weinheimer, A., and Avery, M. A. (2010). Increasing springtime ozone mixing ratios in the free troposphere over western North America. *Nature*, 463(7279):344–348.

Curry, J. (1983). On the formation of Continental Polar Air. *Journal of the Atmospheric Sciences*, 40(9):2278–2292.

Dalsøren, S. B., Myhre, G., Hodnebrog, O., Myhre, C. L., Stohl, A., Pisso, I., Schwietzke, S., Höglund-Isaksson, L., Helmig, D., Reimann, S., Sauvage, S., Schmidbauer, N., Read, K. A., Carpenter, L. J., Lewis, A. C., Punjabi, S., and Wallasch, M. (2018). Discrepancy between simulated and observed ethane and propane levels explained by underestimated fossil emissions. *Nature Geoscience*, 11(3):178–184.

De Mazière, M., Thompson, A. M., Kurylo, M. J., Wild, J. D., Bernhard, G., Blumenstock, T., Braathen, G. O., Hannigan, J. W., Lambert, J.-C., Leblanc, T., Mcgee, T. J., Nedoluha, G., Petropavlovskikh, I., Seckmeyer, G., Simon, P. C., Steinbrecht, W., and Strahan, S. E. (2018). The Network for the Detection of Atmospheric Composition Change (NDACC): history, status and perspectives. *Atmospheric Chemistry and Physics*, 18(7):4935–4964.

De Mazière, M., Vigouroux, C., Bernath, P. F., Baron, P., Blumenstock, T., Boone, C., Brogniez, C., Catoire, V., Coffey, M., Duchatelet, P., Griffith, D., Hannigan, J., Kasai, Y., Kramer, I., Jones, N., Mahieu, E., Manney, G. L., Piccolo, C., Randall, C., Robert, C., Senten, C., Strong, K., Taylor, J., Tétard, C., Walker, K. A., and Wood, S. (2008). Validation of ACE-FTS v2.2 methane profiles from the upper troposphere to the lower mesosphere. *Atmospheric Chemistry and Physics*, 8(9):2421–2435.

De Smedt, I., Stavrakou, T., Hendrick, F., Danckaert, T., Vlemmix, T., Pinardi, G., Theys, N., Lerot, C., Gielen, C., Vigouroux, C., Hermans, C., Fayt, C., Veefkind, P., Müller, J.-F., and Van Roozendael, M. (2015). Diurnal, seasonal and long-term variations of global formaldehyde columns inferred from combined OMI and GOME-2 observations. *Atmospheric Chemistry and Physics*, 15(21):12519–12545.

Deeter, M. N., Edwards, D. P., Francis, G. L., Gille, J. C., Martínez-Alonso, S., Worden, H. M., and Sweeney, C. (2017). A climate-scale satellite record for carbon monoxide: The MOPITT version 7 product. *Atmospheric Measurement Techniques*, 10(7):2533–2555.

Deeter, M. N., Emmons, L. K., Francis, G. L., Edwards, D. P., Gille, J. C., Warner, J. X., Khattatov, B., Ziskin, D., Lamarque, J.-F., Ho, S.-P., Yudin, V., Attié, J.-L., Packman, D., Chen, J., Mao, D., and Drummond, J. R. (2003). Operational carbon monoxide retrieval algorithm and selected results for the MOPITT instrument. *Journal of Geophysical Research*, 108(D14).

Dibb, J. E. and Arsenault, M. (2002). Shouldn't snowpacks be sources of monocarboxylic acids? *Atmospheric Environment*, 36(15–16):2513–2522.

Dolan, W., Payne, V. H., Kualwik, S. S., and Bowman, K. W. (2016). Satellite observations of ethylene (C_2H_4) from the Aura Tropospheric Emission Spectrometer: A scoping study. *Atmospheric Environment*, 141:388–393.

Duflot, V., Wespes, C., Clarisse, L., Hurtmans, D., Ngadi, Y., Jones, N., Paton-Walsh, C., Hadji-Lazaro, J., Vigouroux, C., De Mazière, M., Metzger, J.-M., Mahieu, E., Servais, C., Hase, F., Schneider, M., Clerbaux, C., and Coheur, P.-F. (2015). Acetylene (C_2H_2) and hydrogen cyanide (HCN) from IASI satellite observations: Global Distributions, validation, and comparison with model. *Atmospheric Chemistry and Physics*, 15(18):10509–10527.

Dufour, G., Boone, C. D., Rinsland, C. P., and Bernath, P. F. (2006). First space-borne measurements of methanol inside aged southern tropical to mid-latitude biomass burning plumes using the ACE-FTS instrument. *Atmospheric Chemistry and Physics*, 6(11):3463–3470.

Dufour, G., Szopa, S., Hauglustaine, D. A., Boone, C. D., Rinsland, C. P., and Bernath, P. F. (2007). The influence of biogenic emissions on upper-tropospheric methanol as revealed from space. *Atmospheric Chemistry and Physics*, 7(24):6119–6129.

Eastham, S. D. and Jacob, D. J. (2017). Limits on the ability of global Eulerian models to resolve intercontinental transport of chemical plumes. *Atmospheric Chemistry and Physics*, 17(4):2543–2553.

Eastham, S. D., Long, M. S., Keller, C. A., Lundgren, E., Yantosca, R. M., Zhuang, J., Li, C., Lee, C. J., Yannetti, M., Auer, B. M., Clune, T. L., Kouatchou, J., Putman, W. M., Thompson, M. A., Trayanov, A. L., Molod, A. M., Martin, R. V., and Jacob, D. J. (2018). GEOS-Chem High Performance (GCHP V11-02C): A next-generation implementation of the GEOS-chem chemical transport model for Massively parallel applications. *Geoscientific Model Development*, 11(7):2941–2953.

Eckhardt, S., Quennehen, B., Olivié, D. J. L., Berntsen, T. K., Cherian, R., Christensen, J. H., Collins, W., Crepinsek, S., Daskalakis, N., Flanner, M., Herber, A., Heyes, C., Hodnebrog, Ø., Huang, L., Kanakidou, M., Klimont, Z., Langner, J., Law, K. S., Lund, M. T., Mahmood, R., Massling, A., Myriokefalitakis, S., Nielsen, I. E., Nøjgaard, J. K., Quaas, J., Quinn, P. K., Raut, J.-C., Rumbold, S. T., Schulz, M., Sharma, S., Skeie, R. B., Skov, H., Uttal, T., von Salzen, K., and Stohl, A. (2015). Current model capabilities for simulating black carbon and sulfate concentrations in the Arctic atmosphere: a multi-model evaluation using a comprehensive measurement data set. *Atmospheric Chemistry and Physics*, 15(16):9413–9433.

Erisman, J., Bleeker, A., Galloway, J., and Sutton, M. (2007). Reduced nitrogen in ecology and the environment. *Environmental Pollution*, 150(1):140–149.

Erisman, J., Galloway, J., Seitzinger, S., Bleeker, A., and Butterbach-Bahl, K. (2011). Reactive nitrogen in the environment and its effect on climate change. *Current Opinion in Environmental Sustainability*, 3(5):281–290.

Fadnavis, S., Schultz, M. G., Semeniuk, K., Mahajan, A. S., Pozzoli, L., Sonbawne, S., Ghude, S. D., Kiefer, M., and Eckert, E. (2014). Trends in peroxyacetyl nitrate (PAN) in the upper troposphere and lower stratosphere over southern Asia during the summer monsoon season: Regional impacts. *Atmospheric Chemistry and Physics*, 14(23):12725–12743.

Fall, R. and Benson, A. A. (1996). Leaf methanol — The simplest natural product from plants. *Trends in Plant Science*, 1(9):296–301.

Fast, H., Mittermeier, R. L., and Makino, Y. (2011). A ten-year record of Arctic trace gas total column measurements at Eureka, Canada, from 1997 to 2006. *Atmosphere-Ocean*, 49(2):67–94.

Fischer, E. V., Jacob, D. J., Yantosca, R. M., Sulprizio, M. P., Millet, D. B., Mao, J., Paulot, F., Singh, H. B., Roiger, A., Ries, L., Talbot, R., Dzepina, K., and Pandey Deolal, S. (2014). Atmospheric peroxyacetyl nitrate (PAN): A global budget and source attribution. *Atmospheric Chemistry and Physics*, 14(5):2679–2698.

Fischer, E. V., Jaffe, D. A., and Weatherhead, E. C. (2011). Free tropospheric peroxyacetyl nitrate (PAN) and ozone at Mount Bachelor: Potential causes of variability and timescale for trend detection. *Atmospheric Chemistry and Physics*, 11(12):5641–5654.

Flannigan, M. D., Logan, K. A., Amiro, B. D., Skinner, W. R., and Stocks, B. J. (2005). Future area burned in Canada. *Climatic Change*, 72(1-2):1–16.

Fogal, P. F., Leblanc, L. M., and Drummond, J. R. (2013). The Polar Environment Atmospheric Research Laboratory (PEARL): Sounding the Atmosphere at 80º North. *Arctic*, 66(3):377–386.

Folberth, G. A., Hauglustaine, D. A., Lathière, J., and Brocheton, F. (2006). Interactive chemistry in the Laboratoire de Météorologie Dynamique General Circulation Model: Model description and impact analysis of biogenic hydrocarbons on tropospheric chemistry. *Atmospheric Chemistry and Physics*, 6(8):2273–2319.

Franco, B., Bader, W., Toon, G., Bray, C., Perrin, A., Fischer, E., Sudo, K., Boone, C., Bovy, B., Lejeune, B., Servais, C., and Mahieu, E. (2015). Retrieval of ethane from ground-based FTIR solar spectra using improved spectroscopy: Recent burden increase above Jungfraujoch. *Journal of Quantitative Spectroscopy and Radiative Transfer*, 160:36–49.

Franco, B., Blumenstock, T., Cho, C., Clarisse, L., Clerbaux, C., Coheur, P.-F., De Mazière, M., De Smedt, I., Dorn, H.-P., Emmerichs, T., Fuchs, H., Gkatzelis, G., Griffith, D. W. T., Gromov, S., Hannigan, J. W., Hase, F., Hohaus, T., Jones, N., Kerkweg, A., Kiendler-Scharr, A., Lutsch, E., Mahieu, E., Novelli, A., Ortega, I., Paton-Walsh, C., Pommier, M., Pozzer, A., Reimer, D., Rosanka, S., Sander, R., Schneider, M., Strong, K., Tillmann, R., Van Roozendael, M., Vereecken, L., Vigouroux, C., Wahner, A., and Taraborrelli, D. (2021). Ubiquitous atmospheric production of organic acids mediated by cloud droplets. *Nature*, 593(7858):233–237.

Franco, B., Clarisse, L., Stavrakou, T., Müller, J., Taraborrelli, D., Hadji-Lazaro, J., Hannigan, J. W., Hase, F., Hurtmans, D., Jones, N., Lutsch, E., Mahieu, E., Ortega, I., Schneider, M., Strong, K., Vigouroux, C., Clerbaux, C., and Coheur, P. (2020). Spaceborne measurements of formic and acetic acids: A global view of the regional sources. *Geophysical Research Letters*, 47(4):e2019GL086239.

Franco, B., Clarisse, L., Stavrakou, T., Müller, J., Van Damme, M., Whitburn, S., Hadji-Lazaro, J., Hurtmans, D., Taraborrelli, D., Clerbaux, C., and Coheur, P. (2018). A general framework for global retrievals of trace gases from IASI: Application to methanol, formic acid, and PAN. *Journal of Geophysical Research: Atmospheres*, 123(24).

Franco, B., Clarisse, L., Van Damme, M., Hadji-Lazaro, J., Clerbaux, C., and Coheur, P.-F. (2022). Ethylene industrial emitters seen from space. *Nature Communications*, 13(1).

Franco, B., Mahieu, E., Emmons, L. K., Tzompa-Sosa, Z. A., Fischer, E. V., Sudo, K., Bovy, B., Conway, S., Griffin, D., Hannigan, J. W., Strong, K., and Walker, K. A. (2016a). Evaluating ethane and methane emissions associated with the development of oil and natural gas extraction in North America. *Environmental Research Letters*, 11(4):044010.

Franco, B., Marais, E. A., Bovy, B., Bader, W., Lejeune, B., Roland, G., Servais, C., and Mahieu, E. (2016b). Diurnal cycle and multi-decadal trend of formaldehyde in the remote atmosphere near 46°N. *Atmospheric Chemistry and Physics*, 16(6):4171–4189.

Franklin, J. (2015). *Solar absorption spectroscopy at the Dalhousie Atmospheric Observatory*. PhD thesis, Dalhousie University, Halifax, Canada.

Freitas, S. R., Longo, K. M., and Andreae, M. O. (2006). Impact of including the plume rise of vegetation fires in numerical simulations of associated atmospheric pollutants. *Geophysical Research Letters*, 33(17):L17808.

Friedrich, M., Beutner, E., Reuvers, H., Smeekes, S., Urbain, J.-P., Bader, W., Franco, B., Lejeune, B., and Mahieu, E. (2020). A statistical analysis of time trends in atmospheric ethane. *Climatic Change*, 162(1):105–125.

Fromm, M., Lindsey, D. T., Servranckx, R., Yue, G., Trickl, T., Sica, R., Doucet, P., and Godin-Beekmann, S. (2010). The untold story of pyrocumulonimbus. *Bulletin of the American Meteorological Society*, 91(9):1193–1210.

Fromm, M., Torres, O., Diner, D., Lindsey, D., Vant Hull, B., Servranckx, R., Shettle, E. P., and Li, Z. (2008). Stratospheric impact of the Chisholm Pyrocumulonimbus eruption: 1. Earth-viewing satellite perspective. *Journal of Geophysical Research*, 113(D8).

Fromm, M. D., Kablick, G. P., Peterson, D. A., Kahn, R. A., Flower, V. J., and Seftor, C. J. (2021). Quantifying the source term and uniqueness of the August 12, 2017 Pacific Northwest PyroCb Event. *Journal of Geophysical Research: Atmospheres*, 126(13).

Fu, D., Walker, K. A., Mittermeier, R. L., Strong, K., Sung, K., Fast, H., Bernath, P. F., Boone, C. D., Daffer, W. H., Fogal, P., Kolonjari, F., Loewen, P., Manney, G. L., Mikhailov, O., and Drummond, J. R. (2011). Simultaneous trace gas measurements using two fourier transform spectrometers at eureka, canada during spring 2006, and comparisons with the ace-fts. *Atmospheric Chemistry and Physics*, 11(11):5383–5405.

Fu, T.-M., Jacob, D. J., Palmer, P. I., Chance, K., Wang, Y. X., Barletta, B., Blake, D. R., Stanton, J. C., and Pilling, M. J. (2007). Space-based formaldehyde measurements as constraints on volatile organic compound emissions in east and South Asia and implications for ozone. *Journal of Geophysical Research*, 112(D6).

Gardiner, T., Forbes, A., De Mazière, M., Vigouroux, C., Mahieu, E., Demoulin, P., Velazco, V., Notholt, J., Blumenstock, T., Hase, F., Kramer, I., Sussmann, R., Stremme, W., Mellqvist, J., Strandberg, A., Ellingsen, K., and Gauss, M. (2008). Trend analysis of greenhouse gases over

europe measured by a network of ground-based remote ftir instruments. *Atmospheric Chemistry and Physics*, 8(22):6719–6727.

Gatz, D. F. and Smith, L. (1995). The standard error of a weighted mean concentration—i. bootstrapping vs other methods. *Atmospheric Environment*, 29(11):1185–1193.

Gelaro, R., McCarty, W., Suárez, M. J., Todling, R., Molod, A., Takacs, L., Randles, C. A., Darmenov, A., Bosilovich, M. G., Reichle, R., Wargan, K., Coy, L., Cullather, R., Draper, C., Akella, S., Buchard, V., Conaty, A., Da Silva, A. M., Gu, W., Kim, G.-K., Koster, R., Lucchesi, R., Merkova, D., Nielsen, J. E., Partyka, G., Pawson, S., Putman, W., Rienecker, M., Schubert, S. D., Sienkiewicz, M., and Zhao, B. (2017). The Modern-Era Retrospective Analysis for Research and Applications, Version 2 (MERRA-2). *Journal of Climate*, 30(14):5419–5454.

Gentner, D. R., Worton, D. R., Isaacman, G., Davis, L. C., Dallmann, T. R., Wood, E. C., Herndon, S. C., Goldstein, A. H., and Harley, R. A. (2013). Chemical composition of gas-phase organic carbon emissions from motor vehicles and implications for ozone production. *Environmental Science & Technology*, 47(20):11837–11848.

George, M., Clerbaux, C., Bouarar, I., Coheur, P.-F., Deeter, M. N., Edwards, D. P., Francis, G., Gille, J. C., Hadji-Lazaro, J., Hurtmans, D., Inness, A., Mao, D., and Worden, H. M. (2015). An examination of the long-term CO records from MOPITT and IASI: Comparison of retrieval methodology. *Atmospheric Measurement Techniques*, 8(10):4313–4328.

Glatthor, N., von Clarmann, T., Fischer, H., Funke, B., Grabowski, U., Höpfner, M., Kellmann, S., Kiefer, M., Linden, A., Milz, M., Steck, T., and Stiller, G. P. (2007). Global peroxyacetyl nitrate (PAN) retrieval in the upper troposphere from limb emission spectra of the Michelson interferometer for passive atmospheric sounding (MIPAS). *Atmospheric Chemistry and Physics*, 7(11):2775–2787.

González Abad, G., Bernath, P. F., Boone, C. D., McLeod, S. D., Manney, G. L., and Toon, G. C. (2009). Global distribution of upper tropospheric formic acid from the ACE-FTS. *Atmospheric Chemistry and Physics*, 9(20):8039–8047.

Goode, J. G., Yokelson, R. J., Ward, D. E., Susott, R. A., Babbitt, R. E., Davies, M. A., and Hao, W. M. (2000). Measurements of excess O_3, CO_2, CO, CH_4, C_2H_4, C_2H_2, HCN, NO, NH_3, HCOOH, CH_3COOH, HCHO, and CH_3OH in 1997 Alaskan biomass burning plumes by airborne

Fourier transform infrared spectroscopy (AFTIR). *Journal of Geophysical Research: Atmospheres*, 105(D17):22147–22166.

Gordon, I., Rothman, L., Hill, C., Kochanov, R., Tan, Y., Bernath, P., Birk, M., Boudon, V., Campargue, A., Chance, K., Drouin, B., Flaud, J.-M., Gamache, R., Hodges, J., Jacquemart, D., Perevalov, V., Perrin, A., Shine, K., Smith, M.-A., Tennyson, J., Toon, G., Tran, H., Tyuterev, V., Barbe, A., Császár, A., Devi, V., Furtenbacher, T., Harrison, J., Hartmann, J.-M., Jolly, A., Johnson, T., Karman, T., Kleiner, I., Kyuberis, A., Loos, J., Lyulin, O., Massie, S., Mikhailenko, S., Moazzen-Ahmadi, N., Müller, H., Naumenko, O., Nikitin, A., Polyansky, O., Rey, M., Rotger, M., Sharpe, S., Sung, K., Starikova, E., Tashkun, S., Auwera, J. V., Wagner, G., Wilzewski, J., Wcisło, P., Yu, S., and Zak, E. (2017). The HITRAN2016 Molecular Spectroscopic Database. *Journal of Quantitative Spectroscopy and Radiative Transfer*, 203:3–69.

Griffin, D., Walker, K. A., Conway, S., Kolonjari, F., Strong, K., Batchelor, R., Boone, C. D., Dan, L., Drummond, J. R., Fogal, P. F., Fu, D., Lindenmaier, R., Manney, G. L., and Weaver, D. (2017). Multi-year comparisons of ground-based and space-borne Fourier transform spectrometers in the high Arctic between 2006 and 2013. *Atmospheric Measurement Techniques*, 10(9):3273–3294.

Griffiths, P. R. and De Haseth, J. A. (2007). *Fourier Transform Infrared Spectrometry*. Wiley, 1st edition.

Guenther, A. B., Jiang, X., Heald, C. L., Sakulyanontvittaya, T., Duhl, T., Emmons, L. K., and Wang, X. (2012). The Model of Emissions of Gases and Aerosols from Nature Version 2.1 (MEGAN2.1): An extended and updated framework for modeling biogenic emissions. *Geoscientific Model Development*, 5(6):1471–1492.

Halofsky, J. E., Peterson, D. L., and Harvey, B. J. (2020). Changing wildfire, changing forests: The effects of climate change on fire regimes and vegetation in the Pacific Northwest, USA. *Fire Ecology*, 16(1):4.

Hannigan, J. W., Coffey, M. T., and Goldman, A. (2009). Semiautonomous fts observation system for remote sensing of stratospheric and tropospheric gases. *Journal of Atmospheric and Oceanic Technology*, 26(9):1814–1828.

Hase, F. (2012). Improved instrumental line shape monitoring for the ground-based, high-resolution FTIR spectrometers of the Network for the Detection of Atmospheric Composition Change. *Atmospheric Measurement Techniques*, 5(3):603–610.

Hase, F., Blumenstock, T., and Paton-Walsh, C. (1999). Analysis of the instrumental line shape of high-resolution fourier transform IR spectrometers with gas cell measurements and new retrieval software. *Applied Optics*, 38(15):3417.

Hase, F., Hannigan, J., Coffey, M., Goldman, A., Höpfner, M., Jones, N., Rinsland, C., and Wood, S. (2004). Intercomparison of retrieval codes used for the analysis of high-resolution, ground-based FTIR measurements. *Journal of Quantitative Spectroscopy and Radiative Transfer*, 87(1):25–52.

Helmig, D., Rossabi, S., Hueber, J., Tans, P., Montzka, S. A., Masarie, K., Thoning, K., Plass-Duelmer, C., Claude, A., Carpenter, L. J., Lewis, A. C., Punjabi, S., Reimann, S., Vollmer, M. K., Steinbrecher, R., Hannigan, J. W., Emmons, L. K., Mahieu, E., Franco, B., Smale, D., and Pozzer, A. (2016). Reversal of global atmospheric ethane and propane trends largely due to US oil and natural gas production. *Nature Geoscience*, 9(7):490–495.

Herbin, H., Hurtmans, D., Clarisse, L., Turquety, S., Clerbaux, C., Rinsland, C. P., Boone, C., Bernath, P. F., and Coheur, P.-F. (2009). Distributions and seasonal variations of tropospheric ethene (C_2H_4) from Atmospheric Chemistry Experiment (ACE-FTS) solar occultation spectra. *Geophysical Research Letters*, 36(4):L04801.

Hoesly, R. M., Smith, S. J., Feng, L., Klimont, Z., Janssens-Maenhout, G., Pitkanen, T., Seibert, J. J., Vu, L., Andres, R. J., Bolt, R. M., Bond, T. C., Dawidowski, L., Kholod, N., Kurokawa, J.-i., Li, M., Liu, L., Lu, Z., Moura, M. C. P., O'Rourke, P. R., and Zhang, Q. (2018). Historical (1750–2014) anthropogenic emissions of reactive gases and aerosols from the Community Emissions Data System (CEDS). *Geoscientific Model Development*, 11(1):369–408.

Holl, G., Walker, K. A., Conway, S., Saitoh, N., Boone, C. D., Strong, K., and Drummond, J. R. (2016). Methane cross-validation between three Fourier transform spectrometers: SCISAT ACE-FTS, GOSAT TANSO-FTS, and ground-based FTS measurements in the Canadian high Arctic. *Atmospheric Measurement Techniques*, 9(5):1961–1980.

Hollas, J. M. (2004). *Modern spectroscopy*. J. Wiley.

Holloway, T., Levy, H., and Kasibhatla, P. (2000). Global distribution of carbon monoxide. *Journal of Geophysical Research: Atmospheres*, 105(D10):12123–12147.

Holzinger, R., Warneke, C., Hansel, A., Jordan, A., Lindinger, W., Scharffe, D. H., Schade, G., and Crutzen, P. J. (1999). Biomass burning as a source of formaldehyde, acetaldehyde, methanol, acetone, acetonitrile, and hydrogen cyanide. *Geophysical Research Letters*, 26(8):1161–1164.

Hope, E. S., McKenney, D. W., Pedlar, J. H., Stocks, B. J., and Gauthier, S. (2016). Wildfire suppression costs for Canada under a changing climate. *PLOS ONE*, 11(8):e0157425.

Horowitz, L. W., Walters, S., Mauzerall, D. L., Emmons, L. K., Rasch, P. J., Granier, C., Tie, X., Lamarque, J., Schultz, M. G., Tyndall, G. S., Orlando, J. J., and Brasseur, G. P. (2003). A global simulation of tropospheric ozone and related tracers: Description and evaluation of MOZART, version 2. *Journal of Geophysical Research: Atmospheres*, 108(D24):2002JD002853.

Hurtmans, D., Coheur, P.-F., Wespes, C., Clarisse, L., Scharf, O., Clerbaux, C., Hadji-Lazaro, J., George, M., and Turquety, S. (2012). FORLI radiative transfer and retrieval code for IASI. *Journal of Quantitative Spectroscopy and Radiative Transfer*, 113(11):1391–1408.

Hüve, K., Christ, M., Kleist, E., Uerlings, R., Niinemets, U., Walter, A., and Wildt, J. (2007). Simultaneous growth and emission measurements demonstrate an interactive control of methanol release by leaf expansion and Stomata. *Journal of Experimental Botany*, 58(7):1783–1793.

IPCC (2022). *The Ocean and Cryosphere in a Changing Climate: Special Report of the Intergovernmental Panel on Climate Change*. Cambridge University Press, 1 edition.

Jacob, D. (2000). Heterogeneous chemistry and tropospheric ozone. *Atmospheric Environment*, 34(12-14):2131–2159.

Jaffe, L. S. (1968). Ambient carbon monoxide and its fate in the atmosphere. *Journal of the Air Pollution Control Association*, 18(8):534–540.

Jalali, A., Walker, K. A., Strong, K., Buchholz, R. R., Deeter, M. N., Wunch, D., Roche, S., Wizenberg, T., Lutsch, E., McGee, E., Worden, H. M., Fogal, P., and Drummond, J. R. (2022). A comparison of carbon monoxide retrievals between the MOPITT satellite and Canadian high-arctic ground-based NDACC and TCCON FTIR measurements. *Atmospheric Measurement Techniques*, 15(22):6837–6863.

Jiang, Z., Jones, D. B., Worden, J., Worden, H. M., Henze, D. K., and Wang, Y. X. (2015). Regional data assimilation of multi-spectral MOPITT observations of CO over North America. *Atmospheric Chemistry and Physics*, 15(12):6801–6814.

Jiang, Z., Worden, J. R., Payne, V. H., Zhu, L., Fischer, E., Walker, T., and Jones, D. B. (2016). Ozone Export from East Asia: The role of PAN. *Journal of Geophysical Research: Atmospheres*, 121(11):6555–6563.

Jin, J. J., Semeniuk, K., Jonsson, A. I., Beagley, S. R., McConnell, J. C., Boone, C. D., Walker, K. A., Bernath, P. F., Rinsland, C. P., Dupuy, E., Ricaud, P., De La Noë, J., Urban, J., and Murtagh, D. (2005). Co-located ACE-FTS and Odin/SMR Stratospheric-mesospheric CO 2004 measurements and comparison with a GCM. *Geophysical Research Letters*, 32(15):L15S03.

Juncosa Calahorrano, J. F., Lindaas, J., O'Dell, K., Palm, B. B., Peng, Q., Flocke, F., Pollack, I. B., Garofalo, L. A., Farmer, D. K., Pierce, J. R., Collett, J. L., Weinheimer, A., Campos, T., Hornbrook, R. S., Hall, S. R., Ullmann, K., Pothier, M. A., Apel, E. C., Permar, W., Hu, L., Hills, A. J., Montzka, D., Tyndall, G., Thornton, J. A., and Fischer, E. V. (2020). Daytime oxidized reactive nitrogen partitioning in western U.S. wildfire smoke plumes. *Journal of Geophysical Research: Atmospheres*, 126(4):e2020JD033484.

Kahl, J. D., Serreze, M. C., and Schnell, R. C. (1992). Tropospheric low-level temperature inversions in the Canadian Arctic. *Atmosphere-Ocean*, 30(4):511–529.

Kaiser, J. W., Heil, A., Andreae, M. O., Benedetti, A., Chubarova, N., Jones, L., Morcrette, J.-J., Razinger, M., Schultz, M. G., Suttie, M., and Van Der Werf, G. R. (2012). Biomass burning emissions estimated with a global fire assimilation system based on observed fire radiative power. *Biogeosciences*, 9(1):527–554.

Kasai, Y. J., Koshiro, T., Endo, M., Jones, N. B., and Murayama, Y. (2005). Ground-based measurement of Strato–Mesospheric CO by a FTIR spectrometer over Poker Flat, Alaska. *Advances in Space Research*, 35(11):2024–2030.

Kerzenmacher, T., Dils, B., Kumps, N., Blumenstock, T., Clerbaux, C., Coheur, P.-F., Demoulin, P., García, O., George, M., Griffith, D. W. T., Hase, F., Hadji-Lazaro, J., Hurtmans, D., Jones, N., Mahieu, E., Notholt, J., Paton-Walsh, C., Raffalski, U., Ridder, T., Schneider, M., Servais, C., and De Mazière, M. (2012). Validation of IASI FORLI carbon monoxide retrievals using FTIR data from NDACC. *Atmospheric Measurement Techniques*, 5(11):2751–2761.

Kerzenmacher, T. E., Walker, K. A., Strong, K., Berman, R., Bernath, P. F., Boone, C. D., Drummond, J. R., Fast, H., Fraser, A., MacQuarrie, K., Midwinter, C., Sung, K., McElroy, C. T., Mittermeier, R. L., Walker, J., and Wu, H. (2005). Measurements of o3, no2 and temperature during the 2004 canadian arctic ace validation campaign. *Geophysical Research Letters*, 32(16).

Khalil, M. and Rasmussen, R. (1990). The global cycle of carbon monoxide: Trends and Mass Balance. *Chemosphere*, 20(1–2):227–242.

Khaykin, S. M., Godin-Beekmann, S., Hauchecorne, A., Pelon, J., Ravetta, F., and Keckhut, P. (2018). Stratospheric smoke with unprecedentedly high backscatter observed by lidars above Southern France. *Geophysical Research Letters*, 45(3):1639–1646.

Kim, Y., Hatsushika, H., Muskett, R. R., and Yamazaki, K. (2005). Possible effect of boreal wildfire soot on Arctic sea ice and Alaska Glaciers. *Atmospheric Environment*, 39(19):3513–3520.

Kirchmeier-Young, M. C., Gillett, N. P., Zwiers, F. W., Cannon, A. J., and Anslow, F. S. (2019). Attribution of the influence of human-induced climate change on an extreme fire season. *Earth's Future*, 7(1):2–10.

Klonecki, A. (2003). Seasonal changes in the transport of pollutants into the Arctic troposphere-model study. *Journal of Geophysical Research*, 108(D4):2002JD002199.

Kloss, C., Berthet, G., Sellitto, P., Ploeger, F., Bucci, S., Khaykin, S., Jégou, F., Taha, G., Thomason, L. W., Barret, B., Le Flochmoen, E., Von Hobe, M., Bossolasco, A., Bègue, N., and Legras, B. (2019). Transport of the 2017 Canadian wildfire plume to the tropics via the Asian monsoon circulation. *Atmospheric Chemistry and Physics*, 19(21):13547–13567.

Kopacz, M., Jacob, D. J., Fisher, J. A., Logan, J. A., Zhang, L., Megretskaia, I. A., Yantosca, R. M., Singh, K., Henze, D. K., Burrows, J. P., Buchwitz, M., Khlystova, I., McMillan, W. W., Gille, J. C., Edwards, D. P., Eldering, A., Thouret, V., and Nedelec, P. (2010). Global estimates of CO sources with high resolution by adjoint inversion of multiple satellite datasets (MOPITT, Airs, Sciamachy, TES). *Atmospheric Chemistry and Physics*, 10(3):855–876.

Krol, M., Houweling, S., Bregman, B., Broek, M. V. D., Segers, A., Velthoven, P. V., Peters, W., Dentener, F., and Bergamaschi, P. (2005). The two-way nested global chemistry-transport zoom model TM5: algorithm and applications. *Atmospheric Chemistry and Physics*, 5(2):417–432.

Landgraf, J., aan de Brugh, J., Scheepmaker, R. A., Borsdorff, T., Houweling, S., and Hasekamp, O. P. (2018). Algorithm Theoretical Baseline Document for Sentinel-5 Precursor: Carbon Monoxide Total Column Retrieval V1.1. Technical Report SRON-S5P-LEV2-RP-002, Netherlands Institute for Space Research (SRON).

Landgraf, J., Borsdorff, T., Langerock, B., and Keppens, A. (2020). S5P Mission Performance Centre Carbon Monoxide [L2 CO] Readme V1.4. Technical report, Netherlands Institute for Space Research (SRON).

Landgraf, J., Brugh, J. A. D., Scheepmaker, R., Borsdorff, T., Hu, H., Houweling, S., Butz, A., Aben, I., and Hasekamp, O. (2016). Carbon monoxide total column retrievals from TROPOMI shortwave infrared measurements. *Atmospheric Measurement Techniques*, 9(10):4955–4975.

Law, K. and Stohl, A. (2007). Arctic air pollution: Origins and impacts. *Science*, 315(5818):1537–1540.

Law, K., Stohl, A., Quinn, P., Brock, C., Burkhart, J., Paris, J., Ancellet, G., Singh, H., Roiger, A., Schlager, H., Dibb, J., Jacob, D., Arnold, S., Pelon, J., and Thomas, J. (2014). Arctic Air Pollution: New Insights from POLARCAT-IPY. *Bull. Am. Meteorol. Soc.*, 95(12):1873–1895.

Lelieveld, J., Gromov, S., Pozzer, A., and Taraborrelli, D. (2016). Global tropospheric hydroxyl distribution, budget and reactivity. *Atmospheric Chemistry and Physics*, 16(19):12477–12493.

Liang, Q., Rodriguez, J. M., Douglass, A. R., Crawford, J. H., Olson, J. R., Apel, E., Bian, H., Blake, D. R., Brune, W., Chin, M., Colarco, P. R., Da Silva, A., Diskin, G. S., Duncan, B. N., Huey, L. G., Knapp, D. J., Montzka, D. D., Nielsen, J. E., Pawson, S., Riemer, D. D., Weinheimer, A. J., and Wisthaler, A. (2011). Reactive nitrogen, ozone and ozone production in the Arctic troposphere and the impact of stratosphere-troposphere exchange. *Atmospheric Chemistry and Physics*, 11(24):13181–13199.

Lin, H., Jacob, D. J., Lundgren, E. W., Sulprizio, M. P., Keller, C. A., Fritz, T. M., Eastham, S. D., Emmons, L. K., Campbell, P. C., Baker, B., Saylor, R. D., and Montuoro, R. (2021). Harmonized emissions component (HEMCO) 3.0 as a versatile emissions component for atmospheric models: Application in the GEOS-Chem, NASA GEOS, WRF-GC, CESM2, NOAA GEFS-aerosol, and NOAA UFS models. *Geoscientific Model Development*, 14(9):5487–5506.

Lindenmaier, R. (2012). *Studies of Arctic Middle Atmosphere Chemistry using Infrared Absorption Spectroscopy*. PhD thesis, University of Toronto, Toronto, Canada.

Liou, K.-N. (2002). *An introduction to atmospheric radiation*. Academic Press, 2 edition.

Liu, X., Zhang, Y., Huey, L. G., Yokelson, R. J., Wang, Y., Jimenez, J. L., Campuzano-Jost, P., Beyersdorf, A. J., Blake, D. R., Choi, Y., St. Clair, J. M., Crounse, J. D., Day, D. A., Diskin, G. S., Fried, A., Hall, S. R., Hanisco, T. F., King, L. E., Meinardi, S., Mikoviny, T., Palm, B. B., Peischl, J., Perring, A. E., Pollack, I. B., Ryerson, T. B., Sachse, G., Schwarz, J. P., Simpson, I. J., Tanner, D. J., Thornhill, K. L., Ullmann, K., Weber, R. J., Wennberg, P. O., Wisthaler, A., Wolfe, G. M., and Ziemba, L. D. (2016). Agricultural fires in the south eastern U.S. during

SEAC4RS: Emissions of trace gases and particles and evolution of ozone, reactive nitrogen, and organic aerosol. *Journal of Geophysical Research: Atmospheres*, 121(12):7383–7414.

Liu, Z., Wang, Y., Gu, D., Zhao, C., Huey, L. G., Stickel, R., Liao, J., Shao, M., Zhu, T., Zeng, L., Liu, S.-C., Chang, C.-C., Amoroso, A., and Costabile, F. (2010). Evidence of reactive aromatics as a major source of peroxy acetyl nitrate over China. *Environmental Science & Technology*, 44(18):7017–7022.

Lorentz, H. A. (1906). The absorption and emission lines of gaseous bodies. *Proceedings of the Royal Academy of Amsterdam*, VIII:591–611.

Luecken, D., Hutzell, W., Strum, M., and Pouliot, G. (2012). Regional sources of atmospheric formaldehyde and acetaldehyde, and implications for atmospheric modeling. *Atmospheric Environment*, 47:477–490.

Luecken, D. J., Napelenok, S. L., Strum, M., Scheffe, R., and Phillips, S. (2018). Sensitivity of ambient atmospheric formaldehyde and ozone to precursor species and source types across the united states. *Environmental Science & Technology*, 52(8):4668–4675.

Lutsch, E., Dammers, E., Conway, S., and Strong, K. (2016). Long-range transport of NH_3, CO, HCN, and C_2H_6 from the 2014 Canadian Wildfires. *Geophysical Research Letters*, 43(15):8286–8297.

Lutsch, E., Strong, K., Jones, D., Blumenstock, T., Conway, S., Fisher, J., Hannigan, J., Hase, F., Kasai, Y., Mahieu, E., Makarova, M., Morino, I., Nagahama, T., Notholt, J., Ortega, I., Palm, M., Poberovskii, A. V., Sussmann, R., and Warneke, T. (2020). Detection and attribution of wildfire pollution in the Arctic and northern midlatitudes using a network of Fourier-transform infrared spectrometers and GEOS-Chem. *Atmospheric Chemistry and Physics*, 20(21):12813–12851.

Lutsch, E., Strong, K., Jones, D., Ortega, I., Hannigan, J., Dammers, E., Shephard, M., Morris, E., Murphy, K., Evans, M., Parrington, M., Whitburn, S., Damme, M. V., Clarisse, L., Coheur, P. F., Clerbaux, C., Croft, B., Martin, R. V., Pierce, J. R., and Fisher, J. A. (2019). Unprecedented Atmospheric Ammonia Concentrations Detected in the High Arctic From the 2017 Canadian Wildfires. *Journal of Geophysical Research: Atmospheres*, 124(14):8178–8202.

Lutsch, E. M. (2019). *The Influence of Biomass Burning on the Arctic Atmosphere*. PhD thesis, University of Toronto, Toronto, Canada.

MacDonald, R. C. and Fall, R. (1993). Detection of substantial emissions of methanol from plants to the atmosphere. *Atmospheric Environment. Part A. General Topics*, 27(11):1709–1713.

Maddanu, F. and Proietti, T. (2023). Trends in atmospheric ethane. *Climatic Change*, 176(5):53.

Mahajan, A. S., Whalley, L. K., Kozlova, E., Oetjen, H., Mendez, L., Furneaux, K. L., Goddard, A., Heard, D. E., Plane, J. M., and Saiz-Lopez, A. (2010). DOAS observations of formaldehyde and its impact on the HO_x balance in the tropical Atlantic marine boundary layer. *Journal of Atmospheric Chemistry*, 66(3):167–178.

Mahieu, E., Fischer, E. V., Franco, B., Palm, M., Wizenberg, T., Smale, D., Clarisse, L., Clerbaux, C., Coheur, P.-F., Hannigan, J. W., Lutsch, E., Notholt, J., Cantos, I. P., Prignon, M., Servais, C., and Strong, K. (2021). First retrievals of peroxyacetyl nitrate (PAN) from ground-based FTIR solar spectra recorded at remote sites, comparison with model and satellite data. *Elementa: Science of the Anthropocene*, 9(1):00027.

Manney, G. L., Daffer, W. H., Strawbridge, K. B., Walker, K. A., Boone, C. D., Bernath, P. F., Kerzenmacher, T., Schwartz, M. J., Strong, K., Sica, R. J., Krüger, K., Pumphrey, H. C., Lambert, A., Santee, M. L., Livesey, N. J., Remsberg, E. E., Mlynczak, M. G., and Russell III, J. R. (2008). The high Arctic in extreme winters: vortex, temperature, and MLS and ACE-FTS trace gas evolution. *Atmospheric Chemistry and Physics*, 8(3):505–522.

Marelle, L., Thomas, J. L., Raut, J.-C., Law, K. S., Jalkanen, J.-P., Johansson, L., Roiger, A., Schlager, H., Kim, J., Reiter, A., and Weinzierl, B. (2016). Air Quality and radiative impacts of Arctic shipping emissions in the summertime in Northern Norway: From the local to the regional scale. *Atmospheric Chemistry and Physics*, 16(4):2359–2379.

Marsh, D. R., Mills, M. J., Kinnison, D. E., Lamarque, J.-F., Calvo, N., and Polvani, L. M. (2013). Climate Change from 1850 to 2005 Simulated in CESM1(WACCM). *Journal of Climate*, 26(19):7372–7391.

Martin, R. V., Eastham, S. D., Bindle, L., Lundgren, E. W., Clune, T. L., Keller, C. A., Downs, W., Zhang, D., Lucchesi, R. A., Sulprizio, M. P., Yantosca, R. M., Li, Y., Estrada, L., Putman, W. M., Auer, B. M., Trayanov, A. L., Pawson, S., and Jacob, D. J. (2022). Improved advection, resolution, performance, and community access in the new generation (version 13) of the high-performance GEOS-Chem global atmospheric chemistry model (GCHP). *Geoscientific Model Development*, 15(23):8731–8748.

Martínez-Alonso, S., Deeter, M., Worden, H., Borsdorff, T., Aben, I., Commane, R., Daube, B., Francis, G., George, M., Landgraf, J., Mao, D., Mckain, K., and Wofsy, S. (2020). 1.5 years of TROPOMI CO measurements: comparisons to MOPITT and ATom. *Atmospheric Measurement Techniques*, 13(9):4841–4864.

McElroy, C. T., Nowlan, C. R., Drummond, J. R., Bernath, P. F., Barton, D. V., Dufour, D. G., Midwinter, C., Hall, R. B., Ogyu, A., Ullberg, A., Wardle, D. I., Kar, J., Zou, J., Nichitiu, F., Boone, C. D., Walker, K. A., and Rowlands, N. (2007). The ACE-MAESTRO instrument on SCISAT: description, performance, and preliminary results. *Applied Optics*, 46(20):4341–4356.

Meier, A., Toon, G. C., Rinsland, C. P., Goldman, A., and Hase, F. (2004). *Spectroscopic Atlas of Atmospheric Microwindows in the Middle Infra-Red*, volume 048 of *IRF Technical Report*. Swedish Institute of Space Physics.

Mendonca, J. (2017). *Improving the Retrievals of Greenhouse Gases from Ground-Based Solar Absorption Spectra*. PhD thesis, University of Toronto, Toronto, Canada.

Michelson, A. A. (1881). The relative motion of the Earth and of the Luminiferous Ether. *American Journal of Science*, s3-22(128):120–129.

Millet, D. B., Baasandorj, M., Farmer, D. K., Thornton, J. A., Baumann, K., Brophy, P., Chaliyakunnel, S., De Gouw, J. A., Graus, M., Hu, L., Koss, A., Lee, B. H., Lopez-Hilfiker, F. D., Neuman, J. A., Paulot, F., Peischl, J., Pollack, I. B., Ryerson, T. B., Warneke, C., Williams, B. J., and Xu, J. (2015). A large and ubiquitous source of atmospheric formic acid. *Atmospheric Chemistry and Physics*, 15(11):6283–6304.

Mitchell, J. (1957). Visual range in the polar regions with particular reference to the Alaskan Arctic. *Journal of Atmospheric and Terrestrial Physics*, 17:195–211.

Monks, P. S., Archibald, A. T., Colette, A., Cooper, O., Coyle, M., Derwent, R., Fowler, D., Granier, C., Law, K. S., Mills, G. E., Stevenson, D. S., Tarasova, O., Thouret, V., Von Schneidemesser, E., Sommariva, R., Wild, O., and Williams, M. L. (2015). Tropospheric ozone and its precursors from the urban to the global scale from air quality to short-lived climate forcer. *Atmospheric Chemistry and Physics*, 15(15):8889–8973.

Monks, S. A., Wilson, C., Emmons, L. K., Hannigan, J. W., Helmig, D., Blake, N. J., and Blake, D. R. (2018). Using an inverse model to reconcile differences in simulated and observed global

ethane concentrations and trends between 2008 and 2014. *Journal of Geophysical Research: Atmospheres*, 123(19):11262–11282.

Morgott, D. A. (2015). Anthropogenic and biogenic sources of ethylene and the potential for human exposure: A literature review. *Chemico-Biological Interactions*, 241:10–22.

Moxim, W. J., Levy, H., and Kasibhatla, P. S. (1996). Simulated global tropospheric PAN: Its transport and impact on NO_x. *Journal of Geophysical Research: Atmospheres*, 101(D7):12621–12638.

Mungall, E. L., Abbatt, J. P. D., Wentzell, J. J. B., Wentworth, G. R., Murphy, J. G., Kunkel, D., Gute, E., Tarasick, D. W., Sharma, S., Cox, C. J., Uttal, T., and Liggio, J. (2018). High gas-phase mixing ratios of formic and acetic acid in the high Arctic. *Atmospheric Chemistry and Physics*, 18(14):10237–10254.

National Imagery and Mapping Agency (2000). Department of Defense World Geodetic System 1984: its definition and relationships with local geodetic systems. Technical Report TR8350.2, National Imagery and Mapping Agency, St. Louis, MO, USA.

Nordenskiöld, A. E. (1883). Nordenskiöld on the inland ice of Greenland. *Science*, ns-2(44):732–738.

Notholt, J., Toon, G., Jones, N., Griffith, D., and Warneke, T. (2006). Spectral line finding program for atmospheric remote sensing using full radiation transfer. *Journal of Quantitative Spectroscopy and Radiative Transfer*, 97(1):112–125.

Notholt, J., Toon, G. C., Lehmann, R., Sen, B., and Blavier, J.-F. (1997). Comparison of Arctic and Antarctic Trace gas column abundances from ground-based Fourier transform infrared spectrometry. *Journal of Geophysical Research: Atmospheres*, 102(D11):12863–12869.

Notholt, J., Toon, G. C., Rinsland, C. P., Pougatchev, N. S., Jones, N. B., Connor, B. J., Weller, R., Gautrois, M., and Schrems, O. (2000). Latitudinal variations of trace gas concentrations in the free troposphere measured by solar absorption spectroscopy during a ship cruise. *Journal of Geophysical Research: Atmospheres*, 105(D1):1337–1349.

Nussbaumer, C. M., Crowley, J. N., Schuladen, J., Williams, J., Hafermann, S., Reiffs, A., Axinte, R., Harder, H., Ernest, C., Novelli, A., Sala, K., Martinez, M., Mallik, C., Tomsche, L., Plass-Dülmer, C., Bohn, B., Lelieveld, J., and Fischer, H. (2021). Measurement report: Photochemical production and loss rates of formaldehyde and ozone across Europe. *Atmospheric Chemistry and Physics*, 21(24):18413–18432.

Olsen, K. S., Strong, K., Walker, K. A., Boone, C. D., Raspollini, P., Plieninger, J., Bader, W., Conway, S., Grutter, M., Hannigan, J. W., Hase, F., Jones, N., Mazière, M. D., Notholt, J., Schneider, M., Smale, D., Sussmann, R., and Saitoh, N. (2017). Comparison of the GOSAT TANSO-FTS TIR CH_4 volume mixing ratio vertical profiles with those measured by ACE-FTS, ESA MIPAS, IMK-IAA MIPAS, and 16 NDACC stations. *Atmospheric Measurement Techniques*, 10(10):3697–3718.

Orlando, J. J., Tyndall, G. S., and Calvert, J. G. (1992). Thermal decomposition pathways for peroxyacetyl nitrate (PAN): Implications for atmospheric methyl nitrate levels. *Atmospheric Environment. Part A. General Topics*, 26(17):3111–3118.

Paton-Walsh, C., Deutscher, N. M., Griffith, D. W., Forgan, B. W., Wilson, S. R., Jones, N. B., and Edwards, D. P. (2010). Trace gas emissions from savanna fires in northern Australia. *Journal of Geophysical Research*, 115(D16):D16314.

Paton-Walsh, C., Jones, N. B., Wilson, S. R., Haverd, V., Meier, A., Griffith, D. W., and Rinsland, C. P. (2005). Measurements of trace gas emissions from Australian forest fires and correlations with coincident measurements of aerosol optical depth. *Journal of Geophysical Research*, 110(D24):2005JD006202.

Paulot, F., Paynter, D., Ginoux, P., Naik, V., Whitburn, S., Van Damme, M., Clarisse, L., Coheur, P.-F., and Horowitz, L. W. (2017). Gas-aerosol partitioning of ammonia in biomass burning plumes: Implications for the interpretation of spaceborne observations of ammonia and the radiative forcing of ammonium nitrate. *Geophysical Research Letters*, 44(15):8084–8093.

Paulot, F., Wunch, D., Crounse, J. D., Toon, G. C., Millet, D. B., DeCarlo, P. F., Vigouroux, C., Deutscher, N. M., González Abad, G., Notholt, J., Warneke, T., Hannigan, J. W., Warneke, C., De Gouw, J. A., Dunlea, E. J., De Mazière, M., Griffith, D. W. T., Bernath, P., Jimenez, J. L., and Wennberg, P. O. (2011). Importance of secondary sources in the atmospheric budgets of formic and acetic acids. *Atmospheric Chemistry and Physics*, 11(5):1989–2013.

Payne, V. H., Alvarado, M. J., Cady-Pereira, K. E., Worden, J. R., Kulawik, S. S., and Fischer, E. V. (2014). Satellite observations of peroxyacetyl nitrate from the AURA Tropospheric Emission Spectrometer. *Atmospheric Measurement Techniques*, 7(11):3737–3749.

Payne, V. H., Kulawik, S. S., Fischer, E. V., Brewer, J. F., Huey, L. G., Miyazaki, K., Worden, J. R., Bowman, K. W., Hintsa, E. J., Moore, F., Elkins, J. W., and Juncosa Calahorrano, J. (2022).

Satellite measurements of peroxyacetyl nitrate from the Cross-Track Infrared Sounder: Comparison with ATom Aircraft Measurements. *Atmospheric Measurement Techniques*, 15(11):3497–3511.

Peters, G. P., Nilssen, T. B., Lindholt, L., Eide, M. S., Glomsrød, S., Eide, L. I., and Fuglestvedt, J. S. (2011). Future emissions from shipping and petroleum activities in the arctic. *Atmospheric Chemistry and Physics*, 11(11):5305–5320.

Petersen, A. K., Warneke, T., Lawrence, M. G., Notholt, J., and Schrems, O. (2008). First ground-based FTIR observations of the seasonal variation of carbon monoxide in the Tropics. *Geophysical Research Letters*, 35(3):L03813.

Peterson, D. A., Campbell, J. R., Hyer, E. J., Fromm, M. D., Kablick, G. P., Cossuth, J. H., and DeLand, M. T. (2018). Wildfire-driven thunderstorms cause a volcano-like stratospheric injection of smoke. *npj Climate and Atmospheric Science*, 1(1):30.

Peterson, D. A., Fromm, M. D., McRae, R. H. D., Campbell, J. R., Hyer, E. J., Taha, G., Camacho, C. P., Kablick, G. P., Schmidt, C. C., and DeLand, M. T. (2021). Australia's black summer pyrocumulonimbus super outbreak reveals potential for increasingly extreme stratospheric smoke events. *npj Climate and Atmospheric Science*, 4(1):38.

Philip, S., Martin, R. V., and Keller, C. A. (2016). Sensitivity of chemistry-transport model simulations to the duration of chemical and transport operators: A case study with GEOS-chem V10-01. *Geoscientific Model Development*, 9(5):1683–1695.

Pommier, M., Clerbaux, C., and Coheur, P.-F. (2017). Determination of enhancement ratios of HCOOH relative to CO in biomass burning plumes by the Infrared Atmospheric Sounding Interferometer (IASI). *Atmospheric Chemistry and Physics*, 17(18):11089–11105.

Pommier, M., Clerbaux, C., Coheur, P.-F., Mahieu, E., Müller, J.-F., Paton-Walsh, C., Stavrakou, T., and Vigouroux, C. (2016). HCOOH distributions from IASI for 2008–2014: Comparison with ground-based FTIR measurements and a global chemistry-transport model. *Atmospheric Chemistry and Physics*, 16(14):8963–8981.

Pougatchev, N. S., Connor, B. J., and Rinsland, C. P. (1995). Infrared measurements of the ozone vertical distribution above Kitt Peak. *Journal of Geophysical Research*, 100(D8):16689.

Quinn, P. K., Bates, T. S., Baum, E., Doubleday, N., Fiore, A. M., Flanner, M., Fridlind, A., Garrett, T. J., Koch, D., Menon, S., Shindell, D., Stohl, A., and Warren, S. G. (2008). Short-lived

pollutants in the Arctic: Their climate impact and possible mitigation strategies. *Atmospheric Chemistry and Physics*, 8(6):1723–1735.

Quinn, P. K., Miller, T. L., Bates, T. S., Ogren, J. A., Andrews, E., and Shaw, G. E. (2002). A 3-year record of simultaneously measured aerosol chemical and optical properties at Barrow, Alaska. *Journal of Geophysical Research: Atmospheres*, 107(D11).

Quinn, P. K. and Stohl, A. (2015). *AMAP assessment 2015: Black Carbon and Ozone as arctic climate forcers*. Arctic Monitoring and Assessment Programme (AMAP).

Ranjbar, K., O'Neill, N. T., Lutsch, E., McCullough, E. M., AboEl-Fetouh, Y., Xian, P., Strong, K., Fioletov, V. E., Lesins, G., and Abboud, I. (2019). Extreme smoke event over the high Arctic. *Atmospheric Environment*, 218:117002.

Razavi, A., Karagulian, F., Clarisse, L., Hurtmans, D., Coheur, P. F., Clerbaux, C., Müller, J. F., and Stavrakou, T. (2011). Global distributions of methanol and formic acid retrieved for the first time from the IASI/MetOp Thermal Infrared Sounder. *Atmospheric Chemistry and Physics*, 11(2):857–872.

R'Honi, Y., Clarisse, L., Clerbaux, C., Hurtmans, D., Duflot, V., Turquety, S., Ngadi, Y., and Coheur, P.-F. (2013). Exceptional emissions of NH_3 and HCOOH in the 2010 Russian wildfires. *Atmospheric Chemistry and Physics*, 13(8):4171–4181.

Rinsland, C. P., Boughner, R. E., Larsen, J. C., Stokes, G. M., and Brault, J. W. (1984). Diurnal variations of atmospheric nitric oxide: Ground-based infrared spectroscopic measurements and their interpretation with time-dependent photochemical model calculations. *Journal of Geophysical Research*, 89(D6):9613.

Rinsland, C. P., Dufour, G., Boone, C. D., Bernath, P. F., Chiou, L., Coheur, P.-F., Turquety, S., and Clerbaux, C. (2007). Satellite boreal measurements over Alaska and Canada during June-July 2004: Simultaneous measurements of upper tropospheric CO, C_2H_6, HCN, CH_3Cl, CH_4, C_2H_2, CH_3OH, HCOOH, OCS, and SF_6 mixing Ratios. *Global Biogeochemical Cycles*, 21(3):2006GB002795.

Rinsland, C. P., Paton-Walsh, C., Jones, N. B., Griffith, D. W., Goldman, A., Wood, S. W., Chiou, L., and Meier, A. (2005). High spectral resolution solar absorption measurements of ethylene in a forest fire smoke plume using HITRAN parameters: Tropospheric vertical profile retrieval. *Journal of Quantitative Spectroscopy and Radiative Transfer*, 96(2):301–309.

Ritter, C., Notholt, J., Fischer, J., and Rathke, C. (2005). Direct thermal radiative forcing of tropospheric aerosol in the Arctic measured by ground based infrared spectrometry. *Geophysical Research Letters*, 32(23):L23816.

Rodgers, C. D. (1990). Characterization and error analysis of profiles retrieved from remote sounding measurements. *Journal of Geophysical Research*, 95(D5):5587.

Rodgers, C. D. (2000). *Inverse Methods for Atmospheric Sounding: Theory and Practice (Series on Atmospheric, Oceanic and Planetary Physics)*. World Scientific.

Rodgers, C. D. and Connor, B. J. (2003). Intercomparison of remote sounding instruments. *Journal of Geophysical Research: Atmospheres*, 108(D3):4116.

Roiger, A., Schlager, H., Schäfler, A., Huntrieser, H., Scheibe, M., Aufmhoff, H., Cooper, O. R., Sodemann, H., Stohl, A., Burkhart, J., Lazzara, M., Schiller, C., Law, K. S., and Arnold, F. (2011). In-situ observation of Asian pollution transported into the Arctic lowermost stratosphere. *Atmospheric Chemistry and Physics*, 11(21):10975–10994.

Roiger, A., Thomas, J.-L., Schlager, H., Law, K. S., Kim, J., Schäfler, A., Weinzierl, B., Dahlkötter, F., Krisch, I., Marelle, L., Minikin, A., Raut, J.-C., Reiter, A., Rose, M., Scheibe, M., Stock, P., Baumann, R., Bouarar, I., Clerbaux, C., George, M., Onishi, T., and Flemming, J. (2015). Quantifying emerging local anthropogenic emissions in the Arctic region: The ACCESS Aircraft Campaign Experiment. *Bulletin of the American Meteorological Society*, 96(3):441–460.

Rosanka, S., Franco, B., Clarisse, L., Coheur, P.-F., Pozzer, A., Wahner, A., and Taraborrelli, D. (2021). The impact of organic pollutants from indonesian peatland fires on the tropospheric and lower stratospheric composition. *Atmospheric Chemistry and Physics*, 21(14):11257–11288.

Rothman, L., Gordon, I., Babikov, Y., Barbe, A., Chris Benner, D., Bernath, P., Birk, M., Bizzocchi, L., Boudon, V., Brown, L., Campargue, A., Chance, K., Cohen, E., Coudert, L., Devi, V., Drouin, B., Fayt, A., Flaud, J.-M., Gamache, R., Harrison, J., Hartmann, J.-M., Hill, C., Hodges, J., Jacquemart, D., Jolly, A., Lamouroux, J., Le Roy, R., Li, G., Long, D., Lyulin, O., Mackie, C., Massie, S., Mikhailenko, S., Müller, H., Naumenko, O., Nikitin, A., Orphal, J., Perevalov, V., Perrin, A., Polovtseva, E., Richard, C., Smith, M., Starikova, E., Sung, K., Tashkun, S., Tennyson, J., Toon, G., Tyuterev, V., and Wagner, G. (2013). The HITRAN2012 Molecular Spectroscopic Database. *Journal of Quantitative Spectroscopy and Radiative Transfer*, 130:4–50.

Rothman, L. S., Gordon, I. E., Barbe, A., Benner, D., Bernath, P. F., Birk, M., Boudon, V., Brown, L. R., Campargue, A., Champion, J.-P., Chance, K., Coudert, L., Dana, V., Devi, V., Fally, S., Flaud, J.-M., Gamache, R., Goldman, A., Jacquemart, D., Kleiner, I., Lacome, N., Lafferty, W., Mandin, J.-Y., Massie, S., Mikhailenko, S., Miller, C., Moazzen-Ahmadi, N., Naumenko, O., Nikitin, A., Orphal, J., Perevalov, V., Perrin, A., Predoi-Cross, A., Rinsland, C., Rotger, M., Šimečková, M., Smith, M., Sung, K., Tashkun, S., Tennyson, J., Toth, R., Vandaele, A., and Auwera, J. V. (2009). The HITRAN 2008 molecular spectroscopic database. *Journal of Quantitative Spectroscopy and Radiative Transfer*, 110(9-10):533–572.

Rémy, S., Veira, A., Paugam, R., Sofiev, M., Kaiser, J. W., Marenco, F., Burton, S. P., Benedetti, A., Engelen, R. J., Ferrare, R., and Hair, J. W. (2017). Two global data sets of daily fire emission injection heights since 2003. *Atmospheric Chemistry and Physics*, 17(4):2921–2942.

Sansoulet, J., Therrien, M., Delgove, J., Pouxviel, G., Desriac, J., Sardet, N., and Vanderlinden, J.-P. (2020). An update on Inuit perceptions of their changing environment, Qikiqtaaluk (Baffin Island, Nunavut). *Elementa: Science of the Anthropocene*, 8(1):025.

Sawada, S. and Totsuka, T. (1986). Natural and anthropogenic sources and fate of atmospheric ethylene. *Atmospheric Environment*, 20(5):821–832.

Scheepmaker, R. A., Frankenberg, C., Galli, A., Butz, A., Schrijver, H., Deutscher, N. M., Wunch, D., Warneke, T., Fally, S., and Aben, I. (2013). Improved water vapour spectroscopy in the 4174-4300 cm^{-1} region and its impact on SCIAMACHY HDO/H_2O measurements. *Atmospheric Measurement Techniques*, 6(4):879–894.

Schmale, J., Arnold, S. R., Law, K. S., Thorp, T., Anenberg, S., Simpson, W. R., Mao, J., and Pratt, K. A. (2018). Local Arctic air pollution: A neglected but serious problem. *Earth's Future*, 6(10):1385–1412.

Schnell, R. C. (1984). Arctic haze: Editorial. *Geophysical Research Letters*, 11(5):359–359.

Schobesberger, S., Lopez-Hilfiker, F. D., Taipale, D., Millet, D. B., D'Ambro, E. L., Rantala, P., Mammarella, I., Zhou, P., Wolfe, G. M., Lee, B. H., Boy, M., and Thornton, J. A. (2016). High upward fluxes of formic acid from a boreal forest canopy. *Geophysical Research Letters*, 43(17):9342–9351.

Sha, M. K., Langerock, B., Blavier, J.-F. L., Blumenstock, T., Borsdorff, T., Buschmann, M., Dehn, A., De Mazière, M., Deutscher, N. M., Feist, D. G., García, O. E., Griffith, D. W. T., Grutter, M.,

Hannigan, J. W., Hase, F., Heikkinen, P., Hermans, C., Iraci, L. T., Jeseck, P., Jones, N., Kivi, R., Kumps, N., Landgraf, J., Lorente, A., Mahieu, E., Makarova, M. V., Mellqvist, J., Metzger, J.-M., Morino, I., Nagahama, T., Notholt, J., Ohyama, H., Ortega, I., Palm, M., Petri, C., Pollard, D. F., Rettinger, M., Robinson, J., Roche, S., Roehl, C. M., Röhling, A. N., Rousogenous, C., Schneider, M., Shiomi, K., Smale, D., Stremme, W., Strong, K., Sussmann, R., Té, Y., Uchino, O., Velazco, V. A., Vigouroux, C., Vrekoussis, M., Wang, P., Warneke, T., Wizenberg, T., Wunch, D., Yamanouchi, S., Yang, Y., and Zhou, M. (2021). Validation of methane and carbon monoxide from sentinel-5 precursor using tccon and ndacc-irwg stations. *Atmospheric Measurement Techniques*, 14(9):6249–6304.

Shaw, G. (1981). Eddy Diffusion Transport of Arctic pollution from the mid-latitudes: A preliminary model. *Atmospheric Environment (1967)*, 15(8):1483–1490.

Shaw, G. E. (1995). The Arctic Haze Phenomenon. *Bulletin of the American Meteorological Society*, 76(12):2403–2413.

Sheese, P. E., Boone, C. D., and Walker, K. A. (2015). Detecting physically unrealistic outliers in ACE-FTS atmospheric measurements. *Atmospheric Measurement Techniques*, 8(2):741–750.

Shindell, D. and Faluvegi, G. (2009). Climate response to regional radiative forcing during the twentieth century. *Nature Geoscience*, 2(4):294–300.

Shindell, D. T., Chin, M., Dentener, F., Doherty, R. M., Faluvegi, G., Fiore, A. M., Hess, P., Koch, D. M., MacKenzie, I. A., Sanderson, M. G., Schultz, M. G., Schulz, M., Stevenson, D. S., Teich, H., Textor, C., Wild, O., Bergmann, D. J., Bey, I., Bian, H., Cuvelier, C., Duncan, B. N., Folberth, G., Horowitz, L. W., Jonson, J., Kaminski, J. W., Marmer, E., Park, R., Pringle, K. J., Schroeder, S., Szopa, S., Takemura, T., Zeng, G., Keating, T. J., and Zuber, A. (2008). A multi-model assessment of pollution transport to the Arctic. *Atmospheric Chemistry and Physics*, 8(17):5353–5372.

Shindell, D. T., Faluvegi, G., Stevenson, D. S., Krol, M. C., Emmons, L. K., Lamarque, J., Pétron, G., Dentener, F. J., Ellingsen, K., Schultz, M. G., Wild, O., Amann, M., Atherton, C. S., Bergmann, D. J., Bey, I., Butler, T., Cofala, J., Collins, W. J., Derwent, R. G., Doherty, R. M., Drevet, J., Eskes, H. J., Fiore, A. M., Gauss, M., Hauglustaine, D. A., Horowitz, L. W., Isaksen, I. S. A., Lawrence, M. G., Montanaro, V., Müller, J., Pitari, G., Prather, M. J., Pyle, J. A., Rast, S., Rodriguez, J. M., Sanderson, M. G., Savage, N. H., Strahan, S. E., Sudo, K., Szopa, S., Unger,

N., Van Noije, T. P. C., and Zeng, G. (2006). Multimodel simulations of carbon monoxide: Comparison with observations and projected near-future changes. *Journal of Geophysical Research*, 111(D19):2006JD007100.

Shogrin, M. J., Payne, V. H., Kulawik, S. S., Miyazaki, K., and Fischer, E. V. (2023). Measurement report: Spatiotemporal variability of peroxy acyl nitrates (PANs) over Mexico City from TES and CrIS satellite measurements. *Atmospheric Chemistry and Physics*, 23(4):2667–2682.

Simpson, I. J., Akagi, S. K., Barletta, B., Blake, N. J., Choi, Y., Diskin, G. S., Fried, A., Fuelberg, H. E., Meinardi, S., Rowland, F. S., Vay, S. A., Weinheimer, A. J., Wennberg, P. O., Wiebring, P., Wisthaler, A., Yang, M., Yokelson, R. J., and Blake, D. R. (2011). Boreal forest fire emissions in fresh Canadian smoke plumes: C_1-C_{10} volatile organic compounds (VOCs), CO_2, CO, NO_2, NO, HCN, and CH_3CN. *Atmospheric Chemistry and Physics*, 11(13):6445–6463.

Singh, H. B., Herlth, D., O'Hara, D., Zahnle, K., Bradshaw, J. D., Sandholm, S. T., Talbot, R., Crutzen, P. J., and Kanakidou, M. (1992). Relationship of peroxyacetyl nitrate to active and total odd nitrogen at northern high latitudes: influence of reservoir species on NO_x and O_3. *Journal of Geophysical Research*, 97(D15):16523.

Stanevich, I., Jones, D. B. A., Strong, K., Parker, R. J., Boesch, H., Wunch, D., Notholt, J., Petri, C., Warneke, T., Sussmann, R., Schneider, M., Hase, F., Kivi, R., Deutscher, N. M., Velazco, V. A., Walker, K. A., and Deng, F. (2020). Characterizing model errors in chemical transport modeling of methane: Impact of model resolution in versions V9-02 of GEOS-Chem and V35j of its adjoint model. *Geoscientific Model Development*, 13(9):3839–3862.

Stavrakou, T., Guenther, A., Razavi, A., Clarisse, L., Clerbaux, C., Coheur, P.-F., Hurtmans, D., Karagulian, F., De Mazière, M., Vigouroux, C., Amelynck, C., Schoon, N., Laffineur, Q., Heinesch, B., Aubinet, M., Rinsland, C., and Müller, J.-F. (2011). First space-based derivation of the global atmospheric methanol emission fluxes. *Atmospheric Chemistry and Physics*, 11(10):4873–4898.

Stavrakou, T., Müller, J.-F., Peeters, J., Razavi, A., Clarisse, L., Clerbaux, C., Coheur, P.-F., Hurtmans, D., De Mazière, M., Vigouroux, C., Deutscher, N. M., Griffith, D. W. T., Jones, N., and Paton-Walsh, C. (2012). Satellite evidence for a large source of formic acid from boreal and tropical forests. *Nature Geoscience*, 5(1):26–30.

Stohl, A. (2006). Characteristics of atmospheric transport into the arctic troposphere. *Journal of Geophysical Research: Atmospheres*, 111(D11):2005JD006888.

Stohl, A., Klimont, Z., Eckhardt, S., Kupiainen, K., Shevchenko, V. P., Kopeikin, V. M., and Novigatsky, A. N. (2013). Black Carbon in the Arctic: The underestimated role of gas flaring and residential combustion emissions. *Atmospheric Chemistry and Physics*, 13(17):8833–8855.

Sussmann, R., Forster, F., Rettinger, M., and Jones, N. (2011). Strategy for high-accuracy-and-precision retrieval of atmospheric methane from the mid-infrared ftir network. *Atmospheric Measurement Techniques*, 4(9):1943–1964.

Sutton, M. A., Oenema, O., Erisman, J. W., Leip, A., van Grinsven, H., and Winiwarter, W. (2011). Too much of a good thing. *Nature*, 472(7342):159–161.

Talukdar, R. K., Burkholder, J. B., Schmoltner, A.-M., Roberts, J. M., Wilson, R. R., and Ravishankara, A. R. (1995). Investigation of the loss processes for peroxyacetyl nitrate in the atmosphere: UV photolysis and reaction with OH. *Journal of Geophysical Research*, 100(D7):14163.

Tereszchuk, K. A., González Abad, G., Clerbaux, C., Hadji-Lazaro, J., Hurtmans, D., Coheur, P.-F., and Bernath, P. F. (2013). ACE-FTS observations of pyrogenic trace species in boreal biomass burning plumes during BORTAS. *Atmospheric Chemistry and Physics*, 13(9):4529–4541.

Tie, X., Guenther, A., and Holland, E. (2003). Biogenic methanol and its impacts on tropospheric oxidants. *Geophysical Research Letters*, 30(17):1881.

Tikhonov, A. N. (1963). On the solution of ill-posed problems and the method of regularization. *Dokl. Akad. Nauk*, 151(3):501–504.

Toon, G. C. (2015). Atmospheric Line List for the 2014 TCCON Data Release. https://data.caltech.edu/records/248.

Toon, G. C. (2022). Atmospheric Voigt Line List for the TCCON 2020 Data Release. https://data.caltech.edu/records/8972.

Toon, G. C., Blavier, J.-F., Sung, K., Rothman, L. S., and E. Gordon, I. (2016). HITRAN spectroscopy evaluation using solar occultation FTIR spectra. *Journal of Quantitative Spectroscopy and Radiative Transfer*, 182:324–336.

Toon, G. C., Blavier, J.-F. L., and Sung, K. (2018). Measurements of atmospheric ethene by solar absorption FTIR spectrometry. *Atmospheric Chemistry and Physics*, 18(7):5075–5088.

Toon, G. C., Farmer, C. B., Schaper, P. W., Lowes, L. L., and Norton, R. H. (1992). Composition measurements of the 1989 Arctic Winter Stratosphere by airborne infrared solar absorption spectroscopy. *Journal of Geophysical Research*, 97(D8):7939.

Torres, O., Bhartia, P. K., Taha, G., Jethva, H., Das, S., Colarco, P., Krotkov, N., Omar, A., and Ahn, C. (2020). Stratospheric injection of massive smoke plume from Canadian boreal fires in 2017 as seen by DSCOVR-EPIC, CALIOP, and OMPS-LP observations. *Journal of Geophysical Research: Atmospheres*, 125(10):e2020JD032579.

Tuazon, E. C., Carter, W. P., and Atkinson, R. (1991). Thermal decomposition of peroxyacetyl nitrate and reactions of acetyl peroxy radicals with nitric oxide and nitrogen dioxide over the temperature range 283-313 K. *The Journal of Physical Chemistry*, 95(6):2434–2437.

Tzompa-Sosa, Z. A., Mahieu, E., Franco, B., Keller, C. A., Turner, A. J., Helmig, D., Fried, A., Richter, D., Weibring, P., Walega, J., Yacovitch, T. I., Herndon, S. C., Blake, D. R., Hase, F., Hannigan, J. W., Conway, S., Strong, K., Schneider, M., and Fischer, E. V. (2017). Revisiting global fossil fuel and biofuel emissions of ethane. *Journal of Geophysical Research: Atmospheres*, 122(4):2493–2512.

Van Der Werf, G. R., Randerson, J. T., Giglio, L., Van Leeuwen, T. T., Chen, Y., Rogers, B. M., Mu, M., Van Marle, M. J. E., Morton, D. C., Collatz, G. J., Yokelson, R. J., and Kasibhatla, P. S. (2017). Global Fire Emissions Estimates during 1997–2016. *Earth System Science Data*, 9(2):697–720.

Vander Auwera, J., Fayt, A., Tudorie, M., Rotger, M., Boudon, V., Franco, B., and Mahieu, E. (2014). Self-broadening coefficients and improved line intensities for the ν_7 band of ethylene near 10.5 μm, and impact on ethylene retrievals from jungfraujoch solar spectra. *Journal of Quantitative Spectroscopy and Radiative Transfer*, 148:177–185.

Veefkind, J., Aben, I., Mcmullan, K., Förster, H., Vries, J. D., Otter, G., Claas, J., Eskes, H., Haan, J. D., Kleipool, Q., Weele, M. V., Hasekamp, O., Hoogeveen, R., Landgraf, J., Snel, R., Tol, P., Ingmann, P., Voors, R., Kruizinga, B., Vink, R., Visser, H., and Levelt, P. (2012). TROPOMI on the ESA Sentinel-5 Precursor: A GMES mission for global observations of the atmospheric composition for climate, air quality and ozone layer applications. *Remote Sens. Environ.*, 120:70–83.

Viatte, C., Strong, K., Hannigan, J., Nussbaumer, E., Emmons, L. K., Conway, S., Paton-Walsh,

C., Hartley, J., Benmergui, J., and Lin, J. (2015). Identifying fire plumes in the Arctic with tropospheric FTIR measurements and transport models. *Atmospheric Chemistry and Physics*, 15(5):2227–2246.

Viatte, C., Strong, K., Paton-Walsh, C., Mendonca, J., O'Neill, N. T., and Drummond, J. R. (2013). Measurements of CO, HCN, and C_2H_6 total columns in smoke plumes transported from the 2010 Russian boreal forest fires to the Canadian high Arctic. *Atmosphere-Ocean*, 51(5):522–531.

Viatte, C., Strong, K., Walker, K. A., and Drummond, J. R. (2014). Five years of CO, HCN, C_2H_6, C_2H_2, CH_3OH, HCOOH, and H_2CO total columns measured in the Canadian high Arctic. *Atmospheric Measurement Techniques*, 7(6):1547–1570.

Vidot, J., Landgraf, J., Hasekamp, O., Butz, A., Galli, A., Tol, P., and Aben, I. (2012). Carbon monoxide from shortwave infrared reflectance measurements: A new retrieval approach for clear sky and partially cloudy atmospheres. *Remote Sens. Environ.*, 120:255–266.

Vigouroux, C., Bauer Aquino, C. A., Bauwens, M., Becker, C., Blumenstock, T., De Mazière, M., García, O., Grutter, M., Guarin, C., Hannigan, J., Hase, F., Jones, N., Kivi, R., Koshelev, D., Langerock, B., Lutsch, E., Makarova, M., Metzger, J.-M., Müller, J.-F., Notholt, J., Ortega, I., Palm, M., Paton-Walsh, C., Poberovskii, A., Rettinger, M., Robinson, J., Smale, D., Stavrakou, T., Stremme, W., Strong, K., Sussmann, R., Té, Y., and Toon, G. (2018). NDACC harmonized formaldehyde time series from 21 FTIR stations covering a wide range of column abundances. *Atmospheric Measurement Techniques*, 11(9):5049–5073.

Vigouroux, C., Hendrick, F., Stavrakou, T., Dils, B., De Smedt, I., Hermans, C., Merlaud, A., Scolas, F., Senten, C., Vanhaelewyn, G., Fally, S., Carleer, M., Metzger, J.-M., Müller, J.-F., Van Roozendael, M., and De Mazière, M. (2009). Ground-based FTIR and Max-DOAS observations of formaldehyde at Réunion Island and comparisons with satellite and model data. *Atmospheric Chemistry and Physics*, 9(24):9523–9544.

Vigouroux, C., Langerock, B., Aquino, C. A. B., Blumenstock, T., Cheng, Z., Mazière, M. D., Smedt, I. D., Grutter, M., Hannigan, J. W., Jones, N., Kivi, R., Loyola, D., Lutsch, E., Mahieu, E., Makarova, M., Metzger, J.-M., Morino, I., Murata, I., Nagahama, T., Notholt, J., Ortega, I., Palm, M., Pinardi, G., Röhling, A., Smale, D., Stremme, W., Strong, K., Sussmann, R., Té, Y., Roozendael, M. V., Wang, P., and Winkler, H. (2020). TROPOMI–Sentinel-5 Precursor formaldehyde validation using an extensive network of ground-based Fourier-transform infrared stations. *Atmospheric Measurement Techniques*, 13(7):3751–3767.

Vigouroux, C., Mazière, M. D., Demoulin, P., Servais, C., Hase, F., Blumenstock, T., Kramer, I., Schneider, M., Mellqvist, J., Strandberg, A., Velazco, V., Notholt, J., Sussmann, R., Stremme, W., Rockmann, A., Gardiner, T., Coleman, M., and Woods, P. (2008). Evaluation of tropospheric and stratospheric ozone trends over Western Europe from ground-based FTIR network observations. *Atmospheric Chemistry and Physics*, 8(23):6865–6886.

Vigouroux, C., Stavrakou, T., Whaley, C., Dils, B., Duflot, V., Hermans, C., Kumps, N., Metzger, J.-M., Scolas, F., Vanhaelewyn, G., Müller, J.-F., Jones, D. B. A., Li, Q., and De Mazière, M. (2012). FTIR time-series of biomass burning products (HCN, C_2H_6, C_2H_2, CH_3OH, and HCOOH) at Reunion Island (21° S, 55° E) and comparisons with model Data. *Atmospheric Chemistry and Physics*, 12(21):10367–10385.

Wassmann, A., Borsdorff, T., Brugh, J. M. J. A. D., Hasekamp, O. P., Aben, I., and Landgraf, J. (2015). The direct fitting approach for total ozone column retrievals: a sensitivity study on GOME-2/MetOp-A measurements. *Atmospheric Measurement Techniques*, 8(10):4429–4451.

Weatherhead, E., Gearheard, S., and Barry, R. (2010). Changes in weather persistence: Insight from Inuit knowledge. *Global Environmental Change*, 20(3):523–528.

Weaver, D., Strong, K., Walker, K. A., Sioris, C., Schneider, M., McElroy, C. T., Vömel, H., Sommer, M., Weigel, K., Rozanov, A., Burrows, J. P., Read, W. G., Fishbein, E., and Stiller, G. (2019). Comparison of ground-based and satellite measurements of water vapour vertical profiles over Ellesmere Island, Nunavut. *Atmospheric Measurement Techniques*, 12(7):4039–4063.

Wells, K. C., Millet, D. B., Cady-Pereira, K. E., Shephard, M. W., Henze, D. K., Bousserez, N., Apel, E. C., De Gouw, J., Warneke, C., and Singh, H. B. (2014). Quantifying global terrestrial methanol emissions using observations from the TES satellite sensor. *Atmospheric Chemistry and Physics*, 14(5):2555–2570.

Wentworth, G. R., Aklilu, Y.-a., Landis, M. S., and Hsu, Y.-M. (2018). Impacts of a large boreal wildfire on ground level atmospheric concentrations of PAHs, VOCs and Ozone. *Atmospheric Environment*, 178:19–30.

Whaley, C. H., Law, K. S., Hjorth, J. L., Skov, H., Arnold, S. R., Langner, J., Pernov, J. B., Bergeron, G., Bourgeois, I., Christensen, J. H., Chien, R.-Y., Deushi, M., Dong, X., Effertz, P., Faluvegi, G., Flanner, M., Fu, J. S., Gauss, M., Huey, G., Im, U., Kivi, R., Marelle, L., Onishi, T., Oshima, N., Petropavlovskikh, I., Peischl, J., Plummer, D. A., Pozzoli, L., Raut, J.-C., Ryerson,

T., Skeie, R., Solberg, S., Thomas, M. A., Thompson, C., Tsigaridis, K., Tsyro, S., Turnock, S. T., von Salzen, K., and Tarasick, D. W. (2023). Arctic tropospheric ozone: assessment of current knowledge and model performance. *Atmospheric Chemistry and Physics*, 23(1):637–661.

Whaley, C. H., Mahmood, R., Von Salzen, K., Winter, B., Eckhardt, S., Arnold, S., Beagley, S., Becagli, S., Chien, R.-Y., Christensen, J., Damani, S. M., Dong, X., Eleftheriadis, K., Evangeliou, N., Faluvegi, G., Flanner, M., Fu, J. S., Gauss, M., Giardi, F., Gong, W., Hjorth, J. L., Huang, L., Im, U., Kanaya, Y., Krishnan, S., Klimont, Z., Kühn, T., Langner, J., Law, K. S., Marelle, L., Massling, A., Olivié, D., Onishi, T., Oshima, N., Peng, Y., Plummer, D. A., Popovicheva, O., Pozzoli, L., Raut, J.-C., Sand, M., Saunders, L. N., Schmale, J., Sharma, S., Skeie, R. B., Skov, H., Taketani, F., Thomas, M. A., Traversi, R., Tsigaridis, K., Tsyro, S., Turnock, S., Vitale, V., Walker, K. A., Wang, M., Watson-Parris, D., and Weiss-Gibbons, T. (2022). Model evaluation of short-lived climate forcers for the Arctic Monitoring and Assessment Programme: A multi-species, multi-model study. *Atmospheric Chemistry and Physics*, 22(9):5775–5828.

Whitburn, S., Van Damme, M., Clarisse, L., Hurtmans, D., Clerbaux, C., and Coheur, P.-F. (2017). IASI-derived NH_3 enhancement ratios relative to CO for the tropical biomass burning regions. *Atmospheric Chemistry and Physics*, 17(19):12239–12252.

Whitburn, S., Van Damme, M., Clarisse, L., Turquety, S., Clerbaux, C., and Coheur, P.-F. (2016). Doubling of annual ammonia emissions from the peat fires in Indonesia during the 2015 El Niño. *Geophysical Research Letters*, 43(20):11007–11014.

Whitburn, S., Van Damme, M., Kaiser, J., van der Werf, G., Turquety, S., Hurtmans, D., Clarisse, L., Clerbaux, C., and Coheur, P.-F. (2015). Ammonia emissions in tropical biomass burning regions: Comparison between satellite-derived emissions and bottom-up fire inventories. *Atmospheric Environment*, 121:42–54.

Wittrock, F., Richter, A., Oetjen, H., Burrows, J. P., Kanakidou, M., Myriokefalitakis, S., Volkamer, R., Beirle, S., Platt, U., and Wagner, T. (2006). Simultaneous global observations of glyoxal and formaldehyde from space. *Geophysical Research Letters*, 33(16):L16804.

Wizenberg, T., Strong, K., Jones, D. B., Lutsch, E., Mahieu, E., Franco, B., and Clarisse, L. (2023). Exceptional Wildfire Enhancements of PAN, C_2H_4, CH_3OH, and HCOOH Over the Canadian High Arctic During August 2017. *Journal of Geophysical Research: Atmospheres*, 128(10):e2022JD038052.

Wizenberg, T., Strong, K., Walker, K. A., Lutsch, E. M., Borsdorff, T., and Landgraf, J. (2021). Intercomparison of CO measurements from TROPOMI, ACE-FTS, and a high-arctic ground-based Fourier transform spectrometer. *Atmospheric Measurement Techniques*, 14(12):7707–7728.

Wofsy, S. C., Sachse, G. W., Gregory, G. L., Blake, D. R., Bradshaw, J. D., Sandholm, S. T., Singh, H. B., Barrick, J. A., Harriss, R. C., Talbot, R. W., Shipham, M. A., Browell, E. V., Jacob, D. J., and Logan, J. A. (1992). Atmospheric chemistry in the Arctic and subarctic: Influence of natural fires, industrial emissions, and stratospheric inputs. *Journal of Geophysical Research*, 97(D15):16731.

Wohl, C., Jones, A. E., Sturges, W. T., Nightingale, P. D., Else, B., Butterworth, B. J., and Yang, M. (2022). Sea ice concentration impacts dissolved organic gases in the Canadian Arctic. *Biogeosciences*, 19(4):1021–1045.

Worden, H. M., Deeter, M. N., Frankenberg, C., George, M., Nichitiu, F., Worden, J., Aben, I., Bowman, K. W., Clerbaux, C., Coheur, P. F., De Laat, A. T. J., Detweiler, R., Drummond, J. R., Edwards, D. P., Gille, J. C., Hurtmans, D., Luo, M., Martínez-Alonso, S., Massie, S., Pfister, G., and Warner, J. X. (2013). Decadal record of satellite carbon monoxide observations. *Atmospheric Chemistry and Physics*, 13(2):837–850.

Wunch, D., Toon, G. C., Blavier, J.-F. L., Washenfelder, R. A., Notholt, J., Connor, B. J., Griffith, D. W. T., Sherlock, V., and Wennberg, P. O. (2011). The Total Carbon Column Observing Network. *Philos. Trans. R. Soc. A*, 369(1943):2087–2112.

Xiao, Y., Jacob, D. J., and Turquety, S. (2007). Atmospheric acetylene and its relationship with CO as an indicator of air mass age. *Journal of Geophysical Research*, 112(D12):2006JD008268.

Xiao, Y., Logan, J. A., Jacob, D. J., Hudman, R. C., Yantosca, R., and Blake, D. R. (2008). Global budget of ethane and regional constraints on U.S. sources. *Journal of Geophysical Research*, 113(D21):2007JD009415.

Yamanouchi, S., Strong, K., Colebatch, O., Conway, S., Jones, D. B., Lutsch, E., and Roche, S. (2021). Atmospheric Trace gas trends obtained from FTIR column measurements in Toronto, Canada from 2002-2019. *Environmental Research Communications*, 3(5):051002.

Yamanouchi, S., Strong, K., Lutsch, E., and Jones, D. B. (2020). Detection of HCOOH, CH_3OH, CO, HCN, and C_2H_6 in wildfire plumes transported over Toronto using ground-based FTIR measurements from 2002–2018. *Journal of Geophysical Research: Atmospheres*, 125(16):e2019JD031924.

Yang, H., Waugh, D. W., Orbe, C., and Chen, G. (2020). Dependence of atmospheric transport into the Arctic on the meridional extent of the Hadley Cell. *Geophysical Research Letters*, 47(20):e2020GL090133.

Yang, M., Nightingale, P. D., Beale, R., Liss, P. S., Blomquist, B., and Fairall, C. (2013). Atmospheric deposition of methanol over the Atlantic Ocean. *Proceedings of the National Academy of Sciences*, 110(50):20034–20039.

Yu, K., Keller, C. A., Jacob, D. J., Molod, A. M., Eastham, S. D., and Long, M. S. (2018). Errors and improvements in the use of archived meteorological data for chemical transport modeling: An analysis using GEOS-Chem V11-01 driven by GEOS-5 meteorology. *Geoscientific Model Development*, 11(1):305–319.

Yu, P., Toon, O. B., Bardeen, C. G., Zhu, Y., Rosenlof, K. H., Portmann, R. W., Thornberry, T. D., Gao, R.-S., Davis, S. M., Wolf, E. T., De Gouw, J., Peterson, D. A., Fromm, M. D., and Robock, A. (2019). Black carbon lofts wildfire smoke high into the stratosphere to form a persistent plume. *Science*, 365(6453):587–590.

Yurganov, L. N. (1997). Seasonal cycles of carbon monoxide over the Arctic and Antarctic: total columns versus surface data. *Atmos. Res.*, 44(1-2):223–230.

Zander, R., Duchatelet, P., Mahieu, E., Demoulin, P., Roland, G., Servais, C., Auwera, J. V., Perrin, A., Rinsland, C. P., and Crutzen, P. J. (2010). Formic acid above the Jungfraujoch during 1985–2007: Observed variability, seasonality, but no long-term background evolution. *Atmospheric Chemistry and Physics*, 10(20):10047–10065.

Zellweger, C., Hüglin, C., Klausen, J., Steinbacher, M., Vollmer, M., and Buchmann, B. (2009). Inter-comparison of four different carbon monoxide measurement techniques and evaluation of the long-term carbon monoxide time series of Jungfraujoch. *Atmospheric Chemistry and Physics*, 9(11):3491–3503.

Zhang, L., Jacob, D. J., Boersma, K. F., Jaffe, D. A., Olson, J. R., Bowman, K. W., Worden, J. R., Thompson, A. M., Avery, M. A., Cohen, R. C., Dibb, J. E., Flock, F. M., Fuelberg, H. E., Huey, L. G., McMillan, W. W., Singh, H. B., and Weinheimer, A. J. (2008). Transpacific transport of ozone pollution and the effect of recent Asian emission increases on air quality in North America: An integrated analysis using satellite, aircraft, ozonesonde, and surface observations. *Atmospheric Chemistry and Physics*, 8(20):6117–6136.

Zhang, X., Liu, J., Han, H., Zhang, Y., Jiang, Z., Wang, H., Meng, L., Li, Y. C., and Liu, Y. (2020). Satellite-observed variations and trends in carbon monoxide over Asia and their sensitivities to biomass burning. *Remote Sensing*, 12(5):830.

Zhao, T., Mao, J., Simpson, W. R., De Smedt, I., Zhu, L., Hanisco, T. F., Wolfe, G. M., St. Clair, J. M., González Abad, G., Nowlan, C. R., Barletta, B., Meinardi, S., Blake, D. R., Apel, E. C., and Hornbrook, R. S. (2022). Source and variability of formaldehyde (HCHO) at Northern High Latitudes: An integrated satellite, aircraft, and model study. *Atmospheric Chemistry and Physics*, 22(11):7163–7178.

Zhao, Y., Strong, K., Kondo, Y., Koike, M., Matsumi, Y., Irie, H., Rinsland, C. P., Jones, N. B., Suzuki, K., Nakajima, H., Nakane, H., and Murata, I. (2002). Spectroscopic measurements of tropospheric CO, C_2H_6, C_2H_2, and HCN in northern Japan. *Journal of Geophysical Research: Atmospheres*, 107(D18):ACH 2–1–ACH 2–16.

Zheng, B., Chevallier, F., Yin, Y., Ciais, P., Fortems-Cheiney, A., Deeter, M. N., Parker, R. J., Wang, Y., Worden, H. M., and Zhao, Y. (2019). Global Atmospheric Carbon Monoxide Budget 2000–2017 inferred from multi-species atmospheric inversions. *Earth System Science Data*, 11(3):1411–1436.

Zhou, M., Langerock, B., Vigouroux, C., Sha, M. K., Hermans, C., Metzger, J.-M., Chen, H., Ramonet, M., Kivi, R., Heikkinen, P., Smale, D., Pollard, D. F., Jones, N., Velazco, V. A., García, O. E., Schneider, M., Palm, M., Warneke, T., and Mazière, M. D. (2019). TCCON and NDACC XCO measurements: difference, discussion and application. *Atmospheric Measurement Techniques*, 12(11):5979–5995.

Zhu, L., Val Martin, M., Gatti, L. V., Kahn, R., Hecobian, A., and Fischer, E. V. (2018). Development and implementation of a new biomass burning emissions injection height scheme (BBEIH v1.0) for the GEOS-chem model (V9-01-01). *Geoscientific Model Development*, 11(10):4103–4116.